4

THE UNIVERSITY OF
WARWICK

Calcium Carbonate Growth and Dissolution to the Nanoscale

Lucy Ann Bindley

A thesis submitted for the degree of Doctor of Philosophy

Department of Chemistry
University of Warwick

September 2005

Table of Contents

List of Figures and Tables

Acknowledgements

I would like to extend my thanks firstly to my supervisors, Pat Unwin and Julie Macpherson. Pat has been a continual source of enthusiasm, the infectiousness of which I am eternally grateful, and I thank both him and Julie for their support, encouragement, expertise and feedback over the past three years. Thanks also to Alex Ashcroft, Julie Das and the Unilever team for the opportunity to complete this project, their help throughout and some lovely dinners.

I would like to thank the members of the Warwick Electrochemistry and Interfaces Group who I have had the pleasure (and displeasure) of working with, for their constant friendship, fun, knowledge and abuse. The original group took me under their wing, showed me the ropes, and it has been great making new friends and meeting new people as the group has evolved.

Thanks must go to everyone in the mechanical, electronic and glass blowing workshops, who contributed greatly to the construction of the specially designed apparatus used in this project. Special thanks must go to Steve York, for his SEM expertise and for amusing me on bored Friday afternoons, and Dave Robinson in Engineering for his help with many interferometry problems.

Thanks to my friends, the social workers, Jen and Laura, who made my life over the past three years more real, and less defined by science and logic. Thanks must also go to Ray and the girls at Haileybury who have provided me with laughs, trivia and wine whilst finishing this off. And finally, thanks to my family and of course, Steve, without whose support, encouragement and laughter, I'd never have made it.

Declaration

The work contained in this thesis is entirely original and my own work, except where specifically acknowledged otherwise. In Chapter 3, the hexanethiol-stabilised gold nanoparticles were prepared by Dr Vicky Ruiz. In Chapter 7, work involving the effect of a weak acid inhibitor on calcite growth was performed in collaboration with Dr Phillip Dobson.

I confirm that this thesis has not been submitted for a degree at another university. Parts of this thesis have been accepted or submitted for publication with the following references:

P. S. Dobson, L. A. Bindley, J. V. Macpherson and P. R. Unwin, Atomic Force Microscopy (AFM) Investigation of the Mechanism of Calcite Microcrystal Growth under Kitano Conditions, *Langmuir*, **2005**, *21*, 1255.

L. A. Bindley, V. Ruiz, P. R. Unwin, Functionalized Gold Nanoparticles as Seeds for the Template-Formation of Calcite – submitted for publication.

P. S. Dobson, L. A. Bindley, J. V. Macpherson and P. R. Unwin, Modes of Action of a Weak Acid Modifier of Calcite Growth – submitted for publication.

Abstract

This thesis describes three examples of how the functionality of a growth surface affects the crystallisation of $CaCO_3$; investigates the dissolution of calcium carbonates and phosphates on the microscale; and describes a new atomic force microscopy (AFM) method which has been used to investigate the reactivity of the (104) surface of single calcite microcrystals.

Growth surfaces bearing carboxylic acid- functionalised nanoparticles were prepared by deposition onto glass using a layer-by-layer method with poly(allylamine) hydrochloride as the cross linker. These surfaces were found to influence the extent of $CaCO_3$ crystallisation, which increased with nanoparticle surface coverage. For these nucleation experiments, two crystal growth techniques were used: the Kitano method, in which the supersaturation of the growth solution slowly increased with time; and a jet crystallisation method, incorporating the mixing of two undersaturated solutions to create a supersaturated solution which was jetted onto the surface of interest via a specially designed cell. Calcite was the predominant $CaCO_3$ polymorph formed on these surfaces, with a high proportion of the crystals nucleating on the (015) plane rather than on the stable (104) plane, thus showing that nanoparticles have an orientational effect on $CaCO_3$ crystallisation.

Functionalisation of gold surfaces was achieved via the deposition of self-assembled monolayers (SAMs) and the effect of an applied potential on $CaCO_3$ nucleation was investigated. Application of a potential more negative than the potential of zero charge to any of the functionalised SAM surfaces resulted in the inhibition of $CaCO_3$ nucleation, whereas at more positive potentials, extensive vaterite growth was evident. These studies showed that the extent of $CaCO_3$ nucleation could be tuned readily via the applied potential.

E. coli bacterial biofilms served as substrates for experiments with direct implications on household care. The biofilms dramatically affected the crystallisation of $CaCO_3$, first by acting as nucleation centres for growth, and, secondly, causing significant surface and structural damage to the crystals formed. Stabilisation of crystals from unusual nucleating planes, (012) and (015), was also evident.

As a new approach for investigating proton-promoted dissolution, an ultramicroelectrode was used to direct a flux of protons towards a calcite surface, by the oxidation of water. Etch pit analysis revealed that the pit volumes increased with increasing proton flux, in a linear fashion. Modelling this process using the finite element method allowed the rate constant for dissolution to be calculated. Dissolution of more complex calcium carbonate and phosphate simulated limescale pellets was also addressed using this technique, allowing the reactivity of a range of materials to be ranked.

AFM, combined with an inverted optical microscope, was used to study the growth of individual surfaces of calcite (104) microcrystals, which were shown to exhibit a single spiral growth hillock. Growth rates of the individual spirals were found to be dependent on solution supersaturation and controlled by diffusion of species to the crystal from bulk solution. The step patterns formed were shown to depend strongly on the supersaturation. This methodology also allowed the effects of maleic acid, as a crystal growth inhibitor, to be monitored.

Abbreviations

Abbreviation	Description
AFM	Atomic force microscopy
BCF	Burton, Cabrera and Frank theory
C-AFM	Conducting atomic force microscopy
cfu	Colony forming unit
CLSM	Confocal laser scanning microscopy
DAQ	Data acquisition card
DIC	Differential contrast interference
DMSO	Dimethyl sulfoxide
EDTA	Ethylenediaminetetra-acetic acid
EM	Electron microscopy
EPS	Extracellular polymeric substances
FE-SEM	Field emission scanning electron microscopy
FTIR	Fourier transform infra-red spectroscopy
HAP	Hydroxyapatite
HEDP	1-Hydroxyethane-1,1-diphosphonic acid
ID	Inner diameter
KSV	Kossel, Stranski and Volmer theory
LbL	Layer by layer
LM	Light microscopy
MPC	Monolayer protected cluster
MUA	Mercaptoundecanoic acid

OD	Outer diameter
OHP	Outer Helmholtz Plane
PAH	Poly(allylamine hydrochloride)
PC	Personal computer
PTFE	Polytetrafluoroethylene
PSS	Poly(styrene sulfonic acid) sodium salt
PZC	Potential of zero charge
SAM	Self-assembled monolayer
SHE	Standard hydrogen electrode
SCE	Saturated calomel electrode
SEM	Scanning electron microscopy
SECM	Scanning electrochemical microscopy
SPM	Scanning probe microscopy
STM	Scanning tunnelling microscopy
TEM	Transmission electron microscopy
TSA	Tryptic soy agar
UME	Ultramicroelectrode
WSH	Water of standard hardness

Glossary of Symbols

Symbol	Description
a	Radius of electrode
A	Electrode area
b	Interfacial tension between cluster and solution constant
c^*	Bulk concentration
C	Concentration
C_e	Equilibrium concentration
d	Step height
D	Diffusion coefficient
F	Faraday's constant
ΔG	Free energy change
i	Current
i_T	Tip current
i_∞	Steady state current
j	Flux
k	Rate constant
k_B	Boltzmann constant
K_s	Solubility product
M_w	Molecular weight
n	Number of electrons
r	Radius of a cylinder
r_{glass}	Radius of glass sheath of electrode

R	Growth rate
RG	Ratio of radius of electrode to radius of insulating sheath
S	Supersaturation
t	Time
T	Temperature
x	Charge on ion
y	Step width
z	Crystal size
z_c	Critical crystal size
α	Area shape factor constant
ε	Molar absorptivity
γ	Activity coefficient
μ	Chemical potential
ρ	Density
σ, β	Supersaturation ratio
ν	Lateral step velocity
υ	Solution viscosity

Chapter 1

Introduction

This chapter begins with an introduction to crystal growth, focusing in particular on calcium carbonate as a model system. The mechanisms and kinetics of crystal growth and dissolution are detailed and the effect of surface functionality on the nucleation of calcium carbonate on foreign surfaces is described, where self-assembled monolayers and bacterial biofilms are addressed specifically. Finally, methods of characterisation and analysis of surfaces used in this thesis are described, including scanned probe microscopies, electron microscopy and confocal laser scanning microscopy.

1.1 Calcium carbonate ($CaCO_3$) crystal structure and morphology

Calcium carbonate has been studied extensively due to its importance in industrial[1,2], technological[3,4], biological[5] and geological[6] areas. It is a highly abundant natural mineral, which forms the building block of many shells and exo-skeletal features due to its high lattice energy and low solubility[7], through a process termed biomineralisation[8,9]. It is also important in global carbon dioxide exchange, energy storage and forms strong interactions with heavy metals in the environment[10].

There are six calcium carbonate minerals, each with the same principal composition but different structure[11]. Three of these are hydrated forms[12]; calcium carbonate monohydrate, calcium carbonate hexahydrate and amorphous calcium carbonate. The three non-hydrated polymorphs are calcite, from the Greek 'chalix' meaning lime, aragonite and vaterite. When calcium carbonate nucleates the predominance of each polymorph varies depending on the temperature, pressure, salinity

and any impurities present during growth[13,14]. Calcite is, however, the thermodynamically most stable polymorph[15] which, along with aragonite, accounts for the majority of the world's carbon reserves. Vaterite is the least thermodynamically stable polymorph of calcium carbonate, despite being the most kinetically favourable[7]. When it forms, it tends to rapidly transform to calcite via a solution-mediated process[7,14].

The typical morphology and crystal structure of calcite is shown in Figure 1-1 although the crystal size and shape may be modified by the use of chemical additives[16,17]. Calcite has a perfect (104) rhombohedral cleavage plane (the atomic arrangement is shown in Figure 1-2) indicating that the cleaved surface is of low energy. The surface structure of cleaved calcite has been extensively studied using atomic force microscopy (AFM)[18,19] and the elemental step height has been found to be 0.33 nm[20]. Figure 1-3 shows a scanning electron microscopy (SEM) image of a typical calcite crystal which clearly shows the rhombohedral geometry.

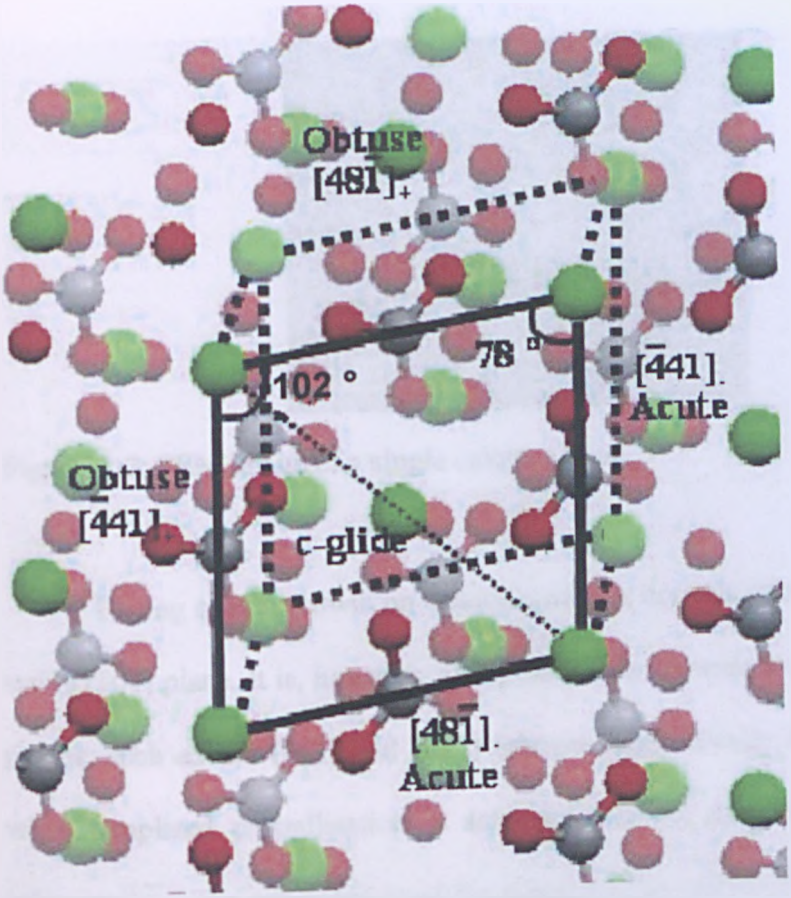

Figure 1-1: Schematic of the calcite unit cell. Green: calcium, grey: carbon, red: oxygen.

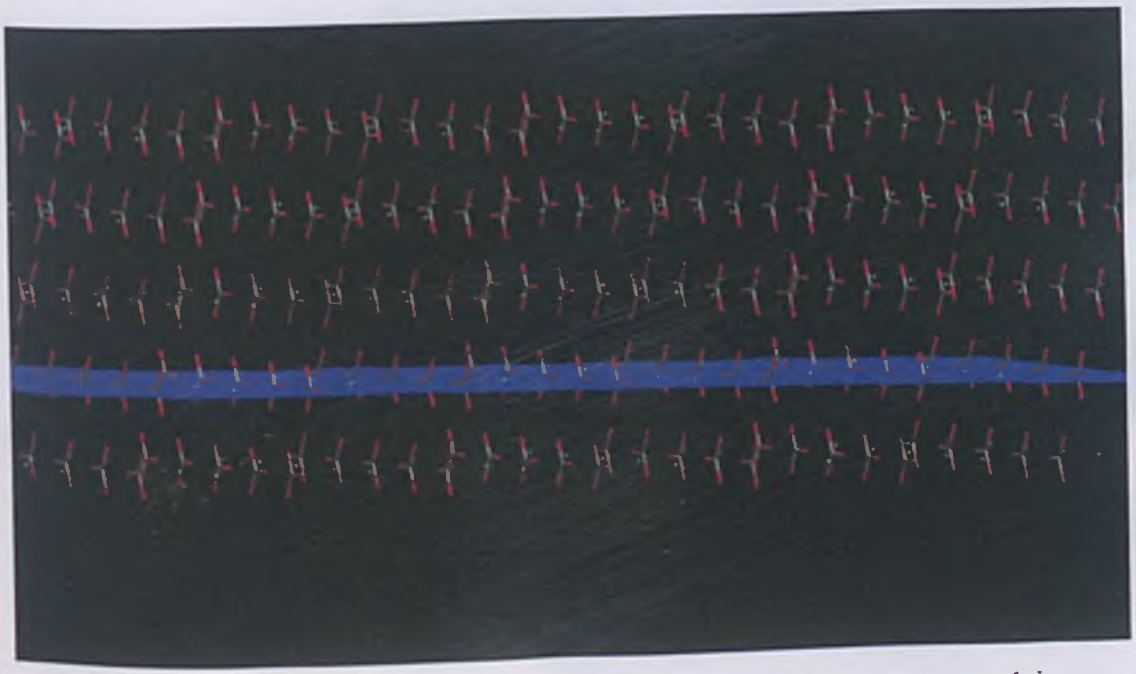

Figure 1-2: The arrangement of atoms on the (104) plane of calcite. Green: calcium, grey: carbon, red: oxygen.

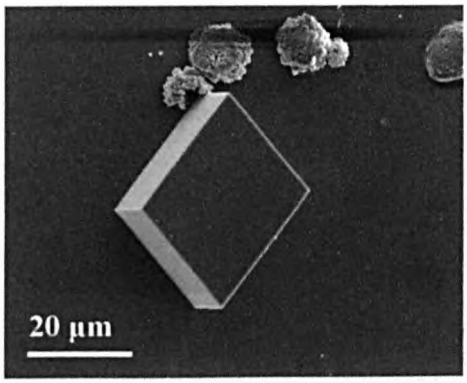

Figure 1-3: SEM image of a single calcite crystal.

During calcite growth on foreign surfaces, crystals usually nucleate on the large, stable (104) plane. It is, however, also possible for crystals to nucleate on more unusual planes, such as the (012) and (015) (shown schematically in Figure 1-4), especially when templated crystallisation is achieved, via the functionalisation of the growth substrate[21,22]. The arrangement of the atoms on the surface of these planes is shown in Figures 1-5 and 1-6.

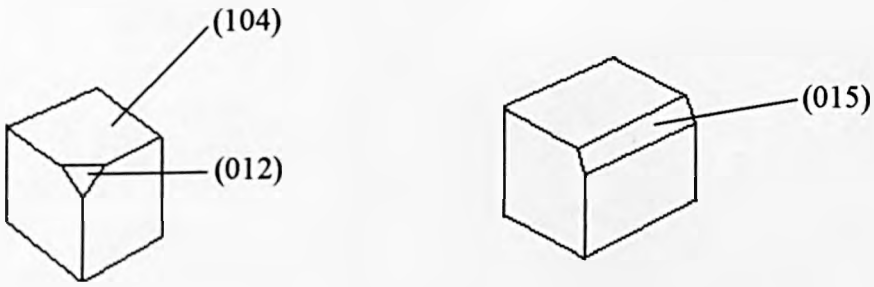

Figure 1-4: Schematic showing calcite planes of nucleation.

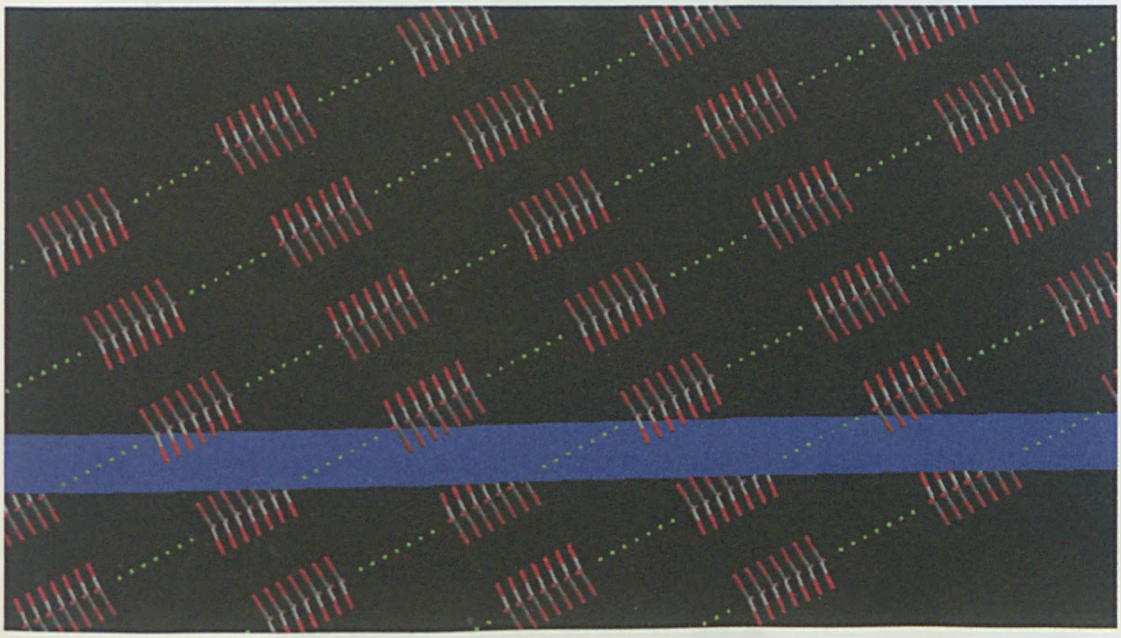

Figure 1-5: The arrangement of atoms on the (012) plane of calcite. Green: calcium, grey: carbon, red: oxygen.

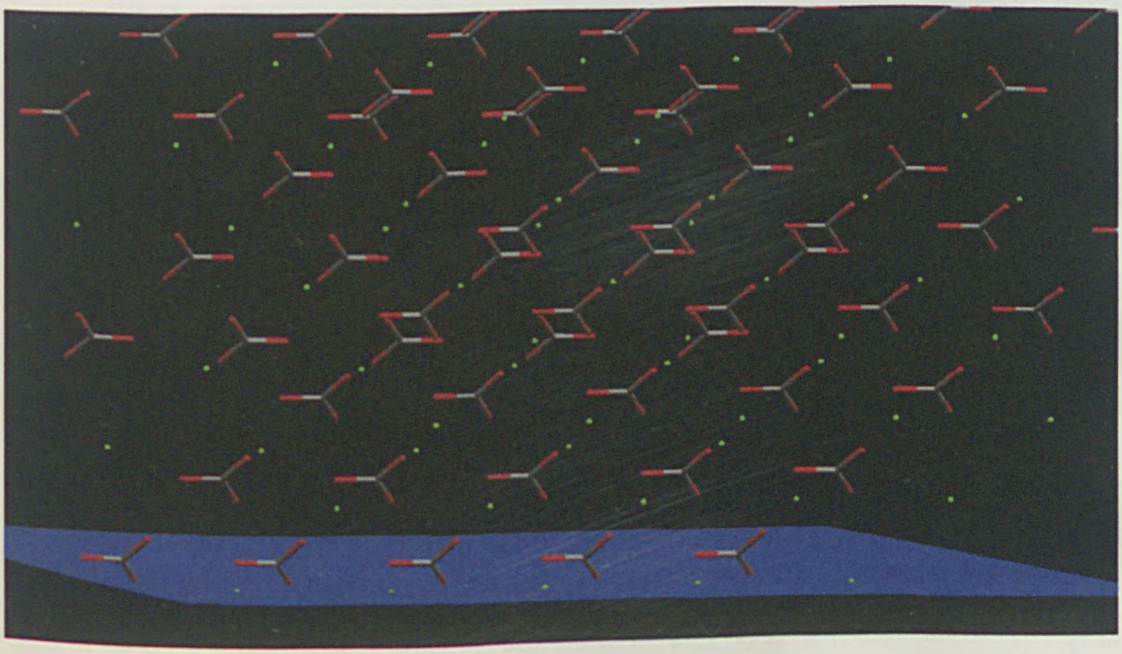

Figure 1-6: The arrangement of atoms on the (015) plane of calcite. Green: calcium, grey: carbon, red: oxygen.

Aragonite is the second most thermodynamically stable polymorph of calcium carbonate[7]. It crystallises in the orthorhombic system and shows poor cleavage characteristics, in contrast to calcite[11]. Figure 1-7 shows an SEM image of a typical aragonite crystal.

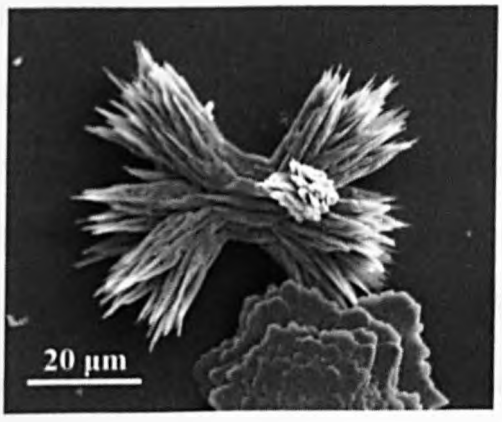

Figure 1-7: SEM image of an aragonite crystal.

Vaterite is the metastable hexagonal form of calcium carbonate and therefore the rarest[7]. It is, however, formed at ambient temperature and pressure before converting readily to aragonite or calcite[23]. Figure 1-8 shows an SEM image of a typical vaterite crystal.

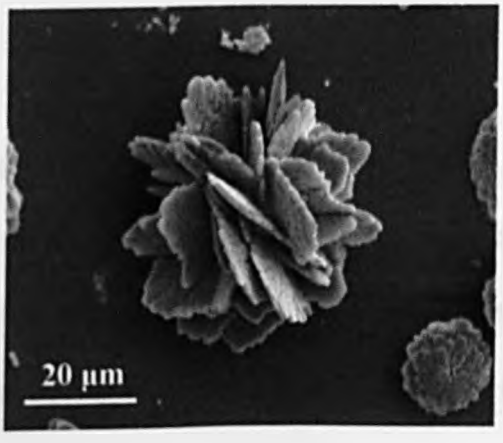

Figure 1-8: SEM image of a vaterite crystal.

1.2 Calcium phosphate

Another common calcium mineral is calcium phosphate, which is observed in several different forms[7] including hydroxyapatite, $Ca_5(PO_4)_3OH$, tricalcium phosphate, $Ca_3(PO_4)_2$, and dicalcium phosphate, $Ca_2HPO_4.2H_2O$.

Hydroxyapatite (HAP) is the most common form of calcium phosphate and is found in bones and tooth enamel[24]. Although formation of this phosphate is very slow and depends on the ionic strength, supersaturation of the growth solution and type of electrolyte present[25] it is the most thermodynamically stable calcium phosphate salt.

The kinetics of nucleation and crystal growth of HAP[26], especially under the influence of monosaccharides and related molecules[27], has been widely studied in relation to coatings for orthopaedic and dental metallic implants[28,29,30,31,32]. In particular, HAP has been found to promote bone growth on titanium implants due to the similarity in chemical composition between bone and calcified cartilage[33]. Kinetics of the crystal growth of HAP have been found to correlate with the Burton-Cabrera-Frank (BCF) theory for spiral growth, as for calcium carbonate[34]. This mechanism is discussed in detail later.

1.3 Scale formation

Calcium carbonates and phosphates form major components of what is commonly termed 'limescale'. The formation of scale is mainly due to the deposition of calcium carbonate and phosphate minerals onto a substrate surface, especially in areas of hard, mineral-containing water[10]. Deposition of scale on pipes and machinery is of

importance in industry, e.g. in desalination plants[23], as the cleaning of pipes in an effort to dissolve the scale is a time-consuming and costly process[4,35,36].

Furthermore, an understanding of the fundamentals of the scaling process impinges on products related to household care, such as the deposition and removal of scale in toilet and water systems[37]. This scale has been found to consist mainly of calcium phosphate along with calcium carbonate and trace minerals including magnesium ammonium phosphates as well as minor quantities of C14-C18 fatty acids, cholesterol and other organic matter[38]. The calcium carbonate and magnesium ammonium phosphates tend to combine to form carbonate-containing apatite.

1.4 Crystal nucleation and growth

In this section, mechanisms of crystal nucleation and growth from solution are described, with particular reference to the calcium carbonate system.

1.4.1 Supersaturation

For crystal nucleation and growth to occur in solution, the solution must be supersaturated with respect to the material of interest. This occurs when the concentration of the species within a solution is increased beyond the solubility product of the solid[39]. There are several practical ways of attaining a supersaturated solution[40], and these include: (i) the evaporation of the solvent, to leave behind a highly supersaturated solution; (ii) cooling or heating of the solution – if the solubility of the solute decreases with increasing temperature, as with calcium carbonate, then heating the solution will lead to an increase in supersaturation; (iii) changing the pH; and (iv)

mixing solutions containing highly soluble species, ultimately leading to the precipitation of a sparingly soluble species.

For a one-component system, the thermodynamic driving force, expressed in terms of the chemical potential ($\Delta\mu$), for crystal nucleation in solution, is governed by the difference in chemical potential of a molecule in the supersaturated solution and saturated solution, respectively, and can be written as:

$$\Delta\mu = k_B T \ln (C / C_e) \tag{1-1}$$

Here, C is the concentration in solution, C_e is the equilibrium concentration, T is the temperature and k_B is the Boltzmann constant. For this one-component system, it is thus possible to define a supersaturation by two, dimensionless terms, given here in Equations 1-2 and 1-3.

$$\beta = C / C_e \tag{1-2}$$

$$\sigma = (C - C_e) / C_e \tag{1-3}$$

As ionic solutes are dissociated in electrolytic solutions, it is common practice to use activities instead of concentrations for calculating supersaturations, leading to Equation 1-4 which describes the supersaturation of a simple 1:1 salt, such as $CaCO_3$. Here, S is the supersaturation, K_s is the solubility constant for the material of interest and γ_A and γ_B are activity coefficients of the solvated ions, A and B, which have charges of $+x$ and $-x$ respectively.

$$S = \left[\frac{\gamma_A \left(A^{+x}\right) \gamma_B \left(B^{-x}\right)}{K_s} \right]^{1/2} \quad (1\text{-}4)$$

Figure 1-9 shows a hypothetical solubility curve[39]. From this, it can be seen that crystals can only grow if a solution is supersaturated; this occurs when $S > 1$, when the solution is supersaturated with respect to the growth surface. A solution whose composition lies below the C_e curve, is undersaturated. Here, when $S < 1$, crystals do not grow from solution, although exisiting crystals do dissolve. At low supersaturations, in the metastable region, existing crystals tend to continue to grow, but the nucleation of new crystals is rare. Once a critical supersaturation is reached, crystals then form spontaneously.

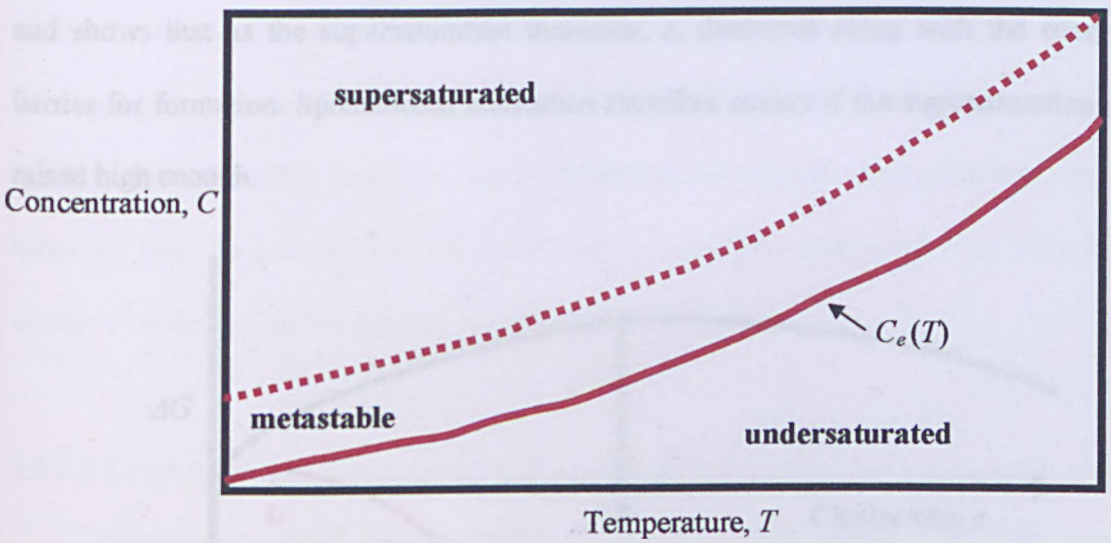

Figure 1-9: Hypothetical solubility curve, of concentration versus temperature.

If the supersaturation is high, the rate of nucleation is fast, but when it exceeds a certain limit, the rate at which atoms or molecules can be incorporated into the crystal

lattice may be exceeded, resulting in dendritic growth[41]. Therefore, an optimum level of supersaturation must be achieved and maintained in order to achieve relatively uniform crystal growth.

At the optimum supersaturation, interactions between the molecules and ions in solution result in the formation of clusters which increase in size until a critical size, z_c, is reached. The free energy change of the system, ΔG, is related to the crystal size (z) by Equation 1-5, where α is an area shape factor, dependent on the nucleus shape, and b is the interfacial tension between the cluster and the solution[39].

$$\Delta G = -zkT\sigma + \alpha bz^{2/3} \quad (1\text{-}5)$$

Figure 1-10 shows a plot of ΔG against z, at two supersaturations (high and low) and shows that as the supersaturation increases, z_c decreases along with the energy barrier for formation. Spontaneous nucleation therefore occurs if the supersaturation is raised high enough.

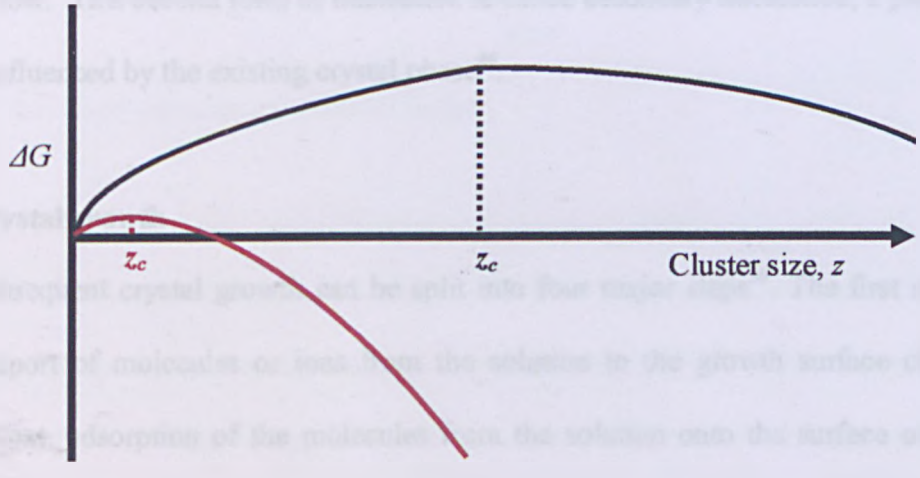

Figure 1-10: Plot to show ΔG as a function of cluster size, z, at a high (red) and low (black) supersaturation.

At the optimum supersaturation, z_c is the cluster size at which further growth will lead to a decrease in free energy; at sizes lower than z_c, a decrease in the free energy is only obtainable via dissolution of the crystal. Growth of critical clusters around one another results in the spontaneous nucleation of the molecules on the surface. Sustained growth can then occur at the surface via the addition of new material[39].

1.4.2 Crystal nucleation and growth mechanisms

1.4.2.1 Crystal nucleation

Two forms of nucleation can occur during the growth of crystals, once supersaturation is achieved[42]. The first is termed primary nucleation, where the crystal forms independently of the existing solid crystal phase. If this occurs homogeneously, it does so without the influence of any existing solid phase[43]. This occurs rarely and only under certain conditions, in pure solutions at high supersaturations. If it occurs heterogeneously, however, it is often catalysed by the presence of a foreign solid phase (such as the walls of the vessel, or dust particles) and occurs when the supersaturation is relatively low. This second form of nucleation is called secondary nucleation, a process which is influenced by the existing crystal phase[44].

1.4.2.2 Crystal growth

Subsequent crystal growth can be split into four major steps[39]. The first is the mass transport of molecules or ions from the solution to the growth surface of the crystal. Next, adsorption of the molecules from the solution onto the surface occurs along with the partial loss of any solvent. Thirdly, the molecules diffuse along the

surface to a position of low energy, usually a kink site. Here, incorporation of the molecules or ions into the crystal lattice occurs along with the loss of any remaining solvent[45].

The processes which could limit the growth rate thus include adsorption, dissociation and desorption at the growth surface, the mobility of the reactants and products on the surface and the incorporation of the atoms or molecules at lattice sites[46]. The slowest step determines the rate of crystal growth, although all steps often combine to control the rate[47].

Usually, the crystal surface will have many defect sites such as kinks and steps (see Figure 1-11), which act as sites for surface integration.

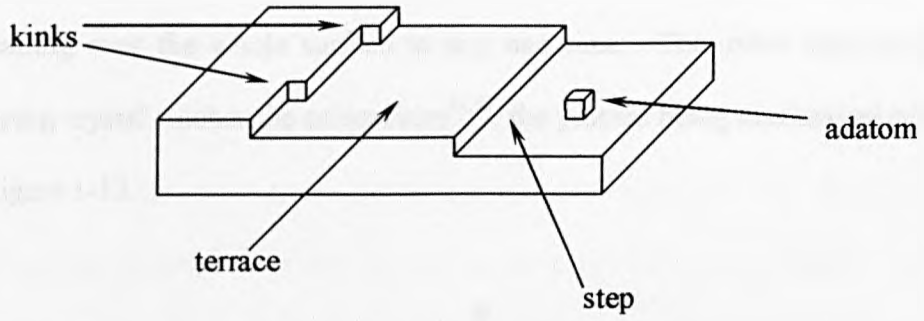

Figure 1-11: Representation of a crystal surface.

In 1939, Kossel, Stranski and Volmer (KSV) devised the first nucleation theory which was to be the basis of modern crystal nucleation theory[48,49,50]. KSV theory states that the maximum binding energy between an adatom and the crystal lattice surface occurs for the incorporation at a kink in a surface ledge (three bonds are made between

the incoming adatom and the surface) and so a kink site is the most energetically favoured incorporation site. At any point on the ledge the binding energy will be greater (two bonds can be made with the surface) than for an adatom attached to the flat surface (only one bond is made between the adatom and surface). This results in there being preferential crystal growth firstly at kink sites, then steps and finally terraces[39].

1.4.2.3 Crystal growth by 2D nucleation

2D nucleation can occur when molecules or ions adsorb onto planar surfaces[51]. Once the molecules or ions have reached a critically sized cluster they can diffuse to the existing crystal face. As this becomes stable, it begins to exhibit kink sites which provide ideal positions into which more nuclei can be incorporated. Here mononuclear growth may occur with a whole new crystal surface being produced by one nucleus spreading over the whole surface at any one time. This often happens just as the growing crystal reaches the critical size[52,53], the process being represented schematically in Figure 1-12.

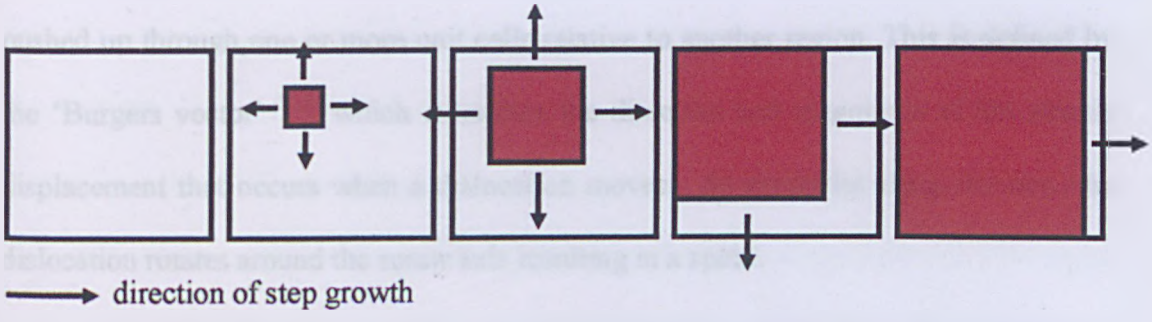

Figure 1-12: Schematic to show the process of mononuclear 2D crystal growth.

Polynuclear growth (Figure 1-13) also occurs quite readily when new nuclei form on incompletely covered terraces whilst other nuclei are still growing[47].

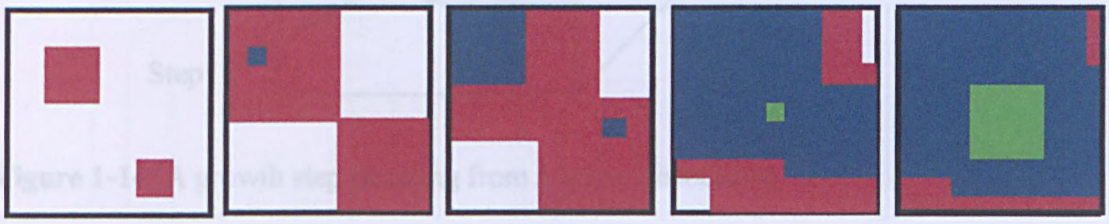

Figure 1-13: Schematic to show the process of polynuclear 2D crystal growth.

1.4.2.4 Crystal growth from a screw dislocation

Following KSV, Burton, Cabrera and Frank presented their work which showed how the emergence of dislocations with screw components at crystal surfaces acted as continuous generators of surface ledges, thus helping the crystal surface to remain as a low energy nucleation site[54,55]. A screw dislocation is a defect that propagates through a surface resulting from a defect in the bulk crystal lattice, as shown in Figure 1-14. These defects can arise from the incorporation of impurities into the crystal or from rapid crystal growth[56]. The screw dislocation occurs where one region of the crystal is pushed up through one or more unit cells relative to another region. This is defined by the 'Burgers vector' [56,57] which quantifies the direction and magnitude of the atomic displacement that occurs when a dislocation moves. As atoms lie along the step, the dislocation rotates around the screw axis resulting in a spiral.

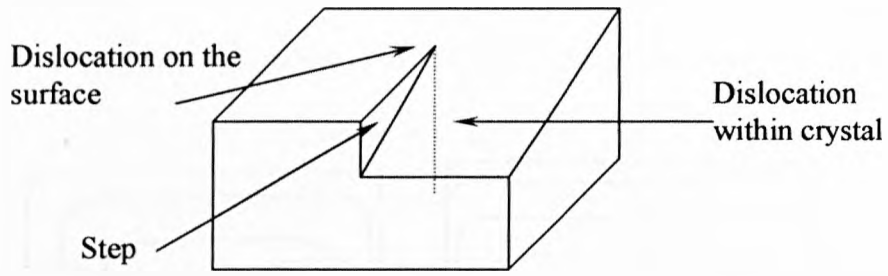

Figure 1-14: A growth step resulting from a screw dislocation.

The growth resulting from the addition of material to a screw dislocation produces a spiral pattern, as shown in Figure 1-15.

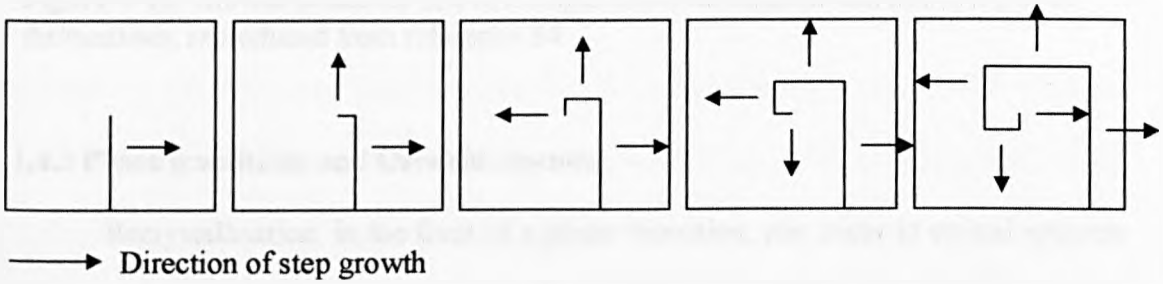

Figure 1-15: Formation of a growth spiral from a screw dislocation.

BCF provided the first theoretical treatment of crystal growth by a screw dislocation in 1951[58], including the outcomes for one dislocation and where two dislocations occur together (Figure 1-16). They showed that the growth rate (R) normal to a spiral face can be calculated from Equation 1-6 where v is the lateral step velocity, d is the height of the step, and y is the step width.

$$R = vd / y \qquad (1\text{-}6)$$

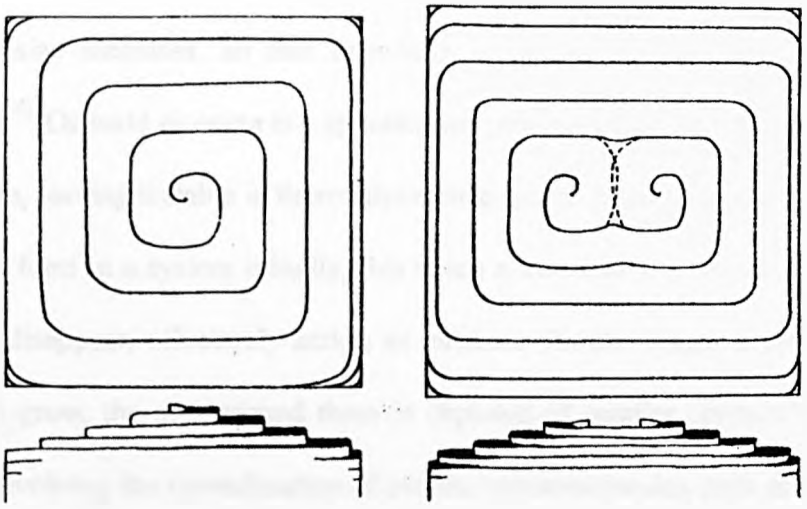

Figure 1-16: Growth pyramids due to a single screw dislocation and due to a pair of dislocations; reproduced from reference 54.

1.4.3 Phase transitions and Ostwald ripening

Recrystallisation, in the form of a phase transition, can occur in crystal systems due to a decrease in nucleation rate and growth kinetics[40]. The process involves the change in size or shape of a crystal by dissolution and re-precipitation, or surface integration, and occurs in order to minimise energy in the system. Although one crystal phase is usually more stable than others, it is unlikely that this phase will form first (when there are two or more possible phases). The first phase to crystallise will be the metastable phase, which, due to resulting changes in the solution supersaturation, will recrystallise and transform to the more stable phase[59]. This process was first documented by Ostwald, in 1897, and is referred to as the 'Rule of Stages'[60,61].

With crystals of the same structure and composition (same polymorph) in solution, a different transition can occur, which is termed 'Ostwald ripening'[60,62]. Here, the number of crystals of the same phase in a closed system decreases, while the mean crystal size increases, so that eventually, if given enough time, only one crystal remains[40]. Ostwald ripening is a spontaneous process which acts to reduce the energy of a system, leaving it stable in thermodynamical terms. It has been shown that many small crystals form in a system initially, this being a kinetically favoured process. They then slowly disappear, effectively acting as nutrients for the bigger crystals. As the larger crystals grow, the area around them is depleted of smaller crystals. Examples of this effect involving the crystallisation of protein macromolecules such as α- amylase, show that when the supersaturation is very high, crystallisation is clearly accompanied by the occurrence of depletion zones around the growing crystals, indicative of Ostwald ripening[63]. This, however, should not be confused with phase transitions where, in the case of thaumatin, crystallisation has been shown to occur by a simple phase transfer mechanism, which is never accompanied by the disappearance of the smallest crystals[63].

1.4.4 Calcium carbonate crystal growth

The kinetics of nucleation and growth of calcium carbonate has been studied extensively over the years, as both a model system and from a practical viewpoint with regards to the need to control its precipitation. Calcium carbonate is used extensively as a filler material, so there are specific requirements on particle shape and size distribution[64]. In this context, Liu et al.[65] used dynamic light scattering to follow the nucleation and size of crystal nuclei in situ, while Compton and Brown used rotating

disc electrodes to monitor particle sizes[66], as this was shown to influence mass transport to the electrode. Many studies have involved growing crystals under a variety of pH's, where the pH has been used to determine induction times[67,68] thereby allowing the kinetics of precipitation to be followed[69,70,71], over a wide range of supersaturations[72] and with the incorporation of various inhibitors[73,74,75].

Kinetics of calcium carbonate precipitation have been measured[76] using various different techniques, including channel-flow methods[77], continuous crystallisers[78] and light scattering techniques which measure the crystal size distribution as a function of time[79]. Spanos and Koutsoukos measured the kinetics of calcium carbonate precipitation in alkaline pH at constant supersaturation, taking into account both seeded and unseeded growth[68], using the most commonly used free-drift growth measurements. Cassford et al. measured the seeded crystallisation kinetics of calcite from calcium bicarbonate solutions between 278.15 and 303.15 K[80], and Shiraki and Brantley conducted their measurements at 373 K[81]. House investigated the same crystallisation process at 298.15 K[82,83] and Buhmann and Dreybodt examined the reaction kinetics under conditions of geologically relevant karst areas[84]. Kinetic measurements have, more recently, been made using AFM measurements of surface reactivity, at low supersaturations, where crystal surface growth kinetics, rather than particulate precipitation rates, have been deduced[85,86].

In 1997, Simpson[87] electrodeposited calcium carbonate scale from karstic waters onto the high pH surface of an iron electrode held at highly reducing potentials, before using FTIR spectroscopy to identify the phases of calcium carbonate formed. In the late 1990's, Gabrielli et al.[88,89] employed this same deposition technique using the gold

electrodes of an electrochemical quartz crystal microbalance to determine the nucleation rate and surface coverage of calcium carbonate. The effects of surface pretreatments on nucleation, including the scale-inhibiting properties of phosphonates such as HEDP (1-hydroxyethane-1,1-diphosphonic acid)[90], iron (III)[91], which is a very effective scale inhibitor and benzotriazoles[92], which have been used successfully for over 25 years in copper pipelines, have also been investigated using this technique.

1.4.5 Kitano growth of calcium carbonate crystals

A method for the growth of calcium carbonate microcrystals was first detailed by Kitano[93] in 1969 and has been used in many applications since[94,95]. Dobson et al. have recently elucidated the mechanism of calcite microcrystal reactivity under Kitano conditions using AFM, which can be related to the changing supersaturation of the Kitano solution[96]. The process itself (see Equations 1-6 to 1-10) involves saturating a solution of calcium carbonate with CO_2, so that high concentrations of Ca^{2+} and HCO_3^- are formed in solution.

$$CO_{2\,(g)} \leftrightarrow CO_{2\,(aq)} \tag{1-6}$$

$$CO_{2\,(aq)} + H_2O_{\,(l)} \leftrightarrow H_2CO_{3\,(aq)} \tag{1-7}$$

$$H_2CO_{3\,(aq)} \leftrightarrow H^+_{\,(aq)} + HCO_3^-{}_{(aq)} \tag{1-8}$$

$$2HCO_3^-{}_{(aq)} \leftrightarrow CO_{2\,(g)} + CO_3^{2-}{}_{(aq)} + H_2O_{\,(l)} \tag{1-9}$$

$$Ca^{2+}{}_{(aq)} + CO_3^{2-}{}_{(aq)} \leftrightarrow CaCO_{3\,(s)} \tag{1-10}$$

When CO_2 is subsequently allowed to evolve from the solution, an increase in pH results, which leads to an increase in the supersaturation of the solution with respect to calcium carbonate. This promotes the formation of microcrystals at the air/solution interface and other interfaces within the reaction vessel. Microcrystals that form are often a mixture of calcite, vaterite and aragonite; the proportion of each is dependent on the time allowed for crystallisation. If left for long enough, calcite will be the predominant polymorph formed due to it being the most thermodynamically stable. Calcite crystals will form from aragonite and vaterite crystals via the process of recrystallisation, in order to minimise the energy of the system. When aragonite and vaterite structures form, they have a relatively large surface area, resulting in a large surface energy making it thermodynamically favourable for these polymorphs to undergo a phase transition, to form the more compact calcite phase.

Work confirming this recrystallisation theory in $CaCO_3$ has been carried out by Ogina et al. who showed that transformations of calcium carbonate proceeded via the dissolution of the metastable aragonite and vaterite phases and the growth of calcite, the rate-determining step being the formation of the stable calcite phase[97].

1.4.6 Calcium carbonate crystallisation on functionalised surfaces

There is much literature regarding the template-directed nucleation of $CaCO_3$, with work focusing on interfaces including: (i) compressed Langmuir monolayers[98,99] where nucleating crystals show increased size and uniformity compared with those nucleated under fully compressed films[100]; (ii) various self-assembled monolayer (SAM) assemblies[94,101,102, 103,104,105,106,107,108,109,110], where notably, intricate patterns of single

calcite crystals have been produced by alternately patterning methyl and carboxylic acid functionalised SAMs onto the support[111]; (iii) polymeric substrates[112,113,114,115,116], and patterned polymer surfaces, where the crystallisation of the calcite polymorph of $CaCO_3$ was found to be favoured after molecularly imprinting the polymer surface with calcite[117]; (iv) liquid-liquid interfaces[118]; and finally (v) nanoparticle prints[119], where Lee et al. have shown that carboxylic acid functionalised gold nanoparticle membranes can be used as nucleation directors for controlled $CaCO_3$ growth[120], enabling $CaCO_3$ films of different conformations and polymorphs to be manufactured[121].

In this section, SAMs and bacterial biofilms will be described, with emphasis on their roles as possible calcium carbonate nucleation directors.

1.4.6.1 Self-assembled monolayers

Self-assembled monolayers were first discovered in 1946, when a paper by Zisman detailed the preparation of a monomolecular layer by adsorption[122]. Since this discovery, there has been extensive research into the characterisation and development of SAMs for various different applications, particularly in the last twenty-five years[123,124,125,126].

SAMs are usually made using thiol-terminated molecules on gold as the relatively strong S-Au bond serves to attach the molecules to the gold substrate. This allows the other end of the alkyl chain to be suitably functionalised in order to provide various properties. Figure 1-17 shows a schematic of the arrangement of a short chained aliphatic SAM with a carboxylic acid termination.

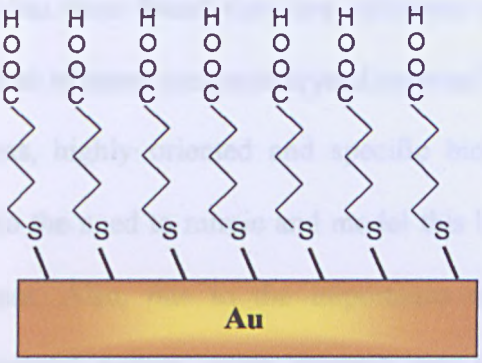

Figure 1-17: Schematic representation of a carboxylic acid-terminated SAM on a gold support.

SAMs with more than 12 carbon atoms in the backbone chain form well-ordered, dense monolayers on Au (111) surfaces[127]. Thiols attach primarily to 3-fold hollow sites on the gold surface[127]. The distance between these pinning sites is 5 Å, so that there is 21.4 $Å^2$ available area for each molecule. The van der Waals diameter of the alkane chain is too small, at 4.6 Å, to completely occupy that area and so the chain tilts by 30 ° with respect to the surface normal[127].

Early work focused on the use of chlorosilanes to hydrophobise glass[128], and in 1983 Nuzzo and Allara showed that SAMs of alkanethiols on gold could be prepared from dilute solutions by adsorption of di-*n*-alkyl disulfides[129]. To date, monolayers of alkanethiols on gold remain the most commonly investigated assemblies[127]. This can be attributed to the fact that monolayers which form on gold surfaces display a densely packed, and often very highly ordered, structure[127]. Since the end groups of the molecules can be tailored to allow the SAM to exhibit a variety of surface properties, such as polarity and hydrophobicity, they have become widely studied in the area of

crystal growth where it has been found that they influence the morphology, density, crystal habit and orientation of many inorganic crystal systems[22,130,131,132,133,134].

In natural systems, highly oriented and specific biological mineralisation is easily achievable[7], and so the need to mimic and model this behaviour synthetically is becoming more important. Also, due to the importance of calcium carbonate, in particular, as a model crystal system, much research into the controlled, templated crystallisation of $CaCO_3$ on various SAMs is underway[102,105,106,110,121,127,135,136,137,138,139,140,141].

1.4.6.2 Crystallisation of $CaCO_3$ on SAM functionalised surfaces

Much work in the field of templated crystallisation using SAMs has been performed by Küther et al. who, in 1998, attempted to model the biomineralisation process by crystallising the three main $CaCO_3$ polymorphs from solution on ώ-substituted alkythiols on gold, at two different temperatures[101]. It was found that at 22 °C, both vaterite and calcite crystals were formed, and at a higher temperature of 45 °C, the aragonite polymorph was also stable, possibly due to the increased rate of decomposition of ammonium carbonate in the solution, resulting in a higher supersaturation. After performing experiments using ten SAMs with differently functionalised head groups, it was found that the nucleation of $CaCO_3$ increased with the polarity of the SAM interface – crystallisation occurred faster and at a higher density when carboxylic acid-terminated SAMs were used compared to methyl-terminated groups.

Notably, in 1999, Aizenberg et al. showed that $CaCO_3$ crystal nucleation could be controlled with the use of patterned SAMs[106]. SAMs of varying functionalities were deposited on gold and silver surfaces and it was found that with carboxylic and hydroxyl functionalised SAMs on both substrates, calcite was the predominantly nucleated calcium carbonate polymorph. The SAMs also appeared to control the orientation of the calcite crystals, with nucleation occurring mostly on the (015) axis with CO^{2-}/Au, and on the stable (104) plane with the OH/Au surfaces. It was also observed that the degree of orientation upon crystallisation was dependent on the time that the substrates were left in the SAM solution (1 minute – 24 hours), showing this response to be solely due to the effect of the SAM. This phenomenon was attributed to the close match between the orientation of the head groups of the SAM and the carbonate groups of the crystal in the specific morphologies.

It has also been shown that patterned crystallisation could be achieved by patterning carboxylic acid- and methyl- terminated SAMs onto metal substrates by microcontact printing with an elastomeric stamp[102]. Calcite crystals were found to form on CO_2H- terminated SAMs preferentially, allowing specific templating to be achieved. This was attributed to the fact that rapidly nucleating regions (carboxylic acid-terminated regions) slowed the rate of mass transport of solution components to slower nucleating regions (methyl- terminated sections), thus in turn allowing highly oriented crystallisation to be restricted solely to carboxylate- terminated regions of SAMs[142].

The so-called 'odd/even' effect has been the subject of more recent work[105]. It has been shown that for alkanethiols, $(SH(CH_2)_nX)$ when n is odd, the terminal group forms a different angle with the interface than when n is even, with the effect that

calcium carbonate is crystallised on different faces. On silver surfaces, the parity of the chain length has no effect whereas on gold, the head groups of the SAMs are at different angles as shown in the schematic in Figure 1-18.

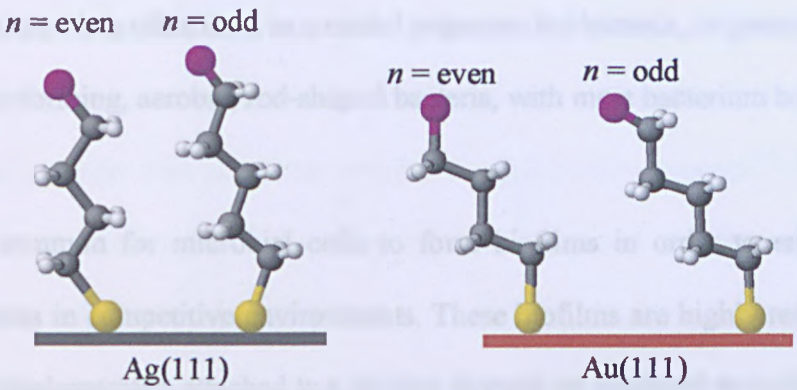

Figure 1-18: Schematic representation of odd and even SAM chain lengths on gold and silver (111) surfaces.

Preliminary experiments[105] have shown that odd length alkylthiols on gold template calcite growth on the (013) nucleating plane whereas the even length alkylthiols induce growth from the (113) plane. A schematic representation of crystals grown from these nucleating planes is shown in Figure 1-19.

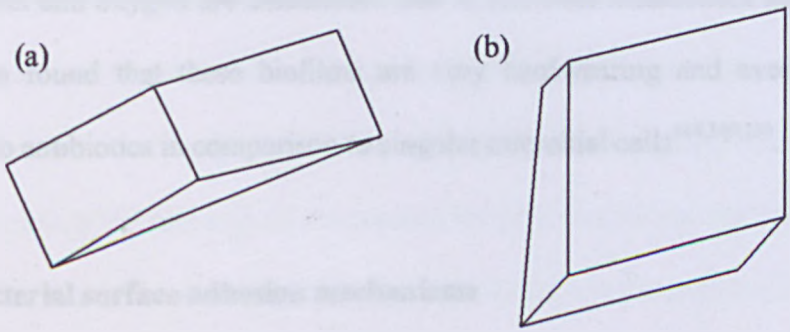

Figure 1-19: Representation of calcite crystals grown on: (a) the (013) nucleating plane; and (b) the (113) nucleation plane.

1.4.6.3 *E. coli* bacteria and biofilms

One of the most common species of bacteria to be found in the lower intestines of warm blooded animals, necessary for the effective digestion of food, is *Esherichia coli* (*E. coli*)[143]. Due to its ease of growth under biological laboratory conditions and its usual non-toxicity, it is often used as a model organism for bacteria, in general[143]. *E. coli* is a non-spore-forming, aerobic, rod-shaped bacteria, with most bacterium being about 2 μm in length.

It is common for microbial cells to form biofilms in order to enhance their survival chances in competitive environments. These biofilms are highly resistant films of bacterial conglomerates, attached to a surface through an extended exopolysaccharide matrix[144]. This matrix extends between 0.1 and 10 μm from the cell surface and serves as both a buffer between the cell walls and the external environment and a barrier to harmful substances as it is physically able to exclude large molecules[145]. The structure and organisation of biofilms is determined largely by the bacterial species, the availability of nutrients and surface properties such as roughness and free energy[146]. Biofilms vary in thickness between 5 and 500 μm, in which, gradients of pH, nutrient concentration and oxygen are established due to bacterial metabolism and diffusion[147]. It has been found that these biofilms are very hardwearing and even have a high resistance to antibiotics in comparison to singular microbial cells[148,149,150].

1.4.6.4 Bacterial surface adhesion mechanisms

Bacterial adhesion to surfaces usually follows three successive steps[151,152,153]. First, small, physiochemical interactions attract the bacteria to the surface. These

interactions can include van der Waals interactions, hydrophobic/hydrophilic interactions, Lewis acid-base interactions and electrostatic interactions[151]. The bacteria thus become reversibly attached to the surface. Once attracted to the surface, irreversible binding occurs through cellular and molecular interactions. This is reinforced by the excretion of extracellular polymeric substances (EPS) from the cell, leading to aggregation and stronger adhesion[154]. Various cell surface features, such as fimbrae and flagella are also known to contribute to this binding process[155]. Thirdly, cell division and multiplication then occurs, leading to an increased mass of bacteria on the surface, forming microcolonies and layers.

The adhesion process can be affected by many different factors, including environmental conditions and the surface properties of both the bacteria and the substrate itself, including the topography and surface free energy. Inhibition and removal of bacterial biofilms can only be performed via surface modification (incorporating antimicrobial agents onto the surface or within the biofilm itself, or by changing the surface adhesion properties)[156].

1.4.6.5 Effects of bacteria and biofilms on scale formation

It has been found that bacteria tend to facilitate the production of scale[157]; this could be due to a combination of two possible mechanisms. Many bacteria present in the body facilitate the removal of ammonium ions by facilitating the decomposition of urea to carbon dioxide and ammonia[157] (Equation 1-11), via the enzyme, urease.

$$CO(NH_2)_2 + H_2O \rightarrow CO_2 + 2NH_3 \qquad (1\text{-}11)$$

In the human digestive system the bacteria *Klebsiella terrigena* and *Proteus vulgaris*, in particular, produce urease[158]. This enzyme catalyses the break down of urea and therefore raises the pH of an unbuffered media to between 10 and 11. Raising the pH decreases the solubility of calcium carbonate and therefore the production of scale is facilitated[159,160,161].

SEM imaging carried out by Folk[162] on bacteria deposited mainly by hot springs in Viterbo, Italy, showed the bacteria to be fossilised in calcite as were bacteria found in Weebubbie Cave, Australia[163]. This was found to occur because bacteria have anionic cell walls which exhibit a strong tendency to absorb aqueous metal cations, particularly calcium, as described by Beveridge and Murray[164], whose work focused on the common bacteria *Bacillus subtilis*. This mechanism acts to stop harmful metals from entering the organisms themselves, as well as being a method of storage for more nutritive metals. Therefore, bacteria present in karstic waters where there is a high calcium concentration will have a high concentration of Ca^{2+} ions bound to their cell walls, specifically due to the anionic phosphate groups present in the phospholipid based EPS, as shown by ^{31}P NMR studies[165]. This promotes the ionic and electrostatic binding of counterions and supports the formation of a diffuse carbonate layer which induces the crystallisation of calcium carbonate within or around bacterial bodies, i.e. the bacteria can be thought to be acting as $CaCO_3$ nucleation centres. An important point to note is that for metal binding to occur, the organisms do not necessarily need to be alive, as it is a passive process which constitutes only electrostatic interactions; only their surfaces must remain intact[145].

1.5 Crystal dissolution

When a solid dissolves in a liquid, the processes of growth, as described in Section 1.4.2 are reversed. The steps involved are illustrated in Figure 1-20 and include detachment of ions or molecules from a dissolution site, surface diffusion, desorption of the ion or molecule and then mass transfer by diffusion, convection or migration to bulk solution[166].

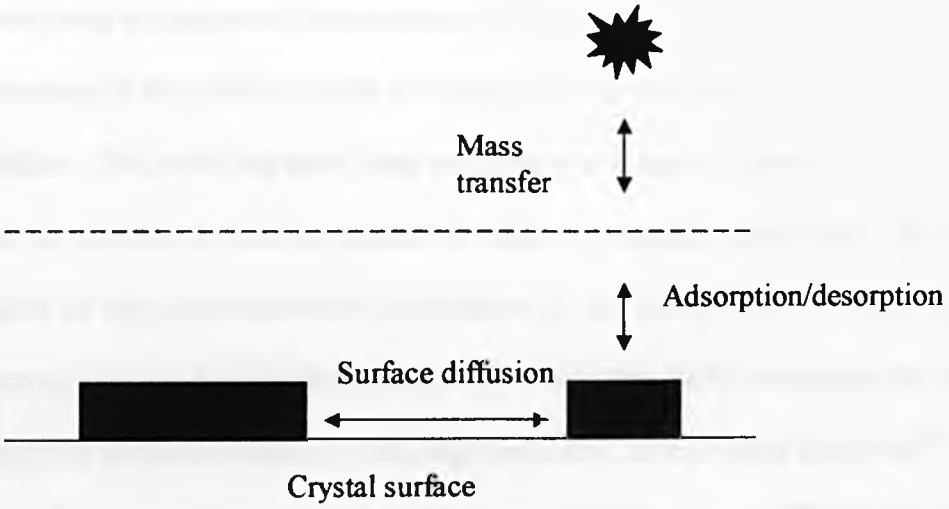

Figure 1-20: Schematic to show the processes involved in crystal dissolution.

A surface-controlled reaction describes the situation when either detachment, surface diffusion or desorption processes are slow compared to the mass transport of species away from the surface. However, if these processes are fast compared to the mass transport step then the reaction is said to be transport controlled, in accordance with Nernst's theory[167].

There has been much research on the dissolution kinetics and mechanisms of calcium carbonate and phosphate[77,168,169], including work on small crystal systems[170,171]

as well as open geological systems[84,172]. The effects of: (i) carboxylic acids[173,174,175,176]; (ii) inorganic orthophosphates[177]; (iii) chelating agents such as EDTA[178]; and (iv) pH levels[179,180] on the kinetics of dissolution have also been investigated. Work in this area has been carried out using a variety of techniques including rotating disc apparatus, channel flow cells[181], AFM[182,183], as well as studies on suspensions of particles[69].

In 1996, Macpherson et al. described a method to image ionic crystal dissolution in situ using an integrated electrochemical-AFM probe[182]. In this method the electrode component of the probe was used to create a local undersaturation at the crystal/solution interface. This work has since been extended to a situation where the electrode can be used to generate a reactive species in order to promote dissolution. This has been applied to the proton-promoted dissolution of the (104) face of calcite, where the electrode was used to locally generate H^+, whilst the AFM component of the device imaged the surface structure, at ultra-high resolution, as the crystal dissolved[183].

Dissolution models such as the screw dislocation model[58] and the adsorption layer model[184] are derived from models proposed from crystal growth, and consider crystal dissolution to initially occur from high energy defect sites, such as dislocations on the crystal surface[185]. They also assume that the crystal surface is in thermodynamic equilibrium with the crystal bulk and that ion motion on the surface is always a consecutive reaction step in the crystal dissolution mechanism[186].

1.5.1 Calcium carbonate crystal dissolution mechanisms

In general, calcium carbonate crystal dissolution occurs when the solution surrounding the crystal is undersaturated (when $S < 1$). The process is mainly affected

by pH and at low pH can be described by Equations 1-12 and 1-13 where the protons react directly with the calcite surface[84,180].

$$CaCO_{3\,(s)} + H^{+}_{\,(aq)} \rightarrow Ca^{2+}_{\,(aq)} + HCO_3^{-}{}_{(aq)} \quad (1\text{-}12)$$

$$HCO_3^{-}{}_{(aq)} + H^{+}_{\,(aq)} \leftrightarrow H_2CO_{3\,(aq)} \rightarrow CO_{2\,(g)} + H_2O_{\,(l)} \quad (1\text{-}13)$$

At higher pH, the interaction of water with calcium carbonate dominates the surface reaction, according to Equations 1-14, 1-15 and 1-16, resulting in much slower dissolution rates[179].

$$CaCO_{3\,(s)} + H_2O_{\,(l)} \rightarrow Ca^{2+}_{\,(aq)} + CO_3^{2-}{}_{(aq)} \quad (1\text{-}14)$$

$$CO_3^{2-}{}_{(aq)} + H_2O_{\,(l)} \leftrightarrow HCO_3^{-}{}_{(aq)} + OH^{-}_{\,(aq)} \quad (1\text{-}15)$$

$$H_2O_{\,(l)} \leftrightarrow H^{+}_{\,(aq)} + OH^{-}_{\,(aq)} \quad (1\text{-}16)$$

1.6 Analysis and characterisation techniques

This section describes the main analytical and characterisation techniques used throughout this thesis.

1.6.1 Electron microscopy (EM)

In electron microscopy, an electron beam is used to create magnified images of a specimen[187]. The major advantage of this technique is that the use of electrons leads to an increased spatial resolution over light microscopy, which is governed by the wavelength of the light and is, at best, 200 nm[188]. A transmission electron microscope

(TEM) can resolve details as small as 0.2 nm and a scanning electron microscope, to about 2-3 nm. The scanning electron microscope can be used to deduce surface morphology on many types of sample specimens and has a magnification range of 20 – 150000 times and a depth of field of 0.003 – 1 mm[188]. High speed electrons are used to illuminate the sample in both transmission and scanning electron microscopes, although in TEM the electron beam passes through the sample, rather than being deflected by it, and so samples for analysis by TEM have to be prepared specially so that they are very thin sections (40 – 150 nm thick) or consist of small particles on thin membranes. Both techniques require operation under high vacuum conditions, as an electron beam cannot be generated or maintained in a gas-filled environment. The one exception is the environmental SEM technique, which can be operated at near atmospheric conditions[188].

In this thesis, the main electron microscopy technique used is scanning electron microscopy. In essence, this instrument uses a beam of electrons, generated from an electron gun from a tungsten filament, which functions as the cathode. As a voltage is passed across the filament, an electron cloud is produced at the end of the filament. Due to this high negative potential produced at the cathode, electrons are attracted and accelerated towards the anode, forming a beam of electrons which are directed down the column to the electromagnetic lenses. The voltage difference between the filament and anode is termed the accelerating voltage and is typically between 5000 V and 30000 V.

After passing through the anode, the beam is passed through an electromagnetic lens, which condenses the beam of electrons, directing them towards the sample surface. After a series of interactions, secondary electrons from the sample are produced and

collected by the detector. Here, they are converted to a voltage and amplified. The configuration of an SEM is shown in Figure 1-21.

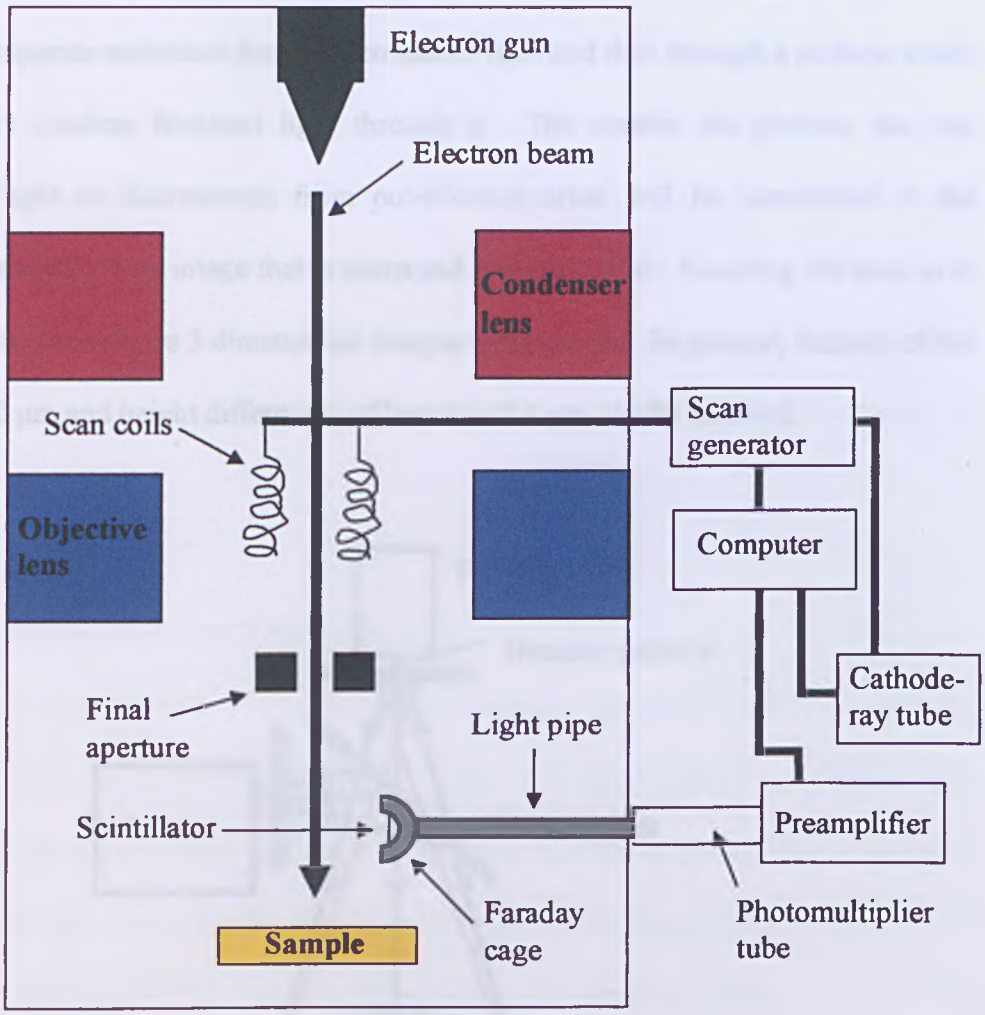

Figure 1-21: Simplified schematic of a typical scanning electron microscope.

1.6.2 Confocal laser scanning microscopy (CLSM)

In this technique, light from a laser is used as the excitation source, and is focussed onto the specimen through an objective lens (see Figure 1-22)[189]. As this is reflected, or as fluorescent light is produced from the specimen, it is passed onto a beam splitter to separate emissions from the excitation light and then through a pinhole which allows only in-plane focussed light through it. The smaller the pinhole, the less unwanted light or fluorescence from out-of-focus areas will be transmitted to the detector, resulting in an image that is sharp and free from blur. Scanning the laser in *x*, *y*, and *z* directions allows 3 dimensional images to be created. In general, features of the order of 0.2 μm and height differences of less than 0.1 μm can be resolved.

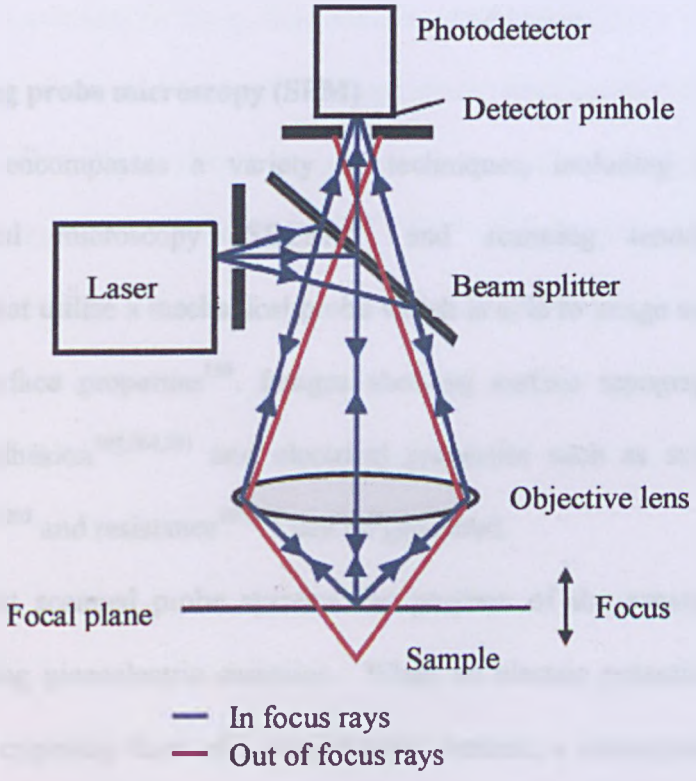

Figure 1-22: Schematic to show the confocal laser scanning microscope.

It is possible to observe bacterial biofilms and cells using CLSM. This is achieved by using two complementary fluorescent nucleic acid stains; one which penetrates all bacteria, and one which only penetrates membranes of bacteria which are dead or damaged. As each stain fluoresces a difference colour, the viability of the bacteria can be ascertained using this technique. The use of this stain, in conjunction with CLSM, has been used most recently by Auty et al. who assessed the viability of the human probiotic strains *Lactobacillus paracasei* NFBC 338 and *Bifidobacterium* sp. strain UCC 35612 in reconstituted skimmed milk[190]. The differentiation between live and dead (heat-killed) bacteria was clear, as was the case when the same technique was used to investigate the antimicrobial activity of silicone rubber, as used in biomedical implants[191].

1.6.3 Scanning probe microscopy (SPM)

SPM encompasses a variety of techniques, including AFM[192], scanning electrochemical microscopy (SECM)[193] and scanning tunnelling microscopy (STM)[194,195] that utilise a mechanical probe which is able to image samples to display a variety of surface properties[196]. Images showing surface topography, friction[197,198], stiffness[199], adhesion[197,200,201] and electrical properties such as surface charge[202,203], capacitance[204,205] and resistance[205,206] can be generated.

In most scanned probe systems the position of the sensing probe is finely controlled using piezoelectric ceramics. When an electric potential is passed across electrodes on opposing faces of a piezoelectric ceramic, a corresponding change in its physical dimensions is observed. Due to the unique expansion coefficients of the

piezoceramics, highly accurate positioning of the probe tip can be achieved. All three axial directions can therefore be scanned with very high spatial resolution[207].

Unlike conventional light microscopy the resolution of SPM is not dependent on the wavelength of the electromagnetic radiation used, rather it is governed mainly by the probe size and geometry. Therefore, very sharp tips with small active dimensions are used in SPM techniques to enable high resolution images to be obtained[208].

1.6.3.1 Atomic force microscopy

AFM was invented in 1986 by Binnig et al.[192] as an extension of STM and has since been used to study a variety of minerals and surfaces[135,136,209]. Unlike STM, it can image any surface irrespective of the conductivity of the sample and it is for this reason it is used on insulating surfaces, the measured interaction being a force between the probe and the surface of interest. Atomic-scale imaging has been performed on hydroxyapatite[210,211,212], brushite and cleaved calcite surfaces under both air and liquid using flow-through fluid cells[19,20,213,214,215,216,217,218,219] enabling the observation of growth and dissolution kinetics in real time. Figure 1-23 shows a schematic of a typical AFM experimental apparatus.

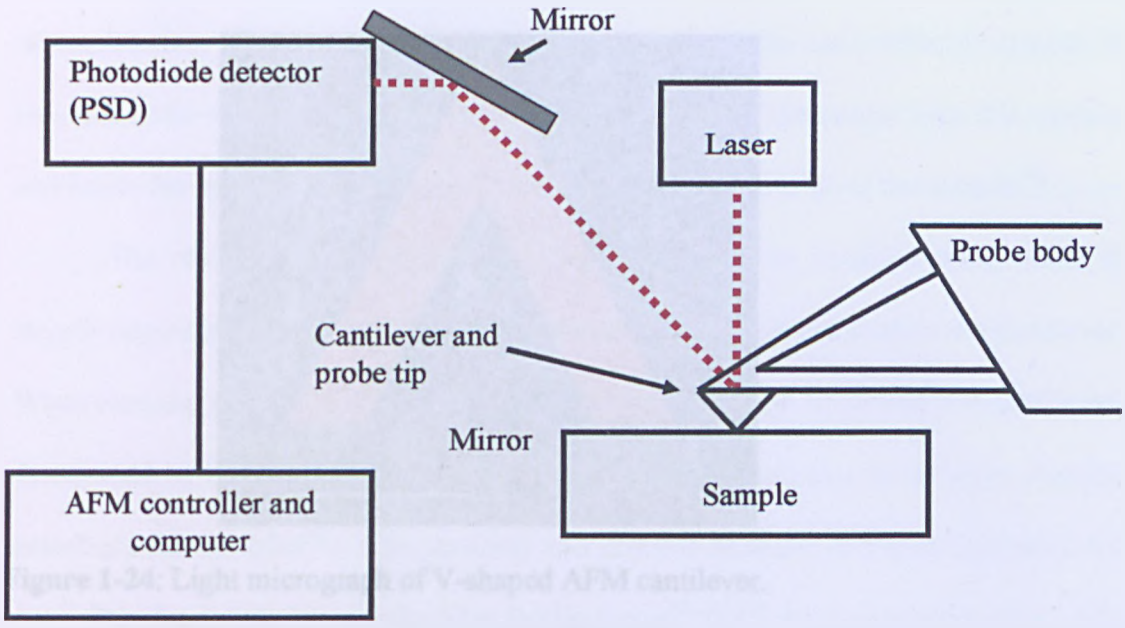

Figure 1-23: Schematic of AFM experimental apparatus.

The probe in AFM is a sharp tip, often made of silicon or silicon nitride[220], which is mounted on the end of a force-sensing cantilever of the same material. These commercially produced cantilevers can have single or V-shaped beams[221] with spring constants usually between 0.01 and 100 N m^{-1}. Stiff cantilevers are most suited to imaging hard surfaces whereas more flexible probes are best used to map delicate surfaces. Figure 1-24 shows a light micrograph of a V-shaped cantilever. The pyramidal geometry of the tip is shown clearly in Figure 1-25.

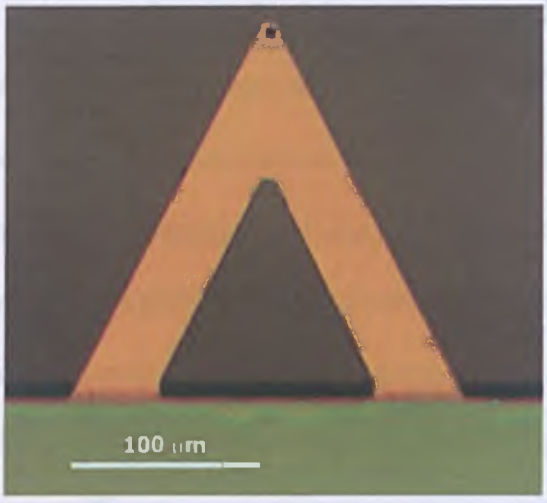

Figure 1-24: Light micrograph of V-shaped AFM cantilever.

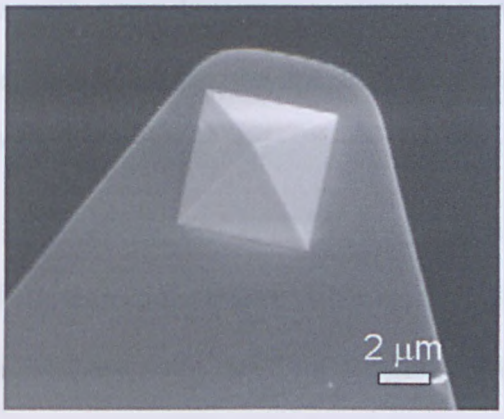

Figure 1-25: SEM image of a silicon nitride pyramidal tip.

In contact mode AFM, the tip is held in direct physical contact with the surface which is scanned under the tip in a raster pattern. As the surface is scanned, topographical features cause the tip and cantilever to deflect due to the variations in the van der Waals forces between the tip and substrate[222]. A light beam from a laser is reflected off the back of the cantilever onto a photosensitive detector and the amount the cantilever is deflected is calculated from the difference in light intensity on the sectors

of the detector. This controls a feedback loop that causes the *z*-piezoelectric ceramic to move, in order to maintain a constant cantilever deflection. The output from this *z*-piezo, and hence the motion of the scanner, forms a topographical image of the sample[192].

The resolution of topographical images of surfaces obtained using AFM is largely dependent on the aspect ratio and geometry of the tip attached to the cantilever. When imaging samples with large surface features, the image resolution and quality are determined by the tip geometry, although tip structure is not as critical when imaging extremely flat samples[207]. Tip geometry can produce artefacts in the image which are not due to the sample but are related to the tip shape[223,224,225]. High aspect tips with ~ nm tip diameters are currently being developed to alleviate these problems; these include the advent of single walled carbon nanotube tips, tens of nanometres in length and less than 1 nm in diameter[226,227,228,229,230,231].

1.6.3.2 SECM and ultramicroelectrodes (UMEs)

SECM is an SPM technique, used for imaging the topography of surfaces under solution and able to probe the reactivity of a surface with a resolution governed by the dimensions of the electrode tip. The technique is dependent on mass transport between an electrode and a sample which is governed, in turn, by chemical reactions occurring at the sample surface[232].

Bard et al.[192,233] produced much of the early work concerning SECM, although work from STM measurements in electrolyte solutions by Bard[234] and mobile UME studies from Engstrom et al.[235,236] form the basis of the technique. SECM can be used to both locally modify surface structure at a quantifiable level and provide information

about the redox activity of a wide variety of surfaces. Since 1989, the technique has been applied to many systems, ranging from biological imaging applications where measurements have been made possible in single cells, due to the small electrode dimensions[237], to the study of fast reaction kinetics at surfaces including crystal growth and dissolution kinetics[238,239,240,241,242]. The imaging probes employed in SECM are often amperometric UMEs having at least one dimension in the micrometre range. UMEs provide enhanced spatial resolution, have small currents, give steady-state responses, short response times and very efficient diffusional mass transport[243]. It is also possible to fabricate the UMEs used in SECM with sub-micrometer to nanometre diameters[244] in order to provide extremely high spatial resolution. For nanoscale electrodes, etched platinum or platinum-iridium wire is used and sealed with insulator so that only the etched end is exposed. Most UMEs are, however, between 10 μm and 25 μm in diameter and are fabricated from platinum[245], gold[246], palladium or carbon, embedded in glass or plastic. The UME tip (shown in Figure 1-26) is often characterised by an *RG* value of 10, where the *RG* is the ratio of the radius of the electrode, a, to the radius of the insulating sheath, r_{glass} ($RG = r_{glass}/a = 10$).

Disc UMEs are most commonly used due to their ease of construction and because the surface of the embedded electrode can be mechanically polished. UMEs of other geometries, such as cylinders, arrays, rings and bands are less commonly used due to their more difficult manufacturing techniques.

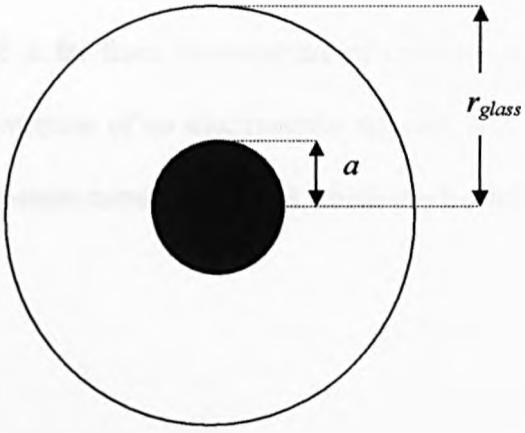

Figure 1-26: Schematic showing top view of a disc-shaped UME.

In SECM, the measured current is caused by an electrochemical reaction at the tip[247]. The UME is held in very close proximity to a conductive, insulating or semiconductive substrate in a solution containing electrolyte and an electroactive solution. The substrate and probe form part of an electrochemical cell along with reference and auxiliary electrodes, as shown in Figure 1-27. A potentiostat is used to control the tip potential and measure the current, and, as in AFM, movement of the tip is controlled by piezopositioners.

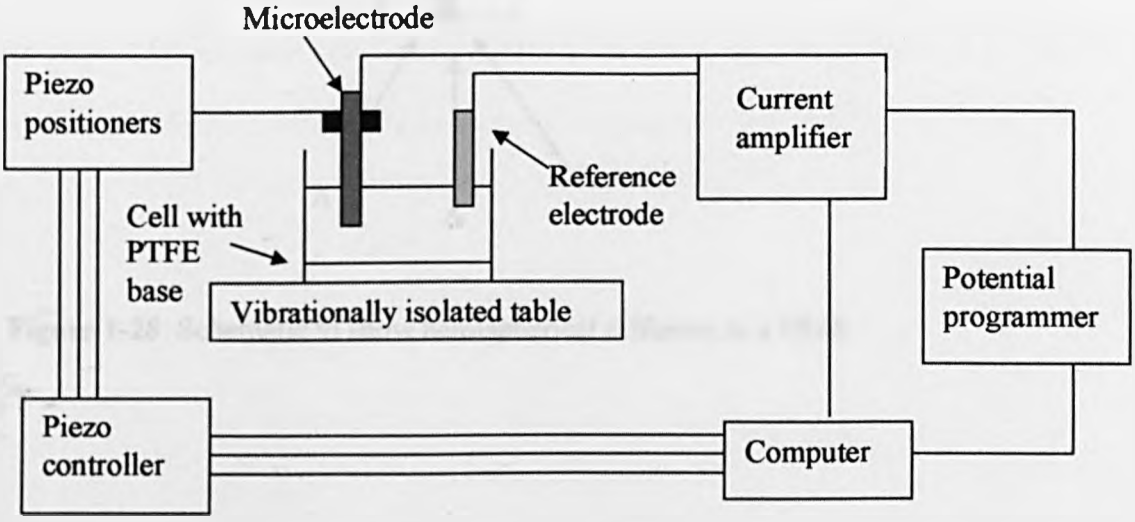

Figure 1-27: Schematic representation of an SECM apparatus.

When the UME is far from the substrate of interest and a potential is applied, sufficient to cause conversion of an electroactive species, A to B, at a mass transport controlled rate, a steady-state current, i_∞, arises which can be defined by Equation 1-17.

$$i_\infty = 4nFDc^*a \qquad (1\text{-}17)$$

Here, n is the number of electrons transferred in the process, F is the Faraday constant, D is the diffusion coefficient of the species of interest (A), c^* is the concentration of this species and a is the radius of the UME. This steady-state current is established due to hemispherical diffusion of the species of interest to the electrode as shown in Figure 1-28.

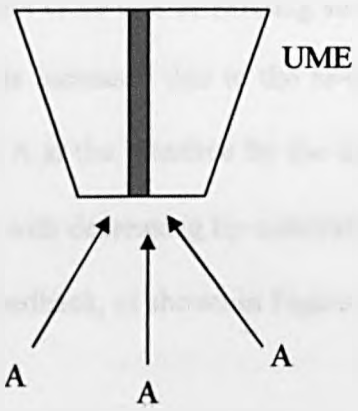

Figure 1-28: Schematic to show hemispherical diffusion to a UME.

If the tip is brought close to an insulating substrate, the hemispherical diffusion field becomes hindered by the substrate as shown in Figure 1-29. The tip current, i_T, decreases as the tip moves closer to the surface, so that $i_\infty > i_T$ giving what is termed negative feedback[248].

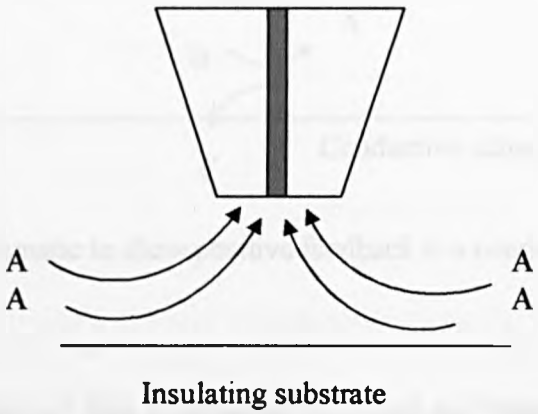

Figure 1-29: Schematic to show negative feedback at an insulating surface.

If the tip is brought close to a conducting substrate, the amount of redox species (A) reaching the UME is increased due to the re-conversion of the electrochemically produced species (B) to A at the interface by the conducting substrate. Therefore, the tip current will increase with decreasing tip-substrate separation, so that $i_\infty < i_T$. This is an example of positive feedback, as shown in Figure 1-30[248,249].

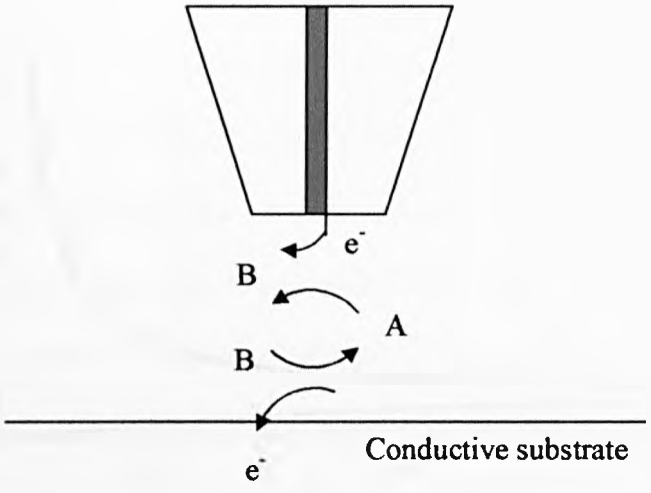

Figure 1-30: Schematic to show positive feedback at a conducting surface.

Using tables of data constructed by Kwak and Bard[233], it is possible to create theoretical approach curves of i_T/i_∞ versus tip-substrate distance, relating to the cases of both negative and positive feedback. Using experimental data it is then possible to construct these plots, compare with theory and characterise the distance of closest approach for both UMEs (using a well-characterised substrate) or the activity of an unknown substrate (using a well-characterised electrode)[250,251].

Figure 1-31 shows an example of the theoretical plots for both positive and negative feedback for when a disc shaped theoretical UME with an *RG* of 10 is approached to a conducting and insulating surface respectively.

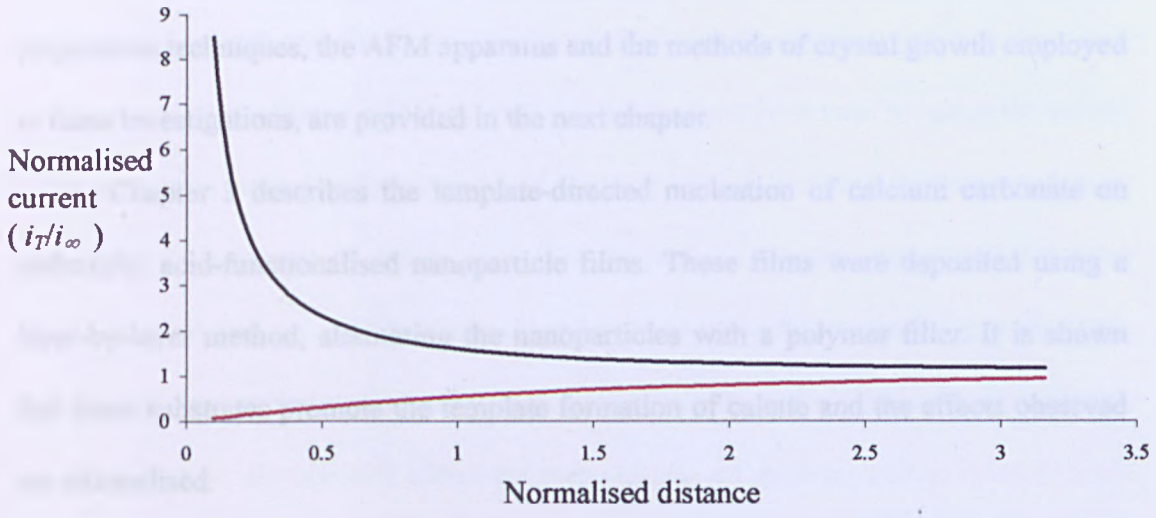

Figure 1-31: Plot to show a theoretical positive feedback curve as a UME is approached to a conducting substrate (black) and theoretical negative feedback curve as a UME is approached to an insulating substrate (red).

In this thesis, the principles of SECM are used not as a tool for scanning surfaces to gain topographical and activity information[252,253,254], as it is often used, but as a tool for etching the surface in order to make a surface modification achievable by applying a potential between the surface and the tip to induce the desired reaction[255].

1.7 Aims of this thesis

The primary aim of this thesis is to describe the visualisation, growth and dissolution of calcium carbonate, on both a macroscopic and microscopic scale, and on various functionalised surfaces, using a variety of microscopical techniques.

The experimental methodologies used in this thesis, with full details of substrate preparation techniques, the AFM apparatus and the methods of crystal growth employed in these investigations, are provided in the next chapter.

Chapter 3 describes the template-directed nucleation of calcium carbonate on carboxylic acid-functionalised nanoparticle films. These films were deposited using a layer-by-layer method, alternating the nanoparticles with a polymer filler. It is shown that these substrates promote the template formation of calcite and the effects observed are rationalised.

Chapter 4 continues with the theme of crystallisation on functionalised surfaces by examining the effect of surface potential (and charge) on SAM-functionalised surfaces on the crystallisation of calcium carbonate polymorphs, both in terms of the extent of nucleation at various potentials, and the morphology and orientation of the resulting crystals. The applied potential is shown to have a major effect.

Calcium carbonate and scale growth on *E. coli* bacterial biofilms is described in Chapter 5, where CLSM and SEM are used to visualise bacterial cells and resulting crystalline components. This is a topic that is important in the context of household care situations.

Chapter 6 describes the dissolution of calcite sections and simulated limescale pellets using a directed electrochemical etching technique, in which protons are generated using a UME, very close to the substrate surface. Subsequent analysis of the etch pits is achieved using interferometry and the dissolution process is modelled using a finite element software package.

A new methodology for investigating the mechanisms of calcite single microcrystal growth and elucidating the kinetics of growth of such crystals is described in Chapter 7. A combined AFM-inverted optical microscope is used to image the calcite (104) surface in air and under solutions of constant calcium carbonate supersaturation as well as in the presence of maleic acid. Growth rates at constant supersaturation have been modelled and are shown to correspond well to diffusion-controlled growth rates, but the surface morphology is shown to depend critically on the supersaturation. Maleic acid is shown to dramatically affect the step patterns on growing calcite microcrystals and to promote pitting under saturated solution conditions.

Finally, Chapter 8 assesses the developments made throughout the thesis in the form of a conclusion and identifies new propositions for further study.

1.8 References

[1] Y. Zhang, H. Shaw, R. Farquhar and R. Dawe, *J. Petrol. Sci. and Eng.*, **2001**, *29*, 85.

[2] T. Chen, A. Neville and M. Yuan, *J. Petrol. Sci. and Eng.*, **2005**, *46*, 185.

[3] Q. Yang, Y. Liu, A. Gu, J. Ding and Z. Shen, *J. Coll. Inter. Sci.*, **2001**, *240*, 608.

[4] P. Kjellin, K. Holmberg and M. Nydén, *Colloids and Surfaces A*, **2001**, *194*, 49.

[5] I. W. Kim, E. DiMasi and J. S. Evans, *Crystal Growth and Design*, **2004**, *4*, 1113.

[6] W. M. Berelson, D. E. Hammond and G. A. Cutter, *Geochim. Cosmochim. Acta*, **1990**, *54*, 3013.

[7] S. Mann, *Biomineralization*, Oxford Chemistry Masters, OUP, **2001**.

[8] G. Fu, S. Valiyaveettill, B. Wopenka and D. E. Morse, *Biomacromolecules*, **2005**, *6*, 1289.

[9] M. Faatz, F. Gröhn and G. Wegner, *Adv. Mater.*, **2004**, *16*, 996.

[10] D. Chakraborty and S. K. Bhatia, *Ind. Eng. Chem. Res.*, **1996**, *35*, 1985.

[11] W. A. Deer, R. A. Howe and J. Zussman, *An Introduction to the Rock-Forming Minerals*, Longman, **1983**.

[12] R. Brooks, L. M. Clark and E. F. Thurston, *Phil. Trans. Roy. Soc. London A*, **1950**, *243*, 145.

[13] J. Bernstein, R. J. Davey and J-O. Henck, *Angew. Chem. Int. Ed.*, **1999**, *38*, 3440.

[14] N. Spanos and P. G. Koutsoukos, *J. Cryst. Growth*, **1998**, *191*, 783.

[15] J. L. Wray and F. Daniels, *J. Am. Chem. Soc.*, **1957**, *79*, 2031.

[16] F. C. Meldrum and S. T. Hyde, *J. Cryst. Growth*, **2001**, *231*, 544.

[17] J. García-Carmona, J. Gómez-Morales, J. Fraile-Sainz and R. Rodríguez-Clemente, *Powder Tech.*, **2003**, *130*, 1307.

[18] Y. Liang, A. S. Lea, D. R. Baer and M. H. Engelhard, *Surface Sci.*, **1996**, *351*, 172.

[19] P. E. Hillner, S. Manne, A. J. Gratz and P. K. Hansma, *Ultramicroscopy*, **1992**, *42*, 1387.

[20] P. E. Hillner, S. Manne, P. K. Hansma and A. J. Gratz, *Faraday Discuss.*, **1993**, *95*, 191.

[21] H. Cölfen, *Current Opinion in Coll. and Inter. Sci 8*, **2003**, 23.

[22] K. Naka and Y. Chujo, *Chem. Mater.*, **2001**, *13*, 3245.

[23] *Mineral Scale Formation and Inhibition*, Ed. Z. Amjad, **1995**, Plenum Press, New York, pp. 93-132.

[24] R. Murugan and S. Ramakrishna, *Crystal Growth and Design*, **2005**, *5*, 111.

[25] G. H. Nancollas and B. Tomazic, *J. Phys. Chem.*, **1974**, *78*, 2218.

[26] W. Wu and G. H. Nancollas, *Colloids and Surfaces B: Biointerfaces*, **1997**, *10*, 87.

[27] D. Walsh, J. L. Kingston, B. R. Heywood and S. Mann, *J. Cryst. Growth*, **1993**, *133*, 1.

[28] J. L. Arias, M. B. Mayor, F. J. Garcia-Sanz, J. Pou, B. Leon, M. Perez-Amor and J. C. Knowles, *J. Mat. Sci.: Mat. in Medicine*, **1997**, *8*, 873.

[29] H. B Wen, J. van den Brink, J. R. de Wijn, F. Z. Cui and K. de Groot, *J. Cryst. Growth*, **1998**, *186*, 616.

[30] B. C. Bunker, P. C. Rieke, B. J Tarasevich, A. A. Campbell, G. E. Fryxell, G. L. Graff, L. Song, J. Liu, J. W.Virden and G. L. McVay, *Science*, **1994**, *264*, 48.

[31] K. de Groot, *J. Ceram. Soc. Jpn.*, **1991**, *99*, 943.

[32] N. Saffari and C-S. Ong, *Rev. of Prog. in Quantitative Nondestructive Eval.*, **2001**, *20*, 1125.

[33] H-M. Kim, Y. Kim, S-J. Park, C. Rey, H. M. Lee, M. J. Glimcher and J. S. Ko, *Biomaterials*, **2000**, *21*, 1129.

[34] S. Koutsopoulos, *Langmuir*, **2001**, *17*, 8092.

[35] P. G. Klepetsanis, N. Lampeas, N. Kioupis and P. G. Koutsoukos, *Mineral Scale Formation and Inhibition*, Ed. Z. Amjad, **1995**, Plenum press, New York, pp. 131-144.

[36] O. Rice and E. P. Partridge, *J. Industrial and Eng. Chem.*, **1939**, *31*, 58.

[37] C. H. Breedlove, Jr., *Chemistry*, **1973**, *46*, 31.

[38] J. Das, *Private Communication*, Unilever Research and Development, **2003**.

[39] R. Davey and J. Garside, *From Molecules to Crystallizers*, OUP, **2002**.

[40] R. Boistelle and J. P. Astier, *J. Cryst. Growth*, **1988**, *90*, 14.

[41] S. Sarig and F. Tartakovsky, *J. Cryst. Growth*, **1975**, *28*, 300.

[42] R. Lacmann, A. Herden and Chr. Mayer, *Chem. Eng. Technol.*, **1999**, *22*, 279.

[43] S. Toschev in *Crystal Growth: An Introduction*, ed. P. Hartman, **1973**, North-Holland Publishing Company, pp. 1-49.

[44] B. K. Chakraverty in *Crystal Growth: An Introduction*, ed. P. Hartman, **1973**, North-Holland Publishing Company, pp. 50-104.

[45] A. E. Nielsen, *J. Cryst. Growth*, **1984**, *67*, 289.

[46] A. A. Chernov, *Cont. Physics*, **1989**, *30*, 251.

[47] A. E. Nielsen and J. M. Toft, *J. Cryst. Growth*, **1984**, *67*, 278.

[48] W. Kossel, *Naoh. Ges. Wiss. Gollingen. Math. Physik Klasse*, **1927**, 135.

[49] I. N. Stranski, *Z. Physik. Chem.*, **1928**, *136*, 259.

[50] H. Brandes and M. Volmer, *Z. Physik. Chem.*, **1931**, *155*, 466.

[51] *Progress in Crystal Growth and Characterisation of Materials*, **1998**, *36*, Ed. J. B. Mullin.

[52] M. J. J. M. van Kemenade and P. L. de Bruyn, *J. Coll. Inter. Sci.*, **1987**, *118*, 564.

[53] F. Veverka, O. Sohnel and M. Hlavad, *Cryst. Res. Technol.*, **1983**, *18*, 527.

[54] W. K. Burton and N. Cabrera, *Discus. Faraday Soc.*, **1949**, *5*, 33.

[55] N. Cabrera and W. K. Burton, *Discus. Faraday Soc.*, **1949**, *5*, 40.

[56] D. Hull and D. J. Bacon, *Introduction to Dislocations*, **1984**, Pergamon Press.

[57] B. Henderson, *Defects in Crystalline Solids*, **1972**, Pitman Press.

[58] W. K. Burton, N. Cabrera and F. C. Frank, *Philos. Trans. Roy. Soc., London*, **1951**, *243*, 299.

[59] M. Kitamura, *Pure and Applied Chem.*, **2005**, *77*, 581.

[60] W. Ostwald, *Z. Phys. Chem.*, **1897**, *22*, 289.

[61] J. Schmelzer, J. Moeller, I. Gutzow, *Z. Phys. Chem.*, **1998**, *204*, 171.

[62] W. Ostwald, *Lehrbruck der Allgemeinen Chemie*, **1896**, *2*.

[63] J. D. Ng, B. Lorber, J. Witz, A. Théobald-Dietrich, D. Kern and R. Giegé, *J. Cryst. Growth*, **1996**, *168*, 50.

[64] M. Vučak, M. N. Pons, J. Perić and H. Vivier, *Powder Tech.*, **1998**, *97*, 1.

[65] X. Y. Liu, K. Tsukamoto and M. Sorai, *Langmuir*, **2000**, *16*, 5499.

[66] R. G. Compton and C. A. Brown, *J. Coll. Inter. Sci.*, **1993**, *158*, 243.

[67] J. Gomez-Morales, J. Torrent-Burgues and R. Rodriguez-Clemente, *J. Cryst. Growth*, **1996**, *169*, 331.

[68] N. Spanos and P. G. Koutsoukos, *J. Phys. Chem. B*, **1998**, *102*, 6679.

[69] A. Gutjahr, H. Dabringhaus and R. Lacmann, *J. Cryst. Growth*, **1996**, *158*, 296.

[70] C. Y. Tai and P-C. Chen, *AIChE Journal*, **1995**, *41*, 68.

[71] M. M. Reddy and G. M. Nancollas, *J. Coll. Inter. Sci.*, **1971**, *36*, 166.

[72] T. F. Kazmierczak, M. B. Thomson and G. H. Nancollas, *J. Phys. Chem.*, **1982**, *86*, 103.

[73] J. R. Clarkson, T. J. Price and C. J. Adams, *J. Chem. Soc., Faraday Trans.*, **1992**, *88*, 243.

[74] P. G. Koutsoukos and C. G. Kontoyannis, *J. Cryst. Growth*, **1984**, *69*, 367.

[75] M. B. Tomson, *J. Cryst. Growth*, **1983**, *62*, 106.

[76] L. D. Swinney, J. D. Stevens and R. W. Peters, *Ind. Eng. Chem. Fundam.*, **1982**, *21*, 31.

[77] C. A. Brown, R. G. Compton and C. A. Narramore, *J. Coll. Inter. Sci.*, **1993**, *160*, 372.

[78] R. Isopescu, M. Mocioi, F. Zahanagiu and L. Filipescu, *J. Cryst. Growth*, **1996**, *167*, 260.

[79] D. Verdoes, D. Kashchiev and G. M. van Rosmalen, *J. Cryst. Growth*, **1992**, *118*, 401.

[80] G. E. Cassford, W. A. House and A. D. Pethybridge, *J. Chem. Soc., Faraday Trans. 1*, **1983**, *79*, 1617.

[81] R. Shiraki and S. L. Brantley, *Geochim. Cosmochim. Acta*, **1995**, *59*, 1457.

[82] W. A. House, *J. Chem. Soc., Faraday Trans. 1*, **1981**, *77*, 341.

[83] W. A. House and J. A. Tutton, *J. Cryst. Growth*, **1982**, *56*, 699.

[84] D. Buhmann and W. Dreybrodt, *Chem. Geol.*, **1985**, *48*, 189.

[85] H. H. Teng, P. M. Dove and J. J. De Yoreo, *Geochim. Cosmochim. Acta*, **2000**, *64*, 2255.

[86] H. H. Teng, P. M. Dove and J. J. De Yoreo, *Geochim. Cosmochim. Acta*, **1999**, *63*, 2507.

[87] L. J. Simpson, *Electrochim. Acta.*, **1998**, *43*, 2543.

[88] C. Gabrielli, G. Maurin, G. Poindessous and R. Rosset, *J. Cryst. Growth*, **1999**, *200*, 236.

[89] C. Gabrielli, M. Keddam, A. Khalil, G. Maurin, H. Perrot, R. Rosset and M. Zidourne, *J. Electrochem. Soc.*, **1998**, *145*, 2386.

[90] C. Garcia, G. Courbin, F. Ropital and C. Fiaud, *Electrochim. Acta.*, **2001**, *46*, 973.

[91] S. Takasaki, K.I. Parsiegla and J. L. Katz, *J. Cryst. Growth*, **1994**, *143*, 261.

[92] A. Zafiropoulo and E. Dalas, *J. Cryst. Growth*, **2000**, *219*, 477.

[93] Y. Kitano, *Bull. Chem. Soc. Japan*, **1962**, *35*, 1980.

[94] S. Mann, B. R. Heywood, S. Rajam and J. D. Birchall, *Proc. R. Soc. Lond.*, **1989**, *423*, 457.

[95] S. Mann, B. R. Heywood, S. Rajam and J. D. Birchall, *Nature*, **1988**, *334*, 692.

[96] P. S. Dobson, L. A. Bindley, J. V. Macpherson and P. R. Unwin, *Langmuir*, **2005**, *21*, 1255.

[97] T. Ogina, T. Suzuki and K. Sawada, *J. Cryst. Growth*, **1990**, *100*, 159.

[98] S. Rajam, B. R. Heywood, J. B. A. Walker, S. Mann, K. K. W. Wong, *J. Chem. Soc. Faraday Trans.*, **1991**, *87*, 727.

[99] A. L. Litvin, S. Valiyaveettil, D. L. Kaplan, S. Mann, *Adv. Mater.*, **1997**, *9*, 124.

[100] S. Mann, B. R. Heywood, S. Rajam, J. B. A. Walker, *J. Phys. D: Appl. Phys.*, **1991**, *24*, 154.

[101] J. Küther, R. Sechadri, W. Knoll and W. Tremel, *J. Mater. Chem.*, **1998**, *8*, 641.

[103] J. Aizenberg, A. J. Black and G. M. Whitesides, *J. Am. Chem. Soc.*, **1999**, *121*, 4500.

[103] P. J. J. A. Buijinsters, J. J. J. M. Donners, S. J. Hill, B. R. Heywood, R. J. M. Nolte, B. Zwanenburg and N. A. J. M. Sommerdijk, *Langmuir*, **2001**, *17*, 3623.

[104] J. Küther, G. Nelles, R. Seshadri, M. Schaub, H-J. Butt and W. Tremel, *Chem. Eur. J.*, **1998**, *4*, 1834.

[105] Y-J. Han and J. Aizenberg, *Angew. Chem. Int. Ed.*, **2003**, *42*, 3668.

[106] J. Aizenberg, A. J. Black and G. M. Whitesides, *Nature*, **1999**, *398*, 495.

[107] D. D. Archibald, S. B. Quadri and B. P. Gaber, *Langmuir*, **1996**, *12*, 538.

[108] J. Küther and W. Tremel, *Chem. Comm.*, **1997**, *21*, 2029.

[109] J. Küther and W. Tremel, *Thin Solid Films*, **1998**, *327*, 554.

[110] A. M. Travaille, J. J. J. M. Donners, J. W. Gerritsen, A. J. M. Sommerdijk, R. J. M. Nolte and H. van Kempen, *Adv. Mater.*, **2002**, *14*, 492.

[111] J. Aizenberg, *J. Cryst. Growth*, **2000**, *211*, 143.

[112] E. Dalas, J. Kallitsis and P. G. Koutsoukos, *J. Cryst. Growth*, **1988**, *89*, 287.

[113] B. J. Brisdon, B. R. Heywood, A. G. W. Hodson, S. Mann and K. K. W. Wong, *J. Mater. Chem.*, **1994**, *4*, 1387.

[114] B. J. Brisdon, B. R. Heywood, A. G. W. Hodson, S. Mann and K. K. W. Wong, *Adv. Mater.*, **1993**, *5*, 49.

[115] J. M. Marentette, J. Norwig, E. Stöckelmann, W. H. Meyer and G. Wegner, *Adv. Mater.*, **1997**, *9*, 647.

[116] G. Falini, M. Gazzoni and A. Ripamonti, *Adv. Mater.*, **1994**, *6*, 46.

[117] S. M. D'Souza, C. Alexander, S. W. Carr, A. M. Waller, M. J. Whitcombe and E. N. Vulfson, *Nature*, **1999**, *398*, 312.

[118] D. Rautaray, R. Kavathekar and M. Sastry, *Faraday Discuss.*, **2005**, *129*, 205.

[119] D. Rautaray, P. S. Kumar, P. P. Wadgaonkar and M. Sastry, *Chem. Mater.*, **2004**, *16*, 988.

[120] I. Lee, S. W. Han, H. J. Choi and K. Kim, *Adv. Mater.*, **2001**, *13*, 1617.

[121] I. Lee, S. W. Han, S. J. Lee, H. J. Choi and K. Kim, *Adv. Mater.*, **2002**, *14*, 1640.

[122] W. A. Zisman, W. C. Bigelow and D. L. Pickett, *J. Colloid Sci.*, **1946**, *1*, 513.

[123] C. D. Bain, E. B. Troughton, Y. T. Tao, J. Evall, G. M. Whitesides and R. G. Nuzzo, *J. Am. Chem. Soc.*, **1989**, *111*, 321.

[124] C. D. Bain, J. Evall and G. M. Whitesides, *J. Am. Chem. Soc.*, **1989**, *111*, 7155.

[125] C. D. Bain and G. M. Whitesides, *J. Am. Chem. Soc.*, **1989**, *111*, 7164.

[126] R. G. Nuzzo, F. A. Fusco and D. L. Allara, *J. Am. Chem. Soc.*, **1987**, *109*, 2358.

[127] J. C. Love, L. A. Estroff, J. K. Kriebel, R. G. Nuzzo and G. M. Whitesides, *Chem. Rev.*, **2005**, *105*, 1103.

[128] A. Ulman, *Chem. Rev.*, **1996**, *96*, 1533.

[129] R. G. Nuzzo and D. L. Allara, *J. Am. Chem. Soc.*, **1983**, *105*, 4481.

[130] A. Y. Lee, A. Ulman and A. S. Myerson, *Langmuir*, **2002**, *18*, 5886.

[131] L. M. Frostman, M. M. Bader and M. D. Ward, *Langmuir*, **1994**, *10*, 576.

[132] J. Küther, M. Bartz, R. Seshadri, G. B. M. Vaughan and W. Tremel, *J. Mater. Chem.*, **2001**, *11*, 503.

[133] N. Banno, T. Nakanishi, M. Matsunaga, T. Asahi and T. Osaka, *J. Amer. Chem. Soc.*, **2004**, *126*, 428.

[134] J. F. Kang, J. Zaccaro, A. Ulman and A. Myerson, *Langmuir*, **2000**, *16*, 3791.

[135] A. L. Weisenhorn, J. E. Macdougall, S. A. C. Gould, S. D. Cox, W. S. Wise, J. Massie, P. Maivald, V. P. Elings, G. D. Stucky and P. K. Hansma, *Science*, **1990**, *247*, 1330.

[136] M. F. Hochella, C. M. Eggleston, V. B. Elings and M. S. Thompson, *Amer. Mineral.*, **1990**, *75*, 723.

[137] Y-J. Han and J. Aizenberg, *J. Amer. Chem. Soc.*, **2003**, *125*, 4032.

[138] A. M. Travaille, L. Kaptijn, P. Verwer, B. Hulsken, J. A. A. W. Elemans, R. J. M. Nolte and H. van Kempen, *J. Amer. Chem. Soc.*, **2003**, *125*, 11571.

[139] J. Aizenberg, D. A. Muller, J. L. Grazul and D. R. Hamann, *Science*, **2003**, *299*, 1205.

[140] J. Küther, R. Seshadri, W. Knoll and W. Tremel, *J. Mater. Chem.*, **1998**, *8*, 641.

[141] J. Aizenberg, *Adv. Mater.*, **2004**, *16*, 1295.

[142] P. E. Hillner, S. Manne, A. J. Gratz and P. K. Hansma, *Ultramicroscopy*, **1992**, *42*, 1387.

[143] D. L. Nelson and M. M. Cox, *Principles of Biochemistry*, **2005**, W. H. Freeman and Company.

[144] D. G. Davies, M. R. Pársec, J. P. Pearson, B. H. Iglewski, J. W. Costerton and E. P. Greenberg, *Science*, **1998**, *280*, 295.

[145] R. J. C. McLean and T. J. Beveridge, *Microbial Mineral Recovery*, ed. H. L. Ehrlich and C. L. Brierley, **1990**, McGraw-Hill Publishing Company, pp. 185-223.

[146] D. R. Korber, J. R. Lawrence, H. M. Lappin-Scott and J. W. Costerton, *Microbial Biofilms*, ed. H. M. Lappin-Scott and J. W. Costerton, **1995**, Cambridge University Press, pp. 15-45.

[147] J. W. T. Wimpenny, S. L. Kinniment and M. A. Scourfield, *Microbial Biofilms: Formation and Control*, ed. S. P. Denyer, S. P. Gorman and M. Sussman, **1993**, Oxford: Blackwell Scientific Publications, pp. 51-94.

[148] H. Anwar, J. L. Strap and J. W. Costerton, *Antimicrob. Agents Chemother.*, **1992**, *36*, 1347.

[149] J. W. Costerton, P. S. Stewart and E. P. Greenberg, *Science*, **1999**, *284*, 1318.

[150] C. A. Fux, J. W. Costerton, P. S. Stewart and P. Stoodley, *Trends in Microbiol.*, **2005**, *13*, 34.

[151] C. Faille, C. Julien, F. Fontaine, M-N. Bellon-Fontaine, C. Slomianny and T. Benezech, *Can. J. Microbiol.*, **2002**, *48*, 728.

[152] A. Sénéchal, S. D. Carrigan and M. Tabrizian, *Langmuir*, **2004**, *20*, 4172.

[153] P. Stoodley, K. Sauer, D. G. Davies and J. W. Costerton, *Annu. Rev. Microbiol.*, **2002**, *56*, 187.

[154] J. W. Costerton, *Inter. J. Antimicrobial Agents*, **1999**, *11*, 217.

[155] S. L. Walker, J. A. Redman and M. Elimelech, *Langmuir*, **2004**, *2*, 7736.

[156] P. Wood, D. E. Caldwell, E. Evans, M. Jones, D. R. Korber, G. M. Wolfhaardt, M. Wilson and P. Gilbert, *J. Appl. Microbiol.*, **1998**, *84*, 1092.

[157] L. A. Warren, N. Parmar and F.G. Ferris, *Ninth Annual V.M. Goldschmidt Conference*, **1999**.

[158] H. L. T. Mobley and R. P. Hausinger, *Microbiol. Rev.*, **1989**, *53*, 85.

[159] L. Clapham, R. J. C. McLean, J. C. Nickel, J. Downey and J. W. Costerton, *J. Cryst. Growth*, **1990**, *104*, 475.

[160] M. Nemati, E. A. Greene and G. Voordouw, *Process Biochem.*, **2005**, *40*, 925.

[161] K. M. Udert, T. A. Larsen, M. Biebow and W. Gujer, *Water Research*, **2003**, 37, 2571.

[162] R. L. Folk, *J. Sed. Petrol.*, **1993**, *63*, 990.

[163] A. K. Contos, J. M. James, B. Heywood, K. Pitt and P. Rogers, *Geomicrobiology J.*, **2001**, *18*, 331.

[164] T. J. Beveridge and R. G. E. Murray, *J. Bacteriol.*, **1976**, *127*, 1502.

[165] S. M. Strain, S. W. Fesik and I. M. Armitage, *J. Biol. Chem.*, **1983**, *258*, 13466.

[166] P. R. Unwin and J. V. Macpherson, *Chem. Soc. Rev.*, **1995**, *99*, 14824.

[167] W. Nernst, *Z. Physik. Chem.*, **1904**, *47*, 52.

[168] J. Christoffersen and M. R. Christoffersen, *J. Cryst. Growth*, **1981**, *53*, 42.

[169] R. G. Compton, K. L. Pritchard and P. R. Unwin, *J. Chem. Soc., Chem. Comm.*, **1989**, *4*, 249.

[170] R. G. Compton and G. H. W. Sanders, *J. Coll. Inter. Sci.*, **1993**, *158*, 439.

[171] J. Schott, S. Brantley, D. Crerar, C. Guy, M. Borcsik and C. Willaime, *Geochim. Cosmochim. Acta*, **1989**, *53*, 373.

[172] R. G. Compton, C. T. Walker, P. R. Unwin and W. A. House, *J. Chem. Soc. Faraday Trans.*, **1990**, *86*, 849.

[173] R. G. Compton, K. L. Pritchard, P. R. Unwin, G. Grigg, P. Silvester, M. Lees and W. A. House, *J. Chem. Soc., Faraday Trans. 1*, **1989**, *85*, 4335.

[174] A. J. Barwise, R. G. Compton and P. R. Unwin, *J. Chem. Soc. Faraday Trans.*, **1990**, *86*, 137.

[175] P. R. Unwin and R. G. Compton, *J. Chem. Soc. Faraday Trans.*, **1990**, *86*, 1517.

[176] R. G. Compton and C. A. Brown, *J. Coll. Inter. Sci.*, **1995**, *170*, 586.

[177] Th. G. Sabbides and P. G. Koutsoukos, *J. Cryst. Growth*, **1996**, *165*, 268.

[178] C. N. Fredd and H. S. Fogler, *J. Coll. Inter. Sci.*, **1998**, *204*, 187.

[179] R. G. Compton and K. L. Pritchard, *Phil. Trans. R. Soc. Lond. A*, **1990**, *330*, 47.

[180] R. G. Compton and P. R. Unwin, *Phil. Trans. R. Soc. Lond. A*, **1990**, *330*, 1.

[181] B. A. Coles, R. G. Compton, M. Suárez, J. Booth, Q. Hong and G. H. W. Sanders, *Langmuir*, **1998**, *14*, 218.

[182] J. V. Macpherson, P. R. Unwin, A. C. Hillier and A. J. Bard, *J. Am. Chem. Soc.*, **1996**, *118*, 6445.

[183] C. E. Jones, P. R. Unwin and J. V. Macpherson, *Chem. Phys. Chem.*, **2002**, *4*, 139.

[184] C. W. Davies and A. L. Jones, *Trans. Faraday Soc.*, **1955**, *51*,812.

[185] J. M. Thomas, G. D. Renshaw and C. Roscoe, *Nature*, **1964**, *203*, 72.

[186] H. G. Linge, *Adv. Coll. Inter. Sci.*, **1981**, *14*, 239.

[187] G. W. Kammlott, *Surface Sci.*, **1971**, *25*, 120.

[188] S. L. Flegler, J. W. Heckman, Jr and K. L. Klomparens, *Scanning and Transmission Electron Microscopy, An Introduction*, OUP, **1993**.

[189] C. J. R. Sheppard and D. M. Shotton, *Confocal Laser Scanning Microscopy*, BIOS Scientific Publishers, **1997**.

[190] M. A. E. Auty, G. E. Gardiner, S. J. McBrearty, E. O. O'Sullivan, D. M. Mulvihill, J. K. Collins, G. F. Fitzgerald, C. Stanton and R. P. Ross, *Appl. Environ. Microbiol.*, **2001**, *67*, 420.

[191] B. Gottenbos, H. C. van der Mei, F. Klatter, P. Nieuwenhuis and H. J. Busscher, *Biomaterials*, **2002**, *23*, 1417.

[192] G. Binnig, C. F. Quate and C. Gerber, *Phy. Rev. Lett.*, **1986**, *56*, 930.

[193] A. J. Bard, F-R. F. Fan, J. Kwak and O. Lev, *Anal. Chem.*, **1989**, *61*, 132.

[194] H. Rohrer, *Surface Sci.*, **1994**, *299*, 956.

[195] I. H. Wilson, *Vacuum*, **1994**, *45*, 817.

[196] L. A. Bottomley, J. E. Coury and P. N. First, *Anal. Chem.*, **1996**, *68*, 185.

[197] B. Bhushan and C. Dandavate, *J. Appl. Physics*, **2000**, *87*, 1201.

[198] A. R. Burns, J. E. Houston, R. W. Carpick and T. A. Michalske, *Langmuir*, **1999**, *15*, 2922.

[199] J. M. Maxwell and M. G. Huson, *Rev. Sci. Instruments*, **2002**, *73*, 3520.

[200] Q. Ouyang, K. Ishida and K. Okada, *Appl. Surf. Sci.*, **2001**, *169-170*, 644.

[201] J. E. Hudson and H. D. Abruña, *J. Am. Chem. Soc.*, **1996**, *118*, 6303.

[202] P. Taboada-Serrano, V. Vithayaveroj, S. Yiacoumi and C. Tsouris, *Environ. Sci. and Tech., Charles O'Melia Tribute Issue*, **2005**.

[203] J. Wang and A. J. Bard, *J. Phys. Chem. B*, **2001**, *105*, 5217.

[204] K. Kobayashi, H. Yamada and K. Matsushigie, *Appl. Physics Lett.*, **2002**, *81*, 2629.

[205] P. De Wolf, E. Brazel and A. Erickson, *Mat. Sci. in Semiconductor Processing*, **2001**, *4*, 71.

[206] A. Layson, S. Gadad and D. Teeters, *Electrochim. Acta*, **2003**, *48*, 2207.

[207] R. J. Colton, *Procedures in Scanning Probe Microscopies*, **1998**, J. Wiley & Sons.

[208] A. J. Melmed, *J. Vac. Sci. and Tech. B*, **1991**, *9*, 601.

[209] B. Drake and R. Hellman, *Amer. Mineral.*, **1991**, *76*, 1773.

[210] L. M. Siperko and W. J. Landis, *Appl. Phys. Lett.*, **1992**, *61*, 2610.

[211] K. Onuma, A. Ito and T. Tateishi, *J. Cryst. Growth*, **1996**, *167*, 773.

[212] K. Onuma, A. Ito, T. Tateishi and T. Kameyama, *J. Cryst. Growth*, **1995**, *154*, 118.

[213] P. E. Hillner, A. J. Gratz, S. Manne and P. K. Hansma, *Geology*, **1992**, *20*, 359.

[214] S. L. S. Stipp, W. Gutmannsbauer and T. Lehmann, *Amer. Mineral.*, **1996**, *81*, 1.

[215] S. L. S. Stipp, C. M. Eggleston and B. S. Nielson, *Geochim. Cosmochim. Acta*, **1994**, *58*, 3023.

[216] Y. Liang, D. R. Baer and A. S. Lea, *Mater. Res. Soc. Symp. Proc.*, **1995**, *335*, 409.

[217] Y. Liang, D. R. Baer, J. M. McCoy and J. P. LaFemina, *J. Vac. Sci. Technol.*, **1996**, *A14*, 1368.

[218] R. Shiraki, P. A. Rock and W. H. Casey, *Aq. Geochem.*, **2000**, *6*, 87.

[219] P. M. Dove and F. M. Platt, *Chem. Geol.*, **1996**, *127*, 331.

[220] T. R. Albrecht and C. F. Quate, *J. Appl. Phys.*, **1987**, *62*, 2599.

[221] T. R. Albrecht, S. Akamine, T. E. Carver and C. F. Quate, *J. Vac. Sci. Technol.*, **1990**, *A8*, 3386.

[222] C. F. Quate, *Surface Sci.*, **1994**, *299*, 980.

[223] S. B. Velegol, S. Pardi, X. Li, D. Velegol and B. E. Logan, *Langmuir*, **2003**, *19*, 851.

[224] K. L. Westra, A. W. Mitchell and D. J. Thomson, *J. Appl. Phys.*, **1993**, *74*, 3608.

[225] M. J. Allen, N. V. Hud, M. Balooch, R. J. Tench, W. J. Siekhaus and R. Balhorn, *Ultramicroscopy*, **1992**, *42*, 1095.

[226] J. H. Hafner, C-L. Cheung, T. J. Oosterkamp and C. M. Lieber, *J. Phys. Chem. B*, **2001**, *105*, 743.

[227] R. M. D. Stevens, N. A. Frederick, B. L. Smith, D. E. Morse, G. D. Stucky and P. K. Hansma, *Nanotech.*, **2000**, *11*, 1.

[228] D. P Burt, N. R. Wilson, J. M. R. Weaver, P. S. Dobson and J. V. Macpherson, *Nano Lett.*, **2005**, *5*, 639.

[229] Q. Ye, A. M. Cassell, H. Liu, K-J. Chao, J. Han and M. Meyyappan, *Nano Lett.*, **2004**, *4*, 1301.

[230] L. Delzeit, C. V. Nguyen, R. M. Stevens, J. Han and M. Meyappann, *Nanotech.*, **2002**, *13*, 280.

[231] E. Yenilmez, Q. Wang, R. J. Chen, D. Wang and H. Dai, *Appl. Phys. Lett.*, **2002**, *80*, 2225.

[232] J. V. Macpherson, *PhD Thesis*, University of Warwick, **1996**.

[233] J. Kwak and A. J. Bard, *Anal. Chem.*, **1989**, *61*, 1221.

[234] H. Y. Lui, F-R. F. Fan, C. W. Lin and A. J. Bard, *J. Am. Chem. Soc.*, **1986**, *108*, 3838.

[235] R. C. Engstrom, M. Webber, D. Wunder, R. Burgess and S. Wunquist , *Anal. Chem.*, **1986**, *58*, 884.

[236] R. C. Engstrom, T. Meaney, R. Tople and R. M. Wightman, *Anal. Chem.*, **1987**, *59*, 2005.

[237] A. Schulte and R. H. Chow, *Anal. Chem.*, **1996**, *68*, 3054.

[238] J. V. Macpherson and P. R. Unwin, *J. Phys. Chem.*, **1996**, *100*, 19475.

[239] J. V. Macpherson and P. R. Unwin, *J. Phys. Chem.*, **1995**, *99*, 3338.

[240] J. V. Macpherson and P. R. Unwin, *J. Phys. Chem.*, **1994**, *98*, 1704.

[241] J. V. Macpherson and P. R. Unwin, *J. Chem. Soc., Faraday Trans.*, **1993**, *89*, 1883.

[242] J. V. Macpherson and P. R. Unwin, *J. Phys. Chem.*, **1994**, *98*, 11764.

[243] R. J. Forster, *Chem. Soc. Rev.*, **1994**, *23*, 289.

[244] R. M. Penner, M. J. Heben, T. L. Longin and N. S. Lewis, *Science*, **1990**, *250*, 1118.

[245] C. J. Slevin, N. J. Gray, J. V. Macpherson, M. A. Webb and P. R. Unwin, *Electrochem. Comm.*, **1999**, *1*, 282.

[246] D. T. Miles, A. Knedlik and D. O. Wipf, *Anal. Chem*, **1997**, *69*, 1240.

[247] C. M. A. Brett and A. M. O. Brett, *Electrochemistry: Principles, Methods and Applications*, OUP, **2002**.

[248] A. J. Bard and L. R. Faulkner, *Electrochemical Methods, Fundamentals and Applications*, Wiley, **2001**.

[249] L. Rajendran and S. P. Ananthi, *J. Electroanal. Chem.*, **2004**, *561*, 113.

[250] J. V. Macpherson and P. R. Unwin, *Electroanalysis*, **2005**, *17*, 197.

[251] B. M. Quinn, I. Prieto, S. K. Haram and A. J. Bard, *J. Phys. Chem. B.*, **2001**, *105*, 7474.

[252] J. V. Macpherson and P. R. Unwin, *Anal. Chem.*, **2000**, *72*, 276.

[253] J. V. Macpherson and P. R. Unwin, *Anal Chem.*, **2001**, *73*, 550.

[254] A. J. Bard, F-R. F. Fan, D. T. Pierce, P. R. Unwin, D. O. Wipf and F. Zhou, *Science*, **1991**, *254*, 68.

[255] A. J. Bard, G. Denuault , C. Lee, D. Mandler and D. O. Wipf, *Acc. Chem. Res.*, **1990**, *23*, 357.

Chapter 2

Experimental Methods

This chapter describes the experimental methods employed in this thesis. First, details of the preparation of solutions, fabrication of electrodes and substrates used in all subsequent chapters is described. This is followed by explanations of the instrumentation used throughout this project including AFM, SECM, CLSM, light and electron microscopy, and the calcium carbonate crystallisation methods. All chemicals used are detailed at the end of the chapter, along with their grade and suppliers.

2.1 Preparation of solutions

All aqueous solutions were made using Milli-Q reagent water (Millipore Corp., resistivity > 18 MΩcm).

2.1.1 Supersaturated $CaCO_3$ solutions for jet experiments

For the jet crystallisation experiments, 100 cm^3 aqueous solutions of $NaHCO_3$ (BDH) and $CaCl_2.2H_2O$ (Aldrich) were prepared. The concentration of each solution was calculated using the MINEQL+ speciation programme (Chemical Equilibrium Modeling System, Version 4.0, 1998, Environmental Research Software[1]). This calculates Ca^{2+} and CO_3^{2-} ion concentrations after speciation has occurred in solution from original reactant concentrations and takes into account the pH and temperature of the solutions. This allows calculation of the solution supersaturation with respect to $CaCO_3$. Speciations obtained from this programme for three different supersaturations (S) used in this work are shown in Table 2-1. For each supersaturation, the concentration

of $CaCl_2.2H_2O$ and $NaHCO_3$ remained constant at 3.2 x 10^{-3} mol dm^{-3} and 4.6 x 10^{-2} mol dm^{-3} respectively, but the pH was 9.5 (for $S = 94$), 8.5 (for $S = 43$) and 8.0 (for $S = 18$).

Aqueous species	Concentration / mol dm^{-3}		
Ca^{2+}	3.47 x 10^{-4}	1.37 x 10^{-3}	1.86 x 10^{-3}
$CaOH^+$	2.77 x 10^{-7}	1.09 x 10^{-7}	4.69 x 10^{-8}
$CaHCO_3^-$	1.30 x 10^{-4}	5.92 x 10^{-4}	8.08 x 10^{-4}
$CaCO_3$	2.72 x 10^{-3}	1.24 x 10^{-3}	5.34 x 10^{-4}
CO_3^{2-}	5.56 x 10^{-3}	6.39 x 10^{-4}	2.03 x 10^{-4}
H_2CO_3	2.67 x 10^{-5}	3.07 x 10^{-4}	9.76 x 10^{-4}
HCO_3^-	3.76 x 10^{-2}	4.32 x 10^{-2}	4.35 x 10^{-2}
H_2O	1.00 x 10^{0}	1.00 x 10^{0}	1.00 x 10^{0}
OH^-	3.18 x 10^{-5}	3.18 x 10^{-6}	1.00 x 10^{-6}
H^+	3.16 x 10^{-10}	3.16 x 10^{-9}	1.00 x 10^{-8}
S	**94**	**43**	**18**

Table 2-1: Speciation concentrations as calculated using MINEQL+ software, for $S = 94$, 43 and 18.

Once the solutions had been prepared they were stored in flasks with the openings covered with parafilm (Pechiney Plastic Packaging, Menasha) and degassed using N_2 (g) (BOC, white spot) for 24 hours prior to use.

2.1.2 $CaCO_3$ solutions for AFM calcite growth experiments

Supersaturated solutions of $CaCO_3$ were prepared as described by Teng et al.[2]. The method involved dissolving $NaHCO_3$ and $CaCl_2.2H_2O$ into Milli-Q water. 0.1 M

NaCl (Fisher) was added to the solution to maintain a constant ionic strength, and the pH of the solution was altered to 8.5 using 0.5 M NaOH (BDH).

The supersaturation of the solutions with respect to $CaCO_3$ was calculated using chemical speciations determined using the MINEQL+ speciation programme, taking into account the solution temperature, pH and ionic strength. Table 2-2 details the salt concentrations used for each solution supersaturation, and the corresponding speciations are shown in Table 2-3.

	Salt concentrations			
$[CaCl_2.2H_2O]$ / 10^{-4} mol dm^{-3}	1.70	2.00	2.45	2.75
$[NaHCO_3]$ / 10^{-3} mol dm^{-3}	5.25	6.15	7.45	8.25
[NaCl] / mol dm^{-3}	0.10	0.10	0.10	0.10
S	1.54	1.81	2.64	3.27

Table 2-2: Summary of salt concentrations used at S = 1.54, 1.81, 2.64 and 3.27.

Aqueous species	Concentration / mol dm^{-3}			
Ca^{2+}	1.62×10^{-4}	1.89×10^{-4}	2.29×10^{-4}	2.56×10^{-4}
$CaOH^{+}$	6.03×10^{-9}	7.04×10^{-9}	8.53×10^{-9}	9.51×10^{-9}
$CaHCO_3^{-}$	2.96×10^{-6}	4.05×10^{-6}	5.94×10^{-6}	7.33×10^{-6}
$CaCO_3$	4.79×10^{-6}	6.55×10^{-6}	9.61×10^{-6}	1.19×10^{-5}
CO_3^{2-}	1.61×10^{-4}	1.88×10^{-4}	2.28×10^{-4}	2.52×10^{-4}
H_2CO_3	2.78×10^{-5}	3.26×10^{-5}	3.94×10^{-5}	4.36×10^{-5}
HCO_3^{-}	5.05×10^{-3}	5.92×10^{-3}	7.17×10^{-3}	7.94×10^{-3}
H_2O	1.00×10^{0}	1.00×10^{0}	1.00×10^{0}	1.00×10^{0}
OH^{-}	4.10×10^{-6}	4.10×10^{-6}	4.10×10^{-6}	4.10×10^{-6}
H^{+}	4.08×10^{-9}	4.08×10^{-9}	4.08×10^{-9}	4.08×10^{-9}
S	**1.54**	**1.81**	**2.64**	**3.27**

Table 2-3: Speciation concentrations as calculated using MINEQL+ software, for S = 1.54, 1.81, 2.64 and 3.27.

2.1.3 Kitano growth solution preparation

Calcium carbonate microcrystals were grown using the Kitano method[3], a technique requiring the preparation of a Kitano growth solution. 2.5 g (an excess) of $CaCO_3$ (Sigma) was added to 1000 cm^3 of Milli-Q reagent water and stirred continuously using a magnetic flea and stirrer (SM1, Stuart Scientific, UK). Carbon dioxide gas from dry ice was then bubbled continually through the solution.

After 90 minutes, the solution was rapidly filtered using a Buchner funnel and filter paper (Qualitative grade, Fisher, UK). CO_2 was then bubbled through the clear

filtrate for a further 60 minutes in order to ensure supersaturation. Finally, the solution was filtered using a 0.2 μm syringe filter (Minisart high flow, Sartorius, Germany) and stored for a maximum of two weeks in a stoppered flask.

2.1.4 *E. coli* biofilm growth media preparation

All bacterial investigations were performed using aseptic technique; work was performed either in a laminar flow fume cupboard or within 30 cm of a blue Bunsen flame to maintain sterile conditions. Solution compositions followed protocols established by Unilever Research and Development[4].

(a) Tryptone water

Tryptone water was prepared by adding 0.10 g of tryptone (Sigma) to 0.85 g of NaCl and made up to 100 cm^3 with Milli-Q water. This was then sterilised by autoclaving (121 °C, 20 minutes).

(b) Microbial limescale build up media

Following a protocol from Unilever[4], microbial limescale build up media were prepared in 100.40 cm^3 batches by combining 39.60 cm^3 of Milli-Q water with 40.00 cm^3 of twice the strength 'water of standard hardness', 7.00 cm^3 of 'Solution C', 7.00 cm^3 of 'Solution D', 0.80 cm^3 of 1% D(+) - glucose (BDH) and 1.00 cm^3 of 1 x 10^4 *E. coli* bacterial suspension.

(c) Water of standard hardness (WSH)

To prepare 100 cm^3 of WSH solution, 0.60 cm^3 of 'Solution A' was combined with 0.80 cm^3 of 'Solution B' and made up to 100 cm^3 with sterile Milli-Q water. Sterilisation of the WSH was carried out by autoclaving.

(d) Solution A

In a 1000 cm^3 flask, 453.50 g of 1 M $CaCl_2.2H_2O$ was added to 346.50 g of Milli-Q water, and 84.64 g of 50 % w/w $MgCl_2.6H_2O$ (Sigma Aldrich). This solution was stored at 4 – 8 °C for 1 month.

(e) Solution B

35.02 g of $NaHCO_3$ was added to a 1 litre flask and made up to 1000 cm^3 with Milli-Q water. This was then filter sterilised through a 0.45 µm syringe filter (Nalgene®, VWR International, UK) and stored at 4 – 8 °C for 5 days.

(f) Solution C

40.00 g of urea (Fisher) was combined with 3.36 g of $CaCl_2.2H_2O$, 13.84 g of NaCl and 3.36 g of Na_2SO_4 (BDH) and made up to 1000 cm^3 with Milli-Q water. This was stored at 4 °C for 2 weeks.

(g) Solution D

3.80 g of KH_2PO_4 (Fisher) was combined with 4.80 g of K_2HPO_4 (Fisher), 4.16 g of NH_4Cl (Sigma) and 4.24 g of $NaHCO_3$ and made up to 1000 cm^3 with Milli-Q water. This was stored at 4 °C for 2 weeks.

(h) Microbial biofilm build-up media

98.20 cm^3 of sterile tryptone water was added to 0.80 cm^3 of 1 % D(+) – glucose and 1.00 cm^3 of 1 x 10^4 *E. coli* bacterial suspension.

2.1.4.1 Bacterial load calibration

(a) Preparation of tryptic soy agar (TSA) slopes

TSA plates and slopes were prepared by dissolving 40 g of tryptic soy agar (Merck) in 1000 cm^3 of Milli-Q water. The solution was autoclaved and carefully pipetted out into sterile plates or tubes. These were stored at 5 °C for one month.

(b) Preparation of the master *E. coli* slope

To prepare the master *E. coli* slope, an *E. coli* bead from the – 80 °C store was placed on a TSA slope, and wiped across the surface. This was incubated at 37 °C for 24 hours before being used to prepare subcultures. The master slope was stored at 5 °C for 1 month.

(c) Preparation of bacterial subcultures

For biofilm growth, only second and third subcultures were used. Figure 2-1 shows the protocol for subculture production.

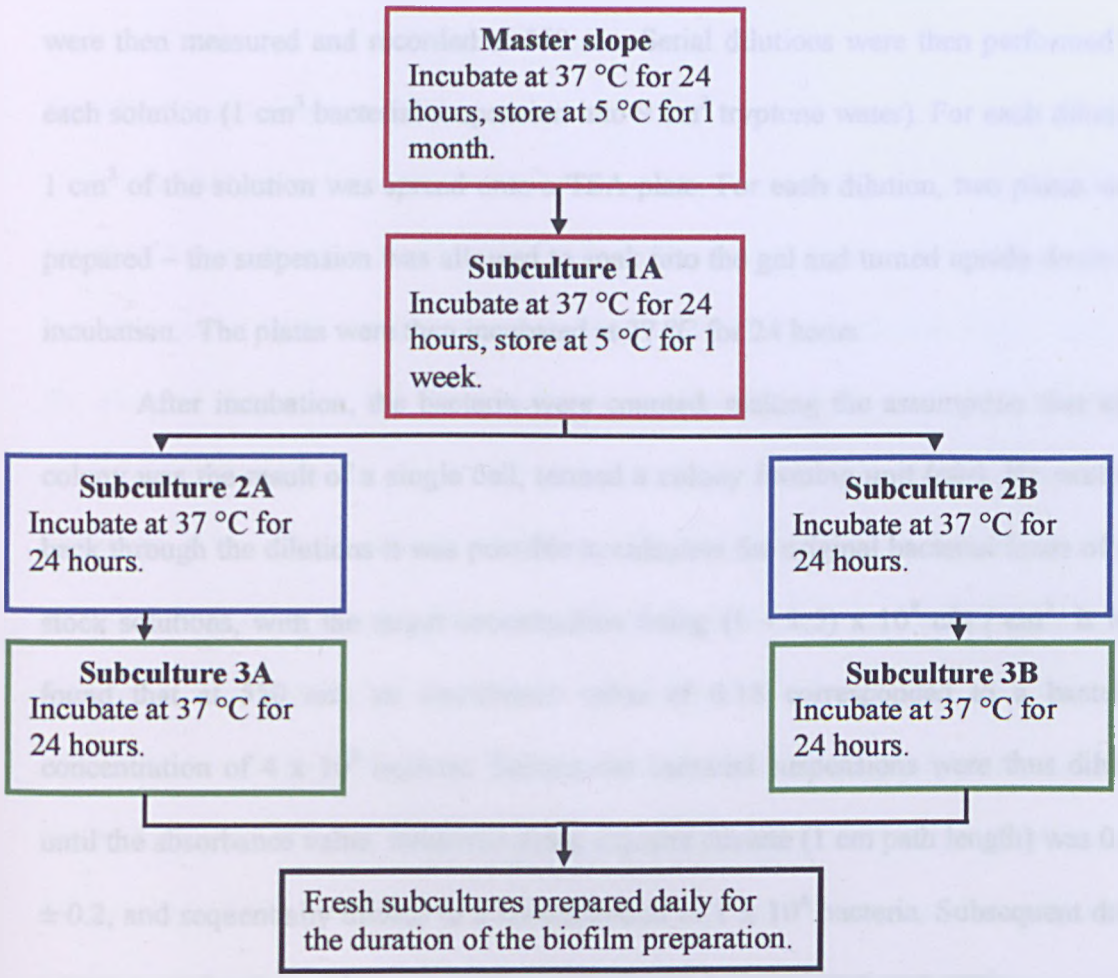

Figure 2-1: *E. coli* protocol for biofilm growth.

(d) Calibration technique

Four solutions, of differing turbidity of *E. coli* in tryptone water, were prepared by taking loops of bacteria, wiping gently on the side of the suspension vessel and suspending in tryptone water by thorough mixing. UV/Visible spectra of each solution were then measured and recorded at 550 nm. Serial dilutions were then performed on each solution (1 cm^3 bacterial suspension into 9 cm^3 tryptone water). For each dilution, 1 cm^3 of the solution was spread onto a TSA plate. For each dilution, two plates were prepared – the suspension was allowed to soak into the gel and turned upside down for incubation. The plates were then incubated at 37 °C for 24 hours.

After incubation, the bacteria were counted, making the assumption that each colony was the result of a single cell, termed a colony forming unit (cfu). By working back through the dilutions it was possible to calculate the original bacterial loads of the stock solutions, with the target concentration being (1 – 1.5) x 10^8 cfu / cm^3. It was found that at 550 nm, an absorbance value of 0.18 corresponded to a bacterial concentration of 4 x 10^8 bacteria. Subsequent bacterial suspensions were thus diluted until the absorbance value, measured using a quartz cuvette (1 cm path length) was 0.18 ± 0.2, and sequentially diluted to a concentration of 1 x 10^4 bacteria. Subsequent daily measurements were made to ensure that a consistent bacterial load was used.

2.1.5 Electrolyte solution for local dissolution experiments

To carry out local dissolution using SECM, 25 cm^3 of 0.2 M KNO_3 (Fisher) aqueous solution was prepared. The pH of the solution was then adjusted to 8.5 using dilute NaOH solution.

2.2 Construction of electrodes

This section describes the methods of fabrication of Pt UMEs, for use in SECM experiments, Ag/AgCl electrodes used as reference electrodes and the preparation of SAM functionalised gold macroelectrodes which were used for the studies in Chapter 4.

2.2.1 Pt ultramicroelectrodes

Pt UMEs were fabricated by hand using a process developed in house. A 10 mm length of 50 μm diameter Pt wire (Goodfellow, Cambridge Science Park, England) was cut. One end of a 100 mm long borosilicate glass capillary tube (2.0 mm OD, 1.16 mm ID, Harvard Apparatus Ltd. Kent, UK) was pulled to a fine point using a gravity operated capillary puller, consisting of a nichrome coil resistance heater (annealed Ni80Cr20, 0.75 mm diameter, Goodfellow) with precise temperature control (Narishige, PB-7 capillary puller, Japan). The pointed end of the capillary tube was trimmed using a glasscutter and then flashed in a blue Bunsen burner flame to seal the end. The length of Pt wire was dropped into the capillary tube and tapped down gently until it reached the sealed end. The capillary was then attached to a vacuum pump (RE-2 pump, Vacuubrand GMBh and Co., Germany). After about 30 minutes under vacuum the heating coil of the capillary puller was used to carefully seal the end of the capillary containing the Pt wire before releasing the tube from the vacuum.

This sealed end was then abraded by hand using a Carbimet paper disc (600 grit, Buehler Ltd., Coventry), thereby exposing the Pt electrode. This was polished using a finer Carbimet paper (240 grit, Buehler Ltd.) and then with diamond lapping discs (Buehler Ltd.), which had successively finer grains (9 μm, 6 μm, 3 μm, 1 μm, 0.1 μm),

using a home built polishing wheel. Finally, the electrode was polished using a slurry of alumina (0.05 μm gamma alumina, Buehler Ltd.) on a cleaning pad (Microcloth, Buehler Ltd.) which gave a smooth finish. Polishing using alumina was carried out prior to each experiment in order to eliminate any slight scratches on the electrode surface that might occur from handling or storage. The glass sheath surrounding the electrode was polished conically using emery paper (Grit 600, Buehler Ltd.) so that the *RG* value (ratio of overall probe diameter to electrode diameter) was 10 (overall probe diameter of ca. 500 μm). Throughout the process of coning and polishing the electrode was periodically inspected using an optical microscope (BH2, Olympus, Japan).

An electrical contact to the microwire was facilitated with a 100 mm length of stripped tinned copper wire (RS Components, Corby). This was attached to the Pt wire in the capillary tube using silver loaded epoxy adhesive (RS Components, UK). Araldite (Bostik Ltd., Leicester) was finally used to seal the whole electrode, leaving the protruding copper wire as a contact. The smoothness and dimensions of the electrodes were determined using optical microscopy. Figure 2-2 shows a schematic of a hand-fabricated UME.

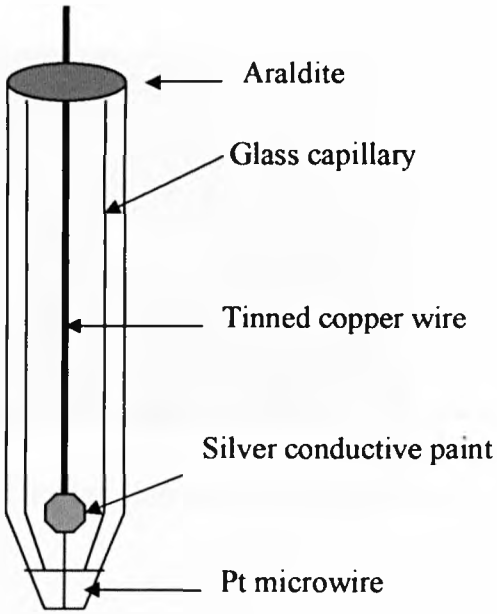

Figure 2-2: Schematic of a hand-fabricated UME.

A linear sweep voltammogram was recorded in order to verify that the connection between the Cu wire and the Pt microwire was good. SECM approach curves were then run to assess the quality and flatness of the electrode surface. This involved translating the probe electrode towards an inert glass surface and recording the steady-state current as a function of separation between the electrode and surface. The data obtained were compared to the theory of Kwak and Bard[5]. Figures 2-3 and 2-4 show optical micrographs of both the top and side views of a 50 μm diameter Pt electrode.

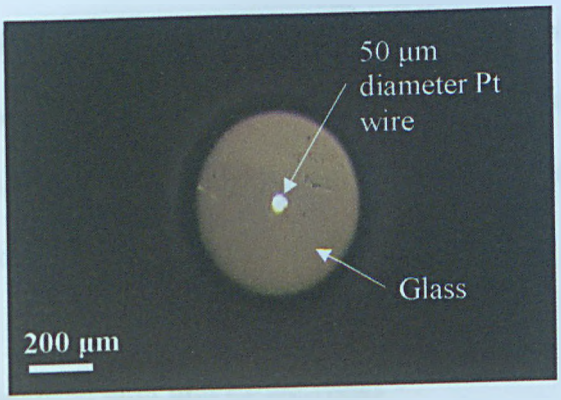

Figure 2-3: Optical micrograph of the top view of a hand-fabricated 50 µm diameter Pt UME.

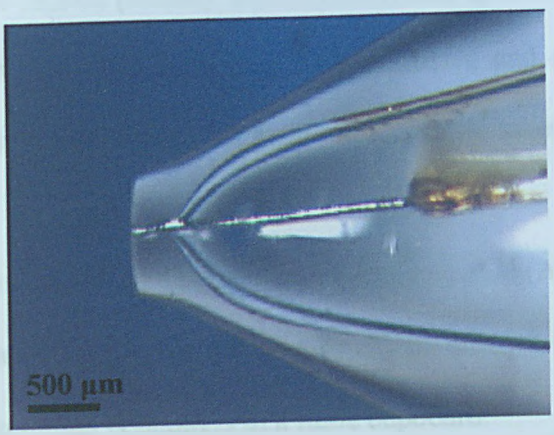

Figure 2-4: Optical micrograph of the side view of a hand-fabricated 50 µm diameter Pt electrode.

2.2.2 Ag/AgCl electrodes

Ag/AgCl reference electrodes were prepared via the anodic oxidation of a piece of silver wire (Goodfellow, Cambridge Science Park, England) in an aqueous KCl (BDH) solution. This was performed by holding the silver wire at 0.3 V with respect to a silver quasi reference electrode in 0.1 M KCl for 5 minutes.

2.2.3 SAM-functionalised gold macroelectrodes

20 nm of chromium was evaporated onto clean borosilicate glass slides, to act as an adhesion layer before the subsequent evaporation of 120 nm of gold to produce gold substrates. After annealing at 300 °C for 4 hours, the surfaces were cleaned using a piranha solution (3:1 H_2SO_4 (Fisher): H_2O_2 (GPR)) and split into smaller 1 cm x 1 cm sections. CAUTION: Piranha solution is very corrosive and reacts explosively with acetone and other organic solvents, so great care must be taken in its use, preparation and disposal.

5 mM SAM solutions of 11-mercaptoundecanoic acid (Aldrich), 1-undecanethiol (Aldrich) and 11-mercapto-1-undecanol (Aldrich) in ethanol (Fisher) were prepared. These were stored in closed containers in a fume cupboard.

The gold substrates were placed in the SAM solutions overnight allowing the monolayers to self-assemble onto the gold surfaces. These substrates were made into macroelectrodes (see Figure 2-5) by attaching a partially stripped insulated length of silver wire (RS Components, UK) to the gold substrate using Acheson Electrodag (silver in methyl isobutyl ketone, Agar Scientific Ltd). This connection was then reinforced via

the application of Araldite and the remaining exposed wire was insulated using a 1:1 mix of non-metallic nail varnish (Rimmel, Lasting Finish) and superglue (Bostik, UK).

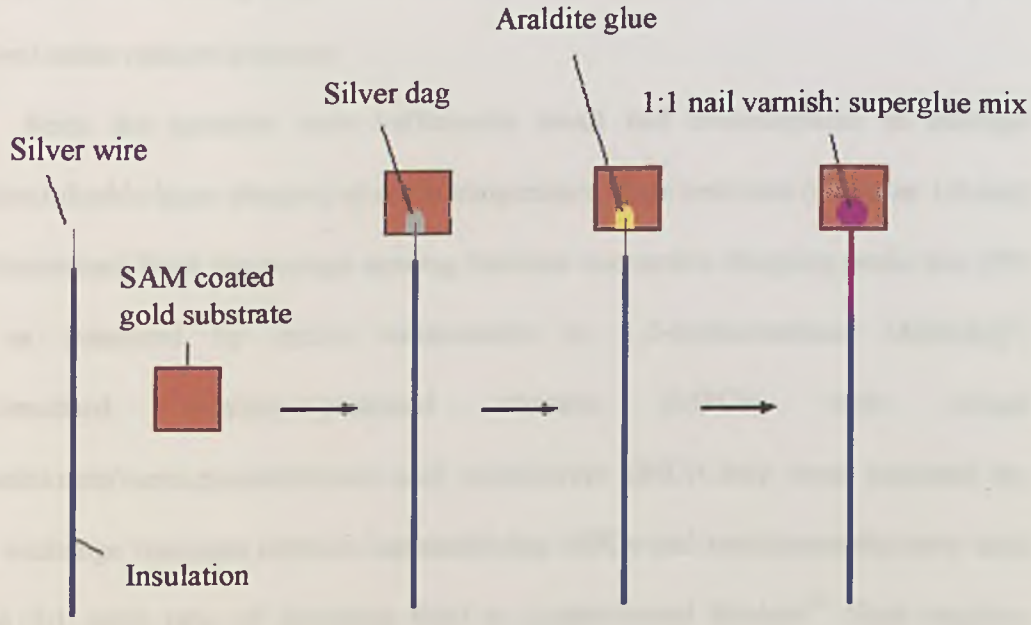

Figure 2-5: Schematic to show the macroelectrode fabrication process.

2.3 Substrate preparation

2.3.1 Functionalised gold nanoparticle film preparation

Hexanethiol-stabilised gold nanoparticles (C6-Au) were prepared as described in various publications[6,78]. Briefly, 0.76 mmol hydrogen tetrachloroaurate trihydrate (Aldrich) and 1.8 mmol *p*-mercaptophenol (Fluka) were dissolved in 150 cm^3 of methanol (Fisher). 3 cm^3 of acetic acid (Aldrich) was added to the mixture to prevent deprotonation and 30 cm^3 of 0.4 mol dm^{-3} aqueous sodium borohydride (Lancaster) was added in 1 cm^3 portions, with stirring. After further stirring for 30 minutes the solvent was removed under reduced pressure at a temperature lower than 50 °C, leaving a

residue which was washed thoroughly with diethyl ether (BDH). After evaporation of the diethyl ether the material was washed with Milli-Q water, dissolved in propan-2-ol (Fisher) and dried using anhydrous sodium sulfate (BDH). Finally, the solvent was removed under reduced pressure.

Since the particles were sufficiently small and monodisperse to undergo quantized double layer charging at room temperature, their core size (diameter 1.6 nm) was determined from the average spacing between successive charging peaks (ca. 250 mV as measured by cyclic voltammetry in 1,2-dichloroethane (Aldrich))[9]. Functionalised monolayer-protected clusters (MPCs) with mixed hexanethiolate/mercaptoundecanoic acid monolayers (MUA-Au) were prepared by place exchange reactions between hexanethiolate MPCs and mercaptoundecanoic acid with a 2:1 mole ratio of incoming thiol to cluster-bound thiolate[10]. Such reaction conditions yield MPCs containing approximately 35 MUA ligands and 20 C6 ligands per MPC core on average[10]. Figure 2-6 shows an FE-SEM image of such nanoparticle clusters.

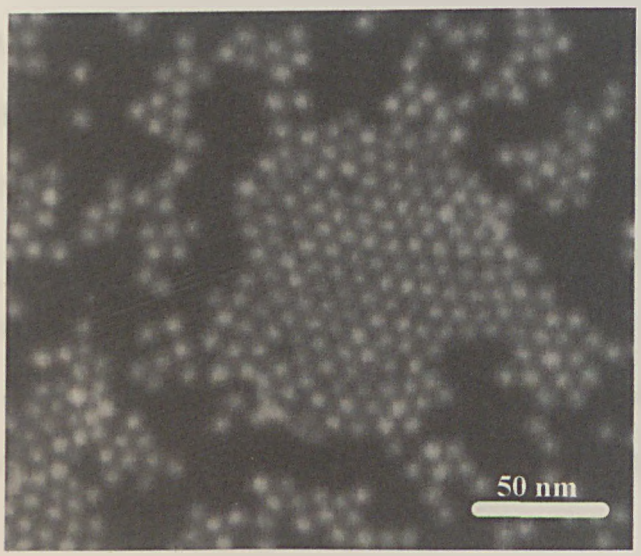

Figure 2-6: FE-SEM image of gold nanoparticle film.

The following polyelectrolytes: 3-aminopropyl-methyl-diethoxysilane (Fluka), poly(styrene sulfonic acid) sodium salt (PSS, M_w ~ 70000 g mol^{-1}, Alfa Aesar) and poly(allylamine hydrochloride) (PAH, M_w ~ 60000 g mol^{-1}, Alfa Aesar) were used as received, with aqueous solutions being prepared using Milli-Q water.

Prior to multilayer assembly, quartz slides were cleaned thoroughly[11] by agitating in an ultrasonic bath in a hot H_2SO_4 /H_2O_2 (7:3) mixture for 1 hour, and then washing with Milli-Q water. To provide a hydrophilic support, the slides were dipped into a $H_2O/H_2O_2/NH_3$ (Fisher) (5:1:1) solution for 20 minutes before being washed thoroughly with Milli-Q water. They were then immersed for 2 minutes each in methanol, then methanol/toluene (Fisher) (1:1) and finally in toluene before being silanised by immersion in a 5 % solution of hexamethyldisilazane (Lancaster) in toluene for 15 hours under an atmosphere of dry nitrogen. This was followed by immersion (1 minute) each in toluene, toluene/methanol (1:1), methanol, and Milli-Q water. For the adsorption of the first anionic layer, the substrates were immersed in an acidic solution of PSS (20 min, 2 mg mL^{-1}) at 0 °C followed by rinsing with Milli-Q water. Subsequent layers (PAH/MUA-Au) were assembled by alternately dipping the negatively terminated slide into the PAH (aqueous, 1 mg mL^{-1}) and MUA-Au (1.5 mg mL^{-1} in ethanol) solutions for different times. The pH of the polycation solution was adjusted to 9.2, by the addition of 0.1 mol dm^{-3} NaOH solution to promote deprotonation of the carboxylic groups of MUA-Au after exposure to the PAH solution.

Evolution of MUA-Au surface coverage after each immersion cycle was followed by UV-visible spectrophotometry (PerkinElmer Lambda 25 UV/VIS

Spectrometer), and derived from the film absorbance at 520 nm (taking a molar absorptivity, $\varepsilon = 3.7 \times 10^5\ M^{-1}\ cm^{-1}$)[6].

2.3.2 *E. coli* bacterial biofilm / microbial limescale preparation

Biofilm growth was performed under aseptic conditions, always working within 30 cm of a Bunsen flame. Before beginning preparation, all surfaces were wiped down with Virkon® solution (Antec Virkon® virucidal disinfectant, Antec International Ltd., UK). The necks of all bottles were flamed in the Bunsen burner briefly on opening and closing to ensure sterility. Racks, 2 cm^2 borosilicate glass substrates (supplied by Unilever Research and Development, Port Sunlight) and boxes were all autoclaved prior to biofilm preparation.

The glass substrates were placed in the racks in the boxes and covered with the necessary biofilm growth solution (biofilm growth medium or microbial limescale medium). Each day, the slides were removed from the box and placed on a paper towel. The used biofilm media was tipped into a waste jar containing Virkon® solution.

To remove loosely adhered cells, the slides were gently rinsed with 25 cm^3 of sterile tryptone water, replaced in the racks and fresh growth medium added, such that the support rack and slides were completely immersed. Slides were placed in alternate slots in the rack to ensure even coverage of bacteria at the substrate surface. This process was repeated daily until the biofilm was shown to be viable using CLSM.

2.3.3 Cleaved calcite surfaces

Sections of naturally occurring calcite (Iceland Spar, Richard Tayler Minerals, Cobham, Surrey), 7 mm x 7 mm and ca. 2 mm thick were produced by the cleavage of larger single crystals along the (104) cleavage plane using a sharp (Stanley knife) blade and a blow from a hammer.

2.3.4 Simulated limescale pellets

Circular simulated limescale pellets, 15 mm in diameter and 2 mm thick, were produced by Unilever (Port Sunlight, UK), consisting of varying proportions of calcium phosphate dibasic anhydrous, calcium carbonate and magnesium stearate, and by Thompson and Capper (consisting of varying proportions of the same compounds but also incorporating acacia gum as a binder).

2.3.5 Kitano grown calcite microcrystals

A Petri dish was filled with filtered $CaCO_3$ Kitano growth solution (ca. 40 cm^3). Borosilicate glass discs (20 mm diameter, 1 mm thick, Apex Services, Cambridge, England) were placed into the solution after being sonicated in acetone (Fisher) and rinsed with Milli-Q water. The Petri dish was left open to the air in a clean environment to allow CO_2 to evolve from the solution, thereby promoting the formation of $CaCO_3$ microcrystals on the glass disc surfaces. After ca. 36 hours, the glass discs were removed from the growth solution and rapidly blown dry with a stream of nitrogen (BOC, white spot). The crystals were characterised using scanning electron microscopy (Jeol JSM 6100, accelerating voltage: 10 kV, equipped with Oxford ISIS Analytical

System), after coating the discs in a thin layer of gold using a sputter coater (Emscope SC500, 25mA). A light microscope was also used to inspect the microcrystals formed, so that their orientation could be ascertained.

2.4 Instrumentation

The instrumentation used throughout this thesis is described here. It includes AFM, incorporating the combined AFM-inverted optical microscope apparatus and the fluid cell used for imaging under solution, SECM, CLSM, light and electron microscopes, and the two crystallisation methods used in subsequent chapters.

2.4.1 Atomic force microscopy

AFM imaging was carried out in a room specifically designed to house SPM instruments, with the microscope (Molecular Imaging (MI) AFM, USA) placed on a home-built vibrationally isolated table. The table consisted of a brick-built support with a granite top (900 x 800 x 80 mm, Frank England, Retford) positioned on four rubber isolation units (Pneumatic mounts, RS Components, UK).

2.4.1.1 Combined AFM – inverted optical microscope

The AFM was equipped with an inverted metallurgical microscope (Willovert, Hund) fitted with filters in the eyepieces to avoid damage to the eyes from the AFM laser light (see Figure 2-7). The AFM was placed on an in-house stage, holding the microscope in the correct position to allow the probe cantilever to be viewed through the

microscope, as part of the recess in the sample plate was removed in order to allow access to the optical lens (see Figure 2-8).

Figure 2-7: Photograph of the combined AFM-inverted microscope.

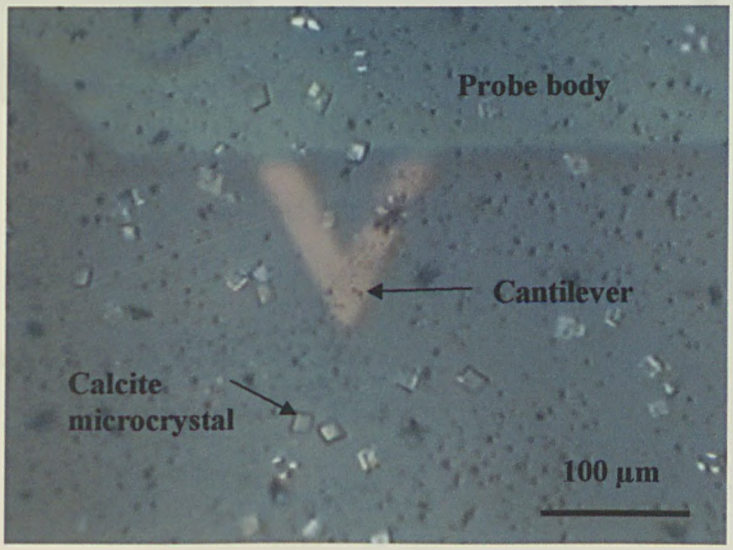

Figure 2-8: Optical micrograph of AFM cantilever and calcite microcrystals as observed through the inverted microscope.

The AFM was fitted with a 30 μm scanner and the cantilevers used were commercially produced V-shaped Si_3N_4 cantilevers with spring constants of 0.12 N m^{-1} and integrated pyramidal tips (model NPG, Veeco, UK).

2.4.1.2 AFM fluid cell

Imaging under solution was performed using the Molecular Imaging AFM and a fluid cell (USA) which could be used in air as well as in solution. This cell consisted of a PTFE lined aluminium block, held onto the baseplate with small nuts and bolts, as shown in Figure 2-9. The baseplate had a recess into which borosilicate glass discs, used as crystallisation substrates, could be fitted.

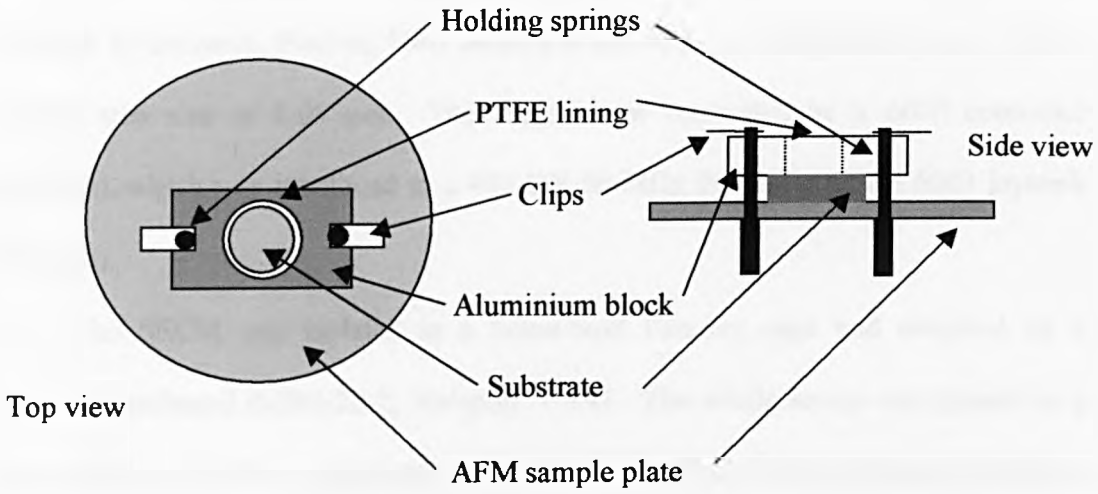

Figure 2-9: Schematic of the MI AFM fluid cell.

Imaging under solution was performed by inserting a short length (ca. 100 mm) of PTFE tubing (0.40 mm ID, 0.90 mm OD, FTL Seals Technology, Leeds, UK) into a hole in the AFM leading to the sample plate. Fluid could then be flowed into the cell using a 1 cm^3 volume syringe.

To change the solution, scanning was halted but the tip was kept in contact with the surface. Solution was withdrawn from the cell using the PTFE tubing and syringe and new solution was carefully flowed in. Contact between the surface and probe was not lost due to the capillary layer of solution always surrounding the tip. Scanning could then be resumed in the same area.

2.4.2 Scanning electrochemical microscopy

The SECM used in this thesis consisted of three TSE-75 piezo-driven stages (Burleigh Instruments, Fischer, New Jersey) in an *x*-, *y*-, *z* configuration, each with a smallest step size of 0.05 μm. The stages were controlled by a 6000 controller (Burleigh), which was interfaced to a 486 DX 66-MHz PC and a model 6003 joystick (Burleigh).

The SECM was isolated in a home-built Faraday cage and mounted on a standard breadboard (MSG-22-2, Newport, USA). The whole set-up was placed on a home-built bench with a granite block (900 x 800 x 20 mm, Frank England, Retford) incorporating vibration isolation units (Pneumatic mounts, RS Components, UK).

2.4.2.1 SECM cell

For SECM experiments, the electrochemical cell consisted of a cylindrical glass body (40 mm ID, Chance Bros) with a PTFE base. A chemically inert 'Viton' O-ring (James Walker & Co. Ltd., Cumbria) placed in a groove in the cell base was used to create a water-tight seal between the base and the body.

The reference electrode used in SECM experiments was a 50 mm length of silver wire (Goodfellow, Cambridge Science Park, England), dipped at least 3 mm into the electrolyte solution. The working electrode was held in position by mounting it on the *z*-piezoelectric positioner.

2.4.3 Confocal laser scanning microscopy

CLSM images were recorded using a Zeiss LSM 510, Axioplan 2 confocal microscope. Images were acquired using a water immersion objective lens (Zeiss, Achroplan 20× / 0.50 W) and an Ar laser ($\lambda = 488$ nm). A long pass filter was employed at 585 nm and a band pass filter at 505 – 530 nm.

2.4.3.1 Staining of bacterial biofilm samples

CLSM was used mainly to visualise bacterial biofilms. These were imaged using a two component staining procedure (LIVE/DEAD® *Bac*Light™ Bacterial Viability Kit, Molecular Probes, USA). The first stain, SYTO® 9 (nucleic acid stain in DMSO, Molecular Probes, USA) green-fluorescent nucleic acid stain, stained all bacteria. The second stain, propidium iodide (solution in DMSO, Molecular Probes, USA) which is red, was only capable of staining bacteria with damaged cell membranes *i.e.* those which

were dead or dying. This allowed living and dead/damaged bacteria to be distinguished easily using CLSM.

When the biofilm samples were ready for analysis (usually after ~ 5 days) each sample was removed from the growth solution using tweezers and placed in a small sterile Petri dish containing 3 cm^3 of tryptone water; enough to cover the slide and keep the film viable. They were stained by soaking in 3 cm^3 of sterile tryptone water to which 5 µl of each of the two stains had been added. The samples were then left in total darkness for 15 minutes to allow staining to occur without photobleaching. The samples were rinsed by allowing them to soak in 3 cm^3 of sterile tryptone water before this was exchanged for a further 3 cm^3 of sterile tryptone water. Samples were then imaged, in solution, using the CLSM.

2.4.4 Optical microscopy

Optical microscopy was carried out using an Olympus BH2 light microscope equipped with Nomarski differential contrast interference (DIC) objectives, giving a magnification range of ×50 to ×1000.

2.4.5 Scanning electron microscopy

Scanning electron microscopy was performed using a Jeol JSM 6100, equipped with an Oxford ISIS Analytical System and using an accelerating voltage of typically 10 kV. This technique required non-conducting samples to be coated with a thin layer of gold, which was achieved using a sputter coater (Emscope SC500, 25mA). Field

emission scanning electron microscopy (FE-SEM) images were recorded using a Zeiss Supra 55 V.P.

2.4.6 Calcium carbonate crystallisation methods

Two methods of calcium carbonate crystallisation were used: the Kitano growth method and a jet crystallisation method. Details of both techniques are given below.

2.4.6.1 Kitano crystallisation method

The Kitano crystallisation technique was first documented in 1962[3], and has been used to crystallise calcium carbonate crystals in many capacities since[12,13,14,15]. The method uses a Kitano growth solution (prepared as detailed in Section 2.1.3) which has a lifetime of ca. two weeks, when kept in a stoppered flask.

(a) Calcite microcrystal samples

Microcrystal samples for AFM imaging were prepared by placing clean borosilicate glass discs into a Petri dish filled with the Kitano solution. The dish was left open to the air in a clean environment to allow dissolved CO_2 to evolve from the solution. This resulted in an increase in the solution pH, reducing the solubility of $CaCO_3$ and thereby inducing the formation of $CaCO_3$ microcrystals at the glass/solution interface. After 18 hours, the discs were removed from the solution, rapidly blown dry under a stream of nitrogen and inspected using an optical microscope.

(b) Crystallisation on nanoparticle substrates

Functionalised gold nanoparticle substrates were prepared as detailed in Section 2.3.1. Samples were placed face down in a Petri dish containing Kitano growth solution, ensuring that the level of solution was sufficient to cover the substrate surface. Crystallisation occurred due to the evolution of CO_2 (g) over a period of 65 hours. The Petri dish was periodically refilled with Kitano solution due to solution evaporation.

(c) Crystallisation on SAM-coated gold macroelectrodes

SAM-coated gold macroelectrodes were prepared as detailed in Section 2.2.3. Growth occurred using the same approach as detailed for the nanoparticle substrates. Throughout the growth period, a potential was applied to the gold electrode via a potentiostat with reference to a saturated calomel electrode (BAS Inc., Japan), also placed in the Kitano solution.

2.4.6.2 Jet crystallisation method

The jet crystallisation method utilised a dual syringe pump (KD Scientific, USA, with Hamilton gas-tight syringes, Nevada, USA), allowing the controlled mixing of two separate solutions (in this case, $CaCl_2.2H_2O$ and $NaHCO_3$). The solutions were mixed via a custom made mixer, after flowing at a constant, defined flow rate, from the syringe pumps through PTFE tubing (see Figure 2-10)[16]. From this mixer, the resulting supersaturated $CaCO_3$ solution was jetted via a nozzle into the PTFE jet cell where it eventually hit the substrate, which was placed face down on the top of the cell, as shown in Figure 2-11. This system ensured that a constant supply of supersaturated $CaCO_3$ was

maintained at the substrate/solution interface throughout the course of the experiment, and the PTFE construction of the cells and tubing ensured that crystallisation did not occur until the solution impinged on the substrate surface.

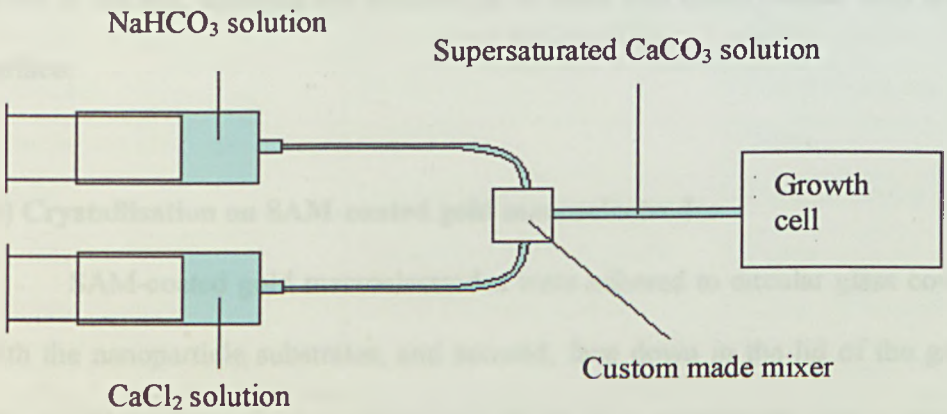

Figure 2-10: Schematic of the apparatus used for the jet crystallisation method.

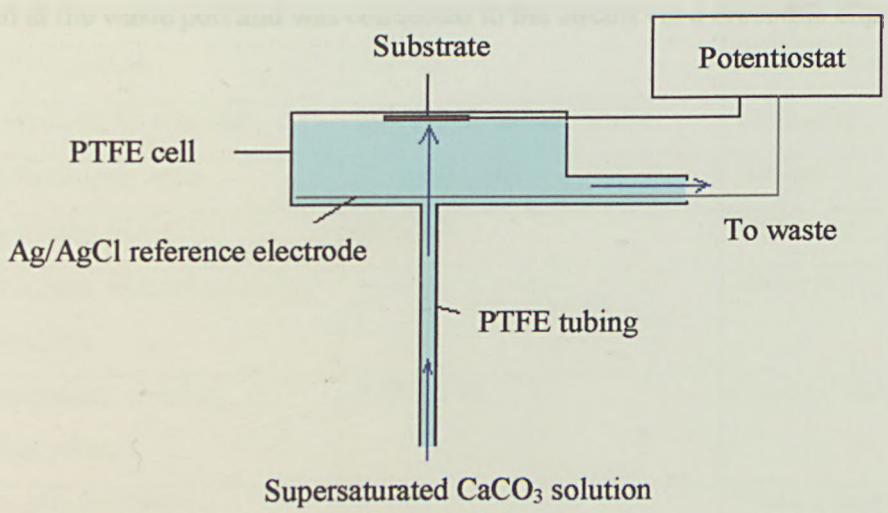

Figure 2-11: Schematic of the PTFE jet growth cell.

(a) Crystallisation on nanoparticle substrates

Functionalised gold nanoparticle substrates were adhered to circular borosilicate glass coverslips (30 mm diameter, 0.13 – 0.17 mm thick, VWR International, UK), enabling them to fit securely in the lid of the PTFE growth cell. They were placed face down in the cell, allowing the solution jet to come into direct contact with the substrate surface.

(b) Crystallisation on SAM-coated gold macroelectrodes

SAM-coated gold macroelectrodes were adhered to circular glass coverslips, as with the nanoparticle substrates, and secured, face down in the lid of the growth cell. The working electrode connection was made to a potentiostat and a potential was applied between this and a reference electrode. In this case, the reference electrode was a length 150 μm Ag/AgCl wire, wound around the base of the cell. This then exited the cell at the waste port and was connected to the circuit via a crocodile clip.

2.5 Chemical suppliers

Chemicals used throughout the project are listed in Table 2-4 below with their source and purity or grade.

Chemical	Grade/Purity	Supplier
Acetic acid	99.7+ %, A.C.S Reagent	Aldrich
Acetone	Laboratory reagent grade	Fisher Chemicals
Ammonia	35 %	Fisher Chemicals
Ammonium chloride	> 99.50 %	Sigma
Calcite	Iceland Spar	Richard Taylor Minerals
Calcium carbonate	Laboratory reagent grade	Sigma
Calcium chloride	1.0 M standard solution	Fluka Chemicals
Calcium chloride dihydrate	99.99 %	Aldrich Reagent Plus
1,2-dichloroethane	99.8 %, HPLC grade	Aldrich
Diethyl ether	AnalaR	BDH Laboratory Supplies
Dipotassium hydrogen phosphate	Laboratory reagent grade	Fisher Scientific
Ethanol	99.70 – 100.00 %	Fisher Chemicals
D(+) - glucose	AnalaR	BDH Laboratory Supplies
Hexamethyldisilazane	99+ %, electronic grade	Lancaster
Hydrochloric acid	Reagent grade	Aldrich
Hydrogen peroxide	30.00 %	GPR
Hydrogen tetrachloroaurate trihydrate		Aldrich
Magnesium chloride hexahydrate	> 99.00 %	Sigma Aldrich
p-mercaptophenol		Fluka Chemicals
11-mercaptoundecanoic acid	95.00 %	Aldrich
11-mercapto-1-undecanol	97.00 %	Aldrich

Chemical	Grade/Purity	Supplier
Methanol	HPLC grade	Fisher
Poly (allylamine hydrochloride)		Alfa Aesar
Poly (styrene sulfonic acid) sodium salt		Alfa Aesar
Potassium chloride	AnalaR	BDH Laboratory Supplies
Potassium dihydrogen phosphate	Analytical grade reagent	Fisher Scientific
Potassium nitrate	Analytical grade > 99.50 %	Fisher Chemicals
Propan-2-ol	HPLC grade	Fisher Scientific
Propidium iodide		Molecular Probes
Sodium borohydride	98 %	Lancaster
Sodium chloride	Analytical reagent grade	Fisher Scientific
Sodium fluoride	99.00 + %, A.C.S Reagent	Aldrich
Sodium hydrogen carbonate	AnalaR	BDH Laboratory Supplies
Sodium hydroxide	AnalaR	BDH Laboratory Supplies
Sodium phosphate dibasic anhydrous	> 99.00 %	Fluka Chemicals
Sodium sulfate	AnalaR	BDH Laboratory Supplies
Sulfuric acid	> 98.00 %	Fisher Chemicals
SYTO® 9		Molecular Probes
Toluene	Analytical grade reagent	Fisher Scientific
Tryptic soy agar		Merck
Tryptone		Sigma
1-undecanethiol	96.00 %	Aldrich
Urea	Analytical reagent grade	Fisher Scientific

Table 2-4: List of chemicals used, including the supplier details and grade/purity.

2.6 References

[1] www.mineql.com

[2] H. H. Teng, P. M. Dove and J. J. De Yoreo, *Geochim. Cosmochim. Acta,* **2000**, *64,* 2255.

[3] Y. Kitano, *Bull. Chem. Soc. Japan,* **1962**, *35*, 1980.

[4] J. Das, *Private Communication,* Unilever Research and Development, **2003**.

[5] J. Kwak and A. J. Bard, *Anal. Chem.*, **1989**, *61*, 1221.

[6] J. F. Hicks, S.-S. Young and R. W. Murray, *Langmuir*, **2002**, *18*, 2288.

[7] V. Ruiz, P. Liljeroth, B. M. Quinn and K. Kontturi, *Nano Lett.* **2003**, *10*, 1459.

[8] M. Brust, J. Fink, D. Bethell, D. J. Schiffrin and C. Kiely, *J. Chem. Soc., Chem. Commun.*, **1995**, 1655.

[9] J. F. Hicks, A. C. Templeton, S. Chen, K. M. Sheran, R. Jasti, R. W. Murray, J. Debord, T. G. Schaaff and R. L. Whetten, *Anal. Chem.*, **1999**, *71*, 3703.

[10] M. J. Hostetler, A. C. Templeton and R. W. Murray, *Langmuir,* **1999**, *15*, 3782.

[11] G. Decher and J. D. Hong, *Thin Solid Films*, **1992**, *210*, 831.

[12] P. S. Dobson, L. A. Bindley, J. V. Macpherson and P. R. Unwin, *Langmuir*, **2005**, *21*, 1255.

[13] K. Sato, Y. Kumagai, K. Watari, and J. Tanaka, *Langmuir*, **2004**, *20*, 2979.

[14] S. Mann, B. R. Heywood, S. Rajam and J. D. Birchall, *Proc. R. Soc. Lond.*, **1989**, *423*, 457.

[15] S. Mann, B. R. Heywood, S. Rajam and J. D. Birchall, *Nature*, **1988**, *334*, 692.

[16] P. S. Dobson, *PhD Thesis*, University of Warwick, **2001**.

Chapter 3

Functionalised Gold Nanoparticles as Seeds for the Template-Formation of Calcite

There is considerable interest in the design of surfaces and interfaces that act as templates for the nucleation and growth of $CaCO_3$, in either a particular polymorph and/or with a specific crystal habit[1]. The motivation for these studies stems partly from a desire to mimic and develop the highly organised calcium mineral systems that occur in nature[2], as well as from a technological viewpoint (e.g. the inhibition of scale formation)[3] where treatments are required that either prevent crystallisation or produce crystal morphologies that can be readily removed from surfaces.

Previous work on surface templates for calcium carbonate crystallisation has considered: (i) compressed Langmuir monolayers at the water/air interface[4,5,6], including stearate monolayers[7]; (ii) various self-assembled monolayers[8,9,10,11,12,13,14,15,16,17,18], including patterned methyl- and carboxylic acid- terminated SAMs that have resulted in the formation of intricate arrangements of single calcite crystals[19]; (iii) polymeric substrates[20,21,22,23,24,25], and patterned polymer surfaces, including molecularly imprinted surfaces[26]; and (iv) liquid-liquid interfaces[27].

In this chapter, the effects of functionalising surfaces with mercaptoundecanoic acid-functionalised Au nanoclusters (MUA-Au) on calcium carbonate nucleation and growth are investigated. It has been demonstrated that MUA-Au nanoparticles serve as templates for the crystallisation of calcite and that the extent of $CaCO_3$ nucleation on MUA-Au multilayer films can be controlled via the nanoparticle surface density.

3.1 Introduction

A core method for the preparation of nanostructured thin films is the layer-by-layer (LbL) method. This process is frequently used due to its simplicity, versatility and low cost[28,29,30,31,32,33,34,35]. The LbL approach is based on the alternating electrostatic adsorption of oppositely charged species to form a multilayered film of controllable thickness. Such strong ionic interactions result in very stable nanostructures. Moreover, the properties of the resulting multilayered film can be tuned by controlling the adsorption conditions, such as concentration of the components and exposure time, which lead to different surface coverages. Polymers are most commonly used as the linking agent in order to combine their high mechanical strength with the desired properties of different functional nanometer-sized building blocks[28,29,30,31,32,33,34,35]. The high degree of functionality that can be incorporated into these multilayered films has implemented a wide range of electronic[28], catalytic[29], sensory[30,31,32], optical[33] and photoelectrochemical applications[31,32,33], as summarised in several recent reviews[28,29,30,31,32,33,34,35]. The aim of the investigations in this chapter was to use ultrathin multilayered arrays consisting of alternating polyelectrolytes and gold nanoparticles functionalised with carboxylic acid groups as templates for $CaCO_3$ crystal growth.

In these studies, the nanoparticles were deposited onto glass surfaces in a layer-by-layer (LbL) manner using poly(allylamine) hydrochloride (PAH) as a cross linker, to form mercaptoundecanoic acid- multilayer protected clusters (MUA-MPC) as shown in Figure 3-1. This allowed the ready investigation of the nature of calcium carbonate formed by microscopy, without complications from homogeneous nucleation and

nucleation on foreign particles that could compromise pure solution-phase studies with these water soluble particles. This approach contrasts with other recent work with functionalised nanoparticles in which dense prints have been used as templates for calcium carbonate nucleation[36,37,38].

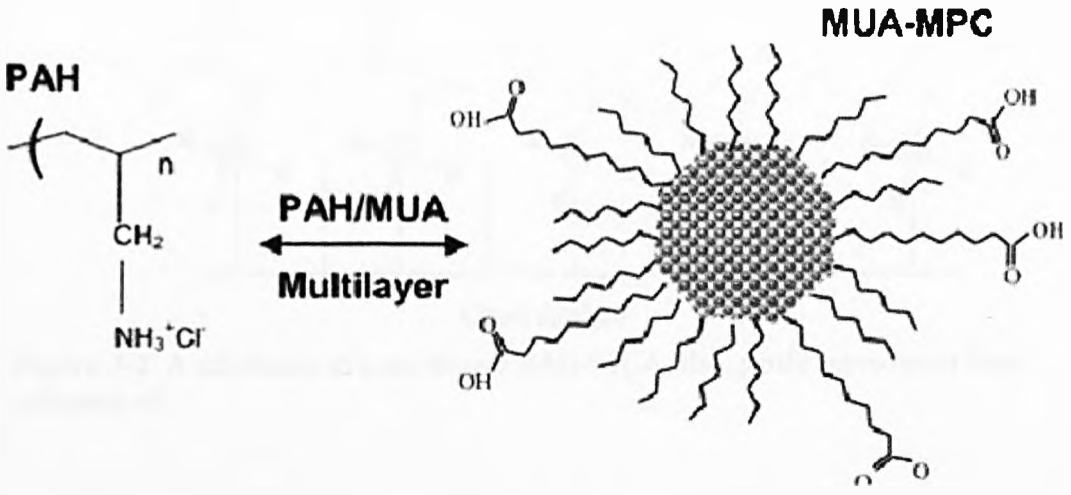

Figure 3-1: Schematic to show the formation of MUA-MPCs; reproduced from reference 41.

3.2 Experimental details

Multilayer films of carboxylic acid-functionalised nanoparticles were created using the methods detailed in Chapter 2. A schematic of the multilayer films of this type is shown in Figure 3-2.

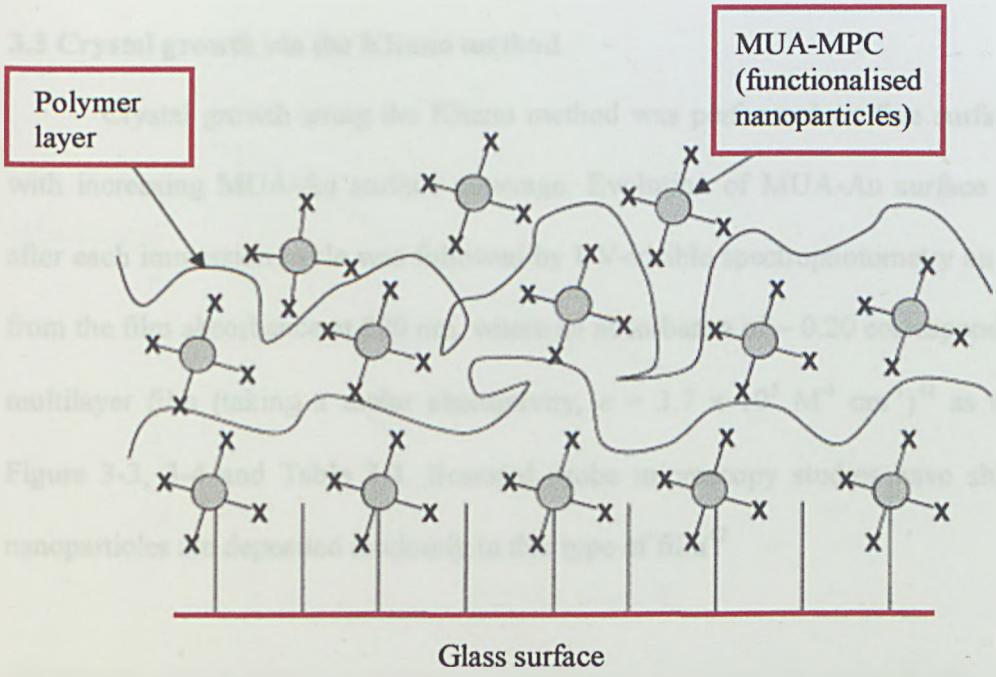

Figure 3-2: A schematic of a multilayer PAH-MUA film, partly reproduced from reference 41.

Calcium carbonate crystallisation was achieved via two methods; the well-documented Kitano method[39,40] and a jet crystallisation method. The supersaturation of the $CaCO_3$ solution used in the jet experiments was 94 (with experiments in Section 3.3.1 also being performed at solution supersaturations of 43 and 18) and the flow rate was 1 cm^3 min^{-1}. A PAH-coated glass slide (immersion time in polymer solution: 25 minutes) was used as a control surface for both crystallisation methods. Examination of the crystals was performed using micro-Raman spectroscopy (RENISHAW Raman Spectrometer) and light microscopy.

3.3 Crystal growth via the Kitano method

Crystal growth using the Kitano method was performed on five surfaces, each with increasing MUA-Au surface coverage. Evolution of MUA-Au surface coverage after each immersion cycle was followed by UV-visible spectrophotometry and derived from the film absorbance at 520 nm, where an absorbance of ~ 0.20 corresponded to a 4 multilayer film (taking a molar absorptivity, ε = 3.7 x 10^5 M^{-1} cm^{-1})[41] as shown in Figure 3-3, 3-4 and Table 3-1. Scanned probe microscopy studies have shown that nanoparticles are deposited randomly in this type of film[42].

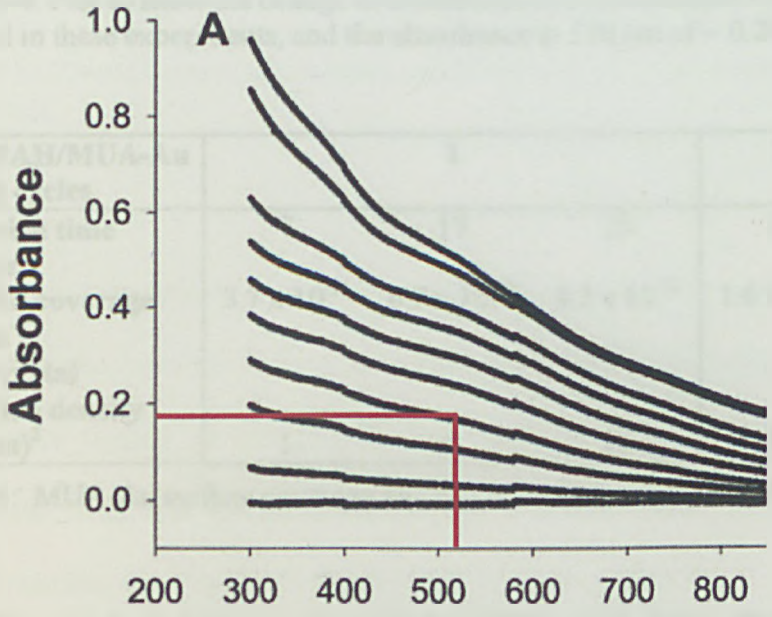

Figure 3-3: Plot to show how the absorbance of PAH-MUA-Au films varies with increasing multilayers; partly reproduced from reference 41.

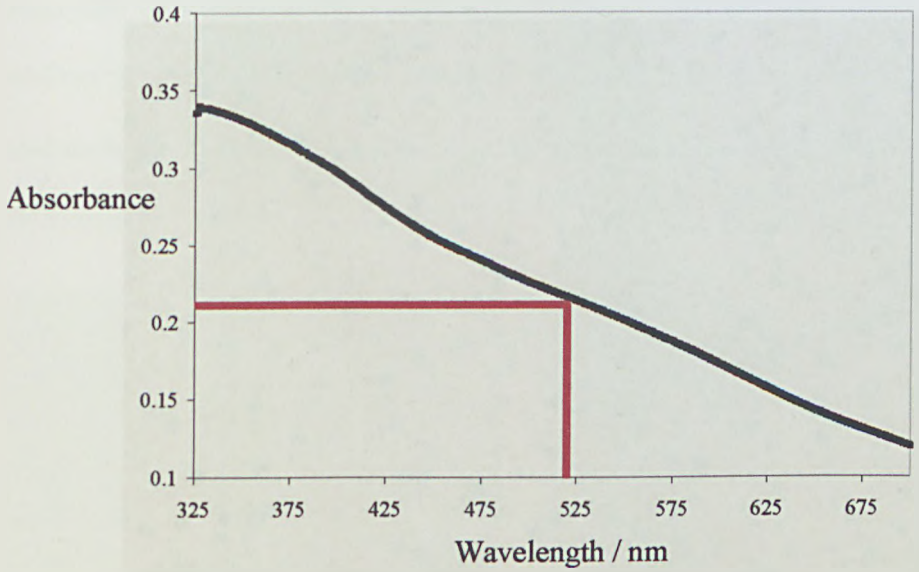

Figure 3-4: Plot to show the change in absorbance of a 4 multilayer PAH-MUA-Au film used in these experiments, and the absorbance at 520 nm of ~ 0.20.

No. of PAH/MUA-Au dipping cycles	**1**			**2**	**4**
Immersion time /minutes	7	17	25	25	25
MUA-Au coverage /mol cm^{-2}	3.7×10^{-11}	6.7×10^{-11}	8.2×10^{-11}	1.6×10^{-10}	5.7×10^{-10}
Mean crystal nucleation density /(100 µm)^2	1	5	12	18	25

Table 3-1: MUA-Au surface coverage and corresponding numbers of nucleating calcite crystals.

The gradual increase in supersaturation and long timescale of these measurements induces the production of all three polymorphs of $CaCO_3$ on bare gold or glass surfaces, but with a tendency for the predominant formation of the thermodynamically stable calcite[43], nucleating on the (104) plane. This is shown in Figure 3-5.

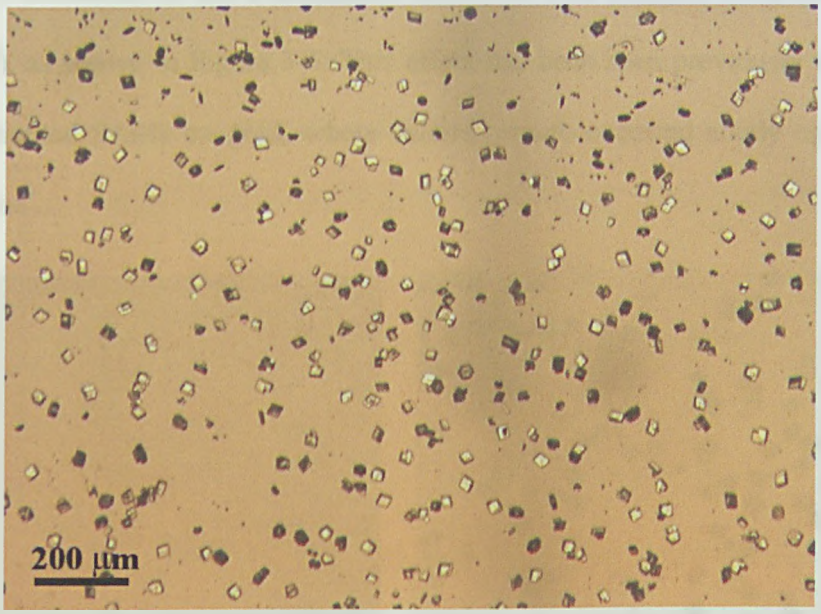

Figure 3-5: Light micrograph to show the high density of calcite microcrystals grown on glass, via the Kitano method, along with a small number of aragonite and vaterite microcrystals.

A very low density of vaterite crystals (< 1 / (100 µm)^2) were nucleated on the PAH-coated glass control surface, as evidenced by light microscopy, and no calcite crystals were formed. In contrast, for the substrates displaying functionalised gold nanoparticle films, the extent of crystal nucleation increased monotonically as the MUA-Au surface coverage increased. This is shown in Table 3-1.

Moreover, calcite was the only calcium carbonate polymorph formed; a phenomenon that was independent of MUA-Au coverage. For comparison, when a gold surface was employed on the same time scale, both calcite (~ 80 %) and vaterite (~ 20 %) polymorphs were evident. Interestingly, a high proportion (> 50 %) of calcite crystals on the MUA-Au surfaces were nucleated on the unusual (015) plane. This was

especially noticeable in the 4 multilayer MUA-Au film (surface coverage: 5.7 x 10^{-10} mol cm^{-2}), as shown in Figure 3-6. This effect has been seen previously on carboxylic acid-terminated SAMs on gold, where calcite growth occurred solely on the unusual (015) plane[9].

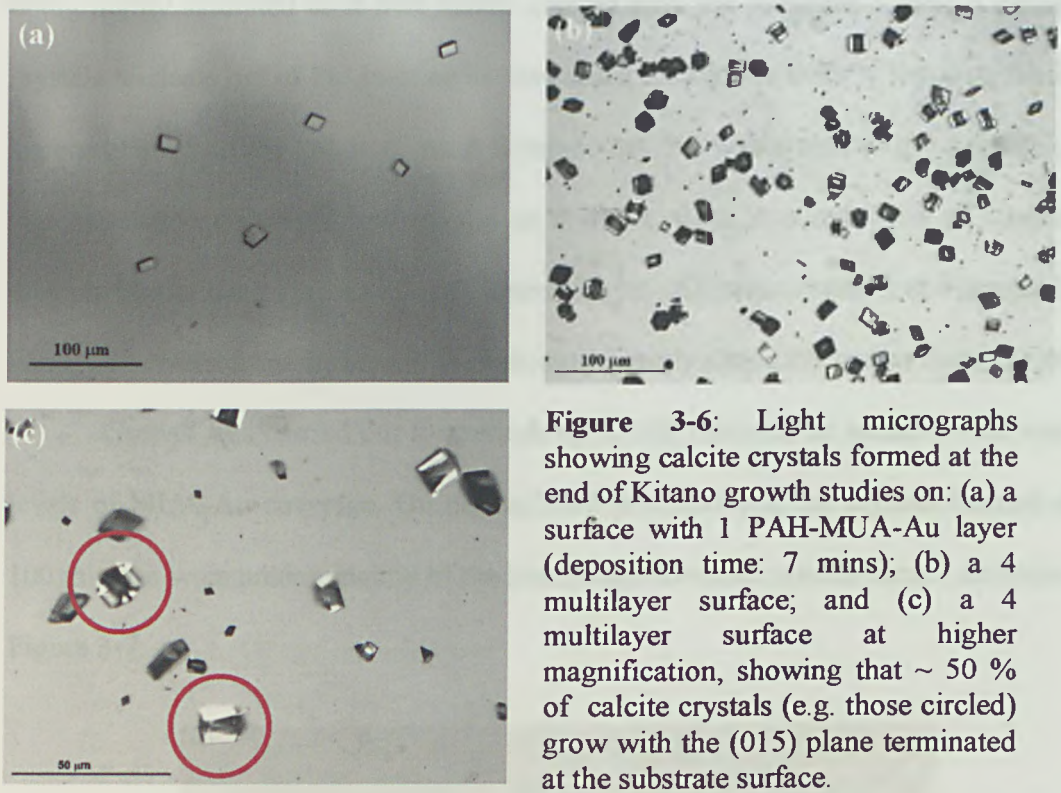

Figure 3-6: Light micrographs showing calcite crystals formed at the end of Kitano growth studies on: (a) a surface with 1 PAH-MUA-Au layer (deposition time: 7 mins); (b) a 4 multilayer surface; and (c) a 4 multilayer surface at higher magnification, showing that ~ 50 % of calcite crystals (e.g. those circled) grow with the (015) plane terminated at the substrate surface.

3.4 Crystal growth via the jet crystallisation method

The jet crystallisation system ensured that a constant supply of highly supersaturated $CaCO_3$ solution was maintained at the substrate/solution interface throughout the course of the experiment. Since Teflon was used to construct the cell and flow system, growth did not occur before solution impinged on the substrate. Due to the slow flow rate employed (1 cm^3 min^{-1}) and the inner diameter of the nozzle being 1.6

mm; the solution velocity was sufficiently slow that mass transport to the isolated micrometre-sized particles occurred predominantly by diffusion[44].

In all cases where crystallisation did occur during the jet crystallisation method, the density of crystals was greatest directly above the jet. This is due to the solution being highly saturated as it first makes contact with the substrate. Calcium carbonate crystals nucleate out of the solution as they reach the surface thereby reducing the local supersaturation of the solution. As it flows across the whole area of the substrate, the supersaturation decreases further, and as a result, there is a reduction of nucleating crystals further from the area directly above the jet. All measurements and images have hence been taken from the area of the substrate directly above the stream from the jet.

Growth was carried out for periods up to 100 minutes, on surfaces with various levels of MUA-Au coverage. On non-tailored gold surfaces, the crystals formed after 100 minutes were predominantly of the kinetically-favoured vaterite form[45], as shown in Figure 3-7.

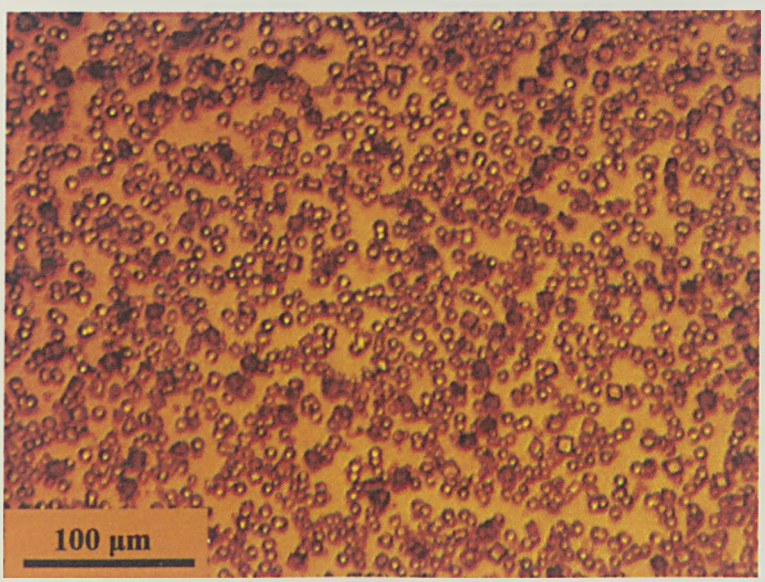

Figure 3.7: Light micrograph showing extensive vaterite microcrystal growth on a gold surface, using the jet crystallisation method (100 minutes, $S = 94$).

Examination of crystals formed on one multilayer MUA-Au films (surface coverage: 8.2×10^{-11} mol cm^{-2}), was performed using micro-Raman spectroscopy in addition to light microscopy. Using this technique, it was possible to distinguish between calcite and vaterite crystals that were not necessarily easily identifiable using light microscopy. The Raman spectrometer used a single wavelength laser light source (514 nm), which was directed towards the microcrystal of particular interest. The Raman spectrum of vaterite exhibits bands at 750 cm^{-1} and 1089 cm^{-1} in comparison to 711 cm^{-1} and 1084 cm^{-1} for calcite[46]. Vaterite also shows the splitting of these v_1 and v_4 peaks due to the two distinct site symmetries for the CO_3^{2-} groups[46]. Figure 3-8 shows overlaid spectra obtained when the laser was focussed on calcite (in red), as inferred from the rhombohedral morphology of the crystals, and vaterite (in green) crystals. Although the peaks at similar wavenumbers overlap and are difficult to distinguish, it is possible to observe the splitting of both peaks in the vaterite spectrum, confirming the deduction of crystal form made by optical inspection.

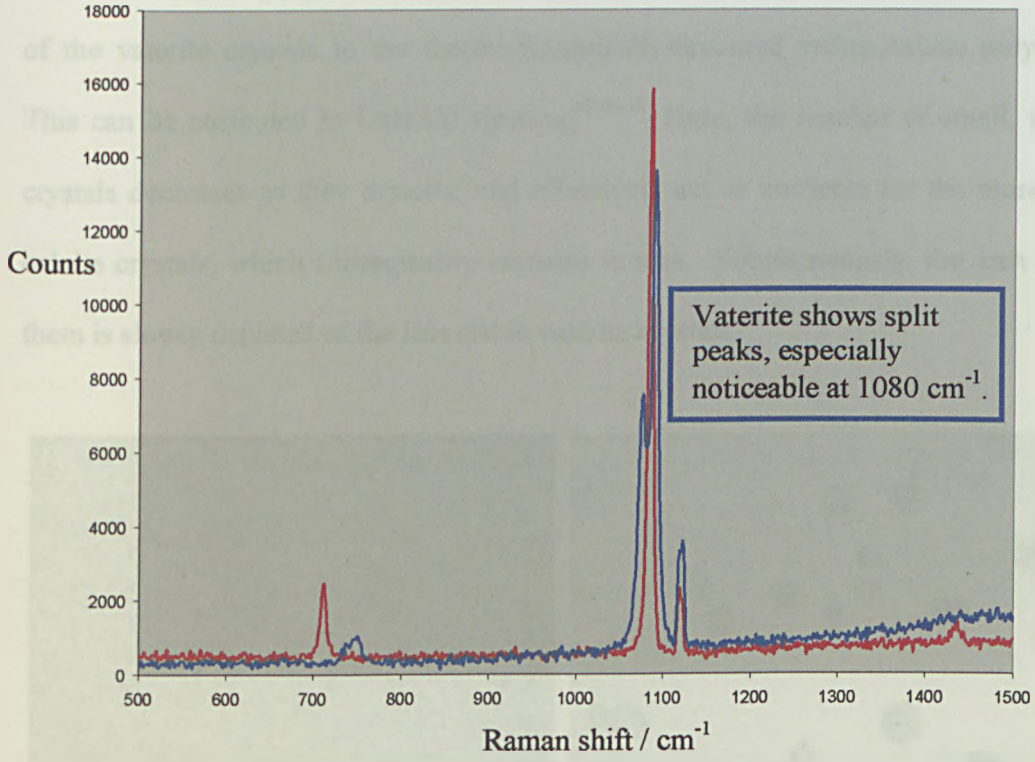

Figure 3-8: Raman spectra of calcite (red line) and vaterite (blue line) crystals.

After times of 40, 60 and 80 minutes, in separate experiments, vaterite was the main polymorph deposited (see Figure 3-9), with only a few individual calcite crystals evident. This was expected from kinetic reasoning as the initial polymorph to form is the thermodynamically stable vaterite, which must undergo two transitions before reaching the kinetically stable calcite phase. The crystal density decreased with increasing jet time, from ~ 320 crystals / (100 μm)^2 after 40 minutes to ~ 200 crystals / (100 μm)^2 after 80 minutes. After 100 minutes, there was a significant decrease in the density of crystals (~ 5 crystals / (100 μm)^2) and calcite was the sole polymorph observed (see Figure 3-9). This indicates the occurrence of a dramatic spontaneous solution recrystallisation

process during the jet growth experiments, which allows for the conformational change of the vaterite crystals to the thermodynamically-favoured stable calcite polymorph. This can be attributed to Ostwald ripening[47,48,49]. Here, the number of small, vaterite crystals decreases as they dissolve and effectively act as nutrients for the more stable calcite crystals, which subsequently increase in size. Simultaneously, the area around them is slowly depleted of the less stable vaterite crystals.

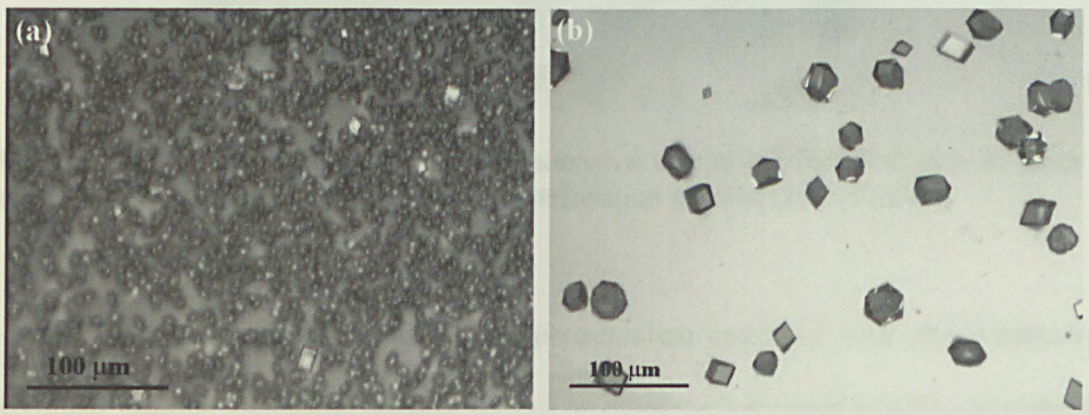

Figure 3-9: Light micrographs showing: (a) extensive vaterite coverage on a 1 PAH-MUA-Au layer (deposition time: 25 minutes) after jet growth (80 minutes); and (b) exclusive calcite formation after jet growth for 100 minutes.

That the density of nanoparticles ultimately controlled the density of calcite crystals formed was confirmed in jet growth studies on the 4 multilayer PAH-MUA-Au film. Calcite was again the exclusive polymorph formed after 100 minutes, with a density of ~ 12 crystals / (100 µm)^2, and ~ 50 % of crystals growing from the (015) plane (Figure 3-10), as seen in the Kitano experiments.

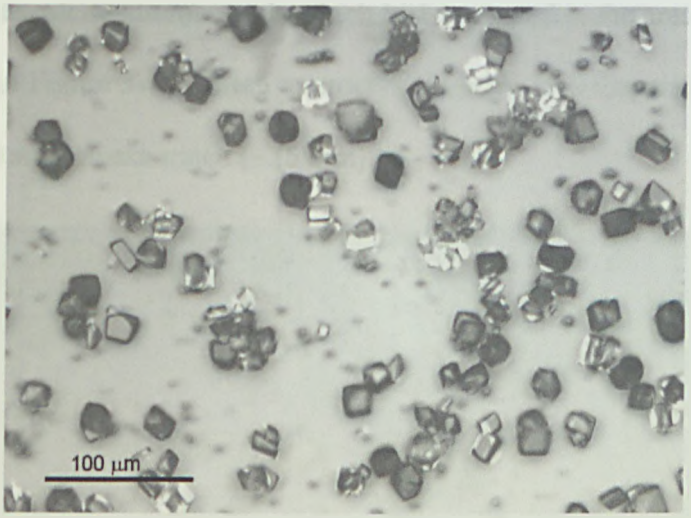

Figure 3-10: Light micrograph showing extensive calcite microcrystal growth from both the (104) and (015) planes after jet crystallisation method (100 minutes).

Under these conditions of high supersaturation and short time, the kinetically-favoured vaterite polymorph tends to prevail on other surfaces such as gold and glass, as shown for a gold surface in Figure 3-7. This was also found to be the case on carboxylic acid-, methyl- and hydroxyl- terminated SAM (on gold) surfaces (see Chapter 4). Thus, the templating effect of the functionalised gold nanoparticles evident in the studies in this chapter is significant.

3.4.1 Effects of varying supersaturation

Using the jet crystallisation technique, crystal growth at two other solution supersaturations (43 and 18) was performed on the 4 multilayer PAH-MUA-Au film, to observe the effects of supersaturation on crystal growth. At $S = 18$, no crystallisation was evident although, directly under the jet, a powdery residue was observed. At $S = 43$,

the residue observed at the lower supersaturation was present on the surface but there were also single calcite microcrystals which had nucleated in the area directly below the jet, as shown in Figure 3-11. These microcrystals were very disperse with > 10 present over the whole surface examined (~ $(5\ mm)^2$).

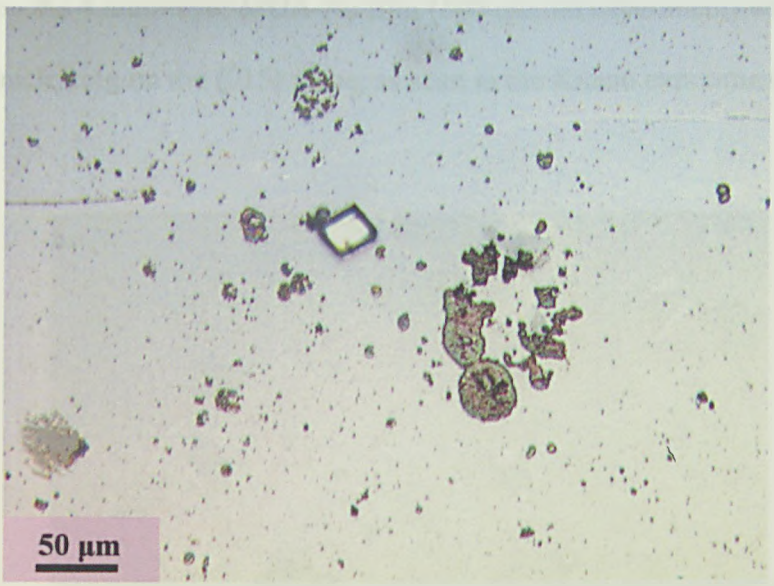

Figure 3-11: Light micrograph to show amorphous $CaCO_3$ residue and single calcite microcrystal present directly under the jet at $S = 43$.

These results show that the extent of calcite crystallisation on the multilayer surfaces is governed ultimately by the supersaturation of the solution, and that the templating effects of the functionalised nanoparticles occurs at high supersaturation only.

3.5 Orientational specificity

Although the thermodynamic nature of the Kitano experiment anticipates that the most stable polymorph should nucleate in preference to other morphologies, the fact that

many crystals nucleate on the (015) plane rather than the more stable (104) plane shows that the functionalised nanoparticles display a face-selective templating effect on the crystallisation process. This result was confirmed when the experiment was run under kinetic control, via the jet growth method. In this case, exclusive calcite growth was observed on the 4 multilayer MUA-Au film (100 minute experiment) with some crystals (~ 50 %) nucleating on the (015) plane, as seen in the Kitano experiments (see Figure 3-12).

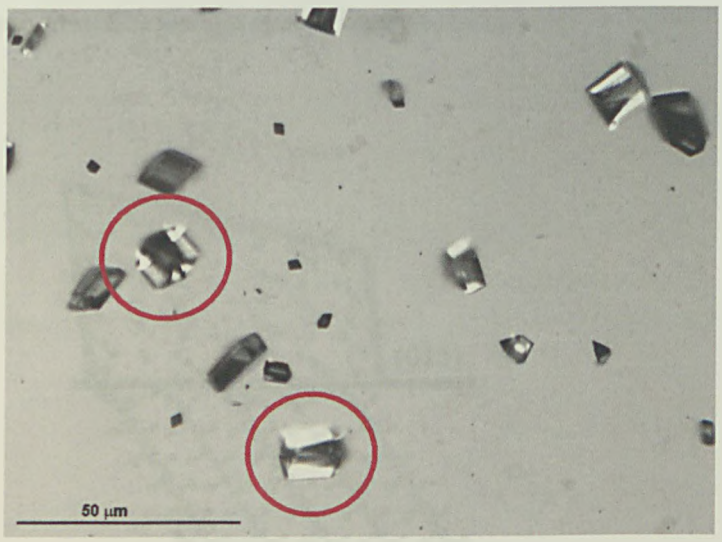

Figure 3-12: Light micrograph to show calcite crystals formed at the end of Kitano growth studies on a 4 multilayer surface showing that ~ 50 % of calcite crystals (e.g. those circled) grow with the (015) plane terminated at the substrate surface.

On carboxylic acid-terminated SAMs on macroscopic gold, calcite was formed exclusively on the (015) plane[9], when crystallisation was carried out on substrates placed in calcium chloride solution in a closed desiccators containing carbon dioxide. Aizenberg et al. have suggested that nucleation on specific planes occurs when the carbonate ions in the calcite plane match the orientation of the carboxylate end groups of

carboxylic acid-terminated alkanethiol SAMs on Au(111) surfaces. It has been shown that the carbonate ions that make an angle of ~ 36 ° with the (015) calcite face (see Figure 3-13) match with the carboxylate end groups of the functionalised alkanethiol SAMs on Au(111)[19] (see Figure 3-13 and 3-14). The acid-terminated SAMs on the gold nanoparticles appear to behave in a similar way to the SAM on the Au(111) surface and induce the face-selective nucleation of the oriented calcite polymorph. However, the presence of additional calcite crystals, nucleated on the (104) plane, indicates that oriented nucleation in this system is not wholly selective.

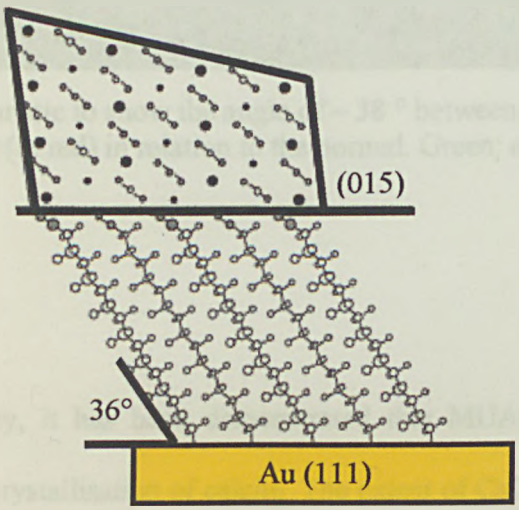

Figure 3-13: Schematic to show alignment of carboxylic acid head groups from a SAM and carbonate ions in the (015) nucleation plane of a calcite crystal.

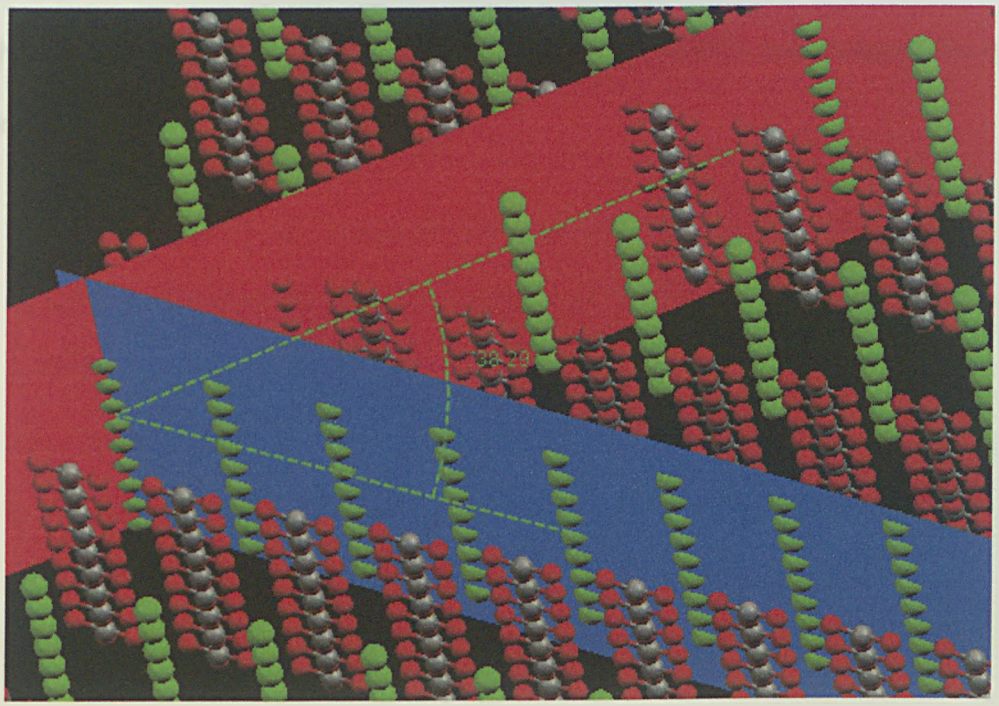

Figure 3-14: Schematic to show the angle of ~ 38 ° between the carbonate ions in the (015) calcite plane (in red) in relation to the normal. Green: calcium, grey: carbon, red: oxygen.

3.6 Conclusions

In summary, it has been demonstrated that MUA-Au nanoparticles serve as templates for the crystallisation of calcite. The extent of $CaCO_3$ nucleation on MUA-Au multilayer films can be controlled via the density of functionalised nanoparticles. Significantly, calcite is formed quickly at high supersaturation via rapid transformation of vaterite, whereas on other surfaces, such as gold, glass and certain functionalised SAM substrates, the kinetically-favoured vaterite polymorph tends to prevail. Since MUA-Au particles are soluble in aqueous solution, it is possible that they might function as dispersed, tailored seeds for crystal growth. In this environment,

nanoparticles would have the attributes of conventional SAMs on Au, but with the advantages of high surface area and the possibility of readily manipulating the crystals formed.

3.7 References

[1] S. Mann, *Biomineralization*, Oxford University Press, **2001**.

[2] J. R Young, S. A. Davis, P. R. Brown and S. Mann, *J. Struct. Biol.*, **1993**, *126*, 195.

[3] Z. Amjad, *Mineral Scale Formation and Inhibition*, Plenum Press, New York, **1995**.

[4] S. Rajam, B. R. Heywood, J. B. A. Walker, S. Mann and K. K. W. Wong, *J. Chem. Soc. Faraday Trans.*, **1991**, *87*, 727.

[5] A. L. Litvin, S. Valiyaveettil, D. L. Kaplan and S. Mann, *Adv. Mater.*, **1997**, *9*, 124.

[6] F. C. Meldrum in *Nanoparticles and Nanostructured Films* (Ed.: J. H. Fendler), Wiley-VCH, **1998**, pp. 45-47.

[7] S. Mann, B. R. Heywood, S. Rajam and J. B. A. Walker, *J. Phys. D: Appl. Phys.*, **1991**, *24*, 154.

[8] J. Küther, R. Sechadri, W. Knoll and W. Tremel, *J. Mater. Chem.*, **1998**, *8*, 641.

[9] J. Aizenberg, A. J. Black and G. M. Whitesides, *J. Am. Chem. Soc.*, **1999**, *121*, 4500.

[10] S. Mann, B. R. Heywood, S. Rajam and J. D. Birchall, *Proc. R. Soc. Lond. A*, **1989**, *423*, 457.

[11] P. J. J. A. Buijinsters, J. J. J. M. Donners, S. J. Hill, B. R. Heywood, R. J. M. Nolte, B. Zwanenburg and N. A. J. M. Sommerdijk, *Langmuir*, **2001**, *17*, 3623.

[12] J. Küther, G. Nelles, R. Seshadri, M. Schaub, H-J. Butt and W. Tremel, *Chem. Eur. J.*, **1998**, *4*, 1834.

[13] Y-J. Han and J. Aizenberg, *Angew. Chem. Int. Ed.*, **2003**, *42*, 3668.

[14] J. Aizenberg, A. J. Black and G. M. Whitesides, *Nature*, **1999**, *398*, 495.

[15] D. D. Archibald, S. B. Quadri and B. P. Gaber, *Langmuir*, **1996**, *12*, 538.

[16] J. Küther and W. Tremel, *Chem. Commun.*, **1997**, *21*, 2029.

[17] J. Küther and W. Tremel, *Thin Solid Films*, **1998**, 327.

[18] A. M. Travaille, J. J. J. M. Donners, J. W. Gerritsen, A. J. M. Sommerdijk, R. J. M. Nolte and H van Kempen, *Adv. Mater.*, **2002**, *14*, 492.

[19] J. Aizenberg, *J. Cryst. Growth*, **2000**, *211*, 143.

[20] E. Dalas, J. Kallitsis and P. G. Koutsoukos, *J. Cryst. Growth*, **1988**, *89*, 287.

[21] B. J. Brisdon, B. R. Heywood, A. G. W. Hodson, S. Mann and K. K. W. Wong, *J. Mater. Chem.*, **1994**, *4*, 1387.

[22] B. J. Brisdon, B. R. Heywood, A. G. W. Hodson, S. Mann and K. K. W. Wong, *Adv. Mater.*, **1993**, *5*, 49.

[23] J. M. Marentette, J. Norwig, E. Stöckelmann, W. H. Meyer and G. Wegner, *Adv. Mater.*, **1997**, *9*, 647.

[24] G. Falini, M. Gazzoni and A. Ripamonti, *Adv. Mater.*, **1994**, *6*, 46.

[25] Q. Shen, Y. Chen, H. Wei, Y. Zhao, D. Wang and D. Xu, *Crystal Growth and Design*, **2005**, *5*, 1387.

[26] S. M. D'Souza, C. Alexander, S. W. Carr, A. M. Waller, M. J. Whitcombe and E. N. Vulfson, *Nature*, **1999**, *398*, 312.

[27] D. Rautaray, R. Kavathekar and M. Sastry, *Faraday Discuss.*, **2005**, *129*, 205.

[28] J. H. Fendler, *Chem. Mater.*, **2001**, *13*, 3196.

[29] T. H. Galow, U. Drechsler, J. A. Hanson and V. M. Rotello, *Chem. Commun.*, **2002**, 1076.

[30] A. N. Shipway and I. Willner, *Chem. Commun.*, **2001**, 2035, and references therein.

[31] A. N. Shipway, M. Lahav and I. Willner, *Adv. Mater.*, **2000**, *12*, 993, and references therein.

[32] A. N. Shipway, E. Katz and I. Willner, *ChemPhysChem*, **2000**, *1*, 18, and references therein.

[33] J. H. Fendler in *Nanoparticles and Nanostructured Films* (Ed.: J. H. Fendler), Wiley-VCH, New York, **1998**, pp. 429-461.

[34] P. T. Hammond, *Adv. Mater.*, **2004**, *16*, 1271, and references therein.

[35] R. Shenhar and V. M. Rotello, *Acc. Chem. Res.*, **2003**, *36*, 549, and references therein.

[36] D. Rautaray, P. S. Kumar, P. P. Wadgaonkar and M. Sastry, *Chem Mater.*, **2004**, *16*, 988.

[37] I. Lee, S. W. Han, H. J. Choi and K. Kim, *Adv. Mater.*, **2001**, *13*, 1617.

[38] I. Lee, S. W. Han, S. J. Lee, H. J. Choi and K. Kim, *Adv. Mater.*, **2002**, *14*, 1640.

[39] Y. Kitano, *Bull. Chem. Soc. Japan*, **1962**, *35*, 1980.

[40] P. S. Dobson, L. A. Bindley, J. V. Macpherson and P. R. Unwin, *Langmuir*, **2005**, *21*, 1255.

[41] J. F. Hicks, S.-S. Young and R. W. Murray, *Langmuir*, **2002**, *18*, 2288.

[42] C. R. Bradbury, S. Huclova, M. Carrara and D. J. Fermín, Poster presentation: Spatial distribution of nanoparticles on electrostatic assemblies at poly-electrolyte modified surfaces, *International Conference on Electrified Interfaces*, Spa, Belgium, **2004**.

[43] K. Sato, Y. Kumagai, K. Watari and J. Tanaka, *Langmuir*, **2004**, *20*, 2979.

[44] J. Melville, N. Simjee, P. R. Unwin, B. A. Coles and R. G. Compton, *J. Phys. Chem. B*, **2002**, *106*, 2690.

[45] P. S. Dobson, *PhD Thesis*, University of Warwick, **1998**.

[46] C. G. Kontoyannis and N. G. Vagenas, *The Analyst*, **2000**, *125*, 251.

[47] R. Boistelle and J. P. Astier, *J. Cryst. Growth*, **1988**, *90*, 14.

[48] J. D. Ng, B. Lorber, J. Witz, A. Théobald-Dietrich, D. Kern and R. Giegé, *J. Cryst. Growth*, **1996**, *168*, 50.

[49] D. E. Kile, D. D. Eberl, A. R. Hoch and M. M. Reddy, *Geochim. Cosmochim. Acta*, **2000**, *64*, 2937.

Chapter 4

The Effect of Surface Potential on the Crystallisation of Calcium Carbonate on Self-Assembled Monolayers

The aim of this chapter is to investigate the effect of the application of a potential to native gold electrodes and gold surfaces functionalised with self-assembled monolayers, on calcium carbonate crystallisation. The influence of surface potential on crystallisation on carboxylic acid-, methyl- and hydroxyl- terminated SAMs on gold is shown to be significant, such that potential control offers the possibility of a 'tunable' surface which can be used to control the nature and extent of crystallisation on chemically-functionalised surfaces.

4.1 Introduction

Calcium carbonate is one of the most widely studied minerals, particularly in the context of biomineralisation[1]. Consequently, there is widespread interest in the controlled crystallisation of calcium carbonate, mainly due to: (i) the geological and biological ubiquity of the various mineral modifications of $CaCO_3$, namely calcite, vaterite and aragonite[2]; and (ii) the interest in it as a model system for studies of heterogeneous nucleation at organic-inorganic boundaries. Many studies have been undertaken to investigate the templated growth of $CaCO_3$ on various different SAMs[3,4,5,6,7], although to date none has focussed on the effects of the surface potential of these SAMs on the nucleation of calcium carbonate.

Research on the growth of calcium carbonate crystals on functionalised interfaces in the form of SAMs has been extensive. The molecular adsorbates, usually based on alkanethiols, bind to gold substrates through strong S-Au linkages. Although SAMs were first discovered in 1946, when Zisman published a paper on the preparation of a monomolecular layer by adsorption (self-assembly)[8], their potential was not realised for a further thirty years with extensive research and characterisation of SAMs only being developed over the last twenty-five years[9,10,11,12,13].

Very early work on SAMs focused on the use of chlorosilanes to hydrophobise glass[14], and in 1983 Nuzzo and Allara showed that SAMs of alkanethiols on gold could be prepared by adsorption of di-*n*-alkyl disulfides from dilute solutions[15]. The movement away from the moisture sensitive chlorosilanes, and the ability to use a crystalline gold surface as a substrate were two important reasons for the continuing use of SAMs and, although many other self-assembly systems have since been investigated[16,17,18], monolayers of alkanethiols on gold remain the most studied SAMs to date[14].

The monolayers that self-assemble on a gold substrate are of a highly ordered, densely packed structure, making them ideal as templates for the study of calcium carbonate growth[6,19,20]. Another particularly attractive feature of SAMs is the fact that both the head and tail groups of the constituent may be tailored to exhibit a variety of surface properties (polarity, hydrophobicity etc.) which may be used to alter crystal morphology and orientation during growth. Küther et al. have found that polar surfaces are capable of nucleating a greater number of crystals than their non-polar counterparts[3], and in 1999, Aizenberg, Black and Whitesides published work on the control of crystal

nucleation using patterned SAMs[5]. It was found that although crystal growth occurred on both CO_2H- and CH_3- terminated SAMs when separate, when mixed, crystal growth occurred only on the CO_2H-terminated areas, an effect which was ascribed to mass transport to the latter regions, induced by the preferential nucleation and growth on the CO_2H- terminated patches[21].

The orientational control of crystal growth has been the subject of extensive research and several papers have been published on this topic[4,22,23,24]. In 1999, Whitesides and Aizenberg concluded that oriented growth of calcite on different faces occurred on CO_2^-/Au, OH/Au and SO_3^-/Au surfaces, with no specific crystallographic orientation observed for either the CH_3/Au interface or the bare gold. Differences in crystal orientations on the same functional groups, but on gold and silver substrates, were observed. For example, on a CO_2^-/Au SAM assembly, calcite nucleated on the (015) face, whereas on a CO_2^-/Ag SAM, calcite was oriented solely on the (012) face. This was thought to be due to the different geometry of the SAMs, i.e. the different tilt of the alkanethiols on the Au(111) surface and the Ag(111) surface[25].

In this chapter, a fast jet crystallisation method has been used, along with the more traditional Kitano growth technique[26], to investigate the effect on calcium carbonate nucleation of changing the potential of a bare gold surface, and carboxylic acid-, methyl- and hydroxyl- terminated SAMs on gold. The effects are shown to be significant, such that potential control offers the possibility of directing the extent and nature of calcium carbonate crystallisation on foreign surfaces.

4.2 Experimental methods

Gold macroelectrodes were fabricated as described in Chapter 2, some of these being functionalised with CO_2H-, CH_3- and OH- terminated SAMs, using the following solutions: 11-mercaptoundecanoic acid ($HS(CH_2)_{11}CO_2H$), 1-undecanethiol ($CH_3(CH_2)_{10}SH$) and 11-mercapto-1-undecanol ($HS(CH_2)_{11}OH$).

To ensure that monolayer coverage had occurred over the surface, contact angle measurements were made, with a drop of water deposited on the chosen surface. Figures 4-1 and 4-2 show examples of these measurements, and how the contact angle differs depending on the functionality of the surface. A hydrophobic surface (e.g. CH_3-terminated) resulted in a higher contact angle than a hydrophilic surface (e.g. CO_2H-terminated). The contact angle for the CH_3- terminated SAM was measured as 110 °, and that for the CO_2H- terminated SAM was 58 °. These values are in good agreement with the corresponding literature values, which are 109 – 112 ° and 60 – 65 ° respectively[27]. The literature value for the water contact angle on bare gold is 68 - 72 ° [28], and that for an OH- terminated SAM is ≤ 10 ° [29].

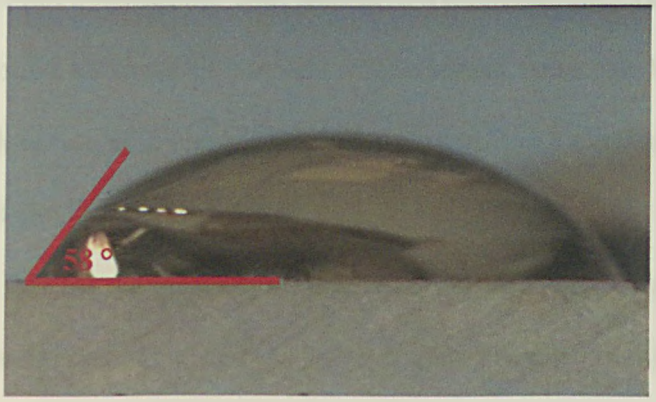

Figure 4-1: Photograph to show contact angle measurement of water on CO_2H-terminated SAM.

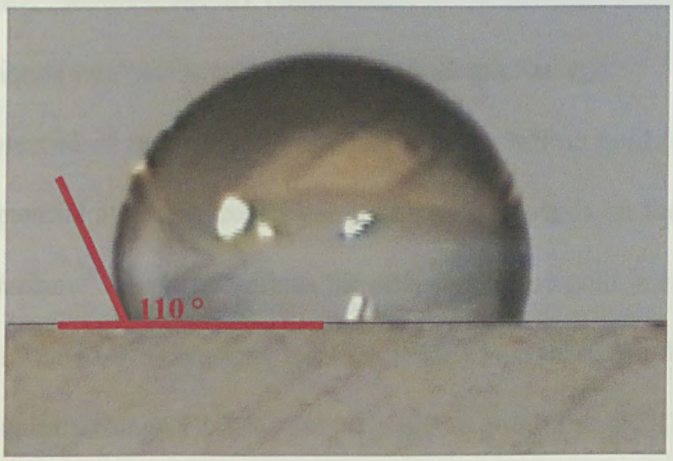

Figure 4-2: Photograph to show contact angle measurement of water on CH_3-terminated SAM.

During jet crystallisation, the SAM-coated gold macroelectrodes were positioned in the roof of the home made jet cell, allowing the flowing solution to impinge on the substrate surface. Solutions with $S = 94$, 43 and 18 were used for these experiments, and were prepared as described in Chapter 2. For the duration of the experiments, a potential (either -0.40 V, -0.05 V, +0.20 V or +0.40 V) was applied to the gold substrate using a portable, home built potentiostat, with respect to a reference electrode (Ag/AgCl), which was wound around the base of the cell. Experiments were ran for a duration of 50 minutes, at a flow rate of 2 cm^3/minute. The surfaces were examined at the end of the experiment using an optical microscope.

During Kitano crystallisation, the SAM-coated gold macroelectrodes were positioned face down on the surface of a Kitano growth solution for 40 hours. A potential (-0.40 V or -0.05 V) was applied to the gold substrate with respect to a

saturated calomel electrode (SCE). Observation of the surfaces following crystal growth via both techniques was performed using an optical microscope.

The potential of zero charge (PZC) of polycrystalline gold (defined as the value of electrode potential at which excess charge is zero) depends on the chemical nature of the electrode surface[30]. Reported values for polycrystalline gold, measured in perchloric acid versus the standard hydrogen electrode (SHE) vary between 90 mV and 150 mV [30,31]. Converting the average PZC for polycrystalline gold to an SCE reference electrode, results in an average PZC value of -0.122 ± 0.03 V. The open circuit potential of gold for both Kitano growth solutions and during jet flow experiments was recorded as 0.04 ± 0.01 V vs. SCE. This indicates that the open circuit potential is positive of the PZC. Figure 4-3 is a simple schematic to show that the open circuit potential of gold (vs. SCE) is positive of the PZC, and how the charge on the surface can be changed via the applied potential.

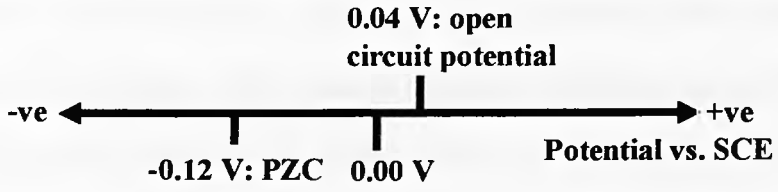

Figure 4-3: Schematic to show the PZC and open circuit potential (vs. SCE) of polycrystalline gold, as a function of positive and negative potential.

Tables 4-1 and 4-2 show the applied potentials, for the jet experiments and Kitano experiments, respectively, with respect to the PZC.

Potential vs. Ag/AgCl	Estimated potential with respect to the PZC
-0.40 V	-0.32 V
-0.05 V	+0.03 V (close to PZC)
+0.20 V	+0.28 V
+0.40 V	+0.48 V

Table 4-1: Applied potentials (±1 mV) used for jet experiments, and their relation with respect to the PZC.

Potential vs. SCE	Estimated potential with respect to the PZC
-0.40 V	-0.28 V
-0.05 V	-0.07 V (close to PZC)

Table 4-2: Applied potentials (±1 mV) for Kitano experiments and their relation to the PZC.

To ensure that there was no electrolysis (of solvent or oxygen) at the surface when held at the operating potentials, cyclic voltammograms were run on each macroelectrode surface, with respect to a Ag/AgCl reference electrode and a Pt gauze counter electrode, between -0.40 V and +0.40 V at 50 mV/s and 100 mV/s, in 0.1 M NaF (Aldrich) at pH 8.5. All resulting voltammograms displayed no peaks over the potential range of interest and just showed a charging current. Figure 4-4 shows typical cyclic voltammograms recorded at 50 mV/s for bare gold and the OH- terminated SAM surface on gold. The adsorption of a SAM on the gold surface resulted in a decrease of the charging currents, as expected[32]. This reduction in capacitance can be attributed to the blocking of the electrode surface by the SAM coating and provided confirmation (in addition to contact angle measurements) of the presence of the SAMs on the surface.

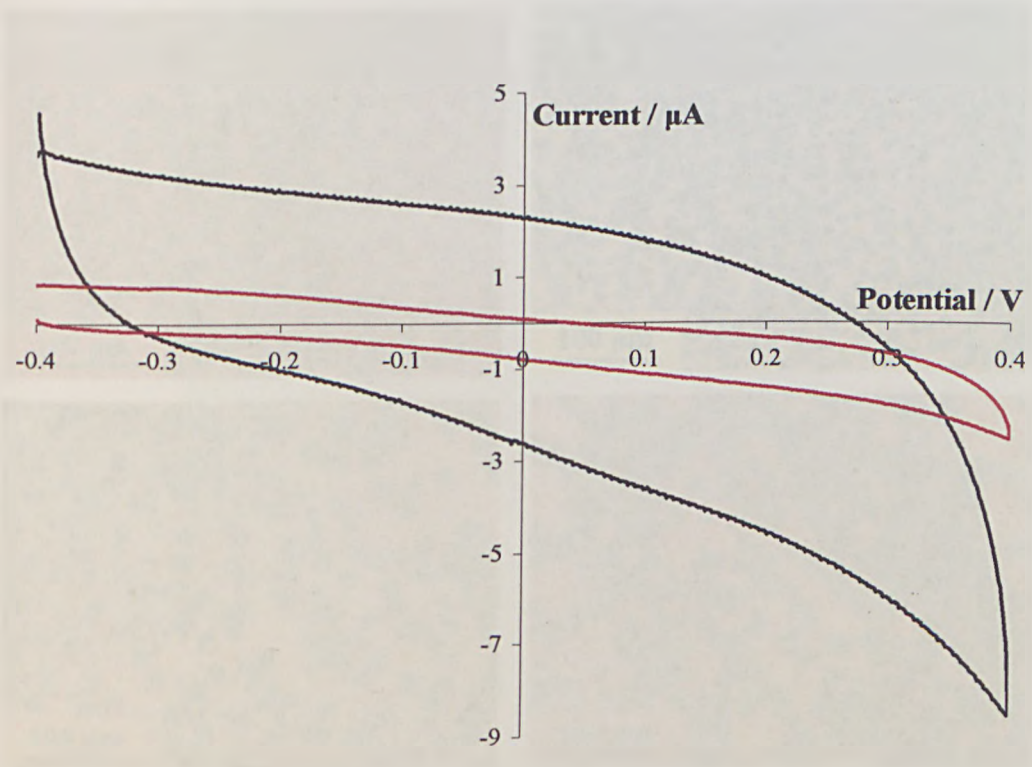

Figure 4-4: Cyclic voltammograms for a gold surface (black) and an OH- terminated SAM (11-mercapto-1-undecanol) surface on gold (red) measured in 0.1 M NaF (pH 8.5), at 50 mV/s. Electrode area: 1 cm^2.

4.3 Jet crystallisation results

Initial experiments were carried out at relatively high supersaturation, $S = 94$. Extensive nucleation occurred on gold and all three of the SAM surfaces where the potential was held near to the PZC at -0.05 V vs. Ag/AgCl (-0.09 V vs. SCE), as shown in Figure 4-5.

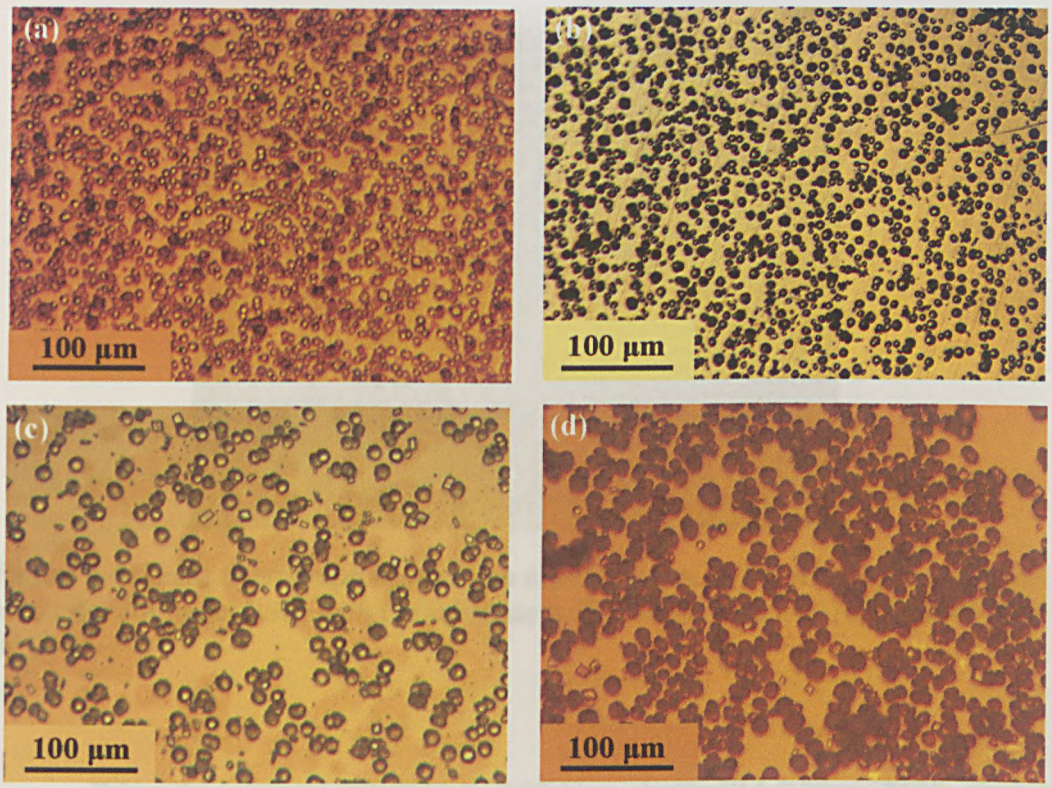

Figure 4-5: Light micrographs showing crystal growth, directly under the jet at $S = 94$, at -0.05 V vs. Ag/AgCl (-0.09 V vs. SCE), on: (a) the gold surface; (b) the CO_2H- terminated SAM surface; (c) the CH_3- terminated SAM surface; and (d) the OH- terminated SAM surface.

However, strikingly, no crystal growth was visible on any of the surfaces held at -0.40 V vs. Ag/AgCl (-0.43 V vs. SCE), for which the potential was significantly negative of the PZC. This lack of crystallisation is evident in the micrograph in Figure 4-6 for the CO_2H- terminated SAM surface.

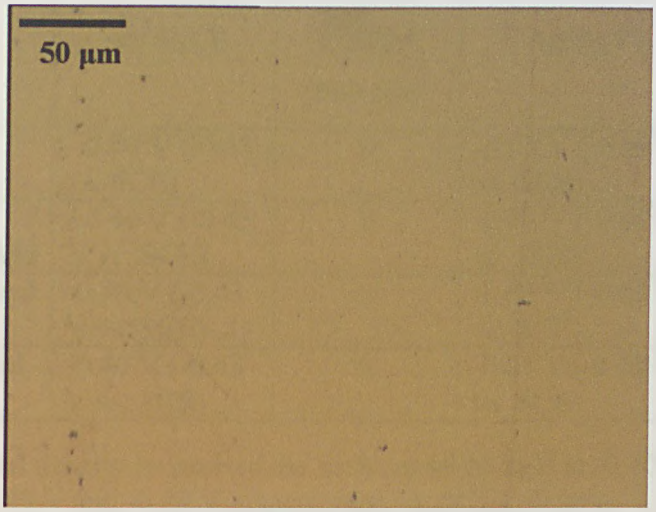

Figure 4-6: Light micrograph showing no crystallisation on CO_2H- terminated SAM substrate, during jet flow, with the substrate held at -0.40 V vs. Ag/AgCl (-0.43 V vs. SCE) ($S = 94$).

When the substrate was held at -0.05 V vs. Ag/AgCl (-0.09 vs. SCE), close to the PZC, the extent of calcium carbonate crystallisation depended on the substrate (Table 4-3). The density of crystals on each of the different surfaces varied, with an average value of 60 ± 5 crystals / (100 µm)^2 on the bare gold surface, 120 ± 5 crystals / (100 µm)^2 on the CO_2H- terminated SAM surface, 25 ± 5 crystals / (100 µm)^2 on the CH_3- terminated SAM surface and 30 ± 5 crystals / (100 µm)^2 on the OH- terminated SAM surface. This data is shown in Table 4-3. The polarity of the surface seems to have an effect on the amount of crystallisation that occurs, with the polar surfaces capable of nucleating a greater number of crystals than their non-polar counterparts[3]. Crystals on the bare gold and CO_2H- terminated SAM surface ranged in diameter between 2 and 7 µm, whereas those on the OH- and CH_3- terminated SAM surfaces were, in general, larger, with diameters in the range of 5 – 10 µm.

Substrate	Potential (vs. Ag/AgCl)	Crystal density/ $(100\ \mu m)^2$	Potential (vs. Ag/AgCl)	Crystal density/ $(100\ \mu m)^2$
Gold	- 0.40 V (-0.43 vs. SCE)	0	-0.05 V (-0.09 V vs. SCE)	60 ± 5
CO_2H-terminated SAM	- 0.40 V (-0.43 V vs. SCE)	0	-0.05 V (-0.09 V vs. SCE)	120 ± 5
CH_3- terminated SAM	-0.40 V (-0.43 V vs. SCE)	0	-0.05 V (-0.09 V vs. SCE)	25 ± 5
OH- terminated SAM	-0.40 V (-0.43 V vs. SCE)	0	-0.05 V (-0.09 V vs. SCE)	30 ± 5

Table 4-3: Crystal density on each of the surfaces when held at -0.40 V and -0.05 V vs. Ag/AgCl (-0.43 V and -0.09 V respectively, vs. SCE), ±1 mV.

When the potential applied to the surfaces was raised higher to +0.20 V vs. Ag/AgCl (+0.16 vs. SCE) and +0.40 V vs. Ag/AgCl (+0.36 vs. SCE), well positive of the PZC, further crystal nucleation was observed on all surfaces, as shown in Table 4-4. As observed previously, crystals were mainly of the vaterite phase, with only a few calcite crystals nucleating.

Substrate	Potential (vs. Ag/AgCl)	Crystal density/ $(100\ \mu m)^2$	Potential (vs. Ag/AgCl)	Crystal density/ $(100\ \mu m)^2$
Gold	+0.20 V (+0.16 V vs. SCE)	80 ± 5	+0.40 V (+0.36 V vs. SCE)	120 ± 5
CO_2H-terminated SAM	+0.20 V (+0.16 V vs. SCE)	125 ± 5	+0.40 V (+0.36 V vs. SCE)	140 ± 5
CH_3- terminated SAM	+0.20 V (+0.16 V vs. SCE)	100 ± 5	+0.40 V (+0.36 V vs. SCE)	200 ± 5
OH- terminated SAM	+0.20 V (+0.16 V vs. SCE)	40 ± 5	+0.40 V (+0.36 V vs. SCE)	60 ± 5

Table 4-4: Crystal density on each of the surfaces when held at +0.20 V and +0.40 V vs. Ag/AgCl (+0.16 V and +0.36 V respectively, vs. SCE), ±1 mV.

This increase in crystal density with increasing positive potential is shown for the CH_3- terminated SAM surface, as an example, in Figure 4-7. It is clear from these images that although the crystal density increases with potential, the size of the crystals decreases. In the case of the CH_3- terminated SAM, the increase in positive potential is accompanied by a decrease in crystal diameter from ~ 7 μm at -0.05 V vs. Ag/AgCl (-0.09 V vs. SCE) to ~ 2 μm at + 0.40 V vs. Ag/AgCl (+0.36 V vs. SCE). In all other cases, the decrease in crystal size was minimal.

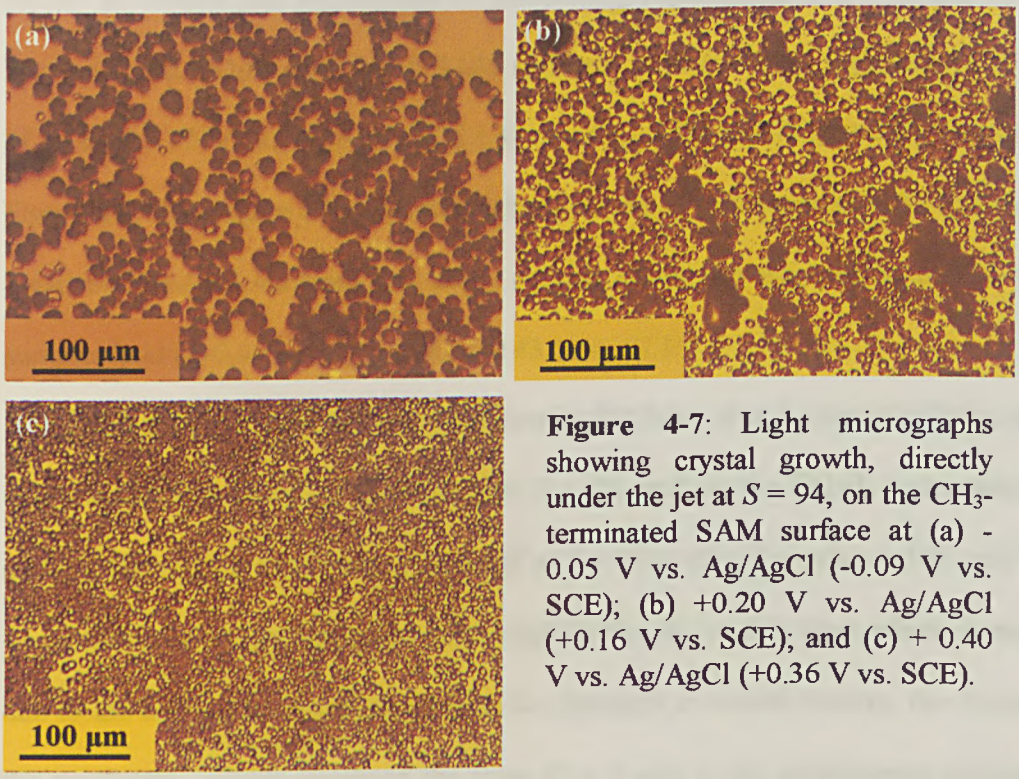

Figure 4-7: Light micrographs showing crystal growth, directly under the jet at $S = 94$, on the CH_3-terminated SAM surface at (a) -0.05 V vs. Ag/AgCl (-0.09 V vs. SCE); (b) +0.20 V vs. Ag/AgCl (+0.16 V vs. SCE); and (c) + 0.40 V vs. Ag/AgCl (+0.36 V vs. SCE).

Also, at open circuit potential on a gold surface, crystal nucleation was again evident, and the crystals grown were predominantly of the kinetically-favoured vaterite form. The extent of crystal nucleation was thus observed to be enhanced with the increasing positive surface charge for all substrates studied.

Nearly all (~ 95 %) of the crystals nucleated on the surfaces at the PZC (and potentials positive of this) were of the vaterite morphology. A very small number of calcite crystals were observed, nucleated on the (104) stable plane, on all surfaces studied. The preferable formation of vaterite, over calcite, can be attributed to the fast nature of the jet experiment, and is due to vaterite being the kinetically favourable polymorph of calcium carbonate[33].

The effect of the supersaturation of the crystallising solution on the extent of crystal nucleation was investigated by performing experiments at $S = 43$ and 18 on the bare gold and CO_2H- terminated SAM surfaces, at -0.40 V vs. Ag/AgCl (-0.43 V vs. SCE) and -0.05 V vs. Ag/AgCl (-0.09 V vs. SCE). The resulting images are shown in Figure 4-8. The degree of crystal nucleation decreased with supersaturation on the more positively charged surfaces and there was no nucleation evident, as before, on the surfaces held at -0.40 V vs. Ag/AgCl (-0.43 V vs. SCE).

On the gold surface, the crystal density fell from 60 ± 5 crystals / (100 μm)^2 at S = 94, to 20 ± 2 crystals / (100 μm)^2 at $S = 43$, and on the CO_2H- terminated SAM surface, from 120 ± 5 crystals / (100 μm)^2 at $S = 94$ to 20 ± 2 crystals / (100 μm)^2 at S = 43, with calcite being the major polymorph nucleating in this case, which is expected due to the low supersaturation. Despite the decrease in crystal density, the diameter of the nucleating crystals remained the same (5 – 7 μm) as for experiments conducted at the higher supersaturation. For $S = 18$, no crystal growth was observed on either of the surfaces at either potential.

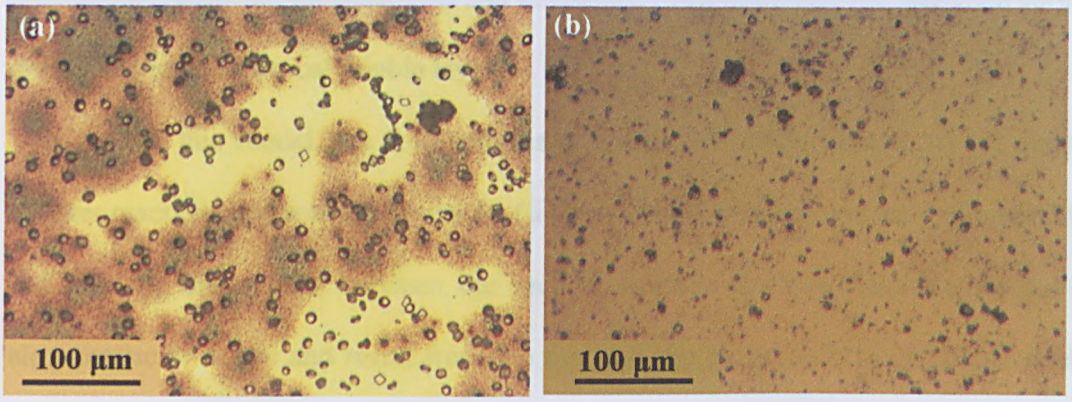

Figure 4-8: Light micrographs showing the decreased density of crystal growth under the jet at $S = 43$, at -0.05 V vs. Ag/AgCl (-0.09 V vs. SCE), on: (a) the gold surface; and (b) the CO_2H- terminated SAM surface.

To confirm that the potential effects were due to the SAMs and that there was no desorption of the monolayer, the jet experiment was repeated with a CO_2H- terminated SAM substrate, where the potential was held at -0.40 V vs. Ag/AgCl (-0.43 V vs. SCE) for 40 minutes, before being increased to -0.05 V vs. Ag/AgCl (-0.09 V vs. SCE) for a further 40 minutes ($S = 94$). After inspection of the substrate with the light microscope, vaterite and calcite nucleation was observed, directly under the jet, as expected, with a density of ~ 100 ± 5 crystals / (100 µm)^2 and a crystal size of 5 – 12 µm. The similarity of this result to that in Table 4-3 indicated that at negative potentials, desorption of the monolayer did not occur, as expected.

The major effect of these 'tunable' surfaces, is that they allow calcium carbonate crystallisation to occur when the surface potential is near to, or positive of, the PZC, but inhibit crystallisation at more negative potentials. This dramatic effect can be rationalised in terms of the Helmholtz diffusion layer model which describes the

interactions occurring between ions and molecules in solution and the electrode surface, giving rise to an electrical double layer[32].

With this model, the following assumptions are made, where: (i) no electron transfer reactions occur at the electrode; (ii) the solution is composed only of electrolyte; and (iii) the interactions between the ions in solution and the electrode surface are electrostatic in nature and result from the fact that the electrode holds a charge density which arises from either an excess or deficiency of electrons at the electrode surface. Thus, in order for the interface to remain neutral the charge held on the electrode is balanced by the redistribution of ions close to the electrode surface.

The attracted ions (in Figure 4-9, cations) can thus approach the electrode surface and form a layer to balance the electrode charge (which is displayed as negative in Figure 4-9). The distance of approach is limited to the radius of the ion and a single sphere of solvation round each ion, in what is termed the 'Outer Helmholtz Plane' (OHP). As ions are able to move in solution, however, the model can be modified so that although there is the region close to the electrode surface containing an excess of one type of ion (in this case, cations) the potential drop moving away from the electrode surface, occurs over a much larger diffuse layer.

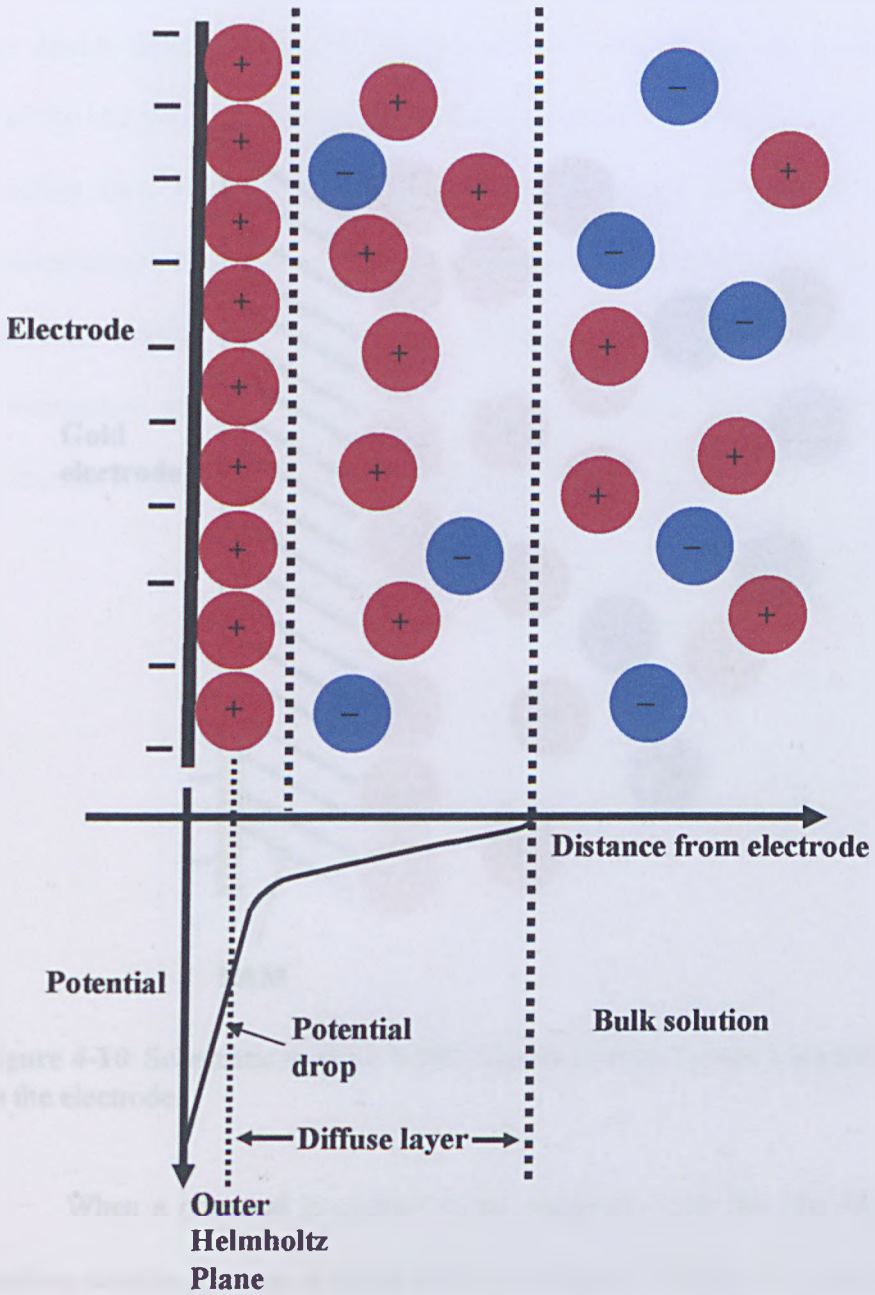

Figure 4-9: Schematic to show the effect of a negative potential on an electrode surface on the ions in the electrolyte solution.

Figure 4-10 shows the situation expected at a SAM-coated gold electrode/solution interface, when a negative charge is applied to the electrode.

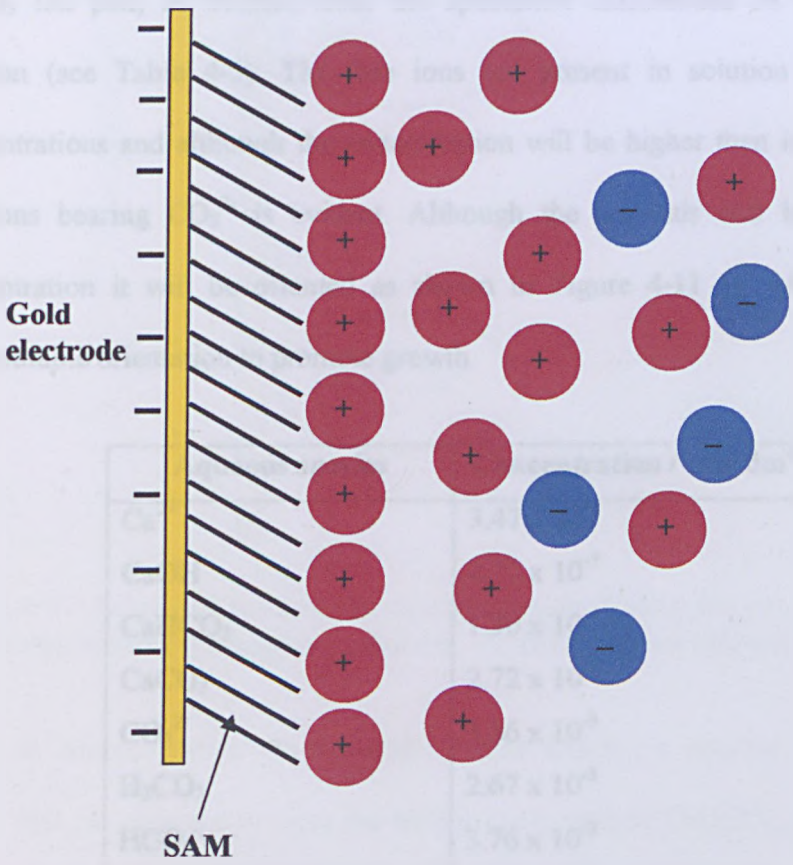

Figure 4-10: Schematic to show SAM/solution interface when a negative charge is on the electrode.

When a potential is applied to the electrode, such that the electrode charge is positive, similar pictures to those shown in Figure 4-9 and 4-10 are expected, except anions in solution balance the charge on the electrode. Additionally, the weaker hydration energy of the anions means that those in the high electric field close to the electrode are likely to be completely dehydrated, such that the closest plane (inner

Helmholtz plane) is located closer to the electrode.

With the electrode bearing a negative charge, the free cations which would form the double layer in these experiments are Ca^{2+}, $CaOH^{+}$ and H^{+} as well as the neutral $CaCO_3$ ion pair, as evident from the speciation calculations of the supersaturated solution (see Table 4-5). The free ions are present in solution at relatively low concentrations and although the concentration will be higher than in bulk, the lack of any ions bearing CO_3^{2-} is evident. Although the ion pair will be present at high concentration it will be oriented as shown in Figure 4-11 (a) which results in an unfavourable orientation to promote growth.

Aqueous species	Concentration / mol dm^{-3}
Ca^{2+}	3.47×10^{-4}
$CaOH^{+}$	2.77×10^{-7}
$CaHCO_3^{-}$	1.30×10^{-4}
$CaCO_3$	2.72×10^{-3}
CO_3^{2-}	5.56×10^{-3}
H_2CO_3	2.67×10^{-5}
HCO_3^{-}	3.76×10^{-2}
H_2O	1.00×10^{0}
OH^{-}	3.18×10^{-5}
H^{+}	3.16×10^{-10}
S	**94**

Table 4-5: Speciation concentrations as calculated using MINEQL+ software, for $S = 94$.

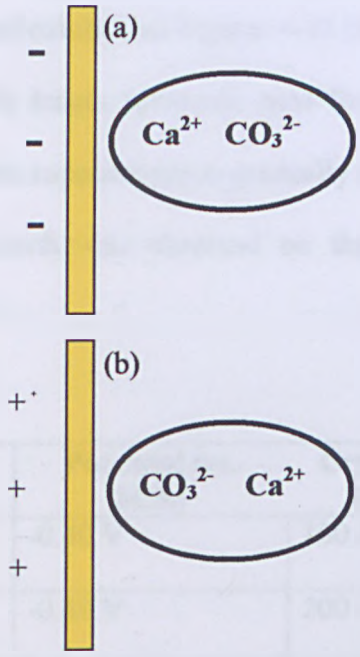

Figure 4-11: Schematic to show the orientation of the $CaCO_3$ ion pair at an electrode surface displaying: (a) a negative potential; and (b) a positive potential.

In contrast, when the electrode surface displays a positive potential, the free anions that are attracted to form the diffuse layer include $CaHCO_3^-$, CO_3^{2-}, HCO_3^- and OH^-, as well as the $CaCO_3$ ion pair. Moreover, the latter will be oriented as shown in Figure 4-11 (b), which is more likely to lead to dehydration of the CO_3^{2-} part of the ion pair, which is a key step in the formation of the crystal as calcite formation preferentially occurs at anionic reaction sites[33]. This would explain the dramatic effect of the electrode potential on the crystallisation process observed.

4.4 Kitano crystallisation method results

At the end of potential-controlled Kitano growth studies, only a very low density

of calcium carbonate nucleation was observed on the bare gold, OH-, and CO_2H-terminated SAM surfaces held at a -0.40 V vs. SCE, with the crystal morphology consisting entirely of calcite (see Figures 4-12 (a), (c) and (e)). The prevalence of calcite is due to the much longer timescale used for the growth of crystals in the Kitano method, in which the supersaturation gradually increases. The results are summarised in Table 4-6. No growth was observed on the CH_3- terminated SAM under these conditions.

Substrate	Potential (vs. SCE)	Crystal density/ $(1000\ \mu m)^2$	Crystal phase
Gold	-0.40 V	100 ±10	Calcite
CO_2H-terminated SAM	-0.40 V	200 ±20	Calcite
CH_3- terminated SAM	-0.40 V	0 ±1	-
OH- terminated SAM	-0.40 V	100 ±10	Calcite

Table 4-6: Crystal density and morphology on all substrates when held at -0.40 V vs. SCE, during Kitano crystallisation.

Consistent with the results of the jet experiments, growth on the more positively charged surfaces was far more extensive, with a higher density of calcium carbonate crystals found to be present (see Figure 4-12 (b) and (d)). As also found at open circuit potential on gold, all three polymorphs of calcium carbonate were observed. The exception was the CO_2H- terminated SAM surface, on which the same extent of nucleation was displayed when the surface was held at each potential (see Figure 4-12 (e) and (f)).

The bare gold surface and the OH- terminated SAM surfaces, when held at -0.05 V vs. SCE, both displayed exclusive nucleation of hexagonal vaterite crystals, with a surface density of about 5 crystals / (100 μm)^2. Crystallisation on the CH_3- terminated SAM was limited to a very small amount of calcite and aragonite on the more positively charged surface (< 1 crystal / (100 μm)^2), as shown in Figure 4-12 (g), with no crystallisation occurring on the surface held at the negative potential. Interestingly, the CO_2H- terminated SAM surface provided a strong templating effect for crystallisation at both surface charges, with calcite forming in strong preference to the other polymorphs (~ 5 crystals / (100 μm)^2). This is shown in Table 4-7.

Substrate	Potential (vs. SCE)	Crystal density/ (1000 μm)^2	Crystal morphology
Gold	-0.05 V	500 ±20	Hexagonal vaterite & calcite
CO_2H- terminated SAM	-0.05 V	500 ±20	Calcite
CH_3- terminated SAM	-0.05 V	100 ±10	Calcite & aragonite
OH- terminated SAM	-0.05 V	500 ±20	Hexagonal vaterite & calcite

Table 4-7: Crystal density and morphology on all substrates when held at -0.05 V vs. SCE, during Kitano crystallisation.

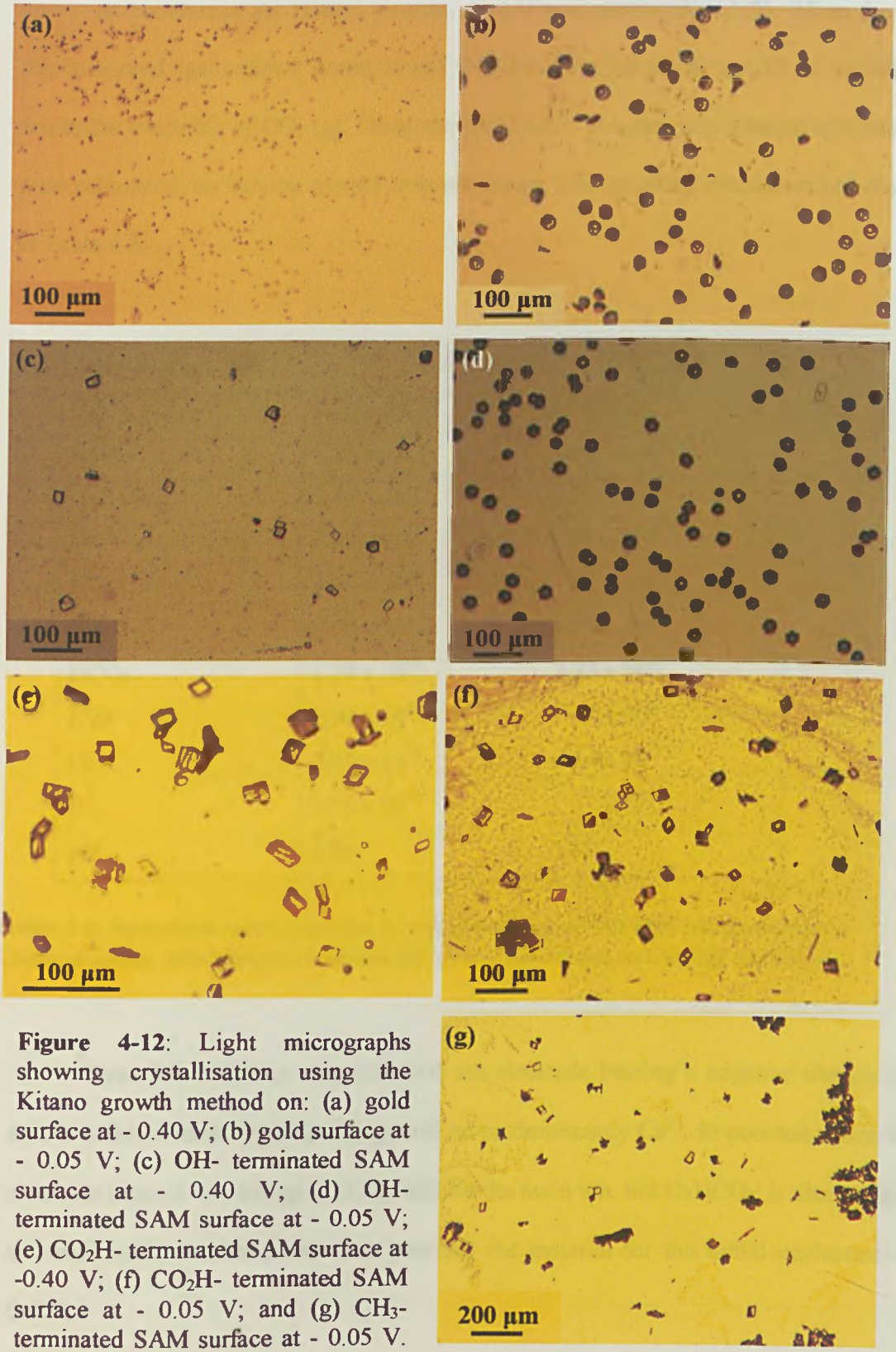

Figure 4-12: Light micrographs showing crystallisation using the Kitano growth method on: (a) gold surface at - 0.40 V; (b) gold surface at - 0.05 V; (c) OH- terminated SAM surface at - 0.40 V; (d) OH- terminated SAM surface at - 0.05 V; (e) CO_2H- terminated SAM surface at -0.40 V; (f) CO_2H- terminated SAM surface at - 0.05 V; and (g) CH_3- terminated SAM surface at - 0.05 V. All potential quoted vs. SCE.

At the start of the Kitano process, the pH was measured as 5.56. When the pH was measured again after 2 hours, it was found to have increased to 5.82, as expected, due to the evolution of CO_2 (g). Using the MINEQL+ program, the solution speciations were calculated, on varying the pH over this range. The resulting speciations are shown in Table 4-8.

Aqueous species	**Concentration / mol dm^{-3}**	
Ca^{2+}	9.99×10^{-4}	9.98×10^{-4}
$CaOH^{+}$	9.15×10^{-11}	1.66×10^{-10}
$CaHCO_3^{-}$	1.39×10^{-6}	2.26×10^{-6}
$CaCO_3$	3.33×10^{-9}	9.88×10^{-9}
CO_3^{2-}	2.36×10^{-9}	7.01×10^{-9}
H_2CO_3	8.60×10^{-4}	7.71×10^{-4}
HCO_3^{-}	1.39×10^{-4}	2.27×10^{-4}
H_2O	1.00×10^{0}	1.00×10^{0}
OH^{-}	3.65×10^{-9}	6.64×10^{-9}
H^{+}	2.75×10^{-6}	1.51×10^{-6}
pH	**5.56**	**5.82**

Table 4-8: Speciation concentrations as calculated using MINEQL+ software, for a Kitano solution, exhibiting a change in pH over 2 hours, due to CO_2 (g) evolution.

From this is can be seen that with the electrode bearing a negative charge, the ions in solution balancing this charge will be predominantly Ca^{2+}. In contrast, when the electrode is positively charged, HCO_3^{-} will be the main ion, but $CaHCO_3^{-}$ is also evident at a reasonable concentration. This provides the material for the initial nucleation of $CaCO_3$.

In the Kitano method, the solution ultimately becomes very highly supersaturated as oxygen and nitrogen replace CO_2 in solution. Thus, all three polymorphs of $CaCO_3$ may form on surfaces unless there is a strong templating effect, as seen with the nanoparticles in Chapter 3. This templating effect is seen again here for the case of the CO_2H- terminated SAM surface. The templating effect of the carboxylic acid groups on the SAM promotes the formation of the thermodynamically stable calcite.

In addition to templating exclusively for calcite on the more negatively charged CO_2H- terminated SAM surface, the orientation of the calcite observed upon this surface from the Kitano method was highly unusual. As well as the typical (104) cleavage plane crystals nucleating upon the surface, crystals nucleating on the less common (012) plane were observed along with the even more unusual, high energy (015) nucleation plane (see Figure 4-13). However, on all of the other surfaces investigated, the calcite observed was found to nucleate solely on the (104) plane, which is the lowest energy surface. This suggests that over long time periods, the carboxylic acid functional group must lead to the stabilisation of these less common crystallographic planes allowing the crystals to nucleate preferentially in this way.

The origin of this effect was discussed previously in Chapter 3. The carbonate ions that make an angle of ~ 36 ° with the (015) calcite face match with the carboxylate end groups of the functionalised alkanethiol SAMs on Au(111) surfaces[21]. This results in the preferential nucleation of calcite crystals on the (015) plane. Similarly, the orientation of carbonate ions in calcite crystals nucleated on the (012) plane is 40 - 45 ° which is also a reasonable match with the carboxylate end groups of these functionalised

alkanethiol SAMs on Au(111)[34].

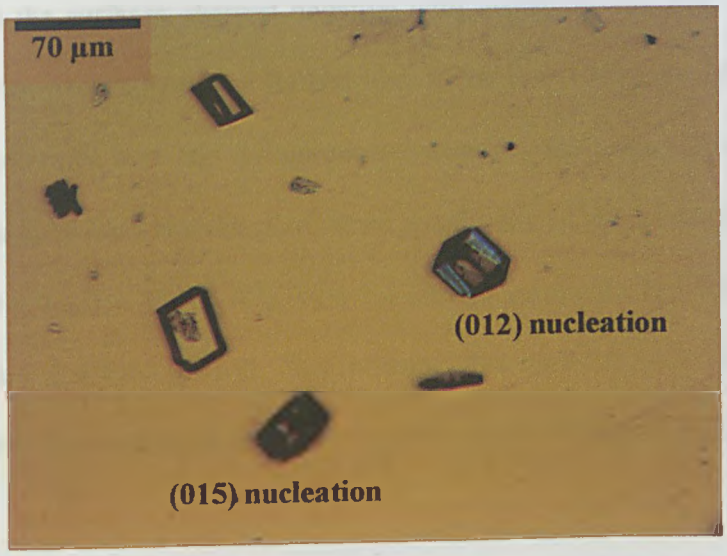

Figure 4-13: Light micrograph showing the unusual orientation of calcite growth on the CO_2H- terminated SAM surface after Kitano growth.

4.5 Conclusions

These studies indicate that a 'tunable' surface can be produced, via the application of potential to a gold or SAM-coated gold surface, to change the extent of calcium carbonate nucleation and possibly alter the morphology of the nucleating crystals.

When a potential negative of the PZC was applied to any of the surfaces in the jet experiments, the surfaces became negatively charged, and this was found to lead to the inhibition of crystal nucleation. When the surface was held at a potential near to the PZC, extensive vaterite growth was evident. Vaterite was the main polymorph of calcium carbonate nucleated in these experiments, because the kinetic nature of the experiment and the fact that vaterite is the least thermodynamically stable polymorph of calcium carbonate means that it is the first to form.

Results from the Kitano crystal growth experiments showed crystal nucleation occurring on the surfaces charged negative with respect to the PZC and at the PZC. Calcite was the main polymorph formed, due to the long timescale of the experiments. However, consistent with the syringe jet experiments, the negatively-charged surfaces appeared to induce less crystallisation. Interestingly, the CO_2H- terminated SAM surface provided the exception to the rule, with the charge seemingly not affecting the crystal nucleation during Kitano growth. This indicates that under these conditions, the CO_2H termination has a strong templating effect and the effect of potential is less significant.

4.6 References

[1] J. R. Young, S. A Davis, P. R. Brown and S. Mann, *J. Struct. Biol.*, **1999**, *126*, 195.

[2] S. Mann, *Biomineralization – Principles and Concepts in Bioinorganic Materials Chemistry*, Oxford Chemistry Masters, UK, **2001**.

[3] J. Küther, R. Seshardi, W. Knoll and W. Tremel, *J. Mater. Chem.*, **1998**, *8*, 641.

[4] J. Aizenberg, A. J. Black and G. M. Whitesides, *J. Am Chem. Soc.*, **1999**, *121*, 4500.

[5] J. Aizenberg, A. J. Black and G. M. Whitesides, *Nature*, **1999**, *398*, 495.

[6] D. D. Archibald, S. B. Qadri and B. P. Gaber, *Langmuir*, **1996**, *12*, 538.

[7] D. M. Duffy, A. M. Travaille, H. van Kempen and J. H. Harding, *J. Phys. Chem. B*, **2005**, *109*, 5713.

[8] W. A. Zisman, W. C. Bigelow and D. L. Pickett, *J. Colloid Sci.*, **1946**, *1*, 513.

[9] C. D. Bain, E. B. Troughton, Y. T. Tao, J. Evall, G. M. Whitesides and R. G. Nuzzo, *J. Am. Chem. Soc.*, **1989**, *111*, 321.

[10] C. D. Bain, J. Evall and G. M. Whitesides, *J. Am. Chem. Soc.*, **1989**, *111*, 7155.

[11] C. D. Bain and G. M. Whitesides, *J. Am. Chem. Soc.*, **1989**, *111*, 7164.

[12] R. G. Nuzzo, F. A. Fusco and D. L. Allara, *J. Am. Chem. Soc.*, **1987**, *109*, 2358.

[13] I. Wenzl, C. M. Yam, D. Barriet and T. R. Lee, *Langmuir*, **2003**, *19*, 10217.

[14] A. Ulman, *Chem. Rev.*, **1996**, *96*, 1533.

[15] R. G. Nuzzo and D. L. Allara, *J. Am. Chem. Soc.*, **1983**, *105*, 4481.

[16] S. W. Han, T. H. Ha, C. H. Kim and K. Kim, *Langmuir*, **1998**, *14*, 6113.

[17] L. S. Xu, D. R. Allee, *J. Vac. Sci. Technol. B*, **1995**, *13*, 2837.

[18] T. Tsuduki, A. Imanishi, K. Isawa, S. Terada, F. Matsui, M. Kiguchi, T. Yokoyama and T. Ohta, *J. Synchrotron Radiation*, **1999**, *6*, 787.

[19] J. Küther, G. Nelles, R. Seshadri, M. Schaub, H-J. Butt and W. Tremel, *Chem. Eur. J.*, **1998**, *4*, 1834.

[20] J. Küther and W. Tremel, *Thin Solid Films*, **1998**, *327-329*, 554.

[21] J. Aizenberg, *J. Crystal Growth*, **2000**, *211*, 143.

[22] D. M. Duffy and J. H. Harding, *J. Mater Chem.*, **2002**, *12*, 3419.

[23] D. M. Duffy and J. H. Harding, *Langmuir*, **2005**, *21*, 3850.

[24] C. Lu, L. Qi, J. Ma, H. Cheng, M. Zhang and W. Cao, *Langmuir*, **2004**, *20*, 7378.

[25] A. M. Travaille, J. J. J. M. Donners, J. W. Gerritsen, N. A. J. M. Sommerdijk, R. J. M. Nolte and H. van Kempen, *Adv. Mater.*, **2002**, *14*, 492.

[26] Y. Kitano, *Bull. Chem. Soc. Japan*, **1962**, *35*, 1980.

[27] J. Drelich, J. L. Wibur, J. D. Miller and G. M. Whitesides, *Langmuir*, **1996**, *12*, 1913.

[28] M. E. Abdelsalam, P. N. Bartlett, T. Kelf and J. Baumberg, *Langmuir*, **2005**, *21*, 1753.

[29] K. M. Wiencek and M. Fletcher, *J. Bacteriology*, **1995**, *177*, 1059.

[30] T. Arai and M. Fujihira, *J. Vac. Sci. Technol. B*, **1996**, *14*, 1378.

[31] R. A. Fredlein and J. O'M. Bockris, *Surf. Sci.*, **1974**, *46*, 641.

[32] A. J. Bard and L. R. Faulkner, *Electrochemical Methods, Fundamentals and Applications*, Wiley, **2001**.

[33] W. A. House, *J. Chem. Soc., Faraday Trans. 1*, **1981**, *77*, 341.

[34] Y-J. Han and J. Aizenberg, *Angew. Chem. Int. Ed.*, **2003**, *42*, 3668.

Chapter 5

Surface Functionalisation via the Growth of Bacterial Biofilms

The main aim of this chapter was to characterise and visualise *E. coli* bacterial biofilms[1], and investigate the interrelationships between the bacterial cells and calcium carbonate crystals and scale matrices. As this impinges directly on the issue of household care, the effect of functionalising surfaces with a developmental bleach formulation (Lever Fabergé Ltd., UK) was also investigated.

5.1 Introduction

Escherichia coli bacteria are often found within the lower intestines of warm-blooded animals; their main role being to facilitate the efficient digestion of food. Up to 1×10^{13} bacteria such as this are passed in human faeces daily and so the occurrence of *E. coli* in toilet systems is consequently high. Bacteria have been found to affect the crystallisation of calcium carbonate dramatically, becoming effectively fossilised, as shown in caves and hot springs[2,3] due to them acting as nucleation centres for crystal growth[4,5].

This work investigates the effects of *E. coli* bacterial biofilms (used specifically due to their ease of growth under biological laboratory conditions and non-toxicity) on the crystallisation of pure $CaCO_3$ and calcium carbonate as a scale component, with particular reference to household care and the effects of the bleach formulation.

5.2 Growth and visualisation of *E. coli* biofilms

E. coli biofilms were established using the general protocol described in Chapter 2, without the presence of any solution additives. Slides were removed from the growth solution daily and observed using CLSM, in conjunction with the dual component stain in order to visualise the bacterial coverage. After 1 day of growth, a limited amount of bacteria had adhered to the surface. Subsequent daily imaging showed bacterial adhesion to the glass surface increased monotonically. Figure 5-1 shows the coverage obtained after 5 and 7 days. The bacteria are shown to be ~ 2 μm in length and ~ 0.5 μm in diameter. After 7 days, a monolayer of mostly live bacteria was achieved. In subsequent growth experiments, the coverage was found to depend on the laboratory temperature (20 ± 4 °C) and so the substrates were observed daily using the confocal microscope to ensure a monolayer biofilm coverage at the time of removal from the solution for further experimentation.

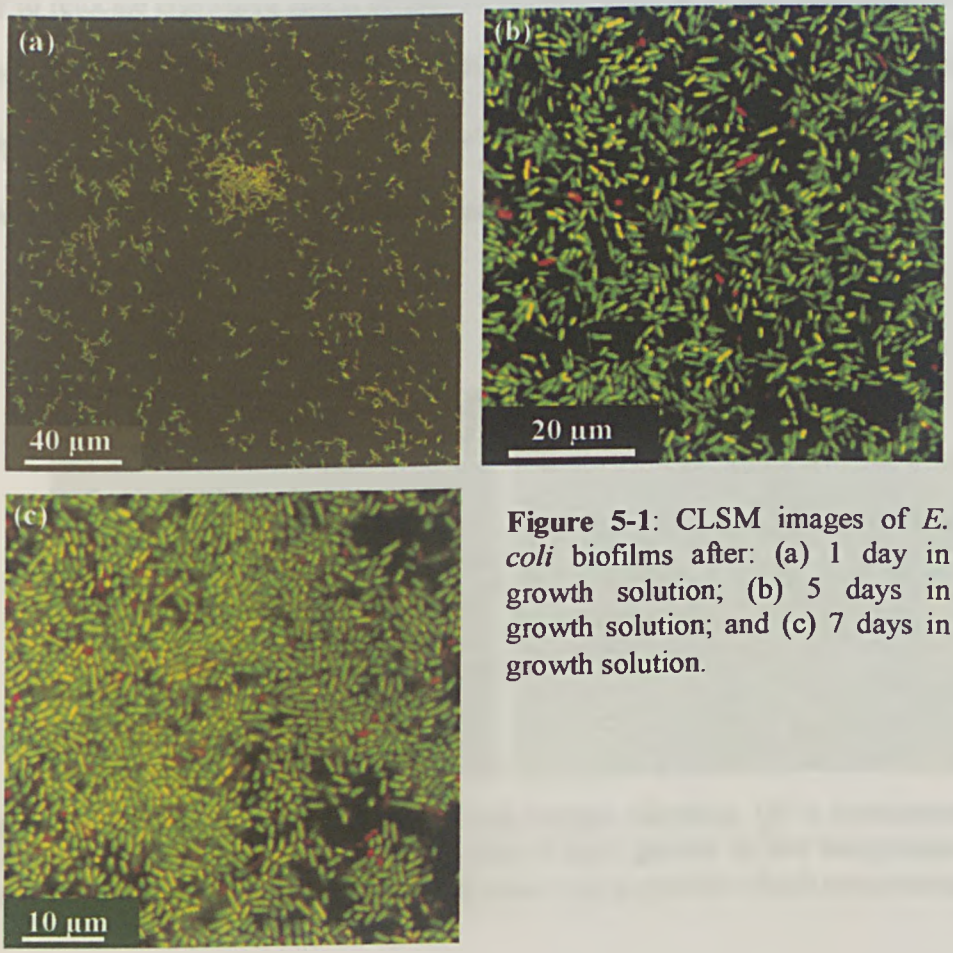

Figure 5-1: CLSM images of *E. coli* biofilms after: (a) 1 day in growth solution; (b) 5 days in growth solution; and (c) 7 days in growth solution.

Using CLSM, it is possible to systematically alter the focal plane through the sample enabling the construction of 3D images, such as those in Figure 5-2 (b). This enables the user to determine monolayer or bilayer coverage, or whether there are aggregations of bacteria on the surface in any particular areas. This example stresses the importance of temperature on biofilm growth as in Figure 5-2 (b), after 5 days of biofilm growth at a high laboratory temperature, it was found that dense clumps of bacteria formed which were able to float free of the substrate surface. This is a form of a bacterial survival mechanism[6,7], with the stacks of bacteria leaving the mother surface to

try to relocate elsewhere and is indicative of toxin build up at the glass/bacteria interface and nutrient and oxygen depletion within the biofilm itself. This can be compared to Figure 5-2 (a) which shows a monolayer coverage of bacteria after 5 days of growth at a lower laboratory temperature, with no bacterial aggregations observable.

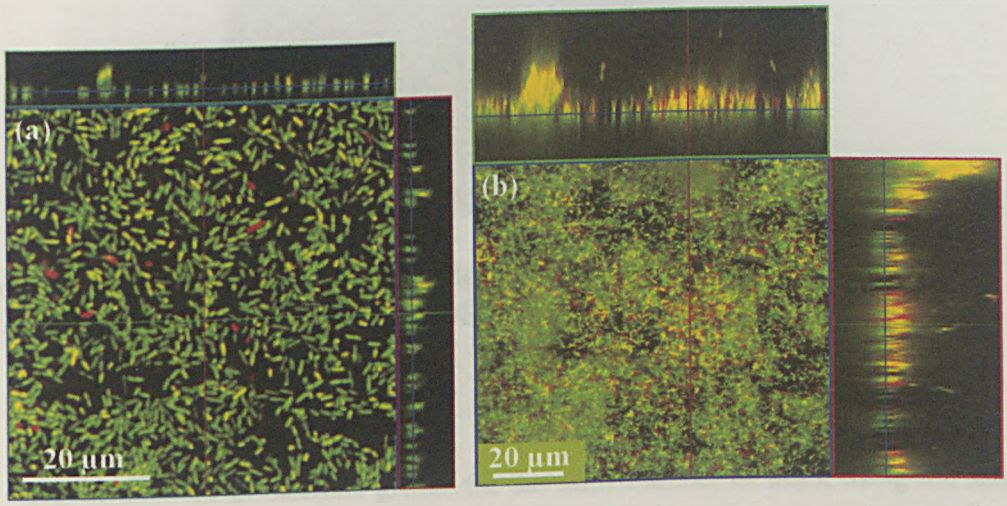

Figure 5-2: Orthogonal 'z-stack' confocal images showing: (a) a monolayer uniform coverage of bacteria on a glass surface after 5 days growth at low temperature; and (b) clumps of bacteria forming on the surface after 5 days growth at high temperature.

Often after approximately 8 days of growth, the uniform biofilm tended to become severely damaged and disrupted and only an uneven dispersion of living and dead cells remained. The bacterial aggregations rapidly died and floated away from the surface, leaving behind a disperse layer of live and damaged cells in approximately equal proportion (Figure 5-3). It was found that, even if the film was allowed to grow further, the degree of dense, uniform coverage seen in Figure 5-2 (a) could not be re-established.

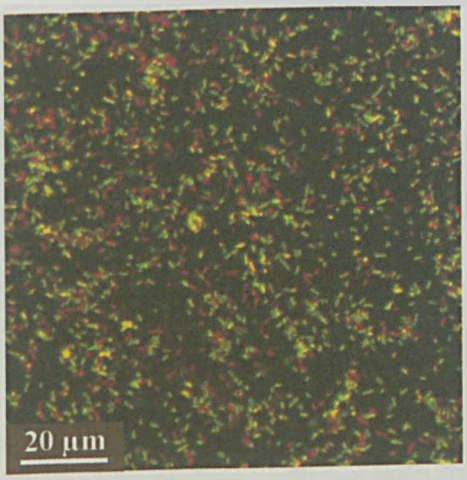

Figure 5-3: CLSM image of bacterial biofilm after 8 days of growth, showing low density of equal amounts of live and dead bacterial cells.

The differences in biofilms grown for the same number of days, using the same growth conditions clearly illustrates the importance of the preparation and analysis of control samples during experiments, due to the lack of suitable temperature control.

5.3 Microbial limescale growth

Biofilms incorporating limescale components were grown using the protocol described in Chapter 2. It was found that the fluorescent stains would not penetrate the scale components, and so characterisation was performed using FE-SEM.

After 1 day of growth a uniform background layer of scale had formed on the slide surfaces (Figure 5-4), although no bacteria was present on the substrate itself. This background layer was a common feature of all of the microbial limescale films formed.

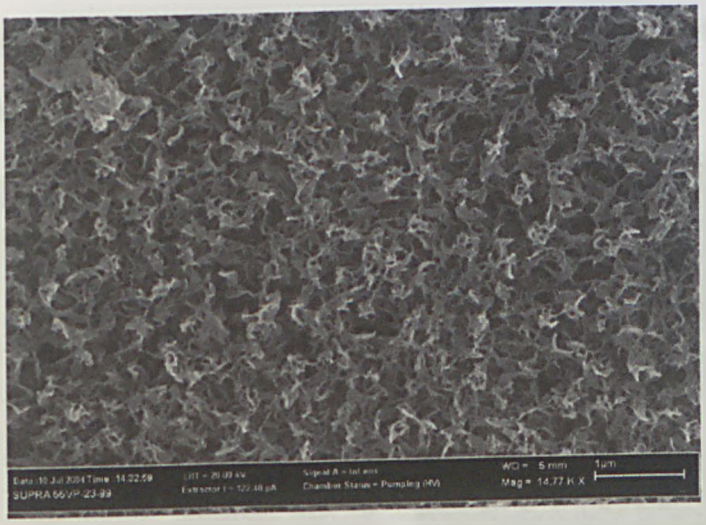

Figure 5-4: FE-SEM image of background scale deposited onto glass slides after 1 day in growth solution.

To determine the composition of this background layer, infra red spectrometry was used. A small sample of the scale was inserted into the diamond window of the IR spectrometer (Spectrum One FT-IR Spectrometer, PerkinElmer Instruments). The resulting spectrum displayed a major peak at 1021 cm^{-1}, characteristic of a PO_4^{3-} stretch. This confirmed that the background layer was made up mostly of phosphates, as expected from the microbial scale build up media, and was not due to any contamination.

It was subsequently observed that following the formation of this base layer, bacteria came to rest upon the surface. In the samples examined, bacteria were always observed to be firstly 'laying' on the surface before being incorporated within the scale film. Bacteria were not seen either integrated into the base scale layer or underneath it. After 2 days in the growth solution, there was evidence of bacteria on the surface, which

seemed to be 'fossilised', and coated with scale components. At the same time, the scale had continued to build up as fine deposits, especially in areas where clumps of bacteria were already present (Figure 5-5).

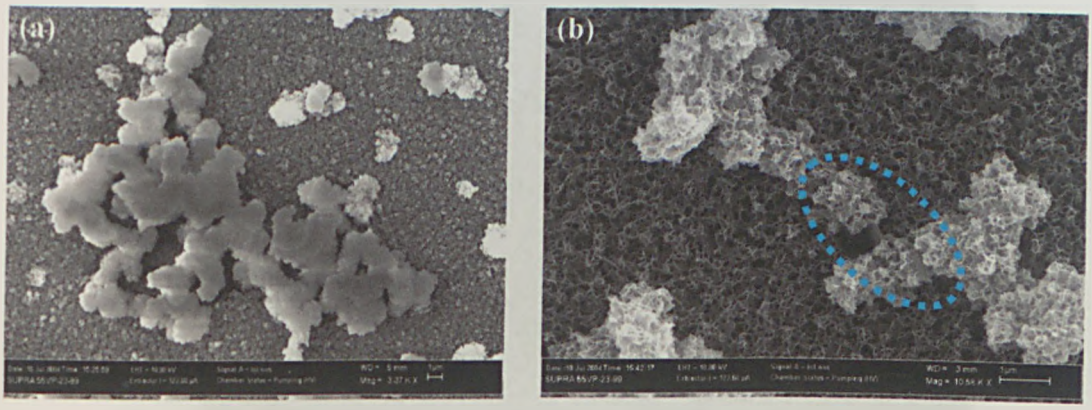

Figure 5-5: FE-SEM images to show the mineralisation of bacteria by the scale components. (b) shows evidence of an exposed bacterium (circled) against the background.

After 7 days, some bacteria were visible on the surface of the scale, and some were very easily identifiable as being coated in the scale (Figure 5-6). In this figure it is also possible to clearly see an intact layer of exopolysaccharide, around the bacterium, serving as a cohesive layer, keeping the cells hydrated.

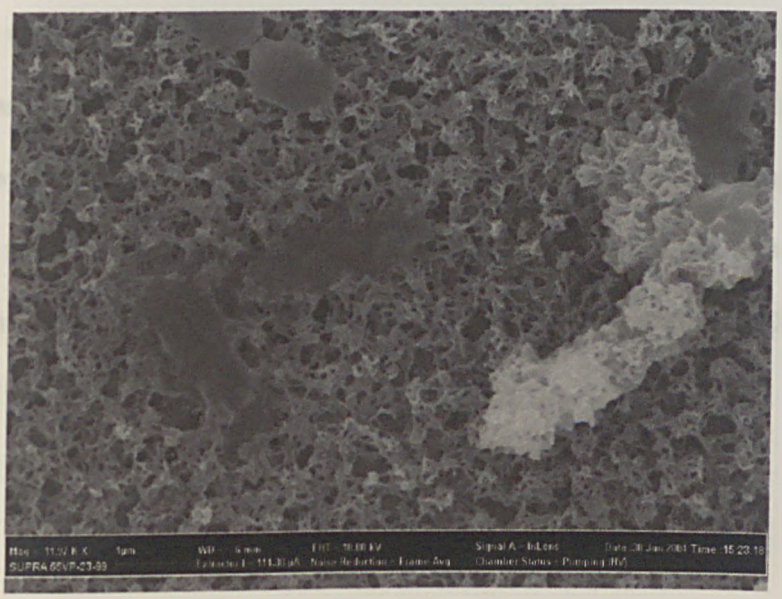

Figure 5-6: FE-SEM image of microbial limescale build up after 7 days. The bacteria are clearly visible on the scale surface.

Figure 5-7 shows a single bacterium resting predominantly on the surface of the scale film. It is, however, possible to see that there are sites around its edges where it appears that the scale film had begun to 'creep' on to the bacterial surface.

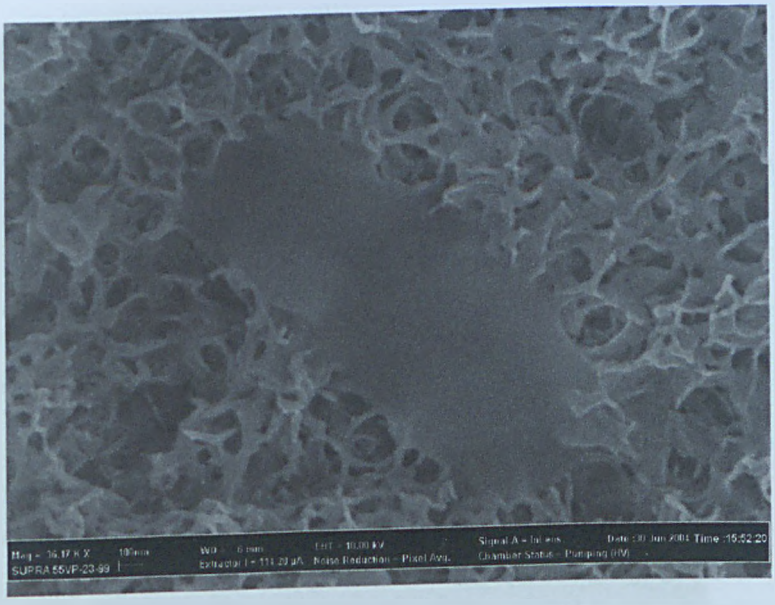

Figure 5-7: High magnification FE-SEM image of a single *E. coli* bacterium.

After further growth, different domains within the microbial scale became apparent. The well-established background scale layer was still evident, but it was present in conjunction with much more prominent features. The dimensions of these larger features suggested that they were due to increased scale build up over the encapsulated bacteria. It should be noted that it was not possible to perform FE-SEM imaging on samples beyond this stage of growth as it became impossible to evaporate an even layer of Au onto the sample surface to prevent the build up of static charge within the SEM and thus distortion of the image.

Figure 5-8 show deposits of this type which are in clear contrast to the underlying background scale layer. Some distortion of these images due to charging effects is apparent.

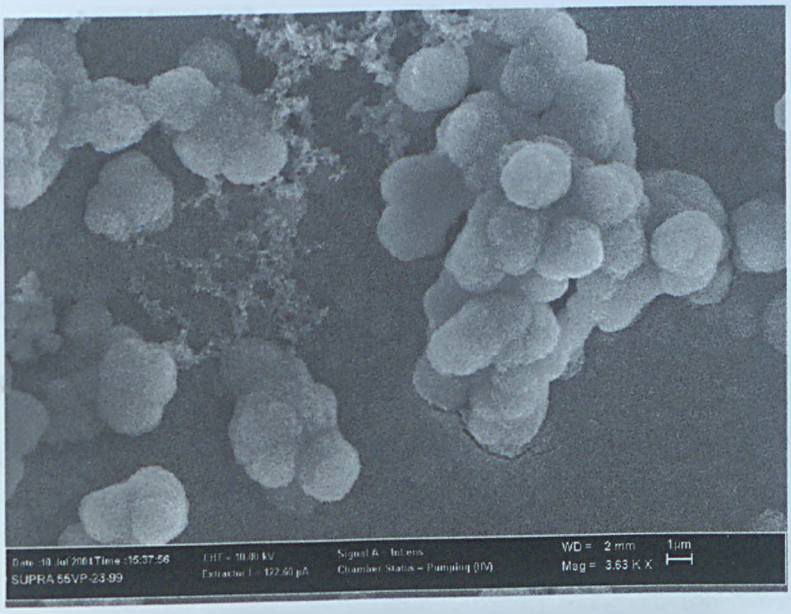

Figure 5-8: FE-SEM image of microbial limescale film after 5 days growth, showing the increasing roughness of the surface.

These images demonstrate that there are complex interactions between the mineral and bacterial components of microbial limescale. The formation of these films appears to proceed via the formation of an amorphous background scale layer onto which bacteria are deposited. Then, over time, the bacteria are encapsulated within a scale layer and thus incorporated into the film. Film build up continues to proceed with increasing deposits of scale onto the encapsulated bacteria leading to the formation of a deposit which has relatively flat areas corresponding to the background scale layer interspersed with roughened areas arising from the encapsulation of bacterial cells.

5.4 The effects of biofilms on calcium carbonate crystallisation

5.4.1 Kitano crystallisation

Biofilms were grown for a suitable time period and visualised using CLSM to ensure a monolayer bacterial coverage on the glass substrate, of mainly viable bacteria. Slides were then immersed in a Kitano growth solution for a period of ~ 65 hours, allowing the formation of $CaCO_3$ microcrystals at the biofilm/solution interface. The resulting crystallisation was thought to be affected by the bacterial presence.

Results using CLSM showed a high proportion of dead bacteria, still adhered to the slides. This was due to the removal of the slides from the sugar and tryptone solution, before input into the Kitano growth solution and was thus expected (see Figure 5-9).

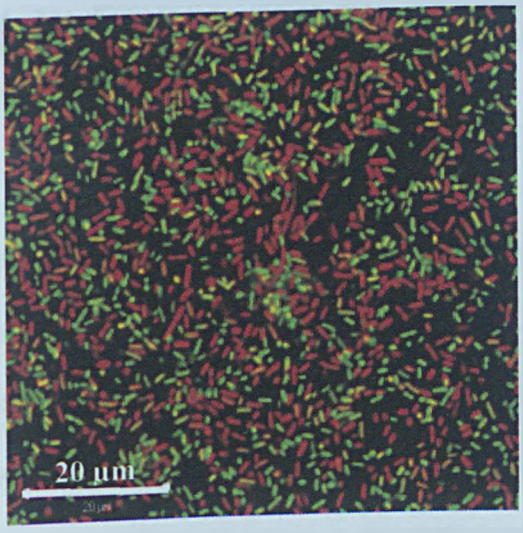

Figure 5-9: CLSM image of bacterial biofilm, removed from growth solution and immersed in Kitano solution for 65 hours. A high proportion of the bacteria are dead or damaged.

Using the confocal microscope, no crystals were visible on the surface. SEM was thus used to visualise the crystalline parts of the surface. Figure 5-10 is a low magnification SEM image, in which all three $CaCO_3$ crystalline polymorphs can be clearly observed to have formed on the surface.

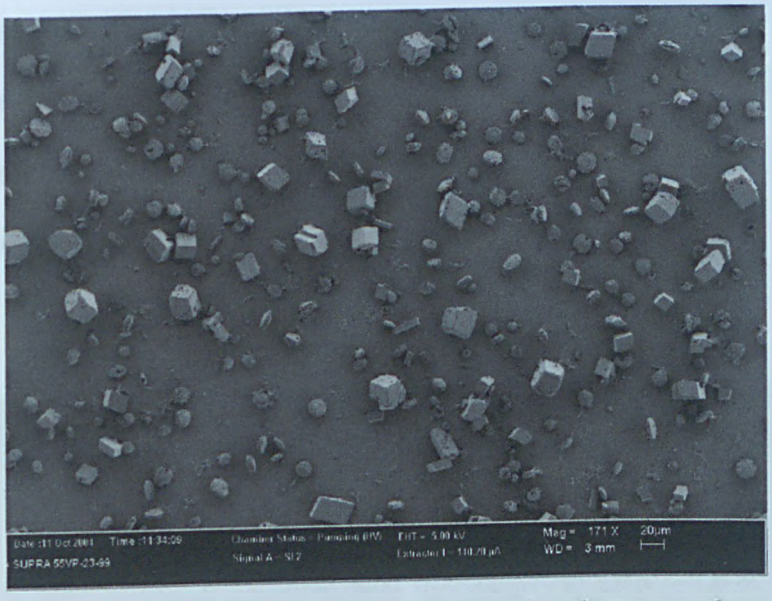

Figure 5-10: SEM showing $CaCO_3$ crystals on a bacterial biofilm, achieved via the Kitano method.

At higher magnifications, it was possible to distinguish the state of the crystals as well as resolve the bacterial cells. Focussing on the calcite crystals, these seemed to have nucleated on the stable (104) plane, but exhibited imperfect tendencies, with the presence of many surface and structural defects. The presence of the hollow crystals can be explained due to the presence of trapped liquid in the crystal structure. These features are uncommon in calcite crystals grown by the Kitano method on bare glass or gold and so can be attributed to the presence of the bacteria. It is thought that the structural damage may be due to the presence of lactic acid at the interface, excreted from the

bacteria, leading to the partial dissolution of the crystals. Figure 5-11 shows this damage clearly, including large voids in the structure of the crystal bodies.

It was also observed that crystallisation had a tendency to occur at areas of the surface where there were patches of bacteria; the bacteria seemingly providing nucleation sites for the calcium carbonate crystals. This can be attributed to the anionic nature of the bacterial cell walls, which exhibit a strong tendency to absorb aqueous metal cations, particularly calcium[8]. This leads to the formation of a diffuse carbonate layer, inducing the crystallisation of calcium carbonate.

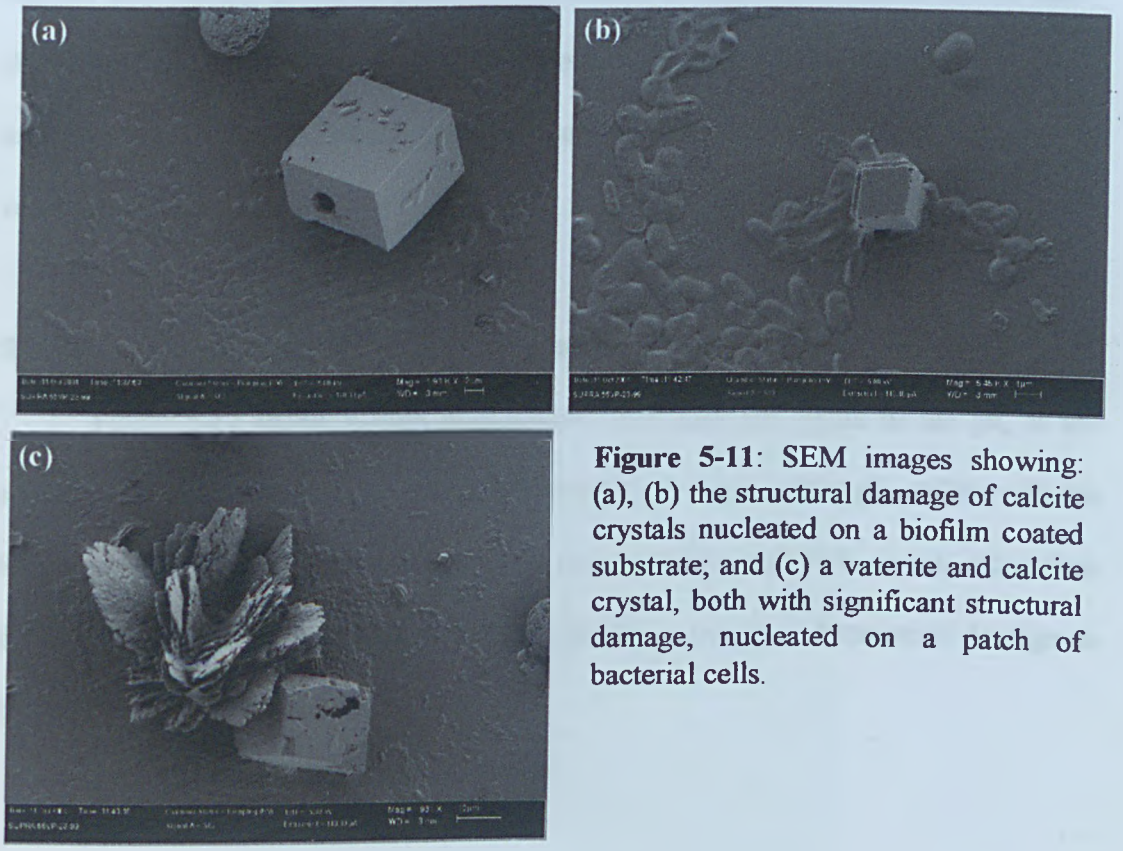

Figure 5-11: SEM images showing: (a), (b) the structural damage of calcite crystals nucleated on a biofilm coated substrate; and (c) a vaterite and calcite crystal, both with significant structural damage, nucleated on a patch of bacterial cells.

5.4.2 Jet crystallisation

As Kitano crystallisation takes place over a long time period, the jet crystallisation method was also used, with bacterial biofilms and microbial scale as substrates. In this case the biofilms were viable for the much shorter duration of the experiment.

5.4.2.1 Experimental details

Biofilm (displaying monolayer coverage) and microbial scale coated glass slides were placed in the jet crystal growth cell and jetted onto with solutions mixed in a custom built mixing device as described in Chapter 2, with a flow rate of 0.5 ml min^{-1}. After jetting was complete, the samples were analysed using a combination of confocal and optical microscopy. Before confocal analyses, samples were stained with the two component fluorescent stain.

5.4.2.2 Jet crystallisation on biofilm substrates

Figure 5-12 shows a light micrograph, from near the centre of the jet, of the substrate surface. The majority of crystals formed are calcite, although, unlike with the Kitano method, ~ 50 % are nucleated on the unusual (012) and (015) planes, rather than the stable (104) plane. Many of the crystals display twinning and structural damage as before.

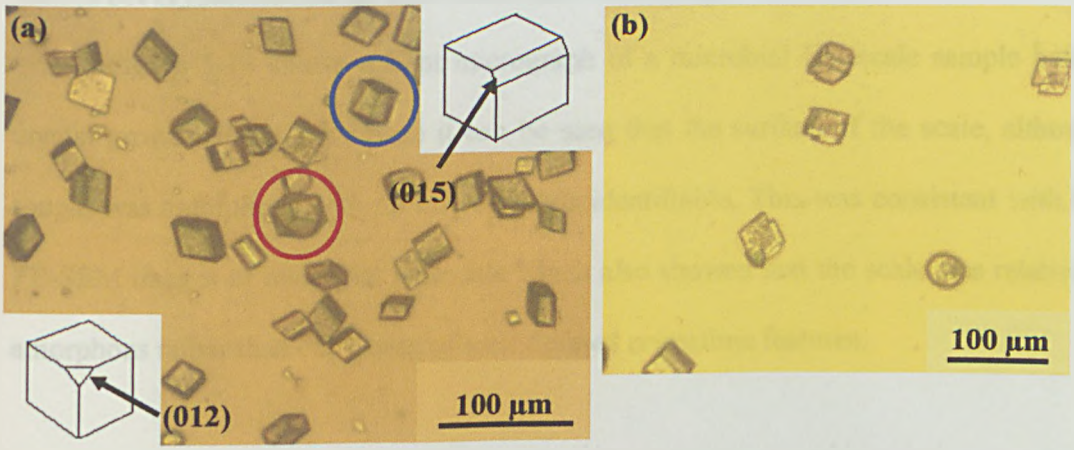

Figure 5-12: Light micrographs showing: (a) mainly calcite nucleation, directly beneath the jet, but with nucleation on unusual (012), circled red, and (015), circled blue, planes as well as the (104) plane; and (b) twinned crystals.

By observing the crystals using CLSM, it was possible to determine that the structure of the biofilm remained intact to some degree and portions of it redeposited onto the crystals which were subsequently formed, as shown in Figure 5-13. Here, the $CaCO_3$ crystals are 'cloaked' in a layer of bacterial matter, which appears to be a dispersion of a small number of live cells in otherwise dead material.

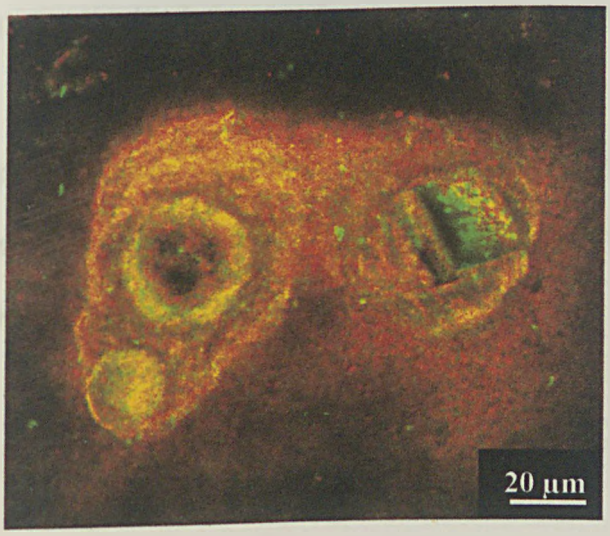

Figure 5-13: CLSM image of a spherical vaterite crystal (left) and a twinned calcite crystal (right), evidently coated in a layer of bacterial material.

5.4.2.3 Jet crystallisation on microbial scale substrates

Figure 5-14 shows a light micrograph of a microbial limescale sample before crystal growth. From this image it can be seen that the surface of the scale, although rough, was amorphous with no microcrystals identifiable. This was consistent with the FE-SEM images of microbial limescale which also showed that the scale was relatively amorphous rather than consisting of well-defined crystalline features.

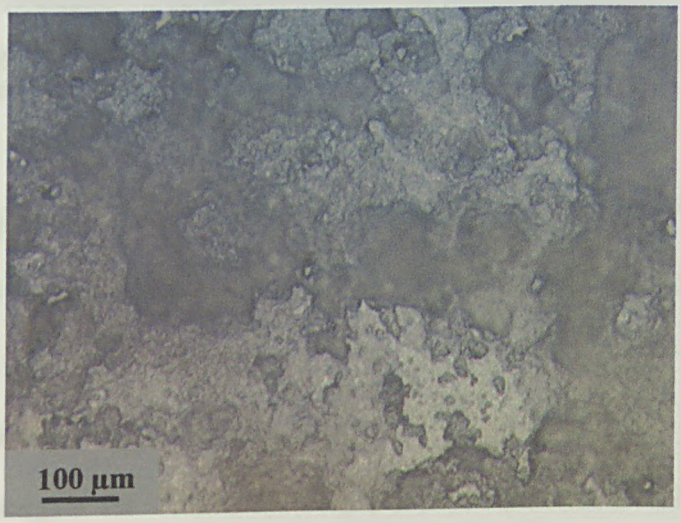

Figure 5-14: Light micrograph of microbial limescale coating on glass.

Subsequent to the sample undergoing jet crystallisation, the substrate surface exhibited a dispersion of a very fine crystalline material, in which calcium carbonate microcrystals were clearly trapped (Figure 5-15).

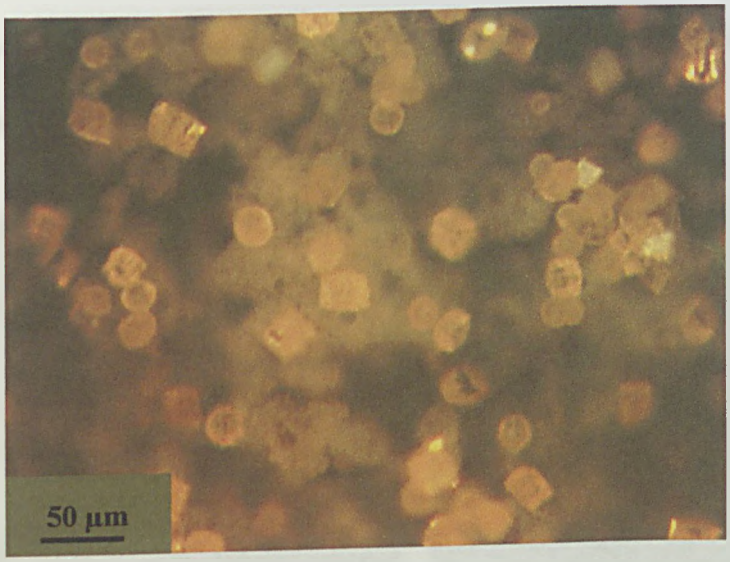

Figure 5-15: Light micrograph of microbial limescale substrate after being subjected to calcium carbonate jet crystallisation.

The majority of these microcrystals are calcite, nucleated on the unusual (015) plane, although the presence of a few spherical vaterite crystals was observed.

5.5 Biofilm growth on crystalline surfaces

To investigate the effects of $CaCO_3$ crystals on biofilm growth, the Kitano method was used to form crystals on clean glass surfaces. These slides were subsequently used as substrates for biofilm growth and immersed in the biofilm growth media. After 5 days, the slides were removed from the solution and stained for confocal microscopy. CLSM imaging displayed a monolayer of bacterial cells on the surface, but as the stain could not penetrate the crystals themselves, these were not resolvable. From the CLSM images, there were no obvious differences in biofilm growth and viability between the crystalline and clean substrates.

FE-SEM was thus used to attempt to visualise the crystals and bacteria on the surface. Figure 5-16 shows two typical SEM images obtained.

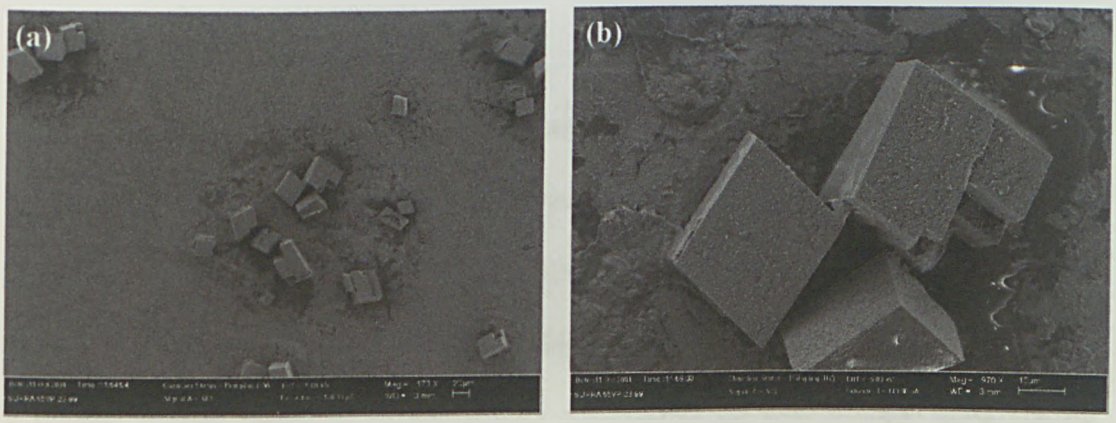

Figure 5-16: FE-SEM images showing: (a) low magnification of calcite crystals, coated in a bacterial layer; and (b) high magnification image to show the topography of the surface of the crystals.

The bacterial layer appeared to have dried out in the EM preparation process, as the bacterial cells themselves were not visible. A layer of bacterial material is, however, evident, and had formed around and over the $CaCO_3$ crystals, effectively encasing them, showing that the presence of the crystals seems to have little effect on the growth and viability of bacterial biofilms.

5.6 Biofilm growth and $CaCO_3$ crystallisation on bleach deposits

Preliminary investigations into the observation of the soap deposits left behind on glass/ceramic substrates after soaking in bleach formulation, and how this affected subsequent calcium carbonate crystallisation (as a model for limescale growth), and bacterial biofilm growth was carried out using: (i) the Kitano method; and (ii) the

biofilm growth protocol, on glass substrates which had been previously treated with a Bleach formulation solution.

5.6.1 Experimental details

The developmental bleach household care formulation contains 5 % non-ionic surfactants and has sodium hypochlorite as its major component. Glass slides were placed upright in a beaker containing a diluted bleach solution (2.5 g bleach formulation in 100 cm^3 water) for 24 hours. Upon removal, slides were allowed to dry and placed in a biofilm growth media or Kitano growth solution along with a clean glass control, following protocol as described previously.

5.6.2 The effects of bleach deposits on $CaCO_3$ crystallisation

After being immersed in the bleach solution for 17 hours, all of the glass samples were coated in soap deposits as seen in Figure 5-17. This image shows the reason for the 'dulling' effects on ceramic and glass surfaces of the bleach formulation.

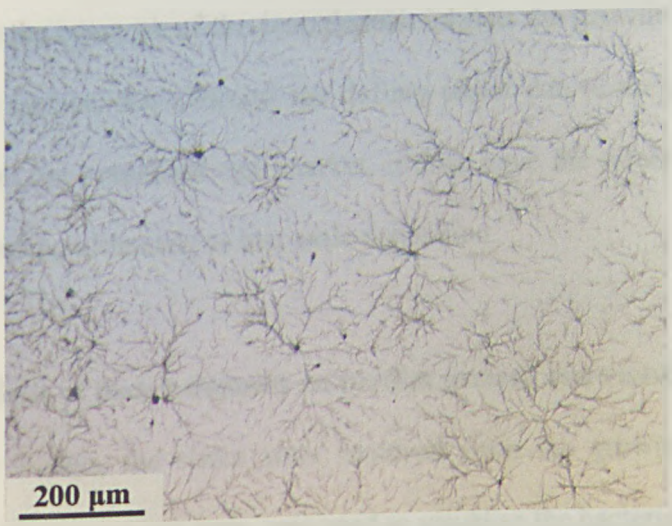

Figure 5-17: Light micrograph of glass surface after being treated with bleach formulation, showing the soap deposits on the surface.

After 24 hours under Kitano solution, a small amount of crystallisation was evident on the surface (Figure 5-18 (a)). When this is compared to the glass substrate without the presence of the soap deposit (b) it seems that the deposit is inhibiting calcium carbonate nucleation as much more crystallisation is observable on the clean surface.

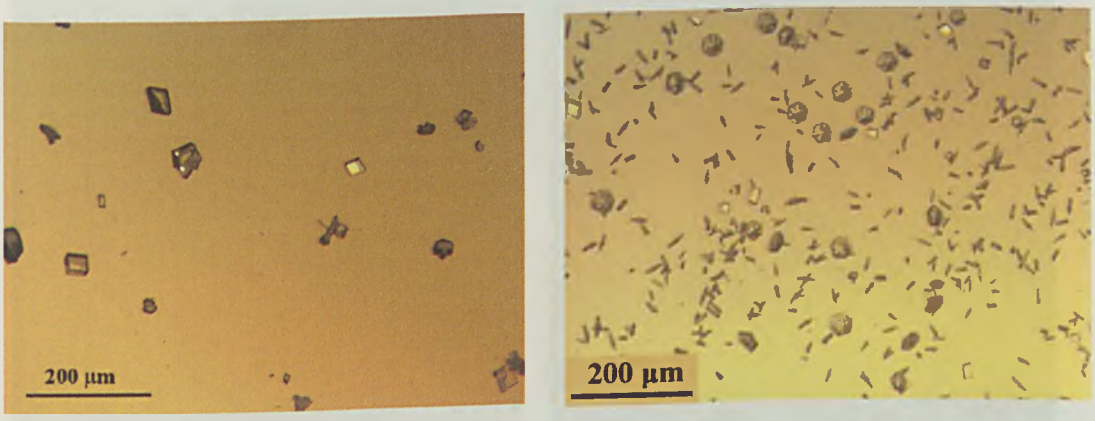

Figure 5-18: Light micrographs to show the extent of $CaCO_3$ crystallisation on: (a) glass surface pre-treated with bleach solution; and (b) clean glass surface.

Results for further time periods, up to 134 hours, showed similar results. This suggests that the presence of the soap deposit inhibits the growth of calcium carbonate on the glass surface. So, although the dulling effect due to the soap residue may be undesirable in the household care market, it does have the effect of inhibiting crystal formation, leading ultimately to less scale deposition.

5.6.3 The effects of bleach deposits on biofilm growth and viability

After 5 days, the slides were removed from the growth media and CLSM, utilising the two component stain, was used to visualise the bacteria on the glass surface.

Typical results are shown in Figure 5-19, where it can be seen that on the bleach-treated surface, there is a sparse coverage of live bacteria, compared to a higher coverage on the clean glass surface, leading to the initial conclusion that soap residues inhibit the adhesion of bacteria to the surface.

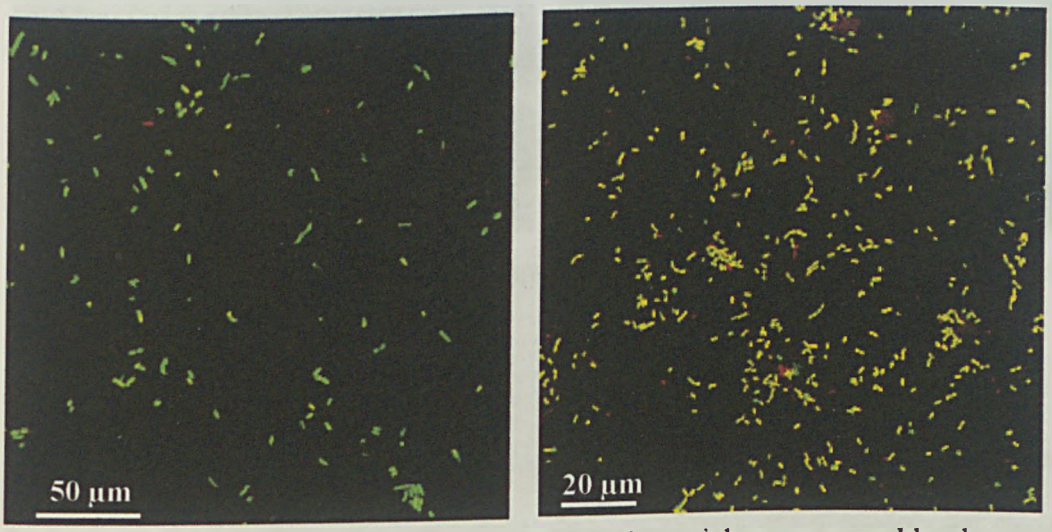

Figure 5-19: CLSM images showing: (a) disperse bacterial coverage on bleach-treated surface; and (b) higher bacterial coverage on clean glass surface.

Clumps of bacteria, several cells thick, were observed on both samples, although on the clean glass slide aggregations were thicker and more frequent, as shown in Figure 5-20.

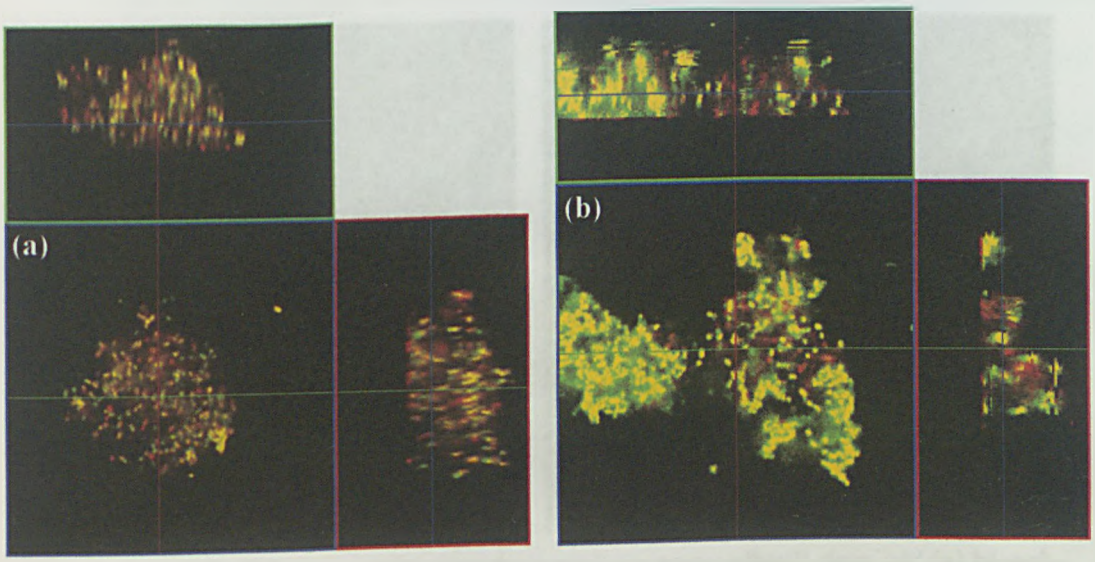

Figure 5-20: Confocal z-stack images showing clump of bacteria on: (a) bleach-treated surface; and (b) clean glass surface.

After 8 days in the biofilm growth media, the incidence of dead/damaged bacteria on the bleach-treated slide increased significantly, these being very disperse. Aggregates of bacteria were rare and those that did form were only 2-3 cells thick (as measured using the z-stack capability) and the bacteria were all dead/damaged. The clean slide however showed a monolayer coverage of live bacteria (Figure 5-21), as expected from previous investigations.

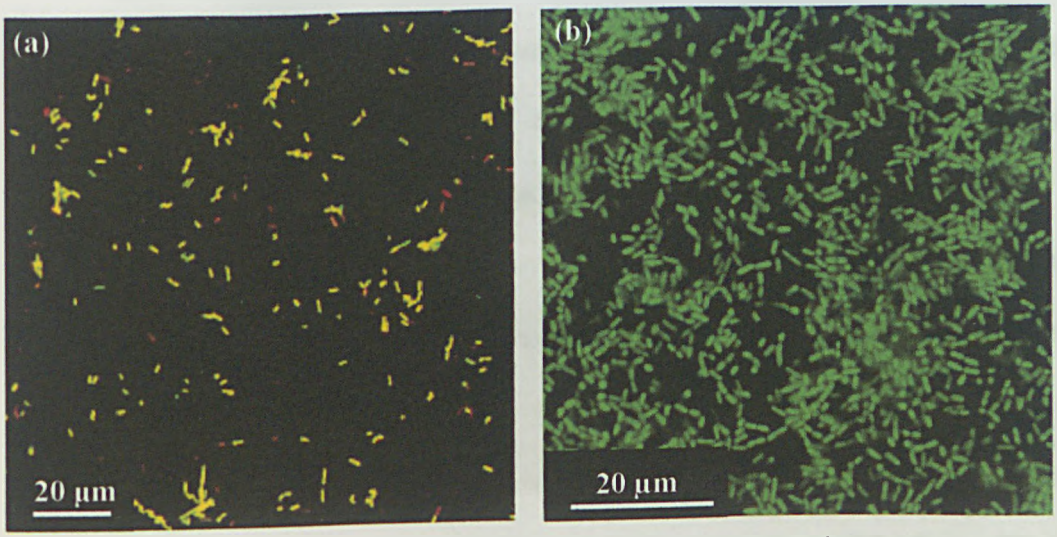

Figure 5-21: CLSM images showing bacterial coverage after 8 days on: (a) bleach-treated surface; and (b) clean glass surface.

In conclusion, it can be seen that after 5 days, bleach formulation soap deposits inhibit the adhesion of bacteria to the surface. Aggregations of bacteria are sparse compared to those on the clean glass surface and the bacteria are mostly dead/damaged. After 8 days of biofilm growth, the clean slide showed a monolayer coverage of live bacteria, whereas the treated sample displayed little evidence of any live bacteria, indicating that the soap residues inhibit bacterial adhesion and damage/kill bacteria when they come into contact with the surface.

5.7 Conclusions

The investigations in this chapter have shown that CLSM can be used easily to visualise bacterial cells and biofilms and determine their viability. The growth of biofilms is highly dependent on temperature, and the thickness of films formed is readily visualised when the orthogonal z-stack capability of the confocal microscope is used.

The mechanism of microbial scale formation has been elucidated using FE-SEM visualisation, showing that after the formation of a background, mainly phosphate scale layer, bacteria become encapsulated and eventually mineralised by the scale components, leading to a highly roughened surface structure.

Bacterial biofilms have been shown to dramatically effect the crystallisation of calcium carbonate, not only by acting as nucleation centres, but by disturbing the crystal structure and causing surface and structural damage as well as twinning. Using the fast, jet crystallisation method, the bacteria also act as orientational templates, by directing calcite nucleation from the unusual (012) and (015) planes as well as the stable (104) plane. Moreover, the presence of calcium carbonate crystals on the surface seem not to inhibit the deposition of a viable bacterial biofilm, with the crystals simply becoming coated in the film.

Finally, the effects of pre-treating glass surfaces with a developmental bleach formulation were investigated. The pre-treatment leaves a dull surface layer, which, although unattractive to the consumer, has been found to inhibit bacterial adhesion to the surface as well as calcium carbonate crystal nucleation and growth.

5.8 References

[1] J. W. Costerton, *Inter. J. Antimicrobial Agents*, **1999**, *11*, 217.

[2] R. L. Folk, *J. Sed. Petrol.*, **1993**, *63(5)*, 990.

[3] A. K. Contos, J. M. James, B. Heywood, K. Pitt and P. Rogers, *Geomicrobiology Journal*, **2001**, *18*, 331.

[4] L. Clapham, R. J. C. McLean, J. C. Nickel, J. Downey and J. W. Costerton, *J. Cryst. Growth*, **1990**, *104*, 475.

[5] R. J. C. McLean and T. J. Beveridge, *Microbial Mineral Recovery*, ed. H. L. Ehrlich and C. L. Brierley, **1990**, McGraw-Hill Publishing Company, pp. 185-223.

[6] C. A. Fux, J. W. Costerton, P. S. Stewart and P. Stoodley, *Trends in Microbiol.*, **2005**, *13*, 34.

[7] P. Stoodley, K. Sauer, D. G. Davies and J. W. Costerton, *Annu. Rev. Microbiol.*, **2002**, *56*, 187.

[8] T. J. Beveridge and R. G. E. Murray, *J. Bacteriol.*, **1976**, *127*, 1502.

Chapter 6

The Local Induced Dissolution of Calcium Carbonate and Phosphate Substrates using an Electrochemical Technique

The local dissolution of cleaved calcite surfaces has been induced by the application of a proton flux to the surface, from an ultramicroelectrode, positioned close to the region of interest, in an aqueous solution. From analysis of the etch pits produced, by interferometry, it was found that etch pit volumes increased linearly with proton flux and this process has been successfully modelled based on diffusion of H^+ ions to the surface followed by reaction with the calcite surface. The induced dissolution of simulated limescale pellets has also been investigated in this manner, with dissolution rates varying substantially depending on the exact composition of the pellets.

6.1 Introduction

Investigations of calcium carbonate and phosphate dissolution[1,2,3] are widespread and include work on small crystals as well as open geological systems[4,5]. The effect of pH on the dissolution of calcite single crystals has been established from channel flow with electrochemical detection studies, among other techniques[6,7,8]. More recently, integrated electrochemical-AFM has been used to image crystal dissolution in situ[9]. Jones et al. utilised this system to inject protons from a Pt-coated AFM tip, whilst using the AFM component of the probe to image the resulting dissolution process[10]. The advantages of electrochemical methods include the ability to quantitatively change the

interfacial reaction conditions and the possibility of measuring surface fluxes and near surface concentrations[11].

This chapter explains the further use of electrochemical methods to investigate the rate of dissolution of cleaved calcite surfaces. Experiments involved using UMEs to produce protons, locally, at the surface of interest, for specified periods of time, via the oxidation of water, under galvanostatic (constant current) control. Simulated limescale pellets and real limescale samples of various compositions were also investigated in this manner to examine the effects of incorporating other minerals such as calcium phosphates into the process and to compare their dissolution rates to those of pure calcium carbonate and calcite. Some of the studies reported herein considered the effect of solution viscosity, as this is of particular relevance to household care products which may be highly viscous.

Etch pits produced on the substrate surfaces were characterised using light microscopy, interferometry and SEM. Quantitative analysis of the etch pit dimensions allow the calcite dissolution process to be modelled using finite element simulations. For the case of calcite single crystals, this resulted in a predicted rate constant for the dissolution process which corresponds well to values in the literature[2,3].

6.2 Experimental details

To carry out the local dissolution experiments, the electrochemical cell was set up as described in Chapter 2, with the substrate positioned flat on the cell base, secured with double sided tape. A 0.2 M KNO_3 aqueous solution was prepared, and its pH altered to 8.5. A 25 μm diameter Pt UME, fabricated as described in Chapter 2, and a

Ag quasi- reference electrode were inserted into the cell with connections being made from the current follower to both electrodes using crocodile clips. The working electrode was positioned using the x and y micromanipulators, over the substrate, initially approximately 4 mm above the substrate surface.

A cyclic voltammogram was run between 0.0 V and –1.0 V in order to facilitate the reduction of oxygen via Equation 6-1. This allowed the bulk limiting current (i_∞) to be recorded, which occurred at a potential of around - 0.70 V.

$$O_2 + 2H_2O + 4e^- \rightarrow 4OH^- \qquad (6\text{-}1)$$

The electrode was held at this reducing potential and moved towards the substrate surface using the z- piezoelectric positioner, until the current began to drop due to the hindered diffusion of species to the electrode. At this point, an approach curve was run, of current against distance. This type of SECM approach curve can be used as a distance calibration method[12], as the diffusion of oxygen is hindered as the probe approaches the surface. An example is shown in Figure 6-1, where the current observed decreases with the tip-substrate separation, allowing the distance of approach to the surface to be calculated. Although this procedure produces OH^-, the raising of the pH did not induce the dissolution of any of the surfaces of interest.

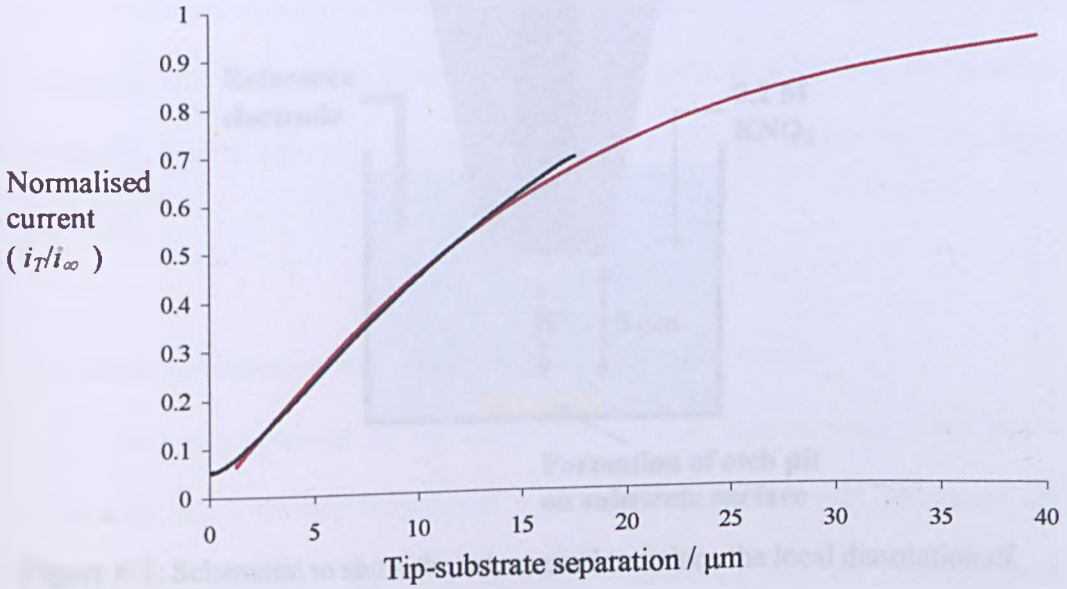

Figure 6-1: Approach curve of a 25 µm diameter Pt UME to insulating substrate, showing decrease in current. **Key:** Black: experimental curve, red: theoretical curve (from reference 12).

For the experiments that followed, the UME was positioned 5 µm from the surface, guided by the results of such curves. For studies of dissolution, currents between 10 nA and 1 µA were applied galvanostatically to the working electrode for between 5 minutes and 120 minutes. This resulted in the oxidation of water, thereby creating a proton flux which was directed towards the substrate surface, inducing the local dissolution of the substrate, as shown in Figure 6-2.

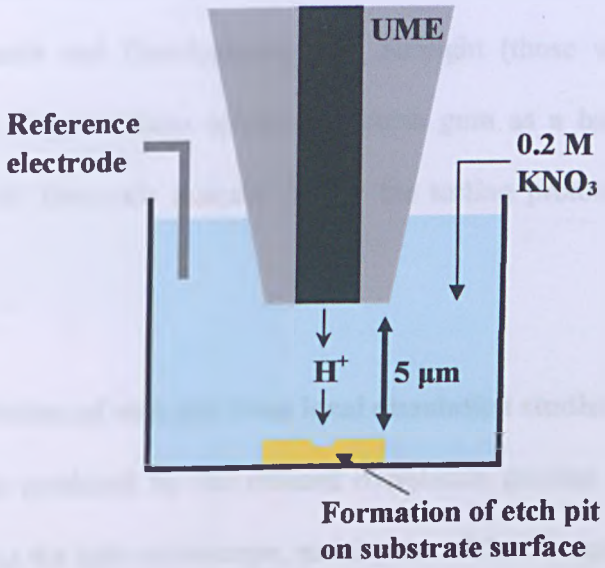

Figure 6-2: Schematic to show the set-up used to induce the local dissolution of substrates using an electrochemical technique.

6.2.1 Calcium carbonate/phosphate substrates

The various calcium carbonate/phosphate substrates which were investigated are listed below (with their densities, ρ).

1) Cleaved calcite (Iceland Spar) sections ($\rho = 2.71$ mg mm^{-3}).
2) Toilet limescale sample ($\rho = 1.70$ mg mm^{-3}).
3) 2:1 calcium phosphate: carbonate mix pressed pellet ($\rho = 1.92$ mg mm^{-3}).
4) Calcium carbonate pressed pellet ($\rho = 1.86$ mg mm^{-3}).
5) Calcium carbonate + acacia gum pressed pellet ($\rho = 1.80$ mg mm^{-3}).
6) Calcium phosphate pressed pellet ($\rho = 2.07$ mg mm^{-3}).
7) Calcium phosphate + acacia gum pressed pellet ($\rho = 1.97$ mg mm^{-3}).
8) Hydroxyapatite pressed pellet ($\rho = 6.00$ mg mm^{-3}).

The simulated limescale pellets (listed in 3-8 above) were provided by either Unilever Research and Development, Port Sunlight (those without acacia gum) or Thompson and Capper (those containing acacia gum as a binder), in an attempt to produce a model limescale material to aid the testing protocols for household care products.

6.3 Characterisation of etch pits from local dissolution studies

Etch pits produced by the induced dissolution process were characterised via observation using the light microscope, making use of the Nomarski differential contrast interference objectives, scanning electron microscopy and by vertical scanning interferometry (Wyko NT-2000 Surface Profiler).

6.3.1 Cleaved calcite

Calcite has a perfect rhombohedral (104) cleavage plane[13] which allows cleavage to leave a planar, flat surface, having few dislocations due to it only having one dislocation per 10000 μm^2 [14]. Etch pits resulting from the local dissolution of these calcite surfaces were visible by light microscopy and could therefore be located easily.

It was possible to perform interferometry on the etch pits produced due to the high reflectivity of the calcite surface. An example of the information that can be obtained is shown in Figure 6-3. This figure shows that the geometry of the pits produced can be measured with high precision.

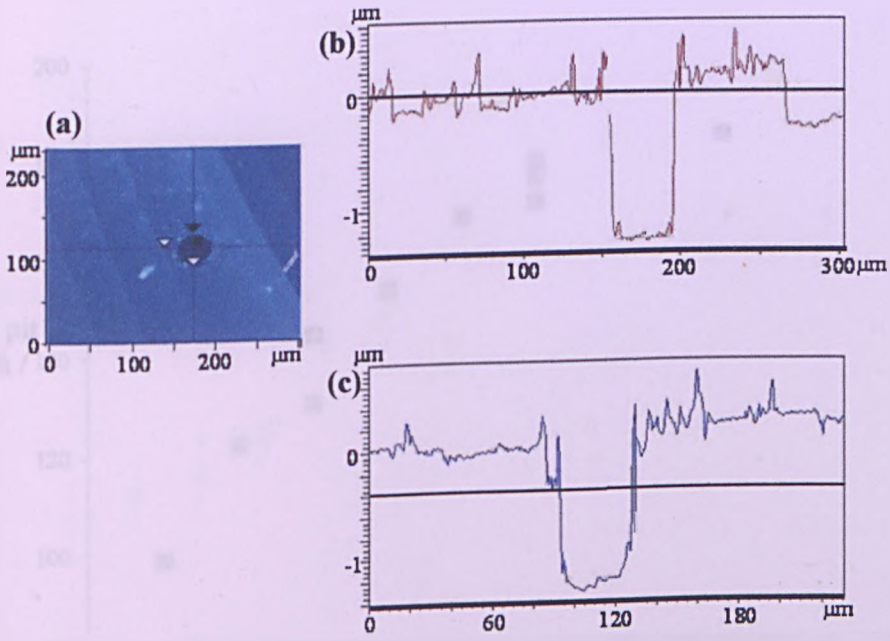

Figure 6-3: Interferometry data (a), showing a cross sections (b and c) of an etch pit on a calcite surface, after the application of 100 nA current for 10 minutes. UME radius: 12.5 µm, tip-substrate separation: 5 µm.

All etch pits produced were found to be circular with pit diameters and depths which increased as a function of time. The pit diameters increased from ~ 30 µm to 200 µm, as either the time or the current applied was increased. The lower limiting width is close to the diameter of the electrode (25 µm) and shows that as the electrode was held 5 µm away from the surface of the calcite, lateral diffusion of the protons did occur during the etching process. Figure 6-4 shows the increasing pit widths with time when a constant current of 100 nA was applied from a UME with a radius of 12.5 µm, at a tip-substrate distance of 5 µm.

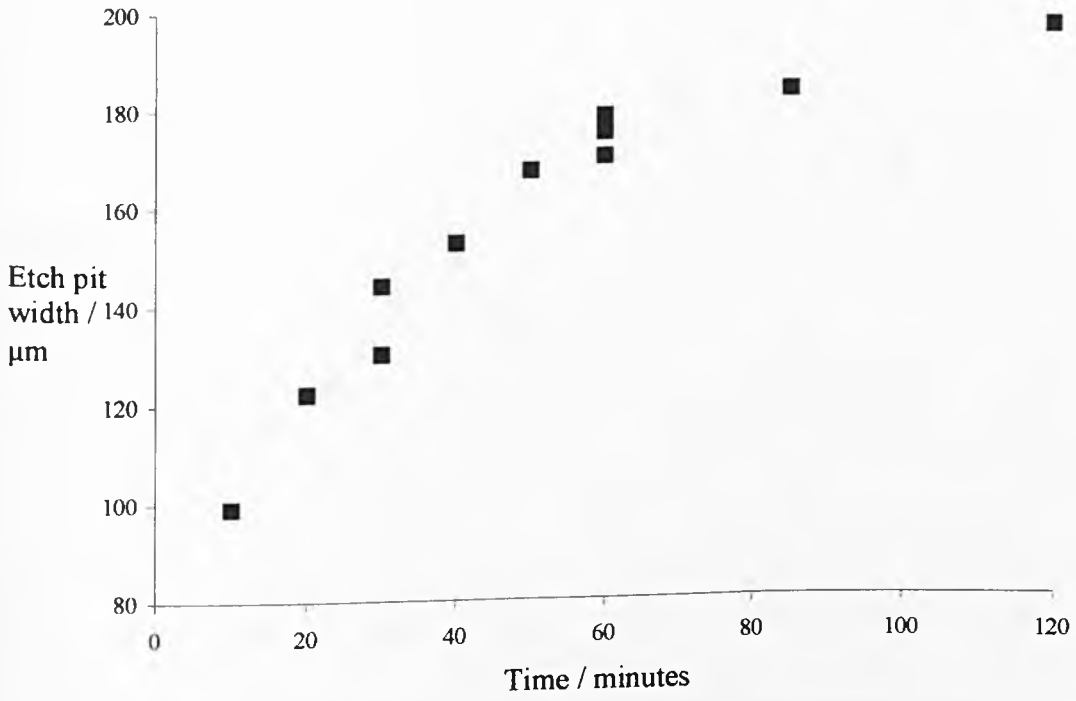

Figure 6-4: Plot to show the increase in calcite etch pit widths (±5 µm) with time (at constant current of 100 nA). UME radius: 12.5 µm, tip-substrate separation: 5 µm.

Figure 6-5 shows the increase in pit depth with increasing experiment time, at constant applied current (100 nA), with a UME with radius 12.5 µm and tip-substrate separation of 5 µm. From this interferometry data, it was possible to calculate pit volumes, making the reasonable assumption that pits were all cylindrical in shape.

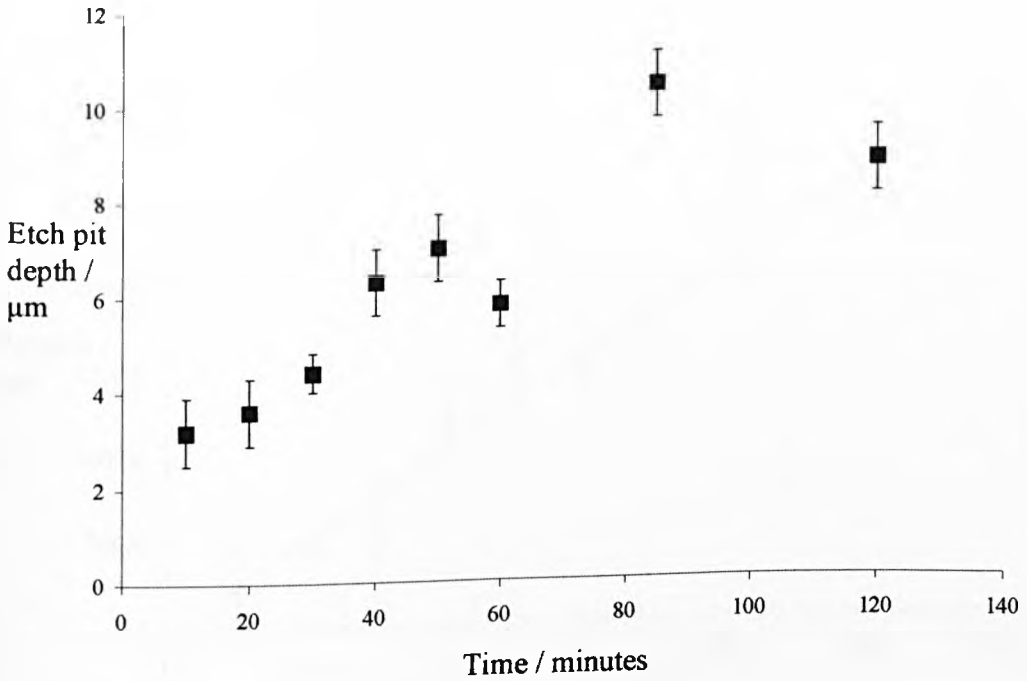

Figure 6-5: Plot to show the increase in calcite etch pit depths with time, at constant current of 100 nA. UME radius: 12.5 µm, tip-substrate separation: 5 µm.

Figure 6-6 shows a plot of etch pit volumes against time for a constant applied current of 100 nA using a UME of radius 12.5 µm, with a tip-substrate separation of 5 µm. The response shows that there is a linear relationship between volume and time of current applied. Although most experiments were conducted at a constant current of 100 nA, experiments were also run at currents between 5 and 100 nA on the cleaved calcite surface to investigate the effect of increasing current on the dissolution process. Figure 6-7 shows the increase in mean etch pit volumes at constant time, when the current was varied between 5 and 100 nA.

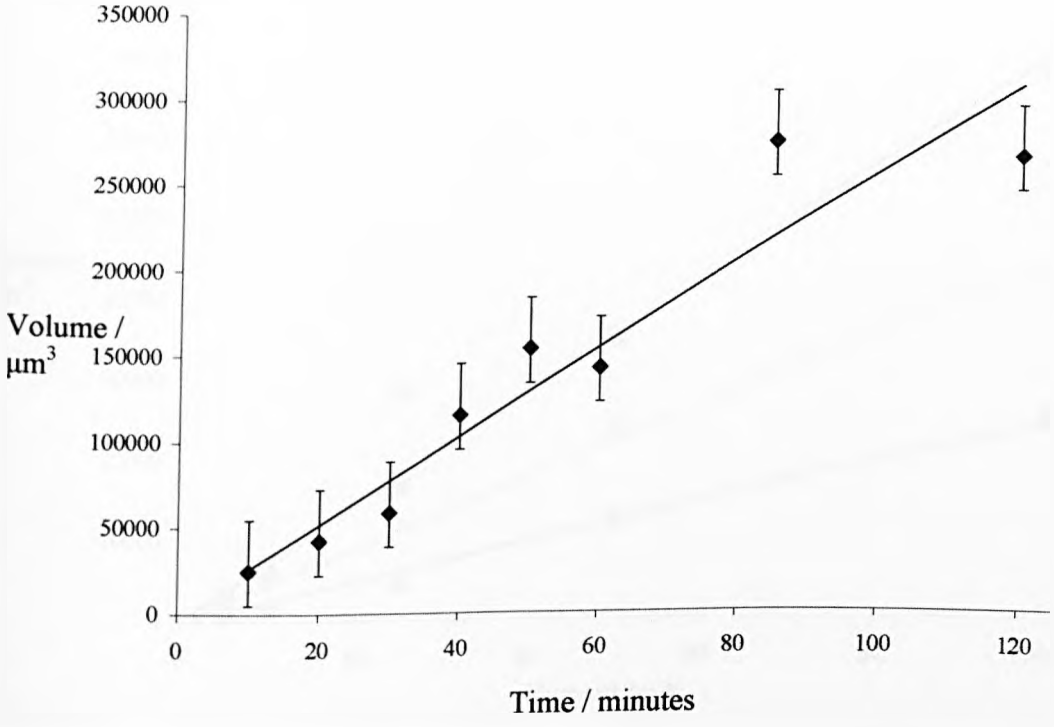

Figure 6-6: Plot to show increasing etch pit volumes on calcite surfaces, when a current of 100 nA was applied for time periods of 10 to 120 minutes. UME radius: 12.5 µm, tip-substrate separation: 5 µm.

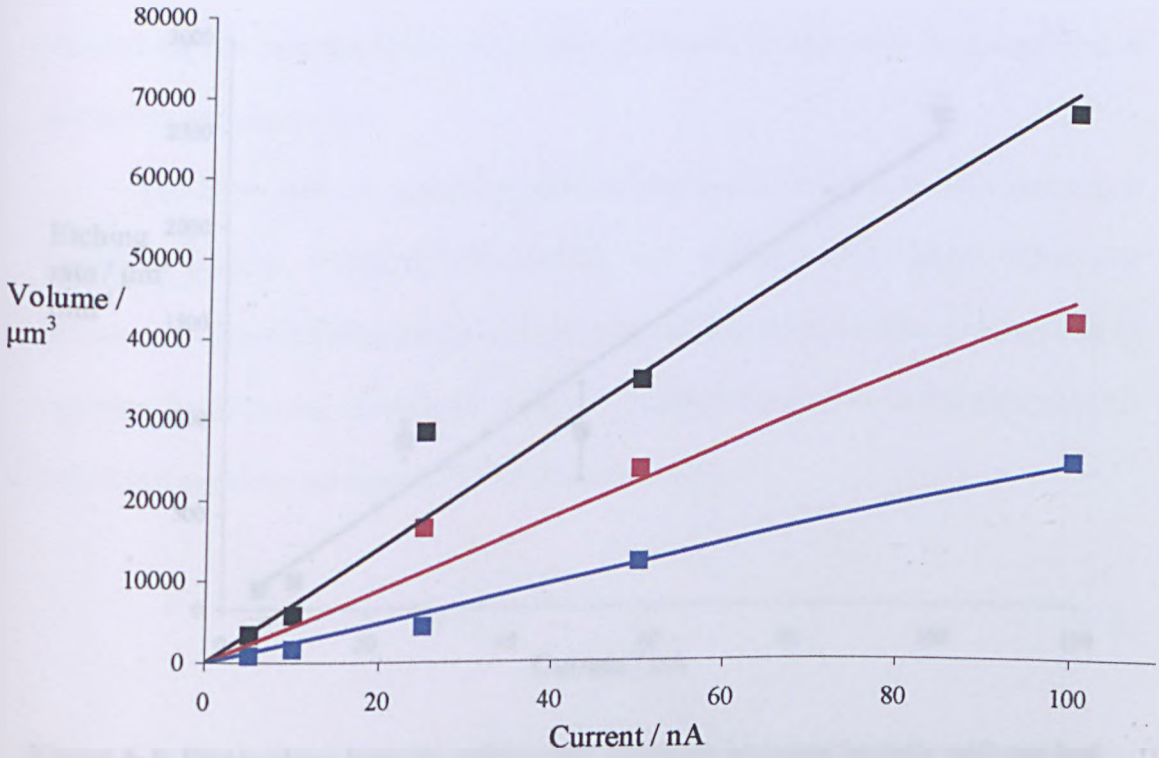

Figure 6-7: Plot to show the linear increase in mean etch pit volume (±250 µm^3) with increasing current. UME radius: 12.5 µm, tip-substrate separation: 5 µm. **Key**: Black: 30 minutes, red: 20 minutes, blue: 10 minutes.

From the data in Figure 6-7, the etching rate, as a function of current, was calculated, which is summarised in Figure 6-8. From this figure, it can be seen that the etching rate has a linear dependence on current, i.e. proton flux.

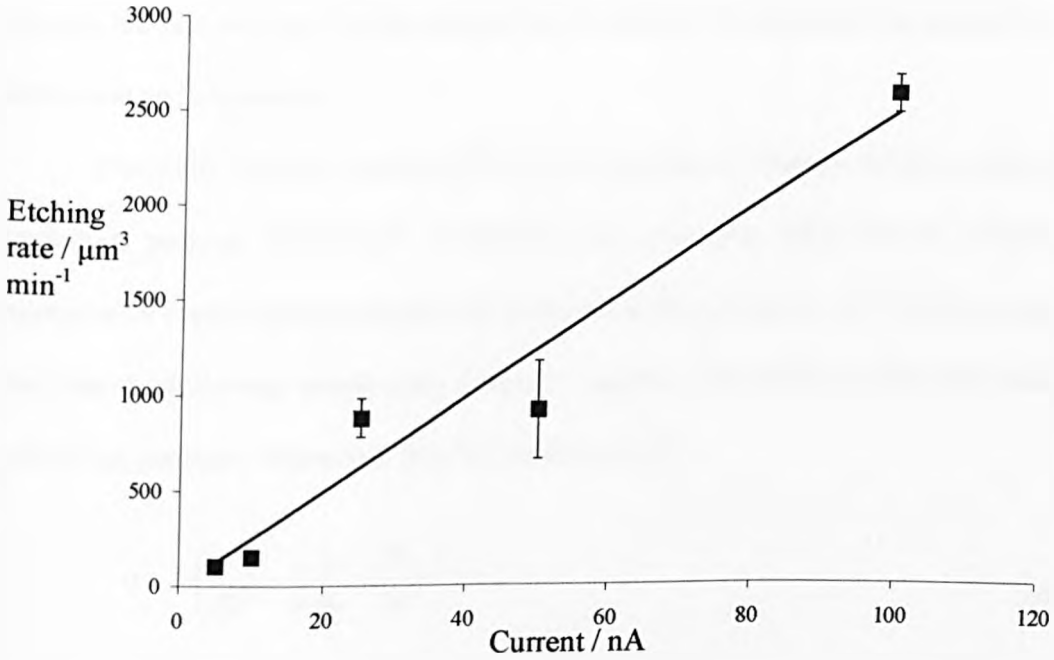

Figure 6-8: Plot to show how the etching rate of calcite increases linearly with applied current.

6.3.2 FEMLAB® diffusion based dissolution model

The localised dissolution of the (104) calcite plane was modelled using the finite element method, using FEMLAB®. Based on prior literature[7], the dissolution process was expected to be governed by a first-order reaction rate in surface protons, as in Equation 6-2:

$$j = k\,[H^+] \tag{6-2}$$

where j is the flux of protons consumed, k is the rate constant and $[H^+]$ is the proton concentration at the crystal/solution interface. Using this simulation, the pH profile at

the calcite surface and the resulting etch pit profiles were simulated. The model has also allowed the rate constant for the dissolution process to be calculated by comparison of simulation and experiment.

The finite element method (Chemical Engineering Module of the commercial modelling package FEMLAB® (COMSOL Ltd., Oxford, UK)) solves differential equations by approximating continuous quantities at discrete points in a mesh system. In this case the following steady-state diffusion equation was solved in the axisymmetric cylindrical geometry relevant to SECM (Equation 6-3):

$$0 = D\left(\frac{\partial^2 c}{\partial r^2} + \frac{1}{r}\frac{\partial c}{\partial r} + \frac{\partial^2 c}{\partial z^2}\right) \tag{6-3}$$

where r is the radial co-ordinate, starting at the centre of the UME, z is the co-ordinate normal to the UME, starting at its centre (see Figure 6-9) and D is the diffusion coefficient of the H^+ ions, which have a concentration, c.

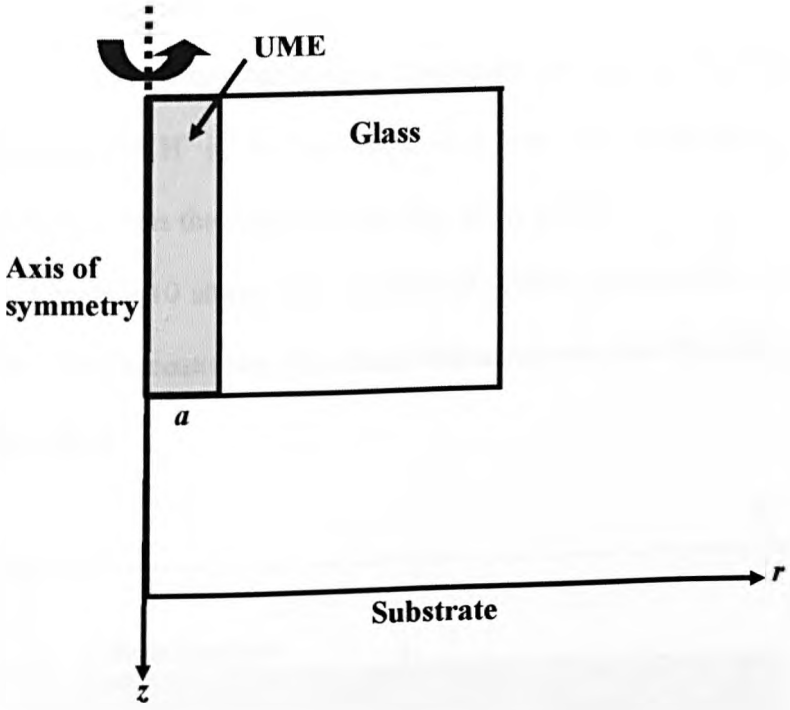

Figure 6-9: Definition of the coordinates used in Equation 6-3.

Figure 6-10 shows a typical graphical output from the model. In this case, the UME was positioned 5 μm away from the calcite surface (all lengths have been normalised with respect to an electrode of radius a = 12.5 μm, as used in the experiments). The concentration at the outside edges of the simulation domain were set to bulk proton concentration values, the domain being large enough for the edges to have no effect on the results. As the pH of the initial solution was pH 8.5, the bulk concentration could be approximated to $1 / 10^{8.5} = 3.1625 \times 10^{-9}$ mol dm^{-3}.

The boundary condition on the sides of the electrode was set so as to make them insulating (no flux boundary condition), and a value for the electrogenerated proton flux, j, was assigned to the active electrode surface boundary (current = 100 nA). Equation 6-

2 constituted the boundary condition at the calcite surface (rate constant = 1 cm s^{-1}). The model was run under steady-state conditions (as implied by Equation 6-3) and the concentration of H^+ in the tip-substrate domain was calculated, in addition to other parameters such as the proton flux at the calcite crystal.

Figure 6-10 shows the variation of proton concentration in the UME-substrate domain. The concentration of protons decreases away from the tip, due to reaction at the calcite surface.

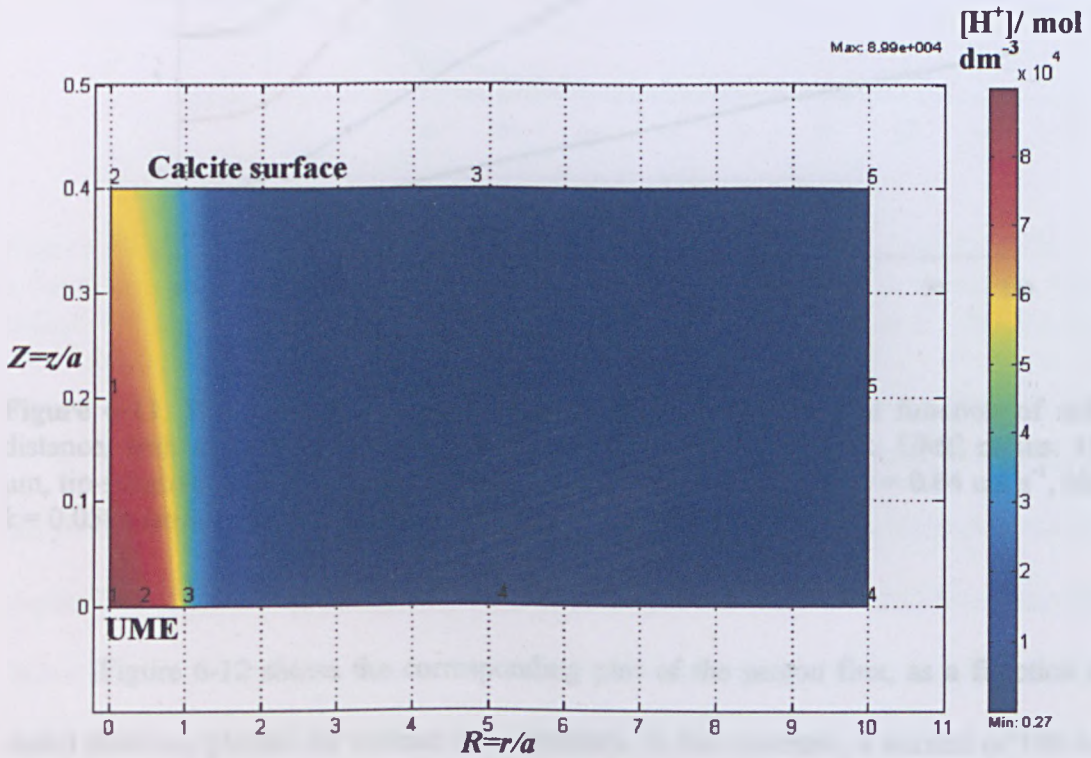

Figure 6-10: Proton concentration profile of UME (a = 12.5 μm) above a calcite surface. Tip-substrate separation: 5 μm.

The pH profile at the calcite surface can readily be extracted from the simulations. Figure 6-11 shows typical profiles for a range of rate constants, k, between 6.4 x 10^{-3} and 6.4 cm s^{-1}. This plot shows the variation in pH across the calcite surface.

The higher the rate constant, the more the reaction is localised on the calcite surface and the higher the interfacial pH.

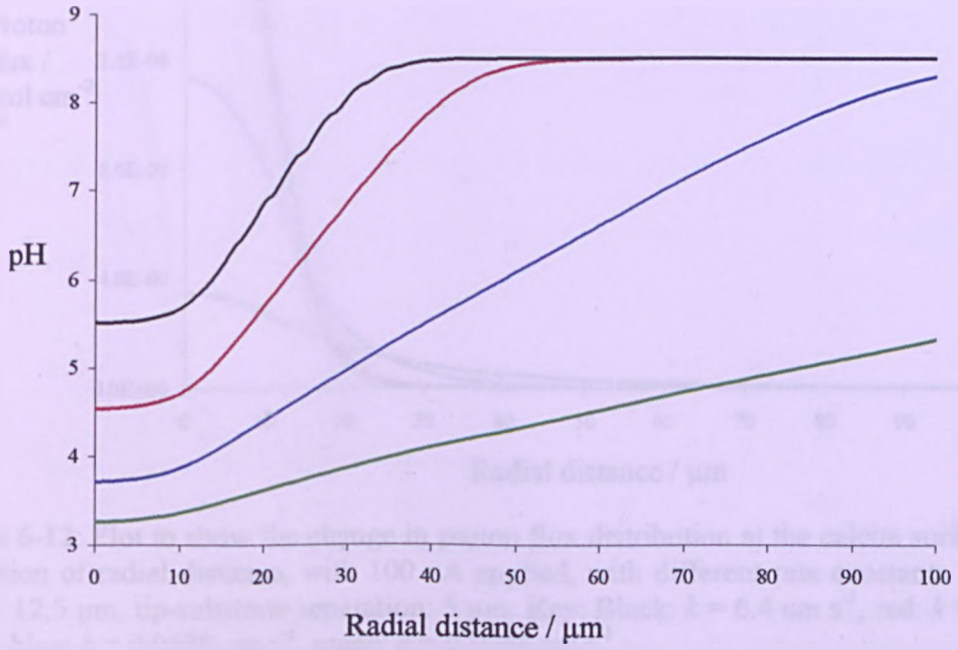

Figure 6-11: Plot to show pH profiles at the calcite surface as a function of radial distance, with 100 nA applied, with different surface rate constants. UME radius: 12.5 μm, tip-substrate separation: 5 μm. **Key**: Black: $k = 6.4$ cm s^{-1}, red: $k = 0.64$ cm s^{-1}, blue: $k = 0.0588$ cm s^{-1}, green: $k = 0.0064$ cm s^{-1}.

Figure 6-12 shows the corresponding plot of the proton flux, as a function of radial distance, plotted for various rate constants. In this example, a current of 100 nA was again applied using a UME ($a = 12.5$ μm), with a tip-substrate distance of 5 μm. As the distance from the UME centre increases, the proton flux also decreases, and the faster the rate constant, the higher the proton flux at the surface (this leads to higher reactivity at the surface). The fluxes in Figure 6-12 thus explain the pH distribution in Figure 6-11.

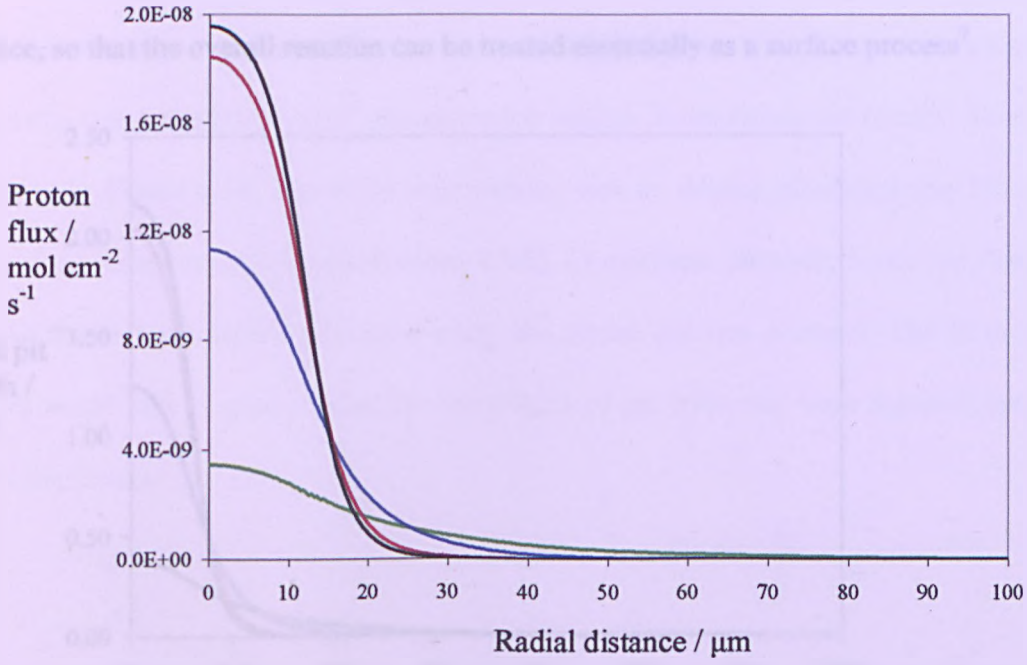

Figure 6-12: Plot to show the change in proton flux distribution at the calcite surface as a function of radial distance, with 100 nA applied, with different rate constants. UME radius: 12.5 µm, tip-substrate separation: 5 µm. **Key**: Black: $k = 6.4$ cm s^{-1}, red: $k = 0.64$ cm s^{-1}, blue: $k = 0.0588$ cm s^{-1}, green: $k = 0.0064$ cm s^{-1}.

Using the density of calcite (0.02708 mol cm^{-3})[13], and multiplying the fluxes by the time for which the current was applied, it was possible to extract simulated etch pit depths (see Figure 6-13, which assumes a current applied for 10 minutes) from this data. When calcite dissolution occurs at low pH, the process essentially involves the reaction of 2 protons with each carbonate ion:

$$CaCO_3 + H^+ \rightarrow Ca^{2+} + HCO_3^- \quad (6\text{-}5)$$

$$HCO_3^- + H^+ \leftrightarrow H_2CO_3 \rightarrow CO_2 + H_2O \quad (6\text{-}6)$$

At low pH, the chemical step in Equation 6-6 occurs very close to the crystal surface, so that the overall reaction can be treated essentially as a surface process[7].

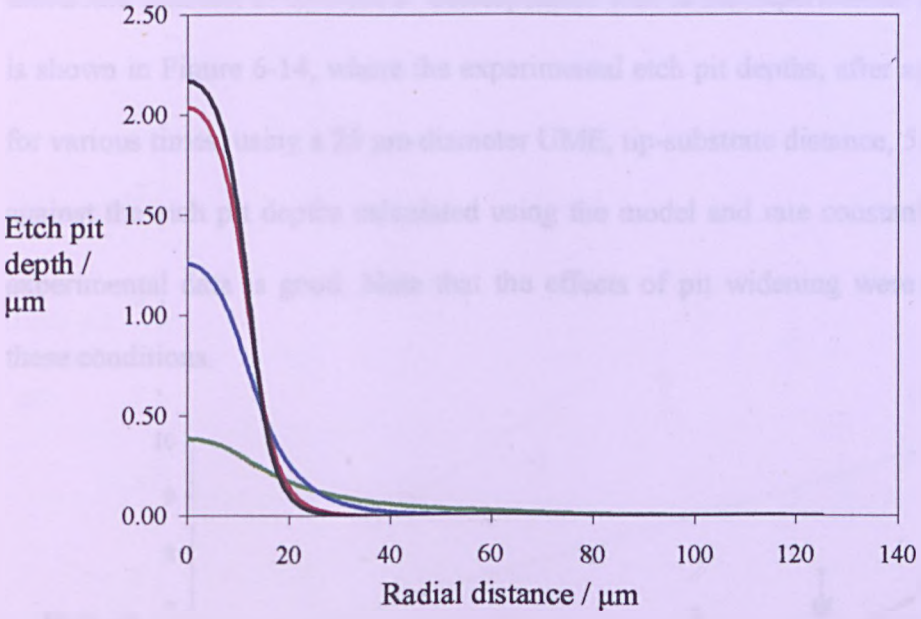

Figure 6-13: Plot to show theoretical etch pits at the calcite surface as a function of radial distance, when 100 nA was applied for 10 minutes, with different rate constants. UME radius: 12.5 µm, tip-substrate separation: 5 µm. **Key**: Black: $k = 6.4$ cm s^{-1}, red: $k = 0.64$ cm s^{-1}, blue: $k = 0.0588$ cm s^{-1}, green: $k = 0.0064$ cm s^{-1}.

It is clear from this that the simulated pit profile is very sensitive to the rate constant. Note that the rate constant of 6.4 cm s^{-1} is essentially diffusion-controlled and the fact that a moderately high rate constant, $k = 0.508$ cm s^{-1}, gives a pit profile which is quite distinct from the diffusion-controlled limit implies that this technique is particularly well-suited to the measurement of fast surface processes. Although the pit shape depends on the rate constant, broadening as the rate constant decreases, the pit depth is most sensitive to the rate constant and so this was used for further analysis.

By manipulating the rate constant employed in the simulation, pit depths which correspond to experimental results were obtained. From these simulations, it was found that a rate constant of 0.06 cm s^{-1} corresponded well to the experimental results. This fit is shown in Figure 6-14, where the experimental etch pit depths, after applying 100 nA for various times, using a 25 μm diameter UME, tip-substrate distance, 5 μm, are plotted against the etch pit depths calculated using the model and rate constant. The fit to the experimental data is good. Note that the effects of pit widening were minimal under these conditions.

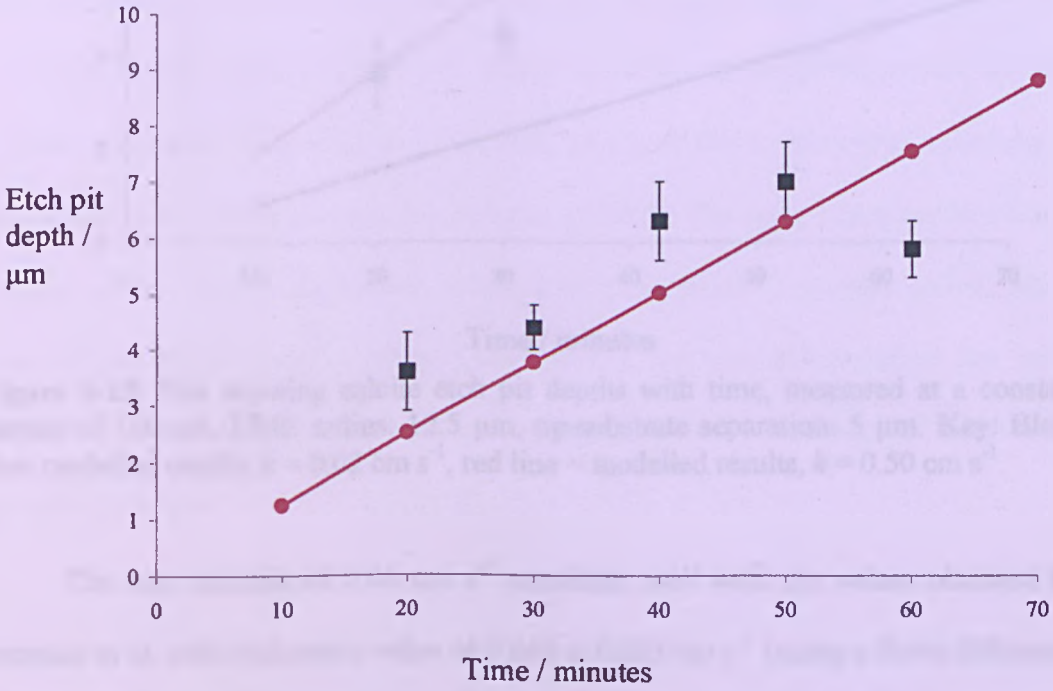

Figure 6-14: Plot showing calcite etch pit depths with time, measured at a constant current of 100 nA. UME radius: 12.5 μm, tip-substrate separation: 5 μm. **Key**: Black: experimental results, red: diffusion-controlled model results.

If the calcite etch pit depths, measured at a constant current of 100 nA, are plotted as a function of time against the model results using rate constants, k, of 0.02 cm s^{-1} and 0.50 cm s^{-1}, it can be seen that the data lie within these bounds.

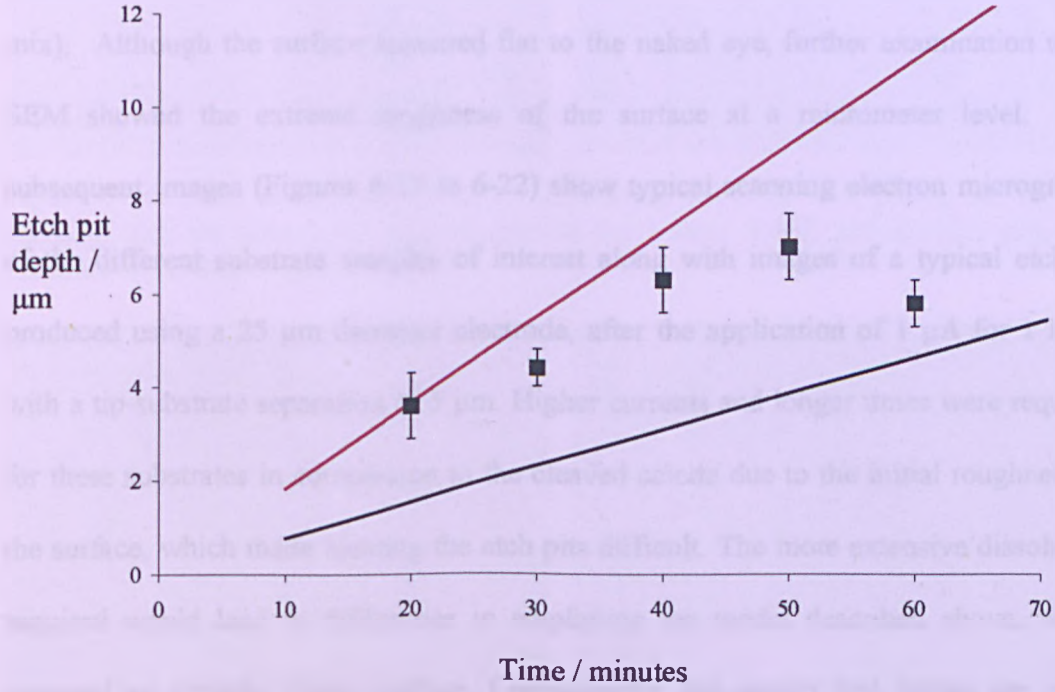

Figure 6-15: Plot showing calcite etch pit depths with time, measured at a constant current of 100 nA. UME radius: 12.5 µm, tip-substrate separation: 5 µm. **Key**: Black line: modelled results, $k = 0.02$ cm s^{-1}, red line = modelled results, $k = 0.50$ cm s^{-1}.

The rate constant of 0.06 cm s^{-1} correlates well with the values obtained by Compton et al. who deduced a value of 0.043 ± 0.015 cm s^{-1} (using a finite difference method) for this rate constant by modelling results obtained using high speed laminar flow measurements[2].

6.3.3 Amorphous scale substrates

Having established the validity of the SECM method on the well known calcite system, attention turned to more complex systems. Figure 6-16 is a scanning electron micrograph of the surface of a simulated limescale pellet (2:1 phosphate: carbonate mix). Although the surface appeared flat to the naked eye, further examination using SEM showed the extreme roughness of the surface at a micrometer level. The subsequent images (Figures 6-17 to 6-22) show typical scanning electron micrographs of the different substrate samples of interest along with images of a typical etch pit produced using a 25 μm diameter electrode, after the application of 1 μA for 1 hour, with a tip-substrate separation of 5 μm. Higher currents and longer times were required for these substrates in comparison to the cleaved calcite due to the initial roughness of the surface, which made locating the etch pits difficult. The more extensive dissolution required would lead to difficulties in employing the model described above, which assumed an initially planar surface. Consequently, the results that follow are semi-quantitative and provide a means of comparing the relative reactivity of these more complex substrates.

The strength of the new UME approach is revealed in these studies, as alternative chemical based methods would require a detailed knowledge of the chemical composition of the substrates. In contrast, the ability to measure material removed at a known proton flux is valuable in terms of developing a basic understanding of the factors controlling the removal of calcified deposits by acid treatment.

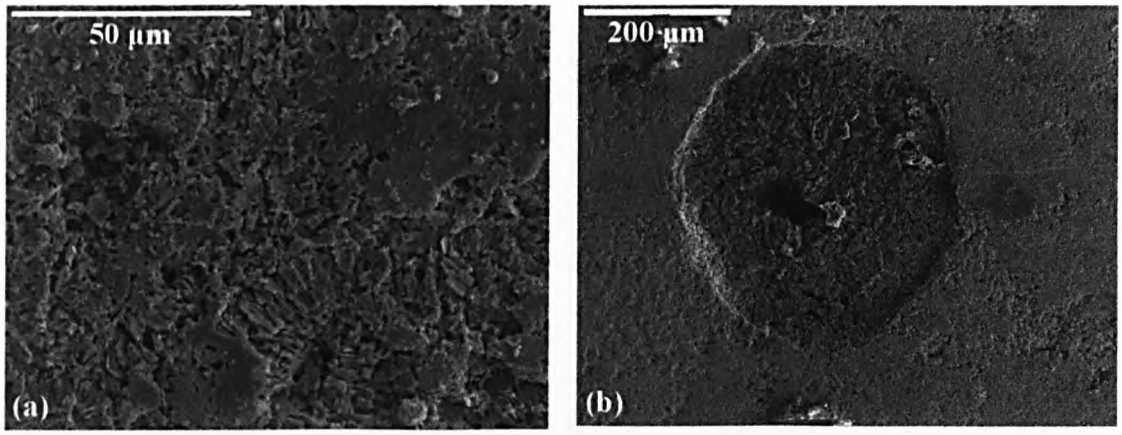

Figure 6-16: SEM of: (a) surface of 2:1 phosphate/carbonate mix pellet; and (b) the resulting etch pit after 1 µA current applied for 1 hour. UME radius: 12.5 µm, tip-substrate separation: 5 µm.

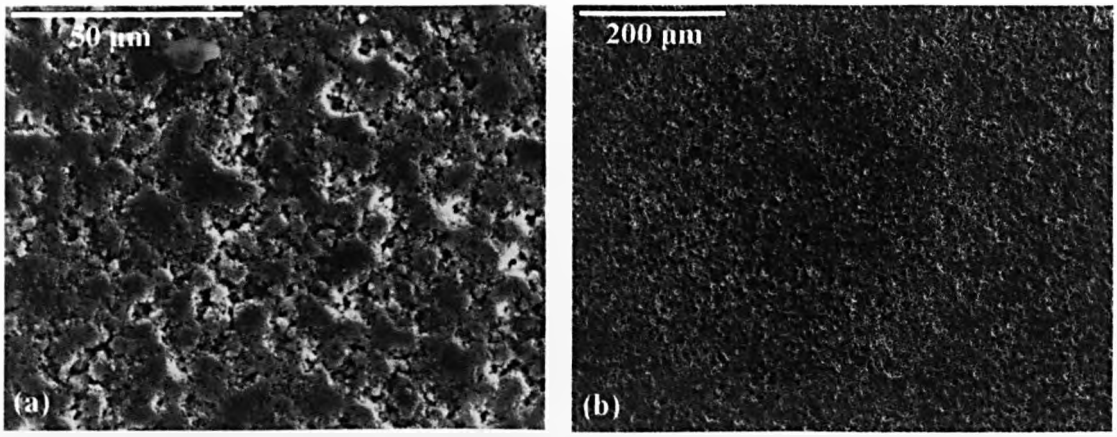

Figure 6-17: SEM of: (a) surface of calcium carbonate pellet; and (b) the resulting etch pit after 1 µA current applied for 1 hour. UME radius: 12.5 µm, tip-substrate separation: 5 µm.

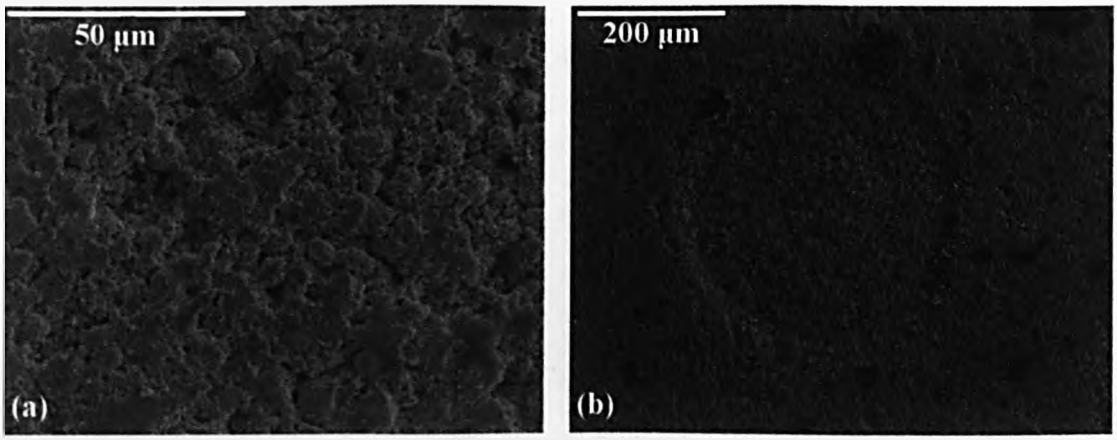

Figure 6-18: SEM of: (a) surface of calcium carbonate + acacia gum pellet; and (b) the resulting etch pit after 1 µA current applied for 1 hour. UME radius: 12.5 µm, tip-substrate separation: 5 µm.

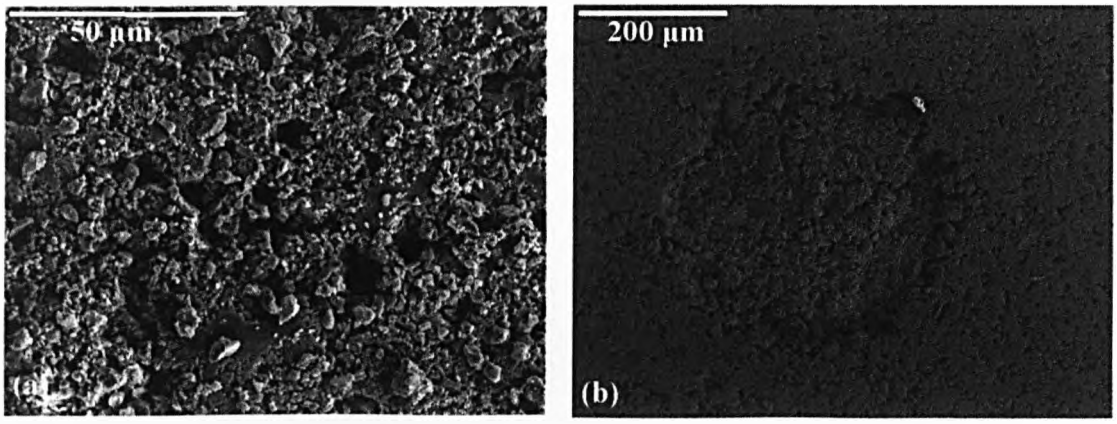

Figure 6-19: SEM of: (a) surface of calcium phosphate pellet; and (b) the resulting etch pit after 1 µA current applied for 1 hour, UME radius: 12.5 µm, tip-substrate separation: 5 µm.

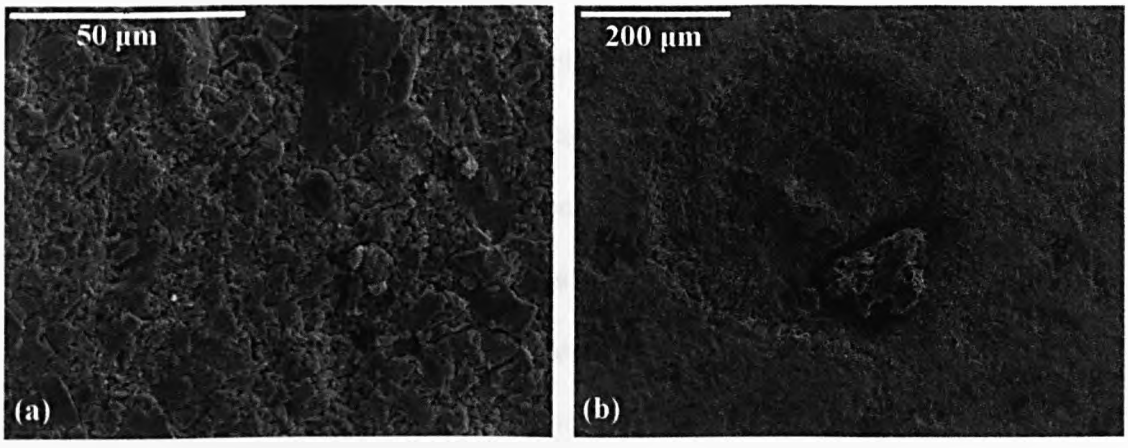

Figure 6-20: SEM of: (a) surface of calcium phosphate + acacia gum pellet; and (b) the resulting etch pit after 1 µA current applied for 1 hour. UME radius: 12.5 µm, tip-substrate separation: 5 µm.

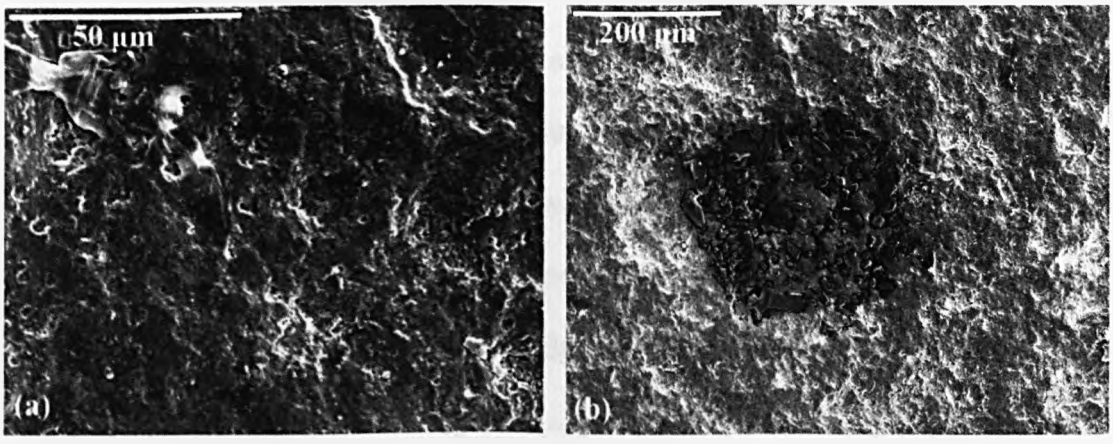

Figure 6-21: SEM of: (a) surface of hydroxyapatite pellet; and (b) the resulting etch pit after 1 µA current applied for 1 hour. UME radius: 12.5 µm, tip-substrate separation: 5 µm.

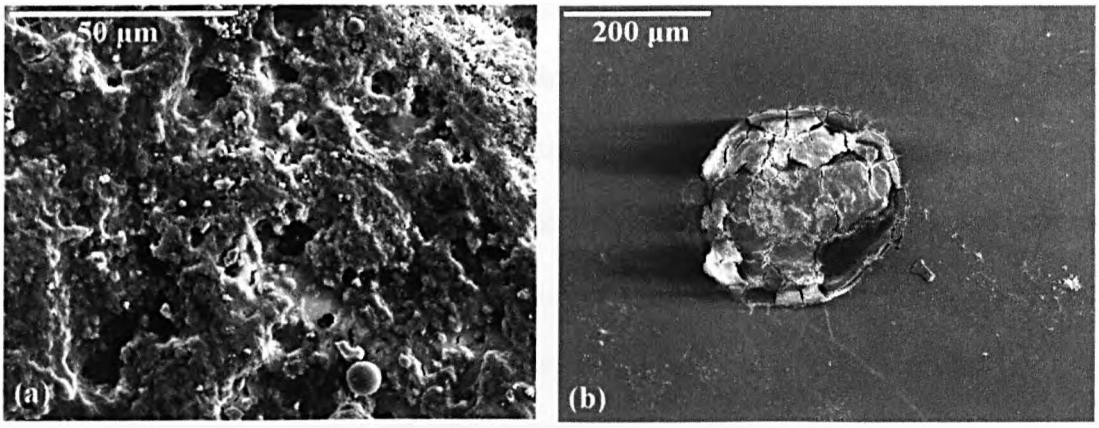

Figure 6-22: SEM of: (a) surface of real limescale sample; and (b) the resulting etch pit after 1 µA current applied for 1 hour. UME radius: 12.5 µm, tip-substrate separation: 5 µm.

These images clearly show the morphological differences between the simulated scale pellets and 'real' scale samples. The calcium carbonate samples (Figures 6-17 and 6-18) appear more amorphous than the phosphate substrates (Figures 6-19 and 6-20), and the etch pits on the carbonate substrates are much less well defined. The phosphate samples (Figures 6-19 and 6-20) exhibit clearer etch pits, similar to the hydroxyapatite substrate (Figure 6-21) and closer in appearance to the real scale sample (Figure 6-22). The presence of the acacia gum as a binding material seems to make little difference to the morphology of the substrates, as shown by the similar images in Figures 6-17 and 6-18 (carbonate samples) and Figures 6-19 and 6-20 (phosphate samples). All etch pits measured were between 200 and 300 µm in diameter, with increasing pit diameter occurring as the proportion of carbonate was introduced into the system. The diameter now approximates to the overall probe size (25 µm diameter) implying that generated protons react in the thin layer between the probe and substrate. The hydroxyapatite substrate appeared most similar to the real scale sample in these images.

To calculate the etch pit volumes, interferometry was performed, although this was difficult due to the low reflectivity of the substrate surfaces. Samples were coated in a very thin layer of gold to aid measurements, and volumes were calculated on the assumption that the etch pits were cylindrical in shape. The presence of loose material around the edges of the pits and amorphous pieces of mineral that had fallen into the pits upon dissolution meant that some uncertainty was introduced into this analysis.

Nonetheless, etch pit volumes were found to increase linearly with time, and current, as expected and as shown in Figure 6-23 for the particular case of the 2:1 phosphate: carbonate mix pellet, after applying 500 nA, with a UME with radius 12.5 μm at a tip-substrate separation of 5 μm.

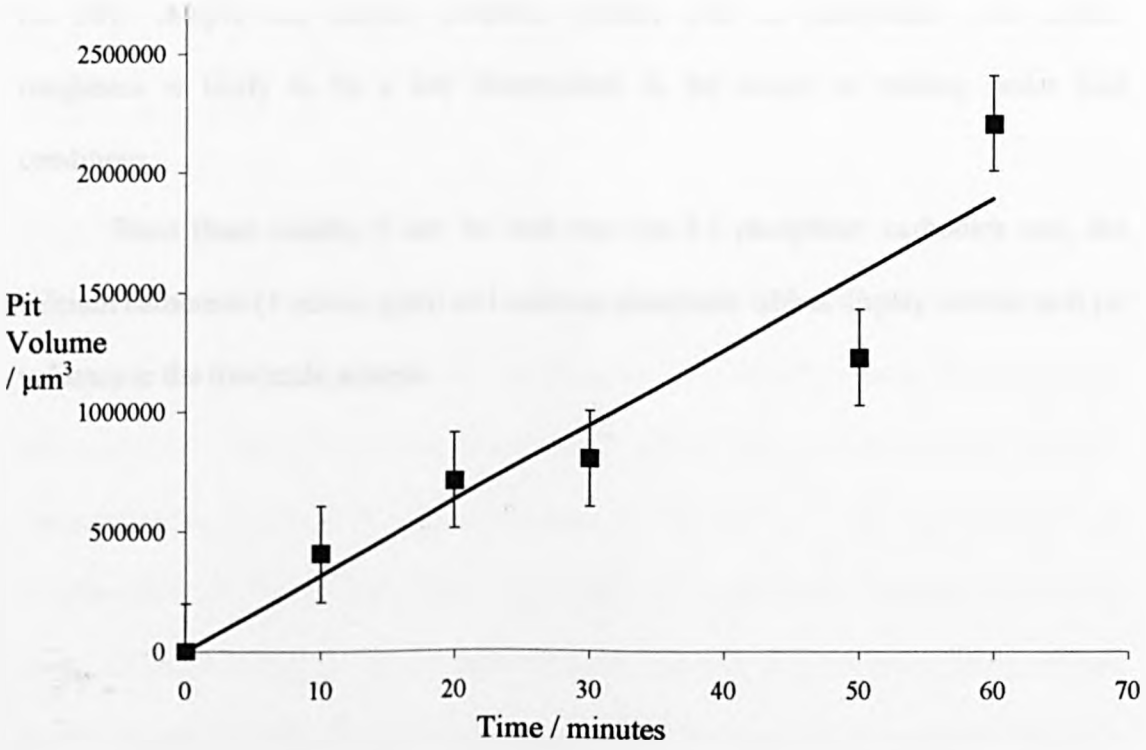

Figure 6-23: Plot to show linear increase in etch pit volume after applying 500 nA for varying time periods to 2:1 phosphate: carbonate mix pellet. Tip-substrate separation: 5 μm, UME radius: 12.5 μm.

In order to compare the different samples, and determine the best pressed pellet model for real limescale, pit volumes of the various calcium carbonate/phosphate substrates (including an extrapolated value for calcite from data in Section 6.3.1), were measured when a current of 1 μA was applied for 1 hour (tip-substrate separation: 5 μm). The plot shows that the pellets containing a high proportion of calcium phosphate were more reactive than the carbonate-containing pellets, although in the case of the calcium phosphate pellets, the acacia gum has much more effect in terms of increasing the reactivity of the sample in acid conditions than for the calcium carbonate tablets, where it had little or no effect. The hydroxyapatite substrate, despite appearing morphologically similar to the true scale sample, appeared to be much less reactive; this could be due to the method of substrate preparation – unlike the other simulated pellets, the HAP sample was slightly polished. Surface area, as manifested from surface roughness is likely to be a key determinant in the extent of etching under acid conditions.

From these results, it can be seen that the 2:1 phosphate: carbonate mix, the calcium carbonate (+ acacia gum) and calcium phosphate tablets display similar etch pit volumes to the true scale sample.

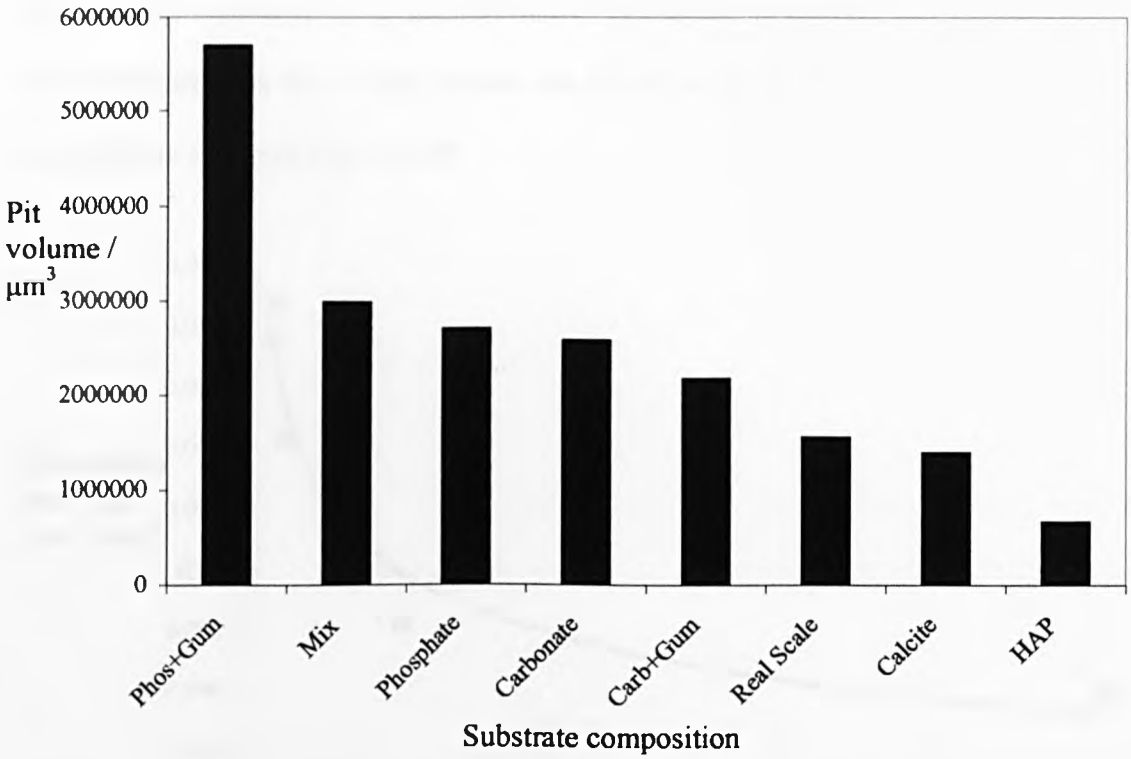

Figure 6-24: Chart to show etch pit volumes on the various calcium carbonate/phosphate substrates (±100000 μm^3), after 1 µA was applied for 1 hour. UME radius: 12.5 µm, tip-substrate separation: 5 µm.

6.3.4 Effects of solution viscosity on calcite dissolution

Sucrose solutions were used to vary the viscosity of the electrolyte solution to investigate the effects of viscosity on the acid dissolution process. Solutions with viscosities of 1.05, 1.29, 1.80, 8.60 and 50.63 mPa s^{-1} were used, with the viscosity measured using a viscometer. The same experimental method used, with the electrode (UME radius: 12.5 µm) positioned 5 µm from a 2:1 phosphate: carbonate simulated limescale pellet, thought to be the most realistic model for real limescale, as determined by its composition (66.6 % calcium phosphate, 33.3 % calcium carbonate) and results in Section 6.3.3. A current of 1 µA was applied for 1 hour and the resulting pit depth and

volume was measured using interferometry. The extent of etching and the dissolution rate, averaged over the 1 hour period, was found to decrease with increasing solution viscosity, as shown in Figure 6-25.

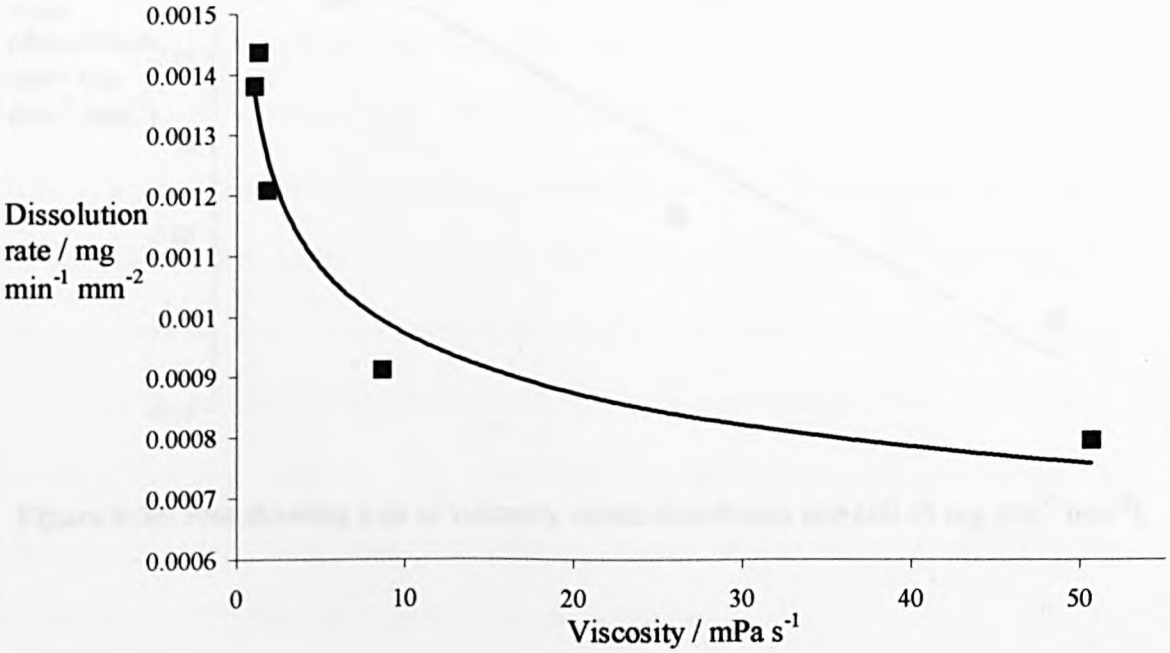

Figure 6-25: Plot of dissolution rate of 2:1 phosphate: carbonate mix pellet (±0.0001 mg min^{-1} mm^{-2}) versus viscosity. Line through the data is a guide to the eye.

To determine the dependence of the dissolution rate on viscosity, a plot of the log of the dissolution rate against log viscosity of the dissolution rate, was constructed (Figure 6-26).

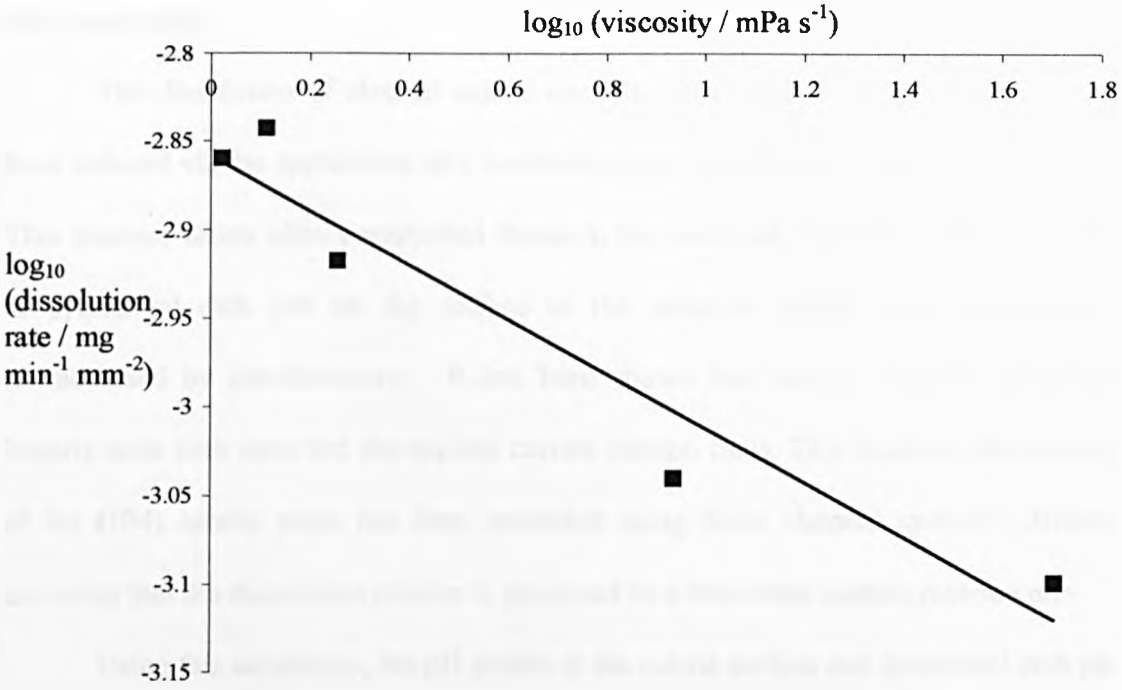

Figure 6-26: Plot showing logs of viscosity versus dissolution rate (±0.05 mg min^{-1} mm^{-2}).

The negative gradient of -0.15 is considerably less than the gradient of -1.0 that would be expected if the dissolution were completely diffusion-controlled, with Stokes Law describing the diffusion coefficient of H^+ on viscosity[15]. Therefore, the dissolution reactions of these more complex materials are mainly surface-controlled, limited only slightly by diffusion of species to the substrate.

These results are important from a commercial viewpoint, as they suggest that the use of household care products, such as bleach or limescale removal formulations would work more efficiently at lower solution viscosities. This does, however, contradict consumer research, where most surveys indicate the preference of thicker products[16].

6.4 Conclusions

The dissolution of cleaved calcite crystals and simulated limescale pellets has been induced via the application of a localised proton flux from an ultramicroelectrode. This process, which allows controlled fluxes to be generated, resulted in the formation of cylindrical etch pits on the surface of the samples, which were subsequently characterised by interferometry. It has been shown that the pit volumes increased linearly with both time and the applied current (proton flux). This localised dissolution of the (104) calcite plane has been modelled using finite element method software assuming that the dissolution process is governed by a first-order surface reaction rate.

Using this simulation, the pH profile at the calcite surface and theoretical etch pit profiles have been obtained. The model has also allowed the rate constant for the dissolution process to be calculated, which compares well to the value suggested by Compton et al.[2,17], thereby validating this new approach.

The effect of solution viscosity on limescale dissolution was also investigated by employing sucrose solutions to increase the viscosity of the electrolyte. Results showed that the dissolution rate decreased only slightly with a large increase in solution viscosity which suggests that the dissolution process is largely surface-controlled.

6.5 References

[1] J. Christoffersen and M. R. Christoffersen, *J. Cryst. Growth*, **1981**, *53*, 42.

[2] R. G. Compton, K. L. Pritchard and P. R. Unwin, *J. Chem. Soc., Chem. Commun.*, **1989**, *4*, 249.

[3] C. A. Brown, R. G. Compton and C. A. Narramore, *J. Coll. Inter. Sci.*, **1993**, *160*, 372.

[4] D. Buhmann and W. Dreybrodt, *Chem. Geol.*, **1985**, *48*, 189.

[5] R. G. Compton, C. T. Walker, P. R. Unwin and W. A. House, *J. Chem. Soc. Faraday Trans.*, **1990**, *86*, 849.

[6] R. G. Compton and K. L. Pritchard, *Phil. Trans. R. Soc. Lond. A*, **1990**, *330*, 47.

[7] R. G. Compton and P. R. Unwin, *Phil. Trans. R. Soc. Lond.A*, **1990**, *330*, 1.

[8] P. R. Unwin and J. V. Macpherson, *Chem. Soc. Rev.*, **1995**, *24*, 109.

[9] J. V. Macpherson, P. R. Unwin, A. C. Hillier and A. J. Bard, *J. Am. Chem. Soc.*, **1996**, *118*, 6445.

[10] C. E. Jones, P. R. Unwin and J. V. Macpherson, *Chem. Phys. Chem.*, **2002**, *4*, 139.

[11] P. R. Unwin, *J. Chem. Soc., Faraday Trans.*, **1998**, *94*, 3183.

[12] J. Kwak and A. J. Bard, *Anal. Chem.*, **1989**, *61*, 1221.

[13] W. A. Deer, R. A. Howe and J. Zussman, *An Introduction to the Rock-Forming Minerals*, Longman, **1983**.

[14] R. G. Compton, K. L. Pritchard, P. R. Unwin, G. Grigg, P. Silvester, M. Lees and W.A. House, *J. Chem. Soc., Faraday Trans. 1*, 1989, **85**, 4335.

[15] P. W. Atkins, *Physical Chemistry*, OUP, **1999**.

[16] For example, see

http://www.marketingsociety.org.uk/downloads/awards/Domestos_Entry.pdf

[17] B. A. Coles, R. G. Compton, M. Suárez, J. Booth, Q. Hong and G. H. W. Sanders, *Langmuir*, **1998**, *14*, 218.

Chapter 7

In Situ Visualisation of Growth Mechanisms and Dynamics on the (104) Calcite Microcrystal Surface

The aim of this chapter is to investigate the step dynamics on the spiral growth hillocks on the calcite (104) crystal surface, primarily under supersaturated conditions, and elucidate the corresponding growth kinetics. Much of the previous work in this area has considered macrocrystals surfaces, on which there are many interacting defects and dislocations. To improve the methodology for studying calcite growth, an AFM technique has been developed that allows individual calcite microcrystals (10 – 20 μm in diameter) to be addressed, resulting in the observation of single spiral growth hillocks on (104) surfaces, and their subsequent reactivity. Growth rates were found to be dependent on solution supersaturation and controlled by diffusion of species to the crystal surface from bulk solution, as opposed to being limited by surface mechanisms.

As an extension of this work, the change in the mechanism of growth of calcite surfaces upon the addition of an inhibitor, in the form of maleic acid, has been investigated.

7.1 Introduction

Since its invention in 1986, AFM[1] has proved to be an invaluable tool for high-resolution topographical investigations of the growth and dissolution of inorganic crystal surfaces[2,3,4]. From observations of the inter-atomic step spacings on crystal surfaces for example, kinetics of crystal growth and dissolution have been obtained[5]. Many of the

initial investigations were conducted ex-situ, following a defined period of exposure of the crystal to an appropriate solution[6].

More recently, in situ imaging of crystal surfaces has become commonplace due to the development of AFM fluid cells, which make it possible to operate the AFM in a solution-filled environment[7,8,9,10]. The AFM tip is usually employed to topographically monitor the dynamic process of interest, while the crystal is exposed to an appropriate solution[11,12,13]. This allows the quantification of surface reactivity as rates of step advancement or retreat across the crystal surface, or step movement at dislocation sites, as the surface grows or dissolves. However, the majority of these studies have involved large macrocrystal faces, several millimetres across, with a high number of defect and dislocation sites[14].

With large crystal surfaces, problems can arise using this method of imaging, as processes occurring at neighbouring sites on the crystal surface outside of the scan area may interfere with growth or dissolution in the area probed by the AFM tip, as the whole crystal surface responds to the imposed solution conditions – not solely the area in the scan field of view. It is also difficult to adequately control mass transport to macro-scale crystal surfaces, which is a key factor to consider when investigating interfacial reactivity[15,16]. To overcome this type of problem, some recent studies have reported imaging of single microcrystals, but these investigations have largely been ex-situ[17,18,19,20].

The importance of calcite, not only as a model mineral system, but due to its relevance in many technological and geological processes, means that it has been studied extensively. The growth and dissolution kinetics of calcite[21] have been

investigated using many different techniques, with the crystal subject to a variety of conditions[22,23,24]. The kinetics of calcium carbonate precipitation have been measured using various different techniques[25], including channel-flow methods[26], continuous crystallisers[27] and light scattering techniques which measure the crystal size distribution as a function of time[28]. Spanos and Koutsoukos measured the kinetics of vaterite precipitation in alkaline pH at constant supersaturation, taking into account both seeded and unseeded growth[29], using the most commonly used free drift growth measurements. Along with Kazmierczak et al.[30], Kralj et al.[31], and Reddy and Nancollas[32,33], they concluded that the growth rate was controlled by surface mechanisms. Cassford et al. and Shiraki and Brantley measured the seeded crystallisation kinetics of calcite from calcium bicarbonate solutions at temperatures varying from 278.15 K to 373 K[34,35]. House investigated the same crystallisation process at 298.15 K[36,37] and Buhmann and Dreybodt examined the reaction kinetics under conditions of geologically relevant karst areas[38]. A summary of the precipitation rate constants from these studies is shown in Table 7-1. With linear spiral growth in the calcite system, most agree with Christoffersen and Christoffersen[39], who have determined the rate constant for seeded growth to be ~ 0.03 nm s^{-1}.

System and conditions	Monitoring of reaction	Results	Ref.
Cleaved calcite $S = 1.14 - 4.16$	AFM measurements of step advancement and hillock slopes.	Rate of growth normal to the surface in range $10^{-13} - 10^{-11}$ m s^{-1}.	41
$CaCO_3$ precipitation, on calcite seeds. Supersaturated solutions prepared by mixing $KHCO_3$ and $Ca(NO_3)_2$.	pH-stat method	Rate constant for linear growth = 3×10^{-11} m s^{-1}.	39
$CaCO_3$ precipitation, on calcite crystals. $S = 0.4 - 4$ 293.15 – 343.15 K	pH-stat method	Surface controlled growth rates increased with increasing temperature.	22
$CaCO_3$ precipitation, on vaterite crystals. 283.15 – 318.15 K Varied ionic strength.	pH-stat method	Displayed parabolic growth kinetics (Growth rate normal to the surface = $k(S\text{-}1)^2$).	31
$CaCO_3$ precipitation on vaterite seeds, seed size known. $S = 3.53 - 12.46$ pH 9.0 &10.0	Constant composition method, reaction monitored by pH measurements.	Crystal growth proceeded by spiral growth mechanism. Process controlled by diffusion of $CaCO_3$ growth units on the surface of supercritical nuclei or seeds. Rate constant in the order of 1×10^{-10} m s^{-1}.	29
$CaCO_3$ precipitation, on calcite crystals. Crystal size not known. pH 8.25 – 10.00 288.15 – 308.15 K	Constant composition method	Rate of crystallisation proportional to the square of the supersaturation. Surface-controlled reaction.	30
Seeded $CaCO_3$ precipitation	Conductivity and pH measurements	Rate depends on the size of the crystal seed. Growth rate constant in the order of 1-7 x 10^{-12} m s^{-1}.	36

System and conditions	Monitoring of reaction	Results	Ref.
$CaCO_3$ precipitation on calcite seeds from dilute $NaHCO_3$ solutions.	Conductivity and pH measurements	Modelled using Davies- Jones equation. Growth is independent of original crystal size. Growth rate constant in the order of $1 - 25 \times 10^{-12}$ m s^{-1}.	37
$CaCO_3$ precipitation, on calcite seeds.	Solution Ca^{2+} and H^+ ion concentrations	Rate of crystal growth proportional to product of $[Ca^{2+}]$ and $[CO_3^{2-}]$.	33
$CaCO_3$ growth on calcite seeds.	Channel flow cell/Ca^{2+} ion selective electrode	Modelling of reaction based on rate equation in which Ca^{2+} and CO_3^{2-} undergo Langmuirian adsorption on the calcite surface.	26
Seeded $CaCO_3$ precipitation, on amorphous $CaCO_3$ powder. Varied stirring speeds 373.15 K	EDTA titration	Surface nucleation found to be rate limiting. Rate dependent on stirring speeds.	35
$CaCO_3$ precipitation on calcite seeds from dilute $Ca(HCO_3)_2$ solutions. 278.15 – 303.15 K	Analysis of seed area	Investigated using Davies Jones equation and rate controlled by reaction between $[Ca\text{-}HCO_3]^+$ ion pair and surface CO_3^{2-} anion sites. Rate does not depend on seed size. Growth rate constant in the order of $1 - 8 \times 10^{-13}$ m s^{-1}.	34

Table 7-1: Summary of $CaCO_3$ growth and precipitation investigations, as measured using various techniques.

AFM has, more recently, proved particularly powerful for investigating calcite surfaces, enabling atomistic theories of growth and dissolution to be validated with experimental surface topographical data[40,41] as well as the evolution of growth kinetics and rate laws. However, these studies have focused largely on natural macroscopic crystals (several mm - cm dimensions) exposed to a solution with a fixed, low

supersaturation. Information has been obtained on the mechanisms of growth[42], as well as the effect on growth of a variety of inhibitors, including macromolecules[43,44,45] and metal ions[46,47]. Using AFM, kinetic measurements of surface reactivity, at low supersaturations, where crystal surface growth kinetics, rather than particulate precipitation rates, have been deduced[41,42]. Growth rates of calcite, normal to the (104) surface, based on step velocity and slope measurements of the steps of growth hillocks, have been measured to be between 10^{-13} and 10^{-11} m s^{-1} [41].

In this chapter, a combined AFM-inverted optical microscope was used to observe the individual spiral growth hillock on the calcite (104) microcrystal surface, and elucidate the mechanisms of growth at varying solution supersaturations. The relationship between these solution supersaturations and the rate of growth normal to the (104) surface has also been quantified.

7.2 Experimental methods

Calcite microcrystals were grown using the Kitano method, onto borosilicate glass discs, as described in detail in Chapter 2. The microcrystals deposited from the growth solution were typically 5-20 microns across and consisted of all three polymorphs of calcium carbonate; calcite, aragonite and vaterite.

Imaging of the surfaces of calcite crystals was carried out by attaching the glass discs onto which crystals had been grown into the recess of the AFM sample plate using double-sided tape. It was then possible to manoeuvre the sample into close proximity of the tip using the screw controlled legs of the AFM. As it was necessary to locate the AFM tip on the top surface of a microcrystal, this was achieved by direct observation

with the optical microscope. By observing the morphology of the crystal with optical microscopy, it was also possible to determine the crystallographic orientation of the surface under investigation. Once the tip was engaged on the crystal surface, an initial scan was obtained over an area much smaller than the microcrystal surface. After an initial preview, the scan area was increased and re-centred until observation using the inverted microscope indicated that the region of the AFM image contained the maximum area, without any risk of the tip moving off the top surface of the crystal.

Microcrystals were imaged both in air, to determine the surface morphology of crystals at the end of the Kitano process, and subsequently under solution. In the latter case, the tip was withdrawn a short distance (< 10 μm) from the surface of the sample (after halting imaging) and the solution introduced through a length of fine PTFE tubing using a 1 cm^3 syringe, avoiding dislodging any crystals from the glass surface. The tip was then re-engaged on the surface of the microcrystal, which was imaged immediately. This procedure did not result in any noticeable offset in the imaging position. Imaging under solution was typically performed at line scan rates of 3-6 Hz, which, although compromising resolution a little, allowed fast growth and dissolution processes to be observed. In air, due to the static nature of the crystal surface, imaging was typically performed at a much slower speed of 1 Hz. Scanning was performed in one direction only (left to right, down only). Supersaturated solutions of calcium carbonate (S = 1.54, 1.81, 2.64 and 3.27) at constant ionic strength and pH were prepared as described in Chapter 2 and injected into the fluid cell. Solution was flowed through the cell regularly to maintain a constant supersaturation at the crystal/solution interface. During imaging, the temperature of the solution was measured to be 26 ± 0.5 °C.

In order to determine growth rates normal to the surface of interest, access to the *z* piezo voltage from the AFM, in order to record accurate height images whilst scanning was in progress, was needed. This was achieved via the use of a 'break-out' box, built in-house. The *z* voltage obtained was fed back into the AFM software via the AUX IN port on the controller. When the raw data was obtained, the *z* values were 1/20 of the actual values (due to the use of a 20:1 attenuator), and the voltages could be converted into height data using the calibrated *z* in Å/V data. Calibration was performed by scanning over a grid, with a known height in the *z* direction of 180 nm. This allowed the relationship between the *z* voltage obtained and the known height to be calculated. Figure 7-1 shows a diagram showing the break-out box in relation to the AFM controller.

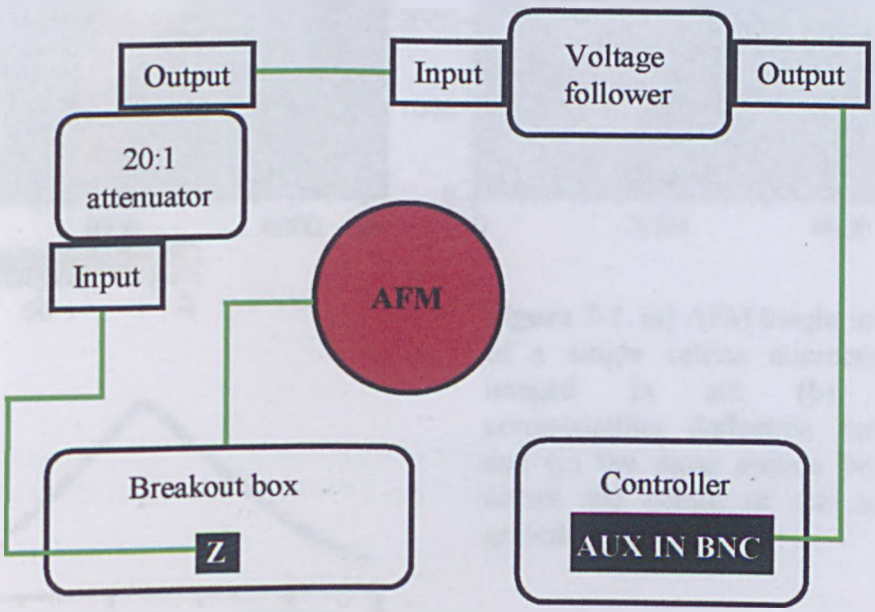

Figure 7-1: Schematic to show how the breakout box is used in conjunction with the AFM.

7.3 Calcite (104) microcrystal surfaces in air

Figure 7-2 shows a typical height and deflection AFM image of the surface of a calcite microcrystal, recorded in air with a scan size of 5 μm x 5 μm. The height image, (a), shows the topography of the microcrystal surface, whereas the deflection image, (b), which is a measure of the change in cantilever deflection, emphasises sharp features such as step edges clearly. It can be seen that the crystal surface exhibits a single spiral growth hillock, diagnostic of growth occurring at an individual screw dislocation via the Burton, Cabrera and Frank type mechanism[48].

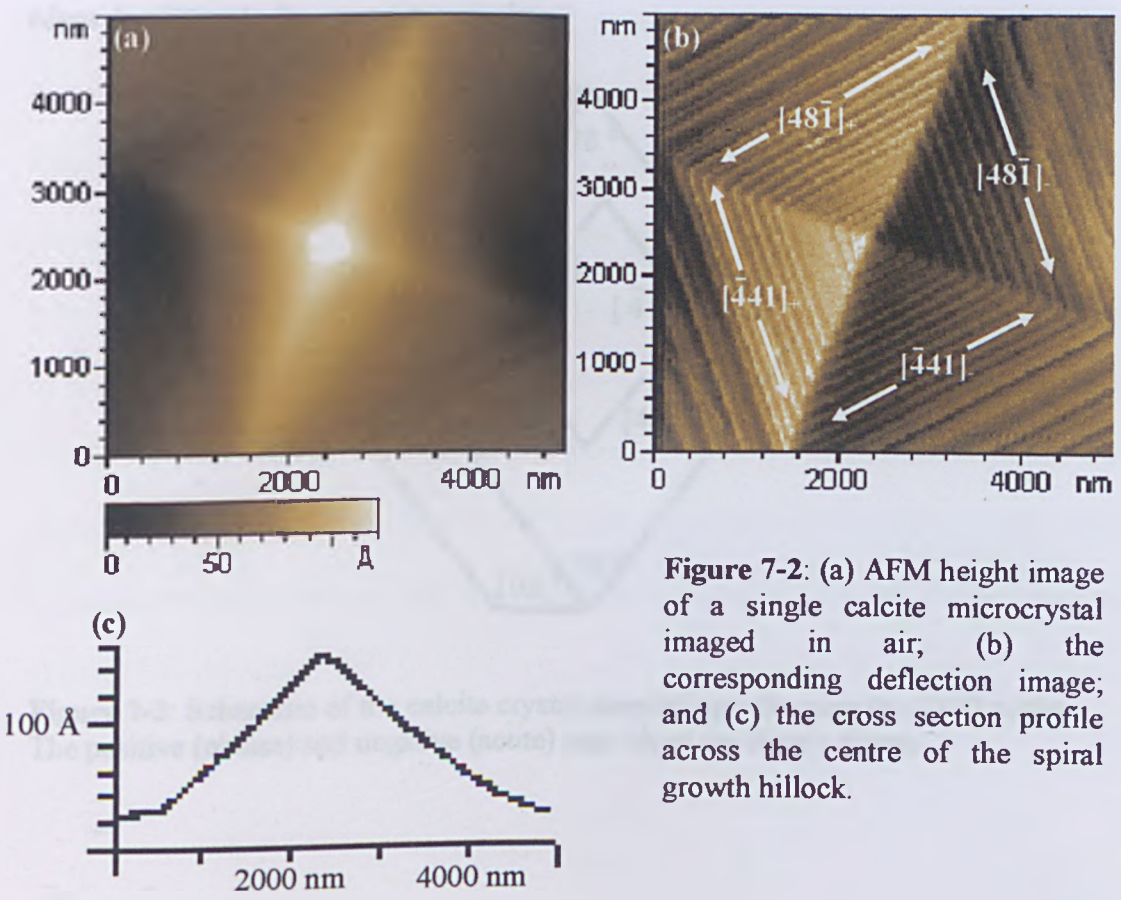

Figure 7-2: (a) AFM height image of a single calcite microcrystal imaged in air; (b) the corresponding deflection image; and (c) the cross section profile across the centre of the spiral growth hillock.

The observation of a single growth spiral was common to all the rhombohedral calcite microcrystals imaged throughout this chapter. These spiral growth hillocks displayed step spacings in the order of 50 to 150 nm, with step heights of ca. 0.3 nm, as expected for the (104) surface of calcite[49]. These measurements were made from line profiles, such as that shown in Figure 7-2 (c), where the step spacing is 125 nm. Figure 7-2 (b) also shows the assignment of the steps on the crystal surface, which were readily deduced from the underlying crystal morphology. Figure 7-3 shows a schematic of the calcite (104) surface, clearly detailing the assignment of the obtuse (+) and acute (-) step edges in relation to the crystal morphology.

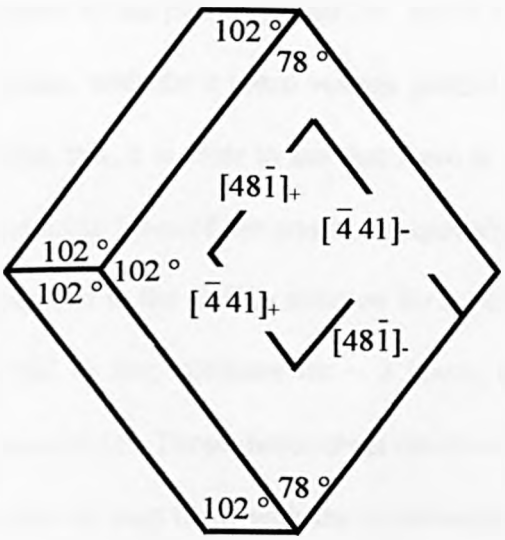

Figure 7-3: Schematic of the calcite crystal morphology showing the (104) surface. The positive (obtuse) and negative (acute) step edges are clearly shown.

7.4 Calcite (104) growth mechanisms under solution

After imaging in air, to ascertain the quality of the growth spiral, crystal surfaces were subsequently imaged under solution, at four supersaturations: 1.54, 1.81, 2.64 and 3.27.

7.4.1 Growth at $S = 1.54$

Figure 7-4 shows deflection AFM images of the (104) calcite surface when exposed to a calcium carbonate solution of supersaturation 1.54. Cross sectional analysis of the images shows that the hillock was growing under these saturations, via layer growth. This is confirmed by the plot in Figure 7-5, which shows a cross section of the hillock during these scans, with the *z* piezo voltage plotted against the distance across the crystal surface. From this, it is clear to see that there is no difference in the growth rates on the obtuse and acute faces of the crystal. Images shown in Figure 7-4 correlate to the crystal being exposed to the $CaCO_3$ solution for a period up to 13 minutes. This pattern of behaviour did in fact, continue for ~ 2 hours, until the experiments were stopped due to time constraints. These direct observations at low supersaturation show that calcite growth occurs by step flow, with the advancement of monomolecular steps, as described elsewhere[41,42,50].

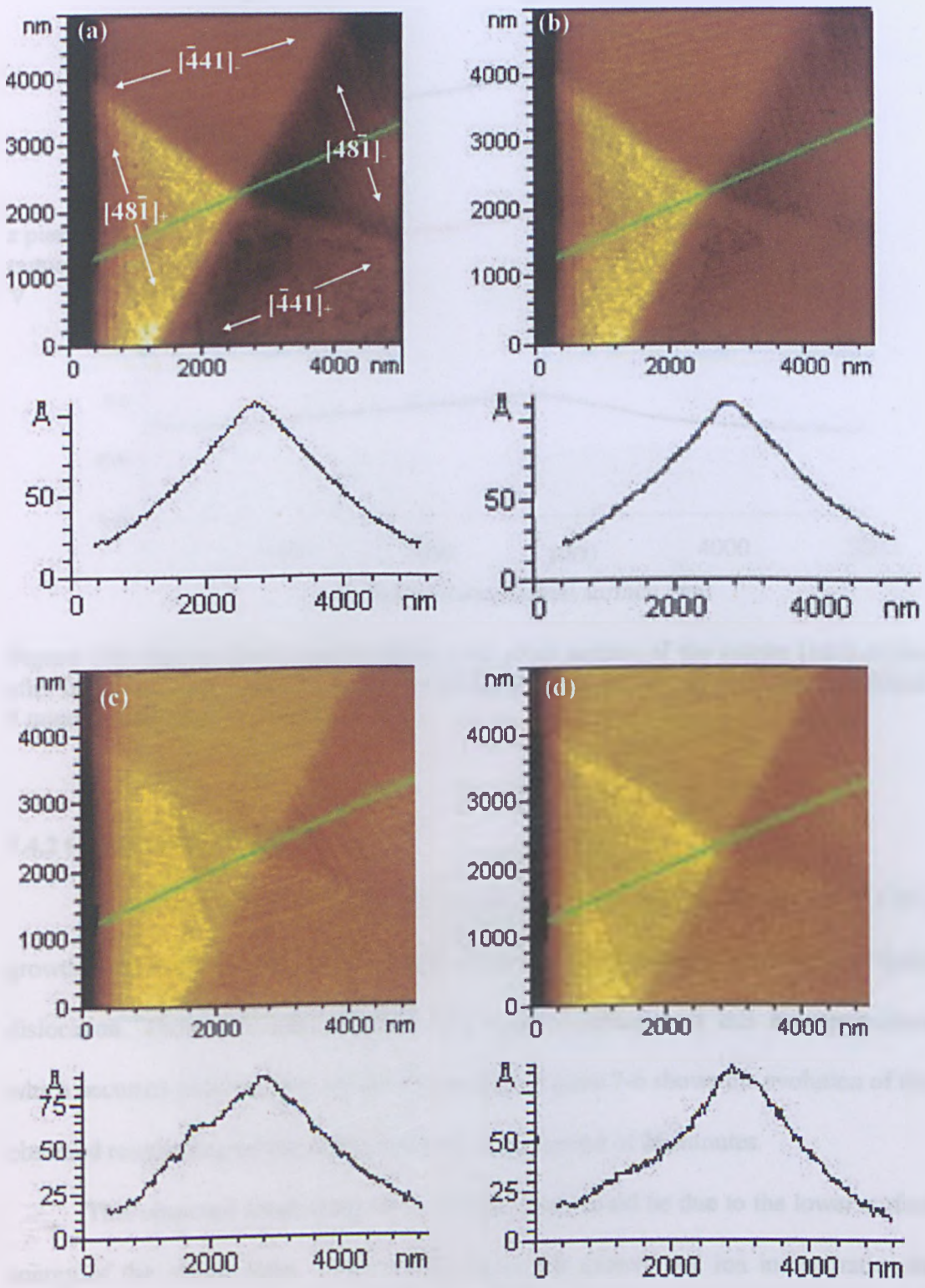

Figure 7-4: Deflection AFM images of growth hillock on the calcite (104) surface under a $CaCO_3$ solution (S = 1.54) after: (a) 2 minutes; (b) 5 minutes; (c) 10 minutes; and (d) 13 minutes.

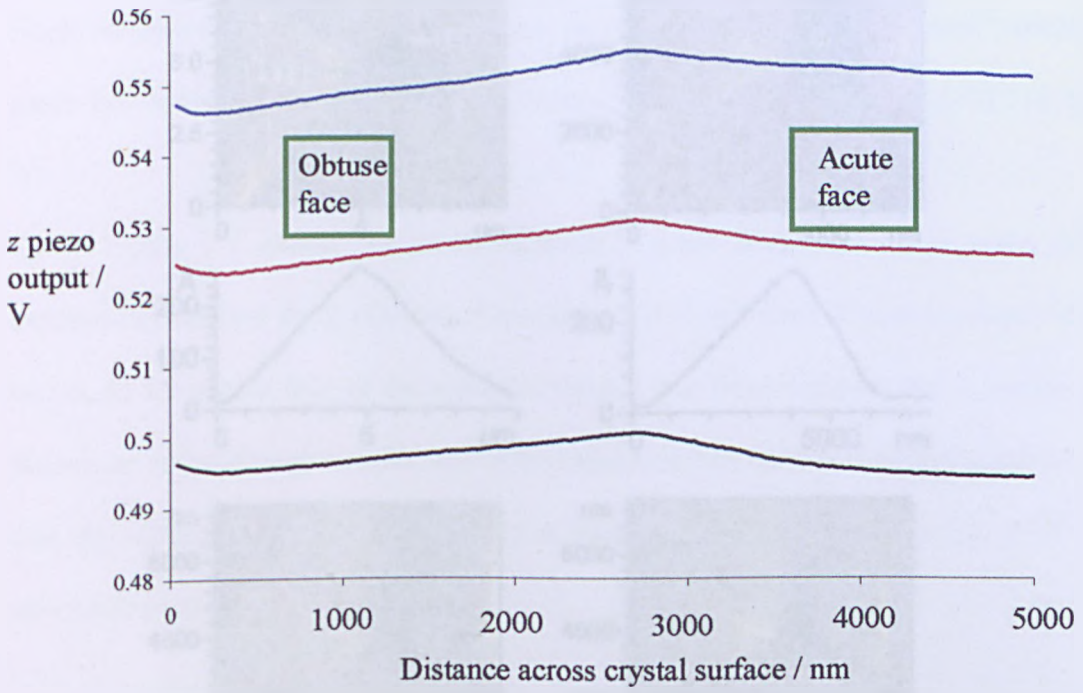

Figure 7-5: Plot to show *z* piezo output over cross section of the calcite (104) surface, after being exposed to a supersaturated $CaCO_3$ solution (S = 1.54) for 2 minutes (black), 5 minutes (red) and 10 minutes (blue).

7.4.2 Growth at $S = 1.81$

When the crystal was exposed to a solution of higher supersaturation ($S = 1.81$), growth continued by the advancement of monomolecular layers from the spiral dislocation. There was also evidence of surface roughening at this supersaturation, which occurred preferentially on the obtuse faces. Figure 7-6 shows the evolution of this observed roughening on the crystal surface, over a period of 26 minutes.

This observed roughening on the obtuse faces could be due to the lower surface energy of the obtuse steps, which would mean that growth and ion incorporation on these faces would occur preferentially to the acute faces, which are of higher energy[51].

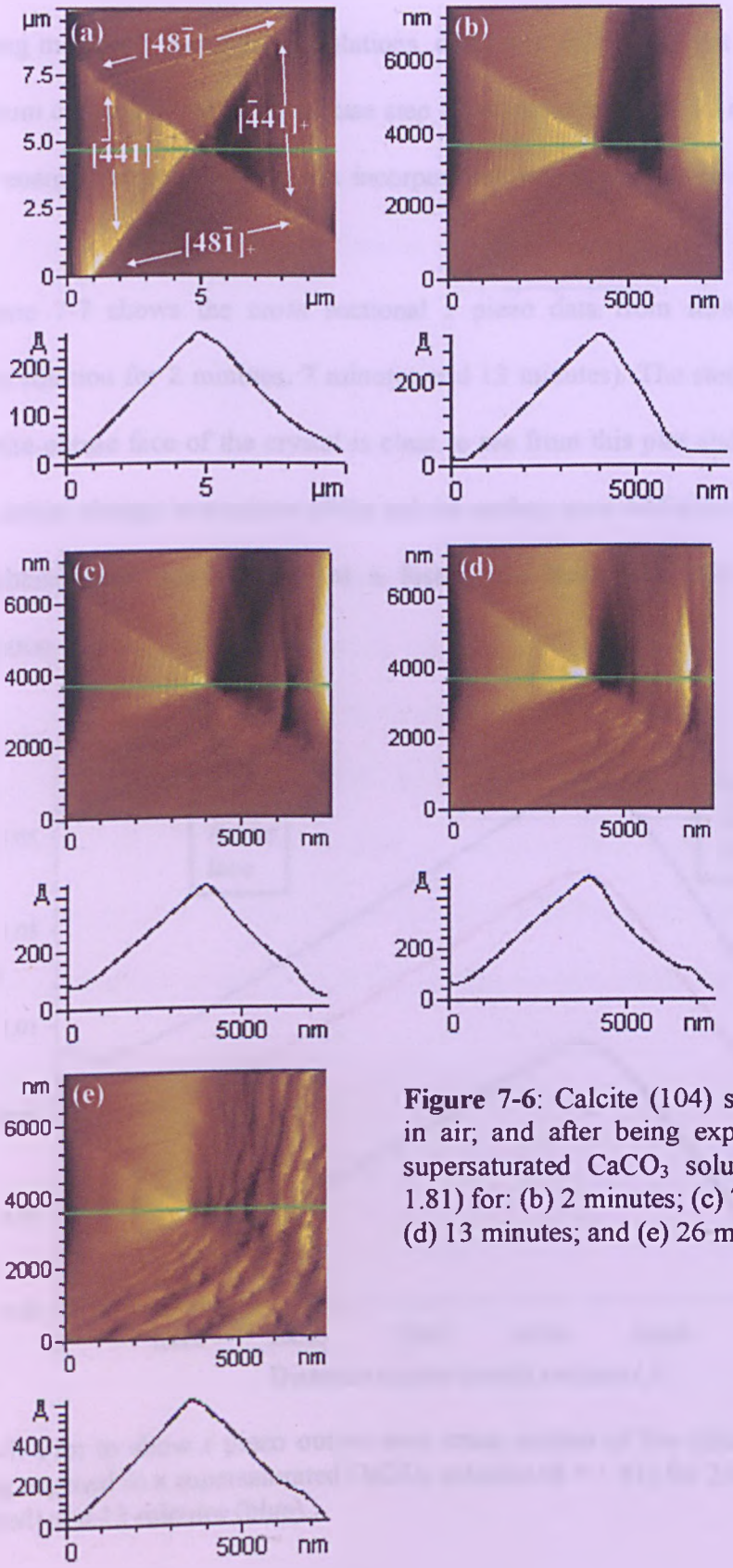

Figure 7-6: Calcite (104) surface (a) in air; and after being exposed to a supersaturated $CaCO_3$ solution (S = 1.81) for: (b) 2 minutes; (c) 7 minutes; (d) 13 minutes; and (e) 26 minutes.

Using molecular dynamics simulations, de Leeuw calculated that to introduce a single calcium carbonate unit at the obtuse step edge would take +82 kJ mol^{-1}, which is much less energetically expensive than incorporation at the acute edge (+123 kJ mol^{-1})[52].

Figure 7-7 shows the cross sectional *z* piezo data from three scans (after exposure to solution for 2 minutes, 7 minutes and 13 minutes). The steep slope which occurs on the obtuse face of the crystal is clear to see from this plot and indicates that there is an initial change in structure of the calcite surface upon addition of solution and that the obtuse faces are growing at a faster rate than the acute faces at this supersaturation.

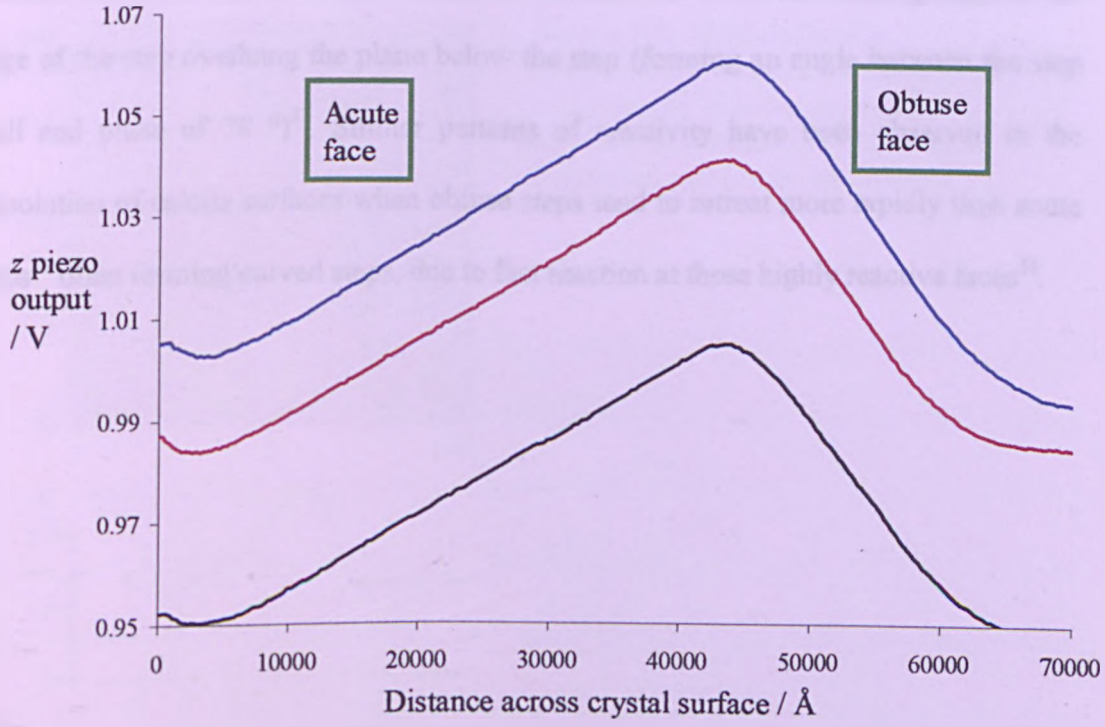

Figure 7-7: Plot to show *z* piezo output over cross section of the calcite (104) surface, after being exposed to a supersaturated $CaCO_3$ solution (S = 1.81) for 2 minutes (black), 7 minutes (red) and 13 minutes (blue).

7.4.3 Growth at $S = 3.27$

At a higher solution supersaturation of 3.27, the growth resulted in the formation of an oval hillock, in stark contrast to the normal rhombic shape. This can be seen from the data in Figure 7-8 which show deflection images of the calcite surface under the highly supersaturated conditions. The output from the *z* piezo, for three scans, has been overlaid and shown in Figure 7-9, which shows the different profiles of the acute and obtuse faces clearly. This change in shape occurs preferentially at the obtuse/obtuse (+/+) corner. As shown in Figure 7-3, the +/+ corner is the most exposed of the corners. The carbonate groups on the step form an angle of 102 ° between the step wall and the (104) plane. At high supersaturations, it appears that ions become preferentially incorporated here than at the acute/acute (-/-) corner where the carbonate groups on the edge of the step overhang the plane below the step (forming an angle between the step wall and plane of 78 °)[52]. Similar patterns of reactivity have been observed in the dissolution of calcite surfaces when obtuse steps tend to retreat more rapidly than acute steps[53] often forming curved steps, due to fast reaction at these highly reactive faces[54].

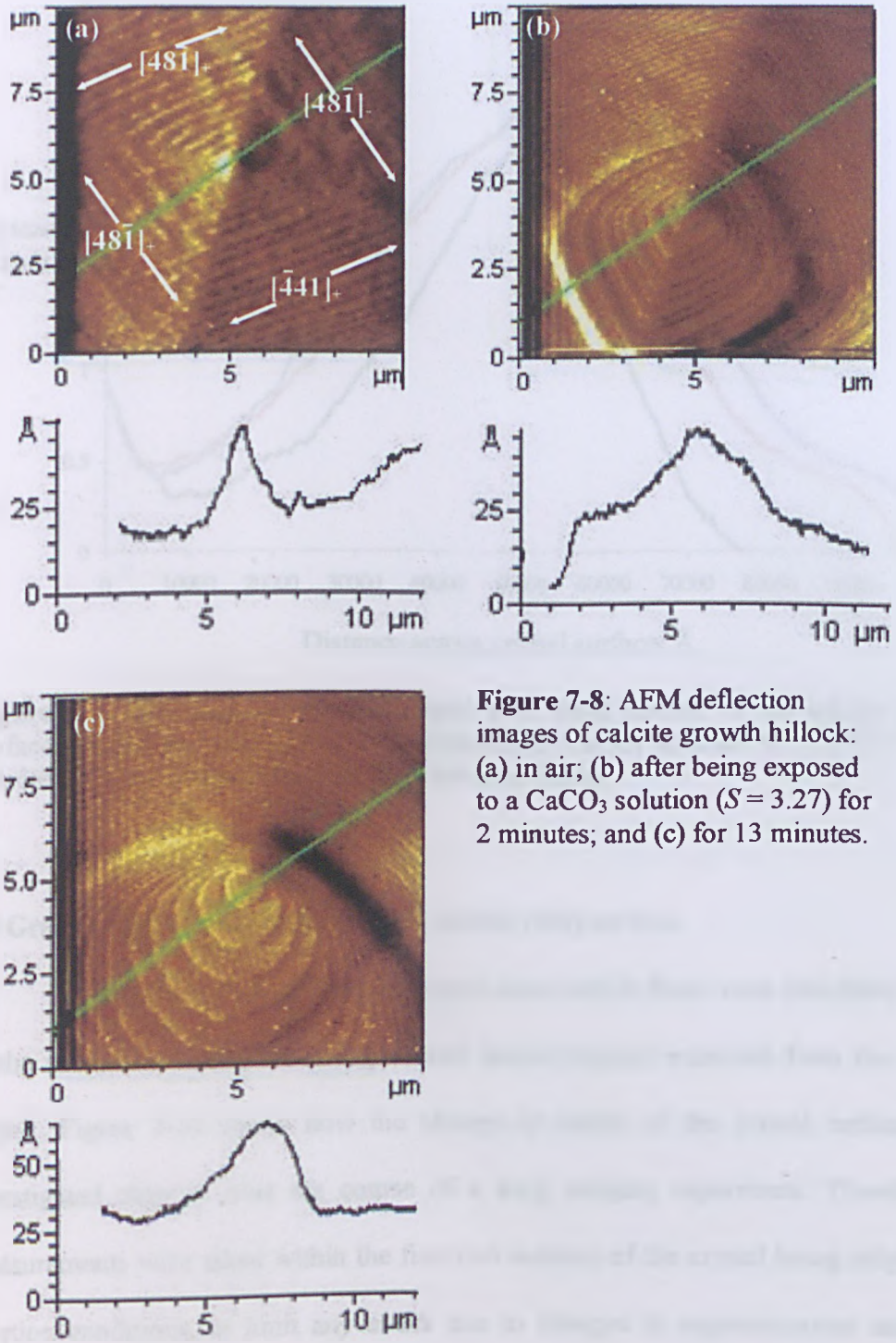

Figure 7-8: AFM deflection images of calcite growth hillock: (a) in air; (b) after being exposed to a $CaCO_3$ solution ($S = 3.27$) for 2 minutes; and (c) for 13 minutes.

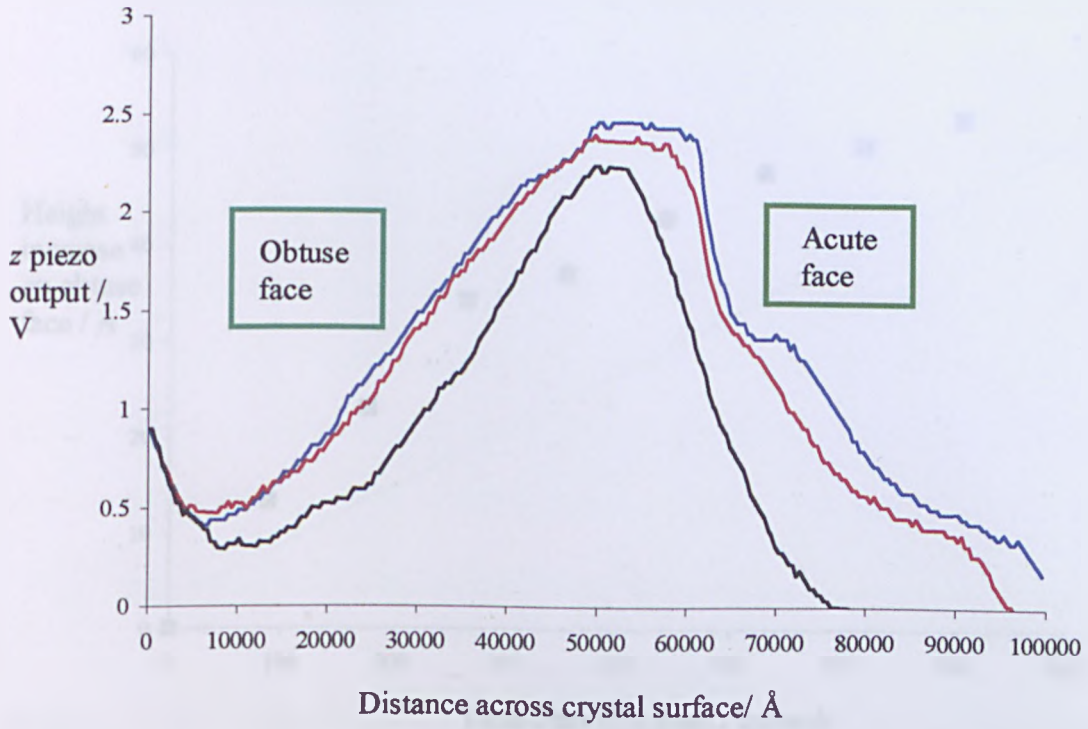

Figure 7-9: Plot to show *z* piezo output over cross section of the calcite (104) surface, after being exposed to a supersaturated $CaCO_3$ solution (S = 3.27) for 2 minutes (black), 7 minutes (red) and 13 minutes (blue).

7.5 Growth rate measurements on the calcite (104) surface

Initial growth rates of the obtuse and acute calcite faces were calculated normal to the (104) face using the voltages (and hence heights) extracted from the *z* piezo output. Figure 7-10 shows how the change in height of the crystal surface being investigated changes over the course of a long imaging experiment. Therefore, all measurements were taken within the first two minutes of the crystal being subjected to solution conditions, to limit any errors due to changes in supersaturation caused by slight changes in temperature in the environment, and to focus on the reactivity of the initially imaged surface.

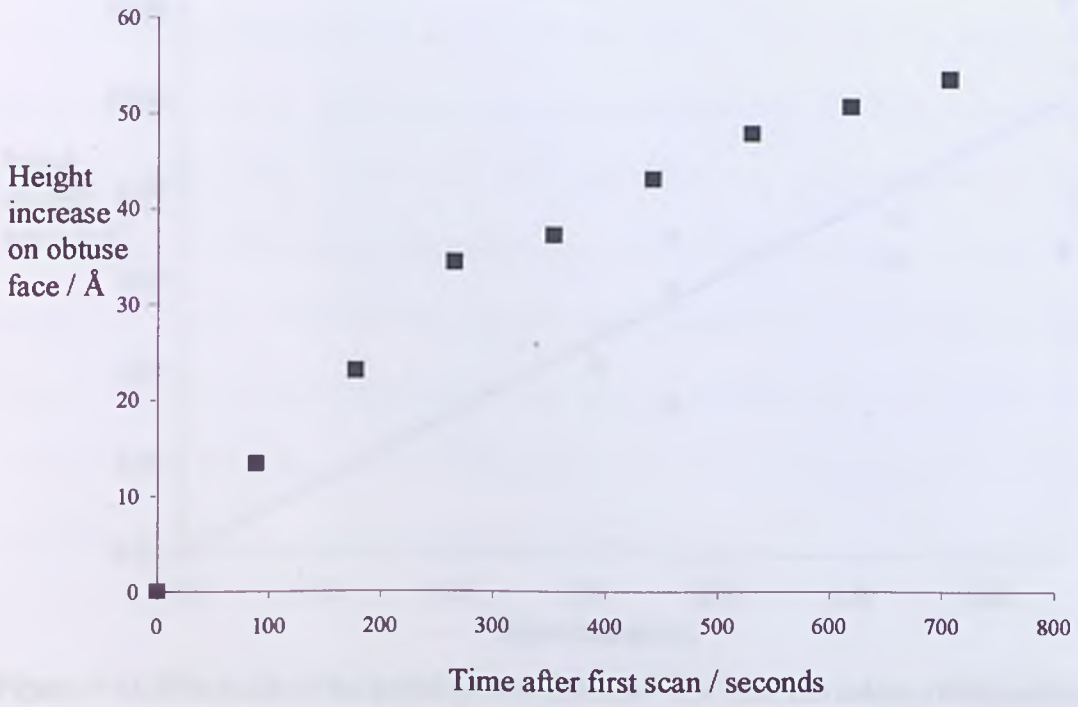

Figure 7-10: Plot to show change in measured height (±3 Å) with time, of the obtuse face of (104) calcite microcrystal surface, subjected to a $CaCO_3$ solution of $S = 1.54$.

Results showed a linear dependence of growth rate with solution supersaturation, as shown in Figure 7-11.

Although there were evidently differences in the reactivity patterns between obtuse and acute faces at the high supersaturations, no significant differences were found between initial growth rates on the obtuse and acute calcite faces, normal to the crystal surface.

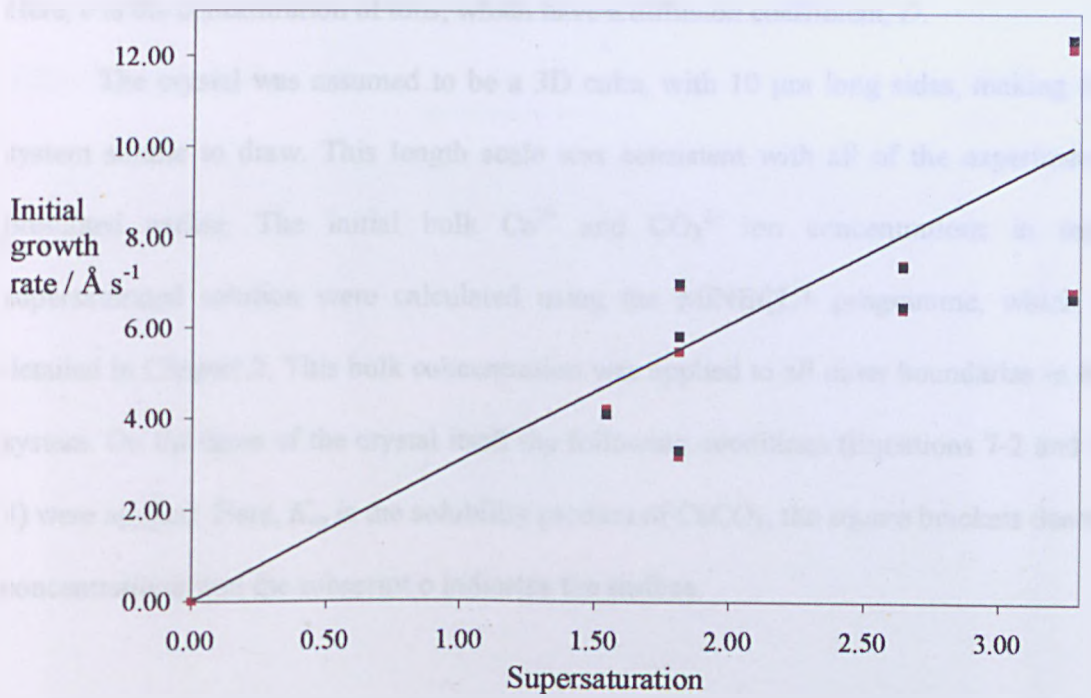

Figure 7-11: Plot to show the initial growth rates (±1 Å s^{-1}) for the calcite (104) surface as a function of supersaturation. **Key-** red: obtuse rates, black: acute rates.

7.6 FEMLAB® diffusion model

The linear dependence of growth rate on supersaturation could be due to a diffusion-controlled process, a reaction controlled by a first-order surface process, or a mixture of the two. The finite element software was used to model diffusion of Ca^{2+} and CO_3^{2-} ions to the surface of the crystal and extract diffusion-controlled growth rates. The method solves differential equations by approximating continuous quantities at discrete points in a mesh system. In this case the following steady state diffusion equation, derived from Fick's second law, in Cartesian coordinates (x, y, z), was solved (Equation 7-1).

$$0 = D\left(\frac{\partial^2 c}{\partial x^2} + \frac{\partial^2 c}{\partial y^2} + \frac{\partial^2 c}{\partial z^2}\right) \quad (7\text{-}1)$$

Here, c is the concentration of ions, which have a diffusion coefficient, D.

The crystal was assumed to be a 3D cube, with 10 μm long sides, making the system simple to draw. This length scale was consistent with all of the experiments presented earlier. The initial bulk Ca^{2+} and CO_3^{2-} ion concentrations in each supersaturated solution were calculated using the MINEQL+ programme, which is detailed in Chapter 2. This bulk concentration was applied to all outer boundaries in the system. On the faces of the crystal itself the following conditions (Equations 7-2 and 7-3) were applied. Here, K_{sp} is the solubility product of $CaCO_3$, the square brackets denote concentrations, and the subscript o indicates the surface.

$$[Ca^{2+}]_o = K_{sp} / [CO_3^{2-}]_o \quad (7\text{-}2)$$

$$[CO_3^{2-}]_o = K_{sp} / [Ca^{2+}]_o \quad (7\text{-}3)$$

The diffusion coefficient used by the program was input as 9.035×10^{-6} cm^2 s^{-1}, adjusted to take the slightly elevated temperature into account (see Section 7.2).

The Ca^{2+} and CO_3^{2-} ion concentrations around the crystal surface were thus simulated at all experimental supersaturations, as was the flux of ions to the crystal surface. When all surfaces of the crystal were designated as active, the flux obtained was only slightly higher than when only the top surface was investigated. Therefore, all data was obtained from the one top surface of the crystal only, ignoring the influence of the other reacting faces. Figure 7-12 shows the plots obtained, which show how the ion concentrations increase as a function of distance, away from the crystal surfaces. This

allowed the growth rate of the crystal face to be calculated, as an estimation of diffusion- controlled growth.

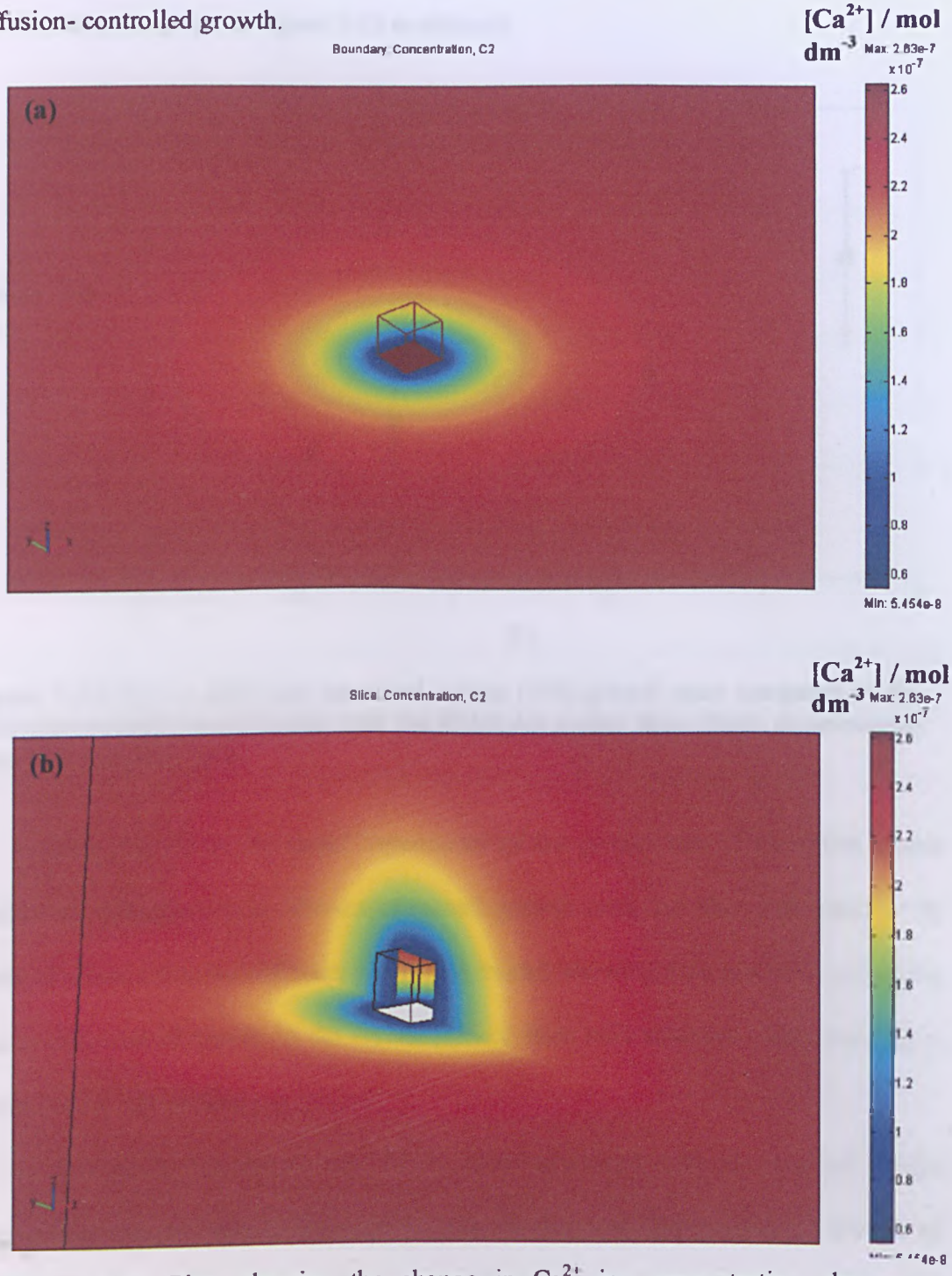

Figure 7-12: Plots showing the change in Ca^{2+} ion concentration, due to diffusion, as modelled using FEMLAB: (a) around the horizontal crystal faces; and (b) around the vertical crystal faces.

If the diffusion-controlled rates are plotted on the same axis as the experimental growth rates, the graph in Figure 7-13 is obtained.

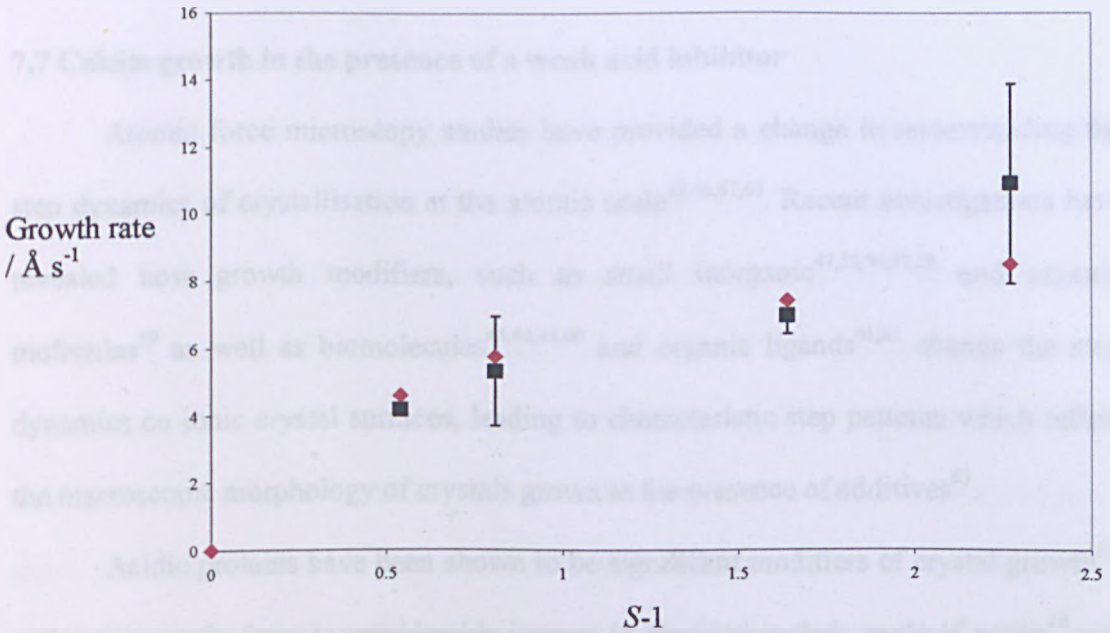

Figure 7-13: Plot to show the measured calcite (104) growth rates compared to the diffusion-controlled growth rates from the FEMLAB model. **Key**- black: experimental rates, red: modelled rates.

This plot shows the linear dependence of the growth rate of the (104) calcite surface on supersaturation. The experimental growth rates are also well matched to those obtained from the diffusion-controlled model, showing that growth is occurring due to diffusion of species to the crystal surface from bulk solution, rather than being controlled by any surface mechanisms.

This study has shown that AFM, when combined with an inverted optical microscope, can be used to measure growth mechanisms and kinetics of growth of single crystal surfaces. The calcite crystals investigated here exhibit only one spiral dislocation on the (104) surface and so any reactions which may occur between

neighbouring dislocation sites on macro-crystal surfaces are eliminated from the investigations.

7.7 Calcite growth in the presence of a weak acid inhibitor

Atomic force microscopy studies have provided a change in understanding the step dynamics of crystallisation at the atomic scale[42,46,67,68]. Recent investigations have revealed how growth modifiers, such as small inorganic[47,55,56,57,58] and organic molecules[59] as well as biomolecules[43,44,45,60] and organic ligands[61,62] change the step dynamics on ionic crystal surfaces, leading to characteristic step patterns which reflect the macroscopic morphology of crystals grown in the presence of additives[63].

Acidic proteins have been shown to be significant modifiers of crystal growth[64], and consequently there is considerable interest in elucidating their mode of action[65] and that of simpler, small weak acid analogues[60] on both crystallisation[60,66] and dissolution[67,68,69,70]. Calcite growth rates have been shown to decrease upon the addition of weak acids[71], including calcium complexing substances such as citric and pyromellitic acids which have been found to retard calcite growth rates[72] and it has been found that polycarboxylic acids inhibit growth, even at low concentration, which has been attributed to the blocking of crystal growth sites[73,74]. The stereochemical orientation of the additive molecule has been shown to play an important part in its inhibitory role[75] but the mechanisms of action are not clearly established[63].

The aim of this part of Chapter 7 is to show that the simple dicarboxylic acid, maleic acid, has a dual action on calcite crystals under growth conditions: (i) serving as a source of protons at low driving force, promoting nano-pitting; and (ii) adsorbing at

specific sites and pinning growth in the acute crystallographic directions, at higher driving force.

7.7.1 Experimental details

A 125 μm diameter iridium/iridium oxide microelectrode was used to monitor the change in pH of the Kitano/maleic acid solution near the glass surface. The pH electrode was calibrated by measuring the potential versus a saturated calomel electrode (SCE) as a function of pH during an acid-base titration. The response was Nernstian over a wide pH range (0-12). To measure the change in pH during the Kitano/maleic acid growth experiment, the electrode was held 5 μm above the glass surface, using a *z*-piezo positioner, and the pH measured over a period of 3 hours.

7.7.2 Results

To investigate dynamic processes on the (104) surface, we employed the well-established Kitano method[76]. It has been established that calcite microcrystals formed in this way are oriented on the basal (104) surface with the exposed microcrystal surface comprising a single spiral growth hillock[77], thus providing an ideal template on which to study subsequent reactivity.

To investigate dynamic processes on the growing (104) surface, the Kitano method was once again employed[73,76]. This involved adding a solution saturated with respect to calcite and CO_2 (1 atm), and containing 3 mM maleic acid, to the AFM cell and allowing CO_2 to evolve. Calcite growth under high CO_2 concentrations is particularly relevant to karstification processes[78,79,80], while understanding the Kitano

process is itself of fundamental interest[76,77]. As CO_2 evolves from the solution, the pH rises and the supersaturation increases. This process begins at the solution/air interface and propagates to the calcite crystal surface, so that the calcite crystal sees an essentially saturated solution for a relatively long period[77] before the supersaturation at the crystal/solution interface begins to gradually increase. This was confirmed by measurements with a pH microelectrode[81,82] (125 μm diameter), positioned in the vicinity of the reactive calcite surface, in which the pH was measured to be ~ 5.56 for a period of 20 minutes before gradually rising in a linear fashion at a rate of ~ 0.003 pH units per minute. This corresponded to an increase in supersaturation of 33 % over 180 minutes and provided an opportunity to investigate the influence of maleic acid on the crystal surface, first under saturated solution conditions and subsequently as a function of rising supersaturation.

Immediately after addition of a Kitano solution, containing 3mM maleic acid, the surface was found to have undergone rapid, extensive pitting (pit depths < 100 Å), as shown in Figure 7-14 (a), during the period required to obtain the first image (< 5 minutes). This is in striking contrast to the situation when a calcite microcrystal was exposed to a pure Kitano solution, where the surface structure remained static[77]. At the initial solution pH of 5.56, maleic acid (pK_1 = 1.83 and pK_2 = 6.07 at 25 °C)[67] is predominantly in the mono-protonated form with a small proportion of the dianion. Although the solution is saturated with respect to bulk calcite, the monoprotonated acid could serve as a source of protons[67] able to directly attack the surface, most likely at high energy sites (e.g. point defects[83]), leading to the nanopitting observed.

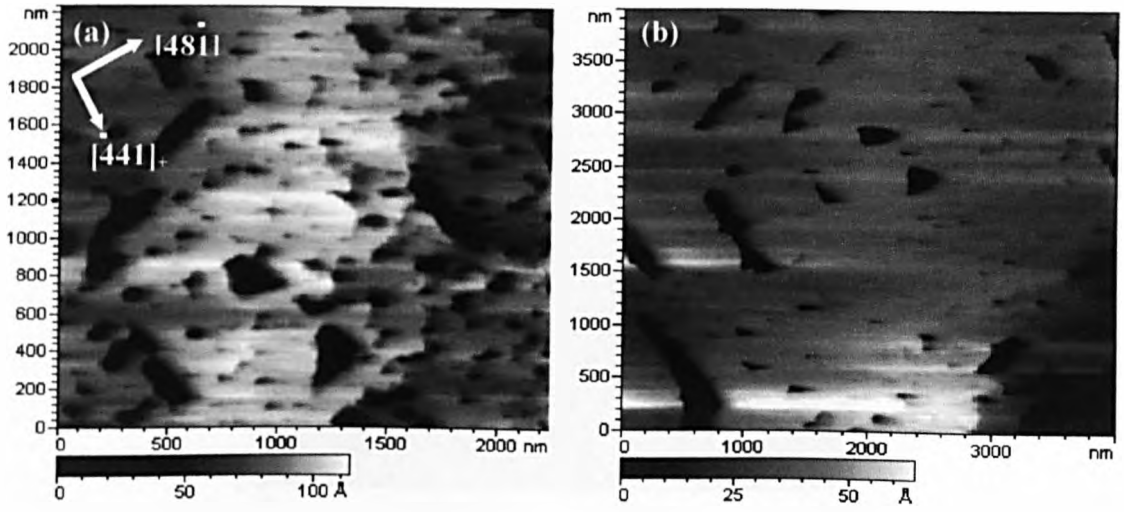

Figure 7-14: AFM images of calcite (104) surface after being exposed to a maleic acid containing Kitano solution for: (a) < 5 minutes; and (b) 100 minutes.

During the following 100 minutes, the increasing solution supersaturation led to replenishment of the surface pits, as shown in Figure 7-14 (b). As the supersaturation increased further with time, spiral growth became the dominant mechanism (Figure 7-15) but the growth hillock developed a distinct morphology, indicating that growth in the acute directions was retarded (step velocity ~ 6.6 nm s^{-1}) compared to the obtuse directions (step velocity ~ 10.6 nm s^{-1}). Step velocities were measured by disengaging the slow scan axis and sequentially recording line scans over the centre of the hillock.

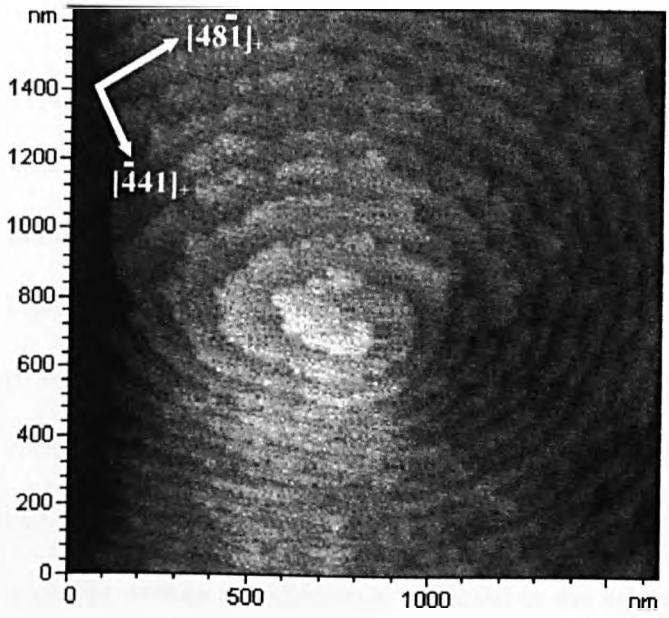

Figure 7-15: Deflection AFM image of the crystal surface after exposure to the solution for 180 minutes, showing the reformation of the spiral growth hillock. Distortion in the image is due to the rapid growth of the surface.

Due to the low local transport conditions associated with this system (i.e. there is no flow), there is a build up, over time, of maleate dianions at the crystal surface. It has been found that the adsorption of the $(O_2C(CH)_2CO_2)^{2-}$ ion by pairs of Ca^{2+} ions that bridge across the narrow angle of the $CaCO_3$ cell in the cleavage plane can occur. In the calcite cleavage plane, the kink sites that comprise either a $[\bar{4}41]_+$ ledge intersecting a $[48\bar{1}]_+$ ledge or a $[\bar{4}41]_-$ ledge intersecting a $[48\bar{1}]_-$ ledge have characteristic Ca^{2+} - Ca^{2+} (or CO_3^{2-} - CO_3^{2-}) separations of 4.99 Å, whereas the kink sites comprising a $[\bar{4}41]_-$ ledge intersecting a $[48\bar{1}]_+$ ledge (or a $[\bar{4}41]_+$ ledge intersecting a $[48\bar{1}]_-$ ledge) has surface ion separations of 4.04 Å (Figure 7-16). The smaller inter-ion separation in the latter cases corresponds well to the distance between the carboxylate groups in the maleate dianion (~ 4 Å) (Figure 7-16) which is a potent inhibitor of calcite growth and dissolution[67]. The match between the carboxylate group separation and the Ca^{2+} - Ca^{2+}

separation in the $[\bar{4}41]_-/[48\bar{1}]_+$ and $[\bar{4}41]_+/[48\bar{1}]_-$ kinks explains why crystal growth is pinned preferentially in the acute directions.

The nanoscale observation of the spiral morphology in the presence of maleic acid are consistent with macroscale measurements of crystal dissolution[67,68] and growth[73] where either macropits (tens of microns in size) or crystals with a similar morphology to the hillock in Figure 7-15 have been observed. Thus, the characteristic step patterns that result from specific molecular scale interactions between the maleate dianion and the calcite surface are ultimately reflected in the macroscale morphology of calcite crystals. Significantly, this work has shown that even under bulk saturated solution conditions, maleic acid (predominantly in the monoprotonated form), reacts with calcite causing extensive nano-pitting on the (104) surface. This hitherto unobserved action of a crystal growth modifier may be important for other weak acid additives.

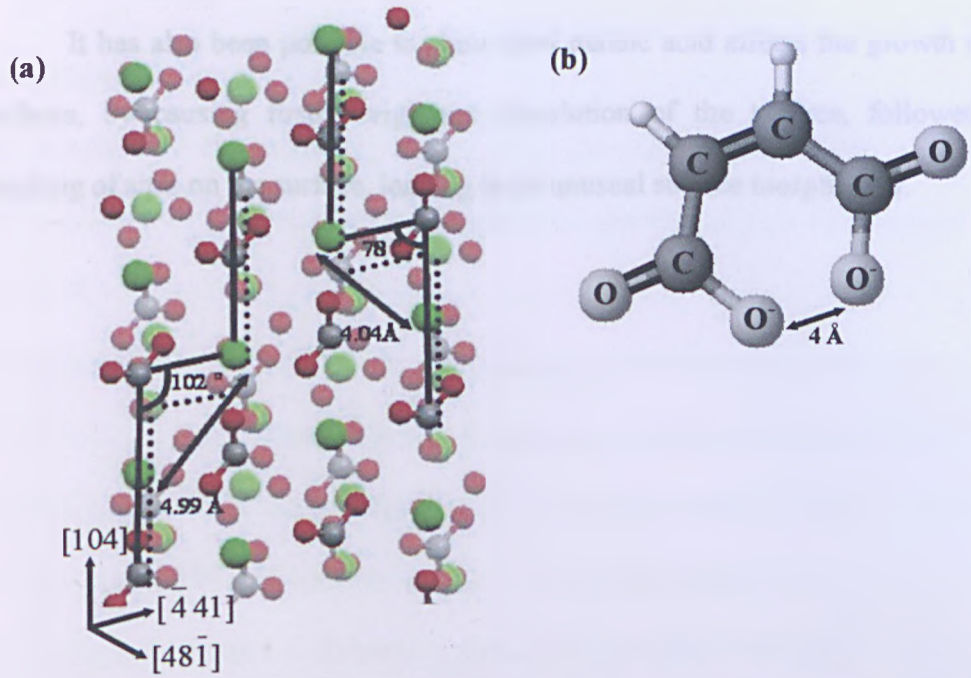

Figure 7-16: Schematic to show: (a) the Ca^{2+} - Ca^{2+} interatomic spacings in the two calcite kink sites (green: calcite, grey: carbon, red: oxygen); and (b) the structure of the maleate dianion.

7.8 Conclusions

Using this combined AFM-inverted optical microscopy technique it has been possible to image the spiral growth hillocks on the (104) calcite surface and deduce the growth mechanisms and rates of growth as a function of supersaturation. It has been found that growth occurs at low supersaturation via layer growth, from the screw dislocation, with roughening occuring at a certain supersaturation. Elucidation of the growth kinetics showed that initial growth rates of the hillock increase linearly with supersaturation, corresponding to diffusion-controlled growth, as confirmed by finite element modelling.

It has also been possible to show how maleic acid affects the growth of crystal surfaces, by causing firstly, vigorous dissolution of the surface, followed by the blocking of sites on the surface, leading to an unusual surface morphology.

7.9 References

[1] G. Binnig, C. F. Quate and Ch. Gerber, *Phys. Rev. Lett.*, **1986**, *56*, 930.

[2] Y. Liang, D. R. Baer, J. M. McCoy and J. P. Lafemina, *J. Vac. Sci. Technol. A*, **1996**, *14*, 1368.

[3] R. Shiraki, P. A. Rock and W. H. Casey, *Aquatic Geochemistry*, **2000**, *6*, 87.

[4] K. Onuma, A. Ito, T. Tateishi and T. Kameyama, *J. Cryst. Growth*, **1995**, *154*, 118.

[5] R. Price, G. R. Ester and P. J. Halfpenny, *Proc. R. Soc. Lond. A*, **1999**, *455*, 4117.

[6] G. R. Ester and P. J. Halfpenny, *J. Cryst. Growth*, **1998**, *187*, 111.

[7] K. Onuma, A. Ito and T. Tateishi, *J. Cryst. Growth*, **1996**, *167*, 773.

[8] P. E. Hillner, A. J. Gratz, S. Manne and P. K. Hansma, *Geology*, **1992**, *20*, 359.

[9] P. E. Hillner, S. Manne, A. J. Gratz and P. K. Hansma, *Ultramicroscopy*, **1992**, *42*, 1387.

[10] Y. Liang, D. R. Baer and A. S. Lea, *Mat. Res. Soc. Symp. Proc.*, **1995**, *355*, 409.

[11] G. R. Ester, R. Price and P. J. Halfpenny, *J. Cryst. Growth*, **1997**, *182*, 95.

[12] P. A. Campbell, G. R. Ester and P. J. Halfpenny, *J. Vac. Sci. Technol. B*, **1996**, *14*, 1373.

[13] C. E. Jones, P. R. Unwin and J. V. Macpherson, *ChemPhysChem*, **2003**, *4*, 139.

[14] P. M. Dove and F. M. Platt, *Chemical Geology*, **1996**, *127*, 331.

[15] P. R. Unwin and J. V. Macpherson, *Chem. Soc. Rev.*, **1995**, *24*, 109.

[16] J. V. Macpherson and P. R. Unwin, *Prog. React. Kinetics*, **1995**, *20*, 185.

[17] M. Plomp, J. G. Buijnsters, G. Bögels, W. J. P. van Enckevort and D. Bollen, *J. Cryst. Growth*, **2000**, *209*, 911.

[18] H. Kim, R. M. Garavito and R. Lal, *Colloids and Surfaces B: Biointerfaces*, **2000**, *19*, 347.

[19] A. A. Baker, W. Helbert, J. Sugiyama and M. J. Miles, *Applied Physics A: Materials Science and Processing*, **1998**, *A66*, S559.

[20] D. D. Archibald, B. P. Gaber, J. D. Hopwood, S. Mann and T. Boland, *J. Cryst. Growth*, **1997**, *172*, 231.

[21] M. M. Reddy *in Mineral Scale Formation and Inhibition*. Ed. Z. Amjad, Plenum Press, New York, **1995**.

[22] A. Gutjar, H. Dabringhaus and R. Lacmann, *J. Cryst. Growth*, **1996**, *158*, 296.

[23] L. D. Swinney, J. D. Stevens and R. W. Peters, *Ind. Eng. Chem. Fundam.*, **1982**, *21*, 31.

[24] R. G. Compton and P. R. Unwin, *Phil. Trans. R. Soc.*, **1990**, *330*, 1.

[25] L. D. Swinney, J. D. Stevens and R. W. Peters, *Ind. Eng. Chem. Fundam.*, **1982**, *21*, 31.

[26] C. A. Brown, R. G. Compton and C. A. Narramore, *J. Coll. Inter. Sci.*, **1993**, *160*, 372.

[27] R. Isopescu, M. Mocioi, F. Zahanagiu and L. Filipescu, *J. Cryst. Growth*, **1996**, *167*, 260.

[28] D. Verdoes, D. Kashchiev and G. M. van Rosmalen, *J. Cryst. Growth*, **1992**, *118*, 401.

[29] N. Spanos and P. G. Koutsoukos, *J. Phys. Chem. B*, **1998**, *102*, 6679.

[30] T. F. Kazmierczak, M. B. Tomson and G. H. Nancollas, *J. Phys. Chem.*, **1982**, *86*, 103.

[31] D. Kralj, L. Brečević and A. E. Nielsen, *J. Cryst. Growth*, **1990**, *104*, 793.

[32] M. M. Reddy and G. H. Nancollas, *J. Coll. Inter. Sci.*, **1971**, *36*, 166.

[33] G. H. Nancollas and M. M. Reddy, *J. Coll. Inter. Sci.*, **1971**, *37*, 824.

[34] G. E. Cassford, W. A. House and A. D. Pethybridge, *J. Chem. Soc., Faraday Trans. 1*, **1983**, *79*, 1617.

[35] R. Shiraki and S. L. Brantley, *Geochim. Cosmochim. Acta*, **1995**, *59*, 1457.

[36] W. A. House, *J. Chem. Soc., Faraday Trans. 1*, **1981**, *77*, 341.

[37] W. A. House and J. A. Tutton, *J. Cryst. Growth*, **1982**, *56*, 699.

[38] D. Buhmann and W. Dreybrodt, *Chem. Geol.*, **1985**, *48*, 189.

[39] J. Christoffersen and M. R. Christoffersen, *J. Cryst. Growth*, **1990**, *100*, 203.

[40] M. Reddy, L. N. Plummer and E. Busenberg, *Geochim. Cosmochim. Acta*, **1981**, *45*, 1281.

[41] H. H. Teng, P. M. Dove, and J. J. DeYoreo, *Geochim. Cosmochim. Acta*, **2000**, *64*, 2255.

[42] H. H. Teng, P. M. Dove and J. J. DeYoreo, *Geochim. Cosmochim. Acta*, **1999**, *63*, 2507.

[43] D. A. Walters, B. L. Smith, A. M. Belcher, G. T. Paloczi, G. D. Stucky, D. E. Morse and P. K. Hansma, *Biophysical Journal*, **1997**, *72*, 1425.

[44] B. L. Smith, G. T. Paloczi, P. K. Hansma and R. P. Levine, *J. Cryst. Growth*, **2000**, *211*, 116.

[45] H. H. Teng and P. M. Dove, *American Mineral.*, **1997**, *82*, 878.

[46] K. J. Davis, P. M. Dove and J. J. DeYoreo, *Science*, **2000**, *290*, 1134.

[47] J. M. Astilleros, C. M. Pina, L. Fernandez-Diaz and A. Putnis, *Geochim. Cosmochim. Acta.*, **2000**, *64*, 2965.

[48] W. K. Burton, N. Cabrera and F. C. Frank, *Philos. Trans. Roy. Soc., London*, **1951**, *A243*, 299.

[49] P. E. Hillner, S. Manne, P. K. Hansma and A. J. Gratz, *Faraday Discuss.*, **1993**, *95*, 191.

[50] A. J. Gratz, P. E. Hillner and P. K. Hansma, *Geochim. Cosmoch. Acta*, **1993**, *57*, 491.

[51] R. Kristensen, S. L. S. Stipp, K. Refson and P. Hedegård, *EGS-AGU-EUG Joint Assembly*, **2003**, 649.

[52] N. H. de Leeuw, *J. Phys. Chem. B*, **2002**, *106*, 5241.

[53] O. W. Duckworth, R. T. Cygan and S. T. Martin, *Langmuir*, **2004**, *20*, 2938.

[54] G. de Giudici, *Am. Mineral.*, **2002**, *87*, 1279.

[55] L. Pastero, E. Costa, M. Bruno, M. Rubbo, G. Sgualdino and D. Aquilano, *Crystal Growth and Design*, **2004**, *4*, 485.

[56] Y.-J. Han and J. Aizenberg, *J. Amer. Chem. Soc.*, **2003**, *125*, 4032.

[57] K. J. Davis, P. M. Dove, L. E. Wasylenki, and J. J. De Yoreo, *Am. Mineral.*, **2004**, *89*, 714.

[58] T. N. Thomas, T. A. Land, J. J. DeYoreo and W. H. Casey, *Langmuir*, **2004**, *20*, 7643.

[59] S. Guo, M. D. Ward and J. A. Wesson, *Langmuir*, **2002**, *18*, 4284.

[60] C. A. Orme, A. Noy, A. Wierzbicki, M. T. McBride, M. Grantham, H. H. Teng, P. M. Dove and J. J. DeYoreo, *Nature*, **2001**, *411*, 775.

[61] T. D. Perry, O. W. Duckworth, T. A. Kendall, S. C. Martin and R. Mitchell, *J. Amer. Chem. Soc.*, **2005**, *127*, 5744.

[62] B. L. Phillips, Y. J. Lee and R. J. Reeder, *Environ. Sci. and Technol.*, **2005**, *39*, 4533.

[63] J. J. DeYoreo and P. M. Dove, *Science*, **2004**, *306*, 1301.

[64] L. Addadi and S. Weiner, *Proc. Natl. Acad. Sci. U.S.A.*, **1985**, *82*, 4110.

[65] G. Fu, S. Valiyaveettil, B. Wopenka, and D. E. Morse, *Biomacromolecules* **2005**, *6*, 1289.

[66] S. Raz, S. Weiner and L. Addadi, *Adv. Mater.*, **2000**, *12*, 38.

[67] R. G. Compton, K. L. Pritchard, P. R. Unwin, G. Grigg, P. Silvester, M. Lees and W. A. House, *J. Chem. Soc. Faraday Trans.*, **1989**, *85*, 4335.

[68] P. R. Unwin and R. G. Compton, *J. Chem. Soc. Faraday Trans.*, **1990**, *86*, 1517.

[69] R. G. Compton and P. R. Unwin, *Phil. Trans. R. Soc.*, **1990**, *330*, 1.

[70] B. A. Coles, R. G. Compton, M. Suárez, J. Booth, Q. Hong and G. H. W. Sanders, *Langmuir*, **1998**, *14*, 218.

[71] N. Wada, K. Kanamura and T. Umegaki, *J. Coll. Inter. Sci.*, **2001**, *233*, 65.

[72] K-J. Westin and A. C. Rasmuson, *J. Coll. Inter. Sci.*, **2005**, *282*, 359.

[73] S. Mann, J. M. Didymus, N. P. Sanderson, B. R. Heywood and E. J. A. Samper, *J. Chem. Soc. Faraday Trans.*, **1990**, *86*, 1873.

[74] Q. Hong, M. F. Suarez, B. A. Coles and R. G. Compton, *J. Phys. Chem. B*, **1997**, *101*, 5557.

[75] M. M. Reddy and A. R. Hoch, *J. Coll. Inter. Sci.*, **2001**, *235*, 365.

[76] Y. Kitano, *Bull. Chem. Soc. Japan*, **1962**, *35*, 1980.

[77] P. S. Dobson, L. A. Bindley, J. V. Macpherson and P. R. Unwin, Langmuir, **2005**, *21*, 1255.

[78] D. Buhmann and W. Dreybodt, *Chem. Geol.*, **1985**, *48*, 189.

[79] W. Dreybodt, J. Lauckner, L. Zaihua, U. Svensson and D. Buhmann, *Geochim. Cosmochim. Acta*, **1996**, *60*, 3375.

[80] M. M. Reddy, L. N. Plummer and E. Busenberg, *Geochim. Cosmochim. Acta*, **1981**, *45*, 1281.

[81] L. D. Burke, J. K. Mulcahy and D. P. Whelan, *J. Electroanal.*, **1984**, *163*, 117.

[82] M. L. Hitchman and S. Ramanathan, *Analyst*, **1988**, *113*, 35.

[83] J. Schott, S. Brantley, D. Crerar, C. Guy, M. Borcsik and C. Willaime, *Geochim. Cosmochim. Acta*, **1989**, *53*, 373.

Chapter 8

Conclusions

This thesis has investigated the factors involved in the crystallisation, growth and dissolution of calcium carbonate crystals, at the micro and nanoscale. This work is important in many areas of industry[1,2], with the topics in this thesis being particularly relevant to the issue of household care. Due to the wide range of components of scale, which include calcium phosphates as well as calcium carbonate and various other minerals, the work presented in this thesis can mainly be viewed as purely a model for limescale. However, if the behaviour of one component of the mixture can be analysed fully and the methods of crystallisation, growth and dissolution of this can be observed and quantified, the path then becomes open for the investigation of other, more complicated components, which will hopefully lead to a better understanding of the full limescale system.

Crystallisation of calcium carbonate has been achieved using two techniques; the first involving the gradual increase in pH of a saturated calcium carbonate solution, via the evolution of CO_2. This leads to the formation of microcrystals at the air solution interface and is described fully by Kitano[3]. This crystallisation technique is widely used and results in the thermodynamically stable calcite crystals being formed in preference to the aragonite and vaterite polymorphs. To complement this process, a second crystallisation technique was also used which involved the controlled mixing of $CaCl_2$ and $NaHCO_3$ solutions via a dual-drive syringe pump, resulting in a supersaturated $CaCO_3$ solution which was then jetted onto the substrate surface via a specially designed cell. This method resulted in the kinetically controlled growth of calcium carbonate

crystals and allowed results from short time scale flow experiments to be compared to results from long time scale bulk solution situations (relevant in particular to toilet systems).

A significant proportion of this thesis has focussed on the effect of surface functionalisation on calcium carbonate crystal growth, using the two crystallisation methods previously described. Surface functionalisation is important in many areas of calcium carbonate crystal growth. In the area of household care it is important to understand the benefits and disadvantages of coating or pre-treating surfaces, with the view of inhibiting crystal growth or eliminating crystal nucleation. Functionalisation of surfaces is also important in such areas as orthopaedic implants, where it is necessary to facilitate the crystallisation of apatite containing compounds. This was the focus in Chapter 3 where a glass surface was functionalised by depositing mercaptoundecanoic acid-functionalised Au nanoclusters in a layer by layer method, using poly(allylamine) hydrochloride as a cross linker. This approach contrasts with other recent work involving functionalised nanoparticles where dense prints have been used as templates for calcium carbonate nucleation[4,5,6].

In the studies herein it was found that the functionalised nanoparticles served as templates for calcite crystallisation, with the extent of crystallisation increasing monotonically with nanoparticle surface coverage. Calcite was the predominant polymorph to be nucleated using both crystallisation techniques with evidence of Ostwald ripening occurring during the jet experiments. This was not the case with surfaces such as glass and gold. Using a high magnification optical microscope, it should be possible, and indeed very interesting, to extend this work further to confirm

the occurrence of this ripening effect by observing the transitions in situ. The effect of the growth solution supersaturation during such experiments was also investigated and the results were very clear, and as expected, with crystal growth becoming less frequent with decreasing supersaturation.

Additionally, a high proportion of the calcite crystals formed on these substrates were nucleated on the (015) plane rather than the more stable (104) plane, which shows that the nanoparticles display at least partial orientational control over the crystallisation. This is thought to be due to the fact that carbonate ions making an angle of ~ 36 ° with the (015) calcite face match with the carboxylate end groups on the functionalised nanoparticles, as described previously by Aizenberg who saw the same templating effect on carboxylic acid functionalised SAM surfaces[7].

Such functionalised films could be used as coatings in orthopaedic implants, as they are stable films which show the ability to template crystals with a specific morphology. Furthermore, although the work described in this thesis has focused on creating films of functionalised monolayers, it may be possible to create suspensions of such nanoclusters, which act as seeds for crystal growth. This would give the advantage of a high surface area from which crystal growth could occur, and may allow ready manipulation of the crystals formed.

Functionalisation via the deposition of SAMs on gold electrodes was achieved in Chapter 4 and the effects of altering the potential of electrodes functionalised with SAMs bearing hydroxyl, methyl and carboxylic acid functional groups on calcium carbonate crystallisation was investigated. Previous work in this area has looked into crystallisation of calcium carbonate on various SAM assemblies[8,9,10] but no one as yet

has performed investigations into the effects of changing the surface charge. It was shown that it is possible to achieve a 'tunable' surface, via the application of potential to a gold or SAM-coated gold surface, which dramatically changes the extent of calcium carbonate nucleation.

Using the jet crystallisation technique, application of a potential negative of the potential of zero charge to any of the SAM-functionalised surfaces led to the inhibition of calcium carbonate nucleation, irrespective of the functionality of the SAM. On more positively charge surfaces, extensive vaterite growth was evident. Again, as expected, the effect of the solution supersaturation was obvious – once the supersaturation was taken below ~20, crystallisation was reduced to a minimum, as shown in the nanoparticle experiments.

Results from the Kitano crystal growth experiments showed crystal nucleation occurring when both negative and positive potentials were applied. However, consistent with the syringe jet experiment, the surfaces displaying a negative potential compared to the estimated potential of zero charge induced less crystallisation, whereas a more positive surface potential resulted in the formation of a higher density of crystals. This result can be attributed to the concentration of positive and negative species in the solution, and their interaction with the surface. When the surface is positively charged, anions are attracted to the surface – in this case, the major anion is CO_3^{2-}. The subsequent dehydration of this ion is then possible, leading to the formation of calcium carbonate on the surface, at these anionic reaction sites.

These results should allow surfaces to be developed which can be altered so to control calcium carbonate crystallisation as and when necessary. By simply changing

the surface charge, the extent of crystallisation can be altered; a process which has possible uses in the water softening industry. By applying a small negative charge to pipelines, it may be now possible to inhibit calcium carbonate nucleation. Alternatively, by applying a more positive charge in one particular area of a water treatment plant, it will be possible to induce fast calcium carbonate crystallisation, resulting in a decrease in the supersaturation of the water with respect to calcium carbonate and hence a possible decrease in the occurrence of calcium carbonate crystallisation elsewhere in the system.

In Chapter 5, the effects of *E. coli* bacterial biofilms on crystal growth were investigated, the work impinging directly on the issue of household care. Previous work in this area has mainly focused on the fossilization of bacteria on a large scale, in caves and hot springs[11,12]. The work presented here is on a much smaller scale and is relevant to toilet systems in particular. It involved growing bacterial biofilms, of monolayer thickness, on glass substrates, which were subjected to the two crystallisation techniques. Bacterial biofilms were shown to dramatically effect the crystallisation of calcium carbonate, not only by acting as nucleation centres[13,14], but by disturbing the crystal structure and causing surface and structural damage in deposited calcite crystals. Using the fast, jet crystallisation method, the bacteria also acted as orientational templates, by directing calcite nucleation from the unusual (012) and (015) planes, as well as the stable (104) plane. Moreover, the presence of calcium carbonate crystals on the surface did not inhibit the deposition of a viable bacterial biofilm, with the crystals simply becoming coated in the film. Implications for household care situations are that if, via the pretreatment or functionalisation of the growth surface, the viability or extent

of any bacterial biofilm can be reduced, this in turn would minimise the extent of calcium carbonate crystallisation, and hence the scaling of the surface would decrease.

Another vast area of interest is the growth and dissolution of calcium carbonate at the microscale. If it is possible to understand the proton promoted dissolution of calcium carbonate on a micro scale, it should then be possible to compare dissolution rates calculated with bulk limescale dissolution rates and determine the actual mechanism of dissolution. In this thesis, by using an electrochemical technique, the localised dissolution of calcite and calcium carbonate and phosphate pellets was investigated. The technique involved producing protons via the oxidation of water, which were directed from an ultramicroelectrode, to the surface of interest. Analysis of the resulting cylindrical etch pits was performed using interferometry, and showed that the pit volumes increased with time and applied current (proton flux). The localised dissolution of the (104) calcite plane was then modelled using finite element software assuming that the dissolution process was governed by a first order reaction rate. Using this simulation, the pH profile at the calcite surface and theoretical etch pit profiles were obtained, allowing the rate constant for the dissolution process to be calculated, which was in good agreement with other values in the literature[15,16]. Simulated limescale pellets were also investigated here in order to try to find a good comparative model for real limescale to be used in bulk dissolution experiments. Different compositions of tablets were investigated to find which had similar characteristics to the real scale in terms of dissolution rate.

In Chapter 7, a technique to improve the methodology for studying calcite growth was developed that allows individual calcite microcrystals (10 – 20 μm in

diameter) to be addressed, resulting in the observation of the single spiral growth hillock on the (104) surface, and the subsequent reactivity of this hillock under supersaturated solution conditions. The AFM was combined with an inverted optical microscope which allowed individual microcrystals to be examined. This is the first time that such work has been carried out and allows the reactivity of single crystals to be examined. An important observation was that all of the microcrystals examined displayed only one spiral growth hillock. In other work in the area, only macroscopic crystal surfaces have been investigated, where these contain several, maybe interacting defects and dislocations[17,18]. Here, the reactivity of the crystal is solely influenced by the solution into which it is immersed and not affected by processes occurring elsewhere on the crystal surface. Growth rates of the spiral calcite (104) growth hillock were found to be dependent on solution supersaturation and controlled by diffusion of species to the crystal surface from bulk solution, as opposed to being limited by surface diffusion mechanisms.

Furthermore, in this chapter, the effects of maleic acid on calcite microcrystal growth were investigated. Using this technique it was possible to demonstrate how weak acid affects the growth of crystal surfaces, by causing firstly, vigorous dissolution of the surface, followed by the blocking of sites on the surface, leading to an unusual surface morphology.

Although investigations into calcium carbonate crystal growth and dissolution are well studied, the technique described here makes it possible to fully quantify crystal surface reactivity, by allowing individual microcrystals to be addressed. This allows single features on the surface to be imaged without the interaction of nearby defects and

dislocations. The scope, therefore, for further work in this field, is immense as the growth mechanisms and kinetics of many inorganic (and organic) crystals could be elucidated in this way.

8.1 References

[1] Y. Zhang, H. Shaw, R. Farquhar and R. Dawe, *J. Petrol. Sci. and Eng.*, **2001**, *29*, 85.

[2] T. Chen, A. Neville and M. Yuan, *J. Petrol. Sci. and Eng.*, **2005**, *46*, 185.

[3] Y. Kitano, *Bull. Chem. Soc. Japan*, **1962**, *35*, 1980.

[4] D. Rautaray, P. S. Kumar, P. P. Wadgaonkar and M. Sastry, *Chem Mater.*, **2004**, *16*, 988.

[5] I. Lee, S. W. Han, H. J. Choi and K. Kim, *Adv. Mater.*, **2001**, *13*, 1617.

[6] I. Lee, S. W. Han, S. J. Lee, H. J. Choi and K. Kim, *Adv. Mater.*, **2002**, *14*, 1640.

[7] J. Aizenberg, *J. Cryst. Growth*, **2000**, *211*, 143.

[8] J. Küther, R. Seshardi, W. Knoll and W. Tremel, *J. Mater. Chem.*, **1998**, *8*, 641.

[9] J. Aizenberg, A. J. Black and G. M. Whitesides, *Nature*, **1999**, *398*, 495.

[10] J. Aizenberg, *J. Crystal Growth*, **2000**, *211*, 143.

[11] R. L. Folk, *J. Sed. Petrol.*, **1993**, *63(5)*, 990.

[12] A. K. Contos, J. M. James, B. Heywood, K. Pitt and P. Rogers, *Geomicrobiology Journal*, **2001**, *18*, 331.

[13] L. Clapham, R. J. C. McLean, J. C. Nickel, J. Downey and J. W. Costerton, *J. Cryst. Growth*, **1990**, *104*, 475.

[14] R. J. C. McLean and T. J. Beveridge, *Microbial Mineral Recovery*, ed. H. L. Ehrlich and C. L. Brierley, **1990**, McGraw-Hill Publishing Company, pp. 185-223.

[15] R. G. Compton, K. L. Pritchard and P. R. Unwin, *J. Chem. Soc., Chem. Commun.*, **1989**, *4*, 249.

[16] C. A. Brown, R. G. Compton and C. A. Narramore, *J. Coll. Inter. Sci.*, **1993**, *160*, 372.

[17] H. H. Teng, P. M. Dove, and J. J. DeYoreo, *Geochim. Cosmochim. Acta*, **2000**, *64*, 2255.

[18] H. H. Teng, P. M. Dove and J. J. DeYoreo, *Geochim. Cosmochim. Acta*, **1999**, *63*, 2507.